

1001

NASA Conference Publication 10030

Structural Integrity and Durability of Reusable Space Propulsion Systems

Date for general release April 1991

*Proceedings of a conference held at
NASA Lewis Research Center
Cleveland, Ohio
April 18 and 19, 1989*

(NASA-CP-10030) STRUCTURAL INTEGRITY AND
DURABILITY OF REUSABLE SPACE PROPULSION
SYSTEMS (NASA) 259 p C S C L 21H

N91-24307
--THRU--
N91-24338
Unclas
G3/20 0019857





NASA Conference Publication 10030

Structural Integrity and Durability of Reusable Space Propulsion Systems

*Proceedings of a conference
held at NASA Lewis Research Center
Cleveland, Ohio
April 18 and 19, 1989*

NASA

National Aeronautics and
Space Administration

**Scientific and Technical
Information Division**

1989



CONTENTS

	Page
Foreword	vii
Preface	ix
 SESSION I - FATIGUE, FRACTURE, AND CONSTITUTIVE MODELING Chair, Michael A. McGaw 	
<i>Overview of the Fatigue/Fracture/Life Working Group Program at the Lewis Research Center</i> Michael A. McGaw, NASA Lewis Research Center	1
<i>Application of Cyclic Damage Accumulation Life Prediction Model to High Temperature Components</i> Richard S. Nelson, United Technologies Corp., Pratt & Whitney	5
<i>Notched Fatigue of Single Crystal PWA 1480 at Turbine Attachment Temperatures</i> T.G. Meyer, United Technologies Research Center, and D.M. Nissley and G.A. Swanson, Pratt and Whitney	17
<i>Tensile and Fatigue Behavior of Tungsten/Copper Composites</i> M.J. Verrilli, T.P. Gabb, and Y.S. Kim, NASA Lewis Research Center	25
<i>Cumulative Creep Fatigue Damage in 316 Stainless Steel</i> Michael A. McGaw, NASA Lewis Research Center	33
<i>Fatigue Behavior of a Single-Crystal Superalloy</i> Sreeramesh Kalluri, Sverdrup Technology, Inc., Lewis Research Center Group, and Michael A. McGaw, NASA Lewis Research Center	39
<i>Elevated Temperature Crack Growth</i> K.S. Kim and R.H. Van Stone, GE Aircraft Engines	45
<i>Analysis of Damage in MMC Components Using an Internal State Variable Model</i> V.K. Arya, University of Toledo	53
<i>The Effect of Hydrogen on the Deformation Behavior of a Single Crystal Nickel-Base Superalloy</i> W.S. Walston and A.W. Thompson, Carnegie Mellon University, and I.M. Bernstein, Illinois Institute of Technology	59

<i>The Influence of Advanced Processing on PWA 1480</i>	
L.G. Fritzscheier and G.D. Schnittgrund, Rockwell International	67

SESSION II - INSTRUMENTATION

Chair, William C. Nieberding

<i>Overview of the Instrumentation Program</i>	
William C. Nieberding, NASA Lewis Research Center	81
<i>Two-Dimensional High Temperature Strain Measurement System</i>	
Christian T. Lant, Sverdrup Technology, Inc., Lewis Research Center Group, and John P. Barranger, NASA Lewis Research Center	83
<i>Optical Inspection of Space-Propulsion Components Using an Injection Seeded Nd:YAG Laser System</i>	
Arthur J. Decker, NASA Lewis Research Center	87
<i>Calibrator Tests of Heat Flux Gauges Mounted in SSME Blades</i>	
Curt H. Liebert, NASA Lewis Research Center	99
<i>Development of Fiber-Based Laser Anemometer for SSME Application</i>	
Dariusz Modarress and Robert Fan, Physical Research, Inc.	105
<i>Analysis of the Transient Calibration of Heat Flux Sensors - One Dimensional Case</i>	
A. Dybbs and J.X. Ling, Case Western Reserve University	113
<i>Thin-Film Sensors for Space Propulsion Technology: Fabrication and Preparation for Testing</i>	
Walter S. Kim and Aloysius F. Hepp, NASA Lewis Research Center	123
<i>Rocket Plume Spectrometry - A System Permitting Engine Condition Monitoring, as Applied to the Technology Test Bed Engine</i>	
W.T. Powers, NASA Marshall Space Flight Center	127

SESSION III - STRUCTURAL DYNAMICS

Chairs, Christos C. Chamis and Dale A. Hopkins

<i>Probabilistic Structural Analysis - Introductory Remarks</i>	
Christos C. Chamis	137
<i>Probabilistic Structural Analysis Methods for Select Space Propulsion System Components</i>	
H.R. Millwater and T.A. Cruse, Southwest Research Institute	139
<i>An Approximate Methods Approach to Probabilistic Structural Analysis</i>	
R.C. McClung, H.R. Millwater, Y.-T. Wu, B.H. Thacker, and O.H. Burnside, Southwest Research Institute	145
<i>Probabilistic Boundary Element Method</i>	
T.A. Cruse and S.T. Raveendra, Southwest Research Institute	153

<i>Composite Load Spectra For Select Space Propulsion Structural Components</i> H. Ho and J.F. Newell, Rockwell International Corp., Rocketdyne Division, and R.E. Kurth, Battell Columbus Laboratory	159
<i>Probabilistic Design Analysis Using Composite Loads Spectra (CLS) Coupled with Probabilistic Structural Analysis Methodologies (PSAM)</i> J.F. Newell, K.R. Rajagopal, and H. Ho, Rockwell International Corp., Rocketdyne Division	167
<i>Probabilistic Finite Elements for Fracture and Fatigue Analysis</i> W.K. Liu, T. Belytschko, M. Lawrence, and G.H. Besterfield, Northwestern University	181
<i>Probability of Failure and Risk Assessment of Propulsion Structural Components</i> Michael C. Shiao, Sverdrup Technology, Inc., Lewis Research Center Group	197

SESSION IV - AEROTHERMODYNAMIC LOADS

Chair, Raymond E. Gaugler

<i>Overview of Aerothermodynamic Loads Definition Study</i> Raymond E. Gaugler, NASA Lewis Research Center	209
<i>Heat-Transfer and Surface-Pressure Measurements for the SSME Fuel-Side Turbopump Turbine</i> Michael G. Dunn, Calspan-UB Research Center	215
<i>A New Facility to Study Three Dimensional Viscous Flow and Rotor- Stator Interaction in Turbines - A Progress Report</i> B. Lakshminarayana and C. Camci, Pennsylvania State University, and I. Halliwell, General Electric Co.	223
<i>An Unconditionally Stable Runge-Kutta Method for Unsteady Rotor- Stator Interaction</i> Rodrick V. Chima and Philip C.E. Jorgenson, NASA Lewis Research Center	237
<i>Average-Passage Flow Model Development</i> John J. Adamczyk, NASA Lewis Research Center, Mark L. Celestina, Tim A. Beach, and Kevin Kirtley, Sverdrup Technology, Inc., Lewis Research Center Group, and Mark Barnett, United Technologies Research Center	247



FOREWORD

As we enter the sixth year of the program to improve the structural integrity and durability of reusable space propulsion systems, it is time to reflect on where we were, where we are, and where we hope to be.

The program was initiated in late 1983 when the NASA Office of Space Flight (OSF) recognized a deficiency in the space shuttle main engine (SSME) technology base and decided to augment the Earth-to-Orbit Propulsion Technology Program sponsored by the Office of Aeronautics and Space Technology (OAST). That deficiency was the inability to predict the life of structural components in high-performance reusable rocket engines. It was manifested by the SSME component replacement and repair requirements. Development of the analytical models for aerothermodynamic loads, structural response, and fatigue/fracture effects was therefore undertaken to produce more accurate life prediction design tools.

Today, several hundred government, industry, and university technologists are involved in establishing the reusable rocket engine design data base. Products of their involvement can be seen in the designs of the advanced launch system (ALS), heavy lift launch vehicle (HLLV), and chemical transfer or orbit transfer vehicle. Developments of a three-dimensional viscous code for multi-stage turbines, of probabilistic structural analysis codes, and of the understanding of the interaction between high and low cycle fatigue are examples of the strides made to date. Advanced instrumentation techniques have been proceeding in parallel to enable validation/calibration of those codes in technology test-bed applications. Fiber optic systems, heat flux gauges, and thin-film sensors developed under this program are now finding their way into propulsion test facilities.

Life prediction algorithms will be utilized in health management and diagnostic expert systems to reduce ground testing maintenance operations and turn-around times. As confidence grows in accuracy, flight systems will be developed. Eventually, these expert systems will be allowed to "close the loop" and provide real-time engine control to prevent operational failures and guarantee mission success.

This third biannual conference provided a forum for representatives from government, industry, and academia to learn about and discuss the latest findings and progress. Extended abstracts and the figures used for each of the presentations at the two-day conference are included in these proceedings.

Sol Gorland
Conference Chairman



PREFACE

A major part of the NASA technology program is focused on advanced propulsion systems designed to meet the future Earth-to-orbit (ETO) space transportation needs of the agency. The objective of this program is to provide the technology base that will allow the design, development, and operation of advanced propulsion systems with pre-defined, predictable performance, service life, and operational characteristics needed to significantly reduce the life-cycle-costs of the ETO vehicles in which they are to be used, whether these vehicles are expendable, partially or fully reusable, manned or unmanned.

A major objective of the ETO propulsion program is to significantly enhance knowledge and understanding of fundamental rocket engine chemical and physical processes. From this understanding will come the ability to analytically simulate internal engine environments; to define steady and unsteady thermal and mechanical loads that these environments impose on critical engine components, as well as the resulting component material behavior and structural response; and to define failure mechanisms and to develop accurate component life predictions. With these tools in hand, means for making internal environments less hostile, as well as for developing design methodologies that will result in more load resistant component designs, will be explored, leading to greatly increased design margins and longer component life and/or increased component performance. Another major objective of the program is to develop technologies for reducing ground operations costs and for ensuring safer, more reliable flight operations through the development and demonstration of on-board integrated condition and safety monitoring systems.

The Structural Integrity and Durability Program is a key part of the first objective and is currently focused on the hot gas sections of typical rocket engines, particularly the hot gas flow through the turbine stages. Specific areas of effort, the status of which will be reviewed during this conference include hot gas flow characterization (CFD), aerothermo loads definition, material behavior and structural analyses (including probabilistic theories), fracture mechanics, high cycle/low cycle fatigue life prediction, and research instrumentation.

The Space Shuttle Main Engine (SSME) development program has provided a unique opportunity to identify technology deficiencies and to initiate the pursuit of technology solutions to overcome these deficiencies. These advanced technologies will be used primarily for the design and development of advanced ETO engines of the future, although the SSME has already benefited to a significant degree from this technology focus. The SSME will also be used as a testbed to verify and validate many of the resulting analytical techniques and design methodologies, as will the large scale combustor and turbomachinery subsystems testbeds that are now an integral part of the ETO propulsion technology program.

Earl VanLandingham
NASA Headquarters
Washington, D.C.



51-39
19858

**OVERVIEW OF THE FATIGUE/FRACTURE/LIFE WORKING GROUP PROGRAM
AT THE LEWIS RESEARCH CENTER**

**Michael A. McGaw
NASA Lewis Research Center
Cleveland, Ohio**

The objective of the Fatigue/Fracture/Life Working Group at Lewis is to develop and verify constitutive and life prediction models for materials typically used in hot gas path components of reusable space propulsion systems over the range of relevant operating environments. The efforts at Lewis have centered on the development of crack initiation life prediction methods, while the efforts of our counterpart group located at the Marshall Space Flight Center have centered on the development of cyclic crack propagation life prediction methods.

The complexion of active tasks is shown in figure 1. The program is a blend of in-house, contract, and grant research. Significant progress has been made during the past year; the papers presented in this session represent contributions from most, but not all, of the tasks currently active in this program.

A significant new task started this year will incorporate the various material constitutive and life prediction models (including materials properties data) developed in this program into a comprehensive creep-fatigue damage analysis and life assessment computer code (fig. 2). The program will function as a postprocessor to general structural analysis programs (such as finite element or boundary element codes) using the output of such analyses (stress, strain, and temperature fields as functions of time) as the input to the damage analysis and life assessment code. The code will be designed to execute on engineering/scientific workstations and will feature a windowing, mouse-driven user interface. Current plans call for the code to be finished and made available for use in mid 1991.

CURRENT STRUCTURAL DURABILITY PROGRAMS AND GOALS

MACROSCOPIC EFFECTS OF HIGH PRESSURE HYDROGEN ON CONSTITUTIVE AND LIFE MODELS

- ESTABLISH VALIDITY OF STRUCTURAL DURABILITY MODELS DEVELOPED UNDER THE PROGRAM

HCF/LCF INTERACTION UNDER MISSION-RELATED LOADING

- INTERSPERSED HCF AND LCF LOADINGS
- TMF INTERACTION WITH HCF LOADINGS
- CUMULATIVE CREEP-FATIGUE INTERACTIONS

APPLICATION OF CONSTITUTIVE AND LIFE MODELS IN STRUCTURAL ANALYSIS

- APPLY MODELS DEVELOPED TO SSME COMPONENTS

THERMAL RATCHETING DAMAGE ANALYSES

- INTERACTION OF RATCHET STRAINS WITH TMF AND HCF
- APPLICATION TO MAIN COMBUSTION CHAMBER MATERIALS

CD-89-39970

CURRENT STRUCTURAL DURABILITY PROGRAMS AND GOALS

ADVANCED CONCEPT MATERIALS MODELS DEVELOPMENT

- METAL MATRIX COMPOSITES MODELING: MATERIAL CONSTITUTIVE AND LIFE MODELS

CYCLIC CRACK GROWTH UNDER THERMOMECHANICAL LOADING CONDITIONS

- APPLICATION OF PATH INDEPENDENT INTEGRALS TO THE DESCRIPTION OF THE CRACK DRIVING FUNCTION

SINGLE CRYSTAL CONSTITUTIVE AND LIFE MODEL DEVELOPMENT

- ANISOTROPIC CONSTITUTIVE AND LIFE MODELS
- ANALYSIS METHODOLOGY FOR ADDRESSING BLADE ROOT ATTACHMENTS

CREEP-FATIGUE DAMAGE ANALYSIS PROCESSOR

- INTEGRATE CONSTITUTIVE AND LIFE PREDICTION MODELS, AS WELL AS RELEVANT MATERIALS PROPERTIES DATA INTO A DAMAGE ANALYSIS AND LIFE ASSESSMENT COMPUTER CODE

CD-89-39971

CREEP-FATIGUE DAMAGE ANALYSIS PROCESSOR

- COMPREHENSIVE COMPONENT DAMAGE ANALYSIS AND LIFE ASSESSMENT SYSTEM
- MOUSE-DRIVEN WINDOWING USER INTERFACE IN A PORTABLE SOFTWARE PACKAGE

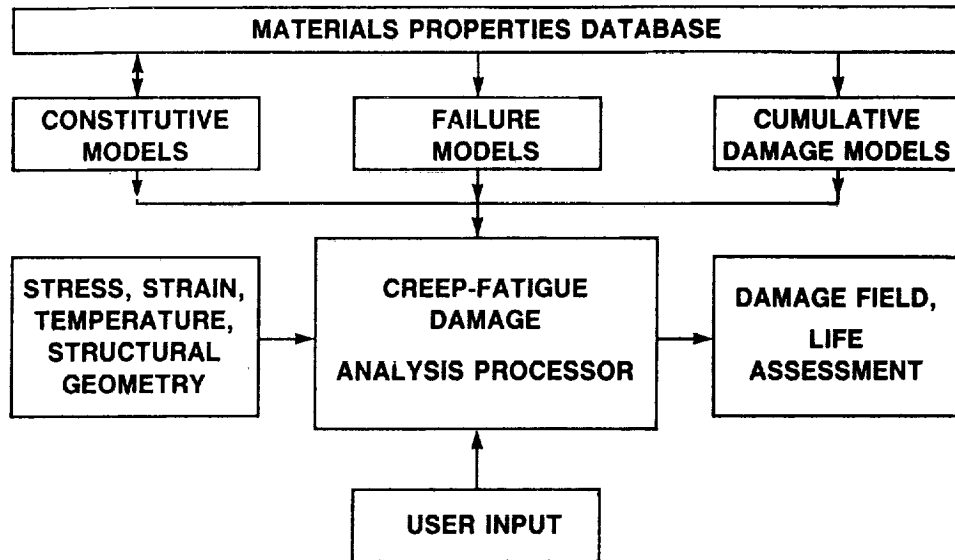


Figure 2

CD-89-39972



APPLICATION OF CYCLIC DAMAGE ACCUMULATION LIFE PREDICTION MODEL
TO HIGH TEMPERATURE COMPONENTS

Richard S. Nelson

United Technologies Corporation
Pratt & Whitney
E. Hartford, Connecticut52-39
19859

INTRODUCTION

A high temperature, low cycle fatigue life prediction method has been developed by Pratt & Whitney under the sponsorship of the Lewis Research Center (Moreno et al, 1984). This method, Cyclic Damage Accumulation, has been developed for use in predicting the crack initiation lifetime of gas turbine engine materials, but it can be applied to other materials as well. The method is designed to account for the effects on creep-fatigue life of complex loadings such as thermomechanical fatigue, hold periods, waveshapes, mean stresses, multiaxiality, cumulative damage, coatings, and environmental attack (Nelson et al, 1986). Several features of the model were developed to make it practical for application to actual component analysis, such as the ability to handle non-isothermal loadings (including TMF), arbitrary cycle paths, and multiple damage modes.

The CDA life prediction model was derived from extensive specimen tests conducted as part of the contract activity on the cast nickel-base superalloy B1900+Hf. These included both monotonic tests (tensile and creep) and strain-controlled fatigue experiments (uniaxial, biaxial, TMF, mixed creep-fatigue, and controlled mean stress). Additional specimen tests were conducted on wrought INCO 718 to verify the applicability of the final CDA model to other high-temperature alloys. The model will be available to potential users in the near future in the form of a FORTRAN-77 computer program.

FEATURES OF CDA LIFE PREDICTION MODEL

The CDA model is based on the fundamental assumption that an instantaneous damage rate can be calculated and integrated on a cycle-by-cycle basis until a damage of unity is achieved. The current constants in the program reflect the definition of damage as the initiation of detectable cracks (0.030 in. {0.76 mm.}) at the location being considered. Other definitions of damage may also be modeled by recalibration of the various constants. Different rates are calculated simultaneously for whatever modes of damage may apply to a particular material. Currently defined modes in the CDA program include transgranular and intergranular fatigue, oxidation, and coating cracking.

One of the most significant features of the CDA model is its use of ratios of stress/strain parameters rather than absolute levels. This technique greatly simplifies practical application of the model to actual

Work performed under NASA Contract NAS3-23288; Dr. Gary R. Halford, LeRC, serves as NASA Technical Monitor.

components, since these ratios are generally easier to calculate than the absolute levels. The model also makes use of total strain rather than inelastic strain; this avoids the problem of having to calculate the very small inelastic strains associated with the typically high design lives for components made of modern superalloys. The transgranular damage model incorporates a loading history term derived from primary creep data. This captures the effects of overloads and other previous load excursions which can set up compliant dislocation structures and thereby affect subsequent fatigue behavior. Mean stress effects are handled through an exponential term based on the ratio of maximum cycle stress to a reference maximum stress. Subcycles are determined by the computer program using the traditional rainflow cycle counting method, based on reversals of stress range ratio rather than stress or strain alone.

Temperature effects are very important to any high temperature model, and these are included in the CDA transgranular model in several ways. First, time dependence (hold time, strain rate, etc.) is introduced through the use of a multiplier term based on the integral of an Arrhenius function. This will automatically handle any arbitrary periodic waveform, eliminating the need to estimate average strain rate, frequency, or other such parameters from a component loading history. Second, an additional strain term is postulated to result from microscopic thermal expansion mismatch within the material structure. This is added to the macroscopic total strain, and the resulting strain range is used by CDA to compute the life. Finally, temperature effects are included implicitly through the temperature dependence of certain reference stress/strain quantities.

The second major damage mode currently active in the CDA model is the intergranular mode. This is based on an integral of an Arrhenius function which is calibrated to data from creep testing. This was found adequate for many components which fail simply from cyclic loadings in the creep regime. Other damage modes include cyclic oxidation (which modifies the transgranular damage term) and coating cracking (based on the coating life model from a companion NASA contract {Swanson et al, 1987}).

APPLICATION TO HIGH TEMPERATURE COMPONENTS

The CDA computer program is designed to accept one or more "defined cycles" for which a complete stress/strain/temperature/time history is known. These may be obtained from several sources, including simplified methods or full inelastic analysis programs. The program accepts this data (interpolating where required) and directly integrates the rates of the various damage modes until one of them reaches unity.

REFERENCES

Moreno, V., Nissley, D. M., and Lin, L. S., 1984, "Creep Fatigue Life Prediction for Engine Hot Section Materials (Isotropic) Second Annual Report," NASA CR-174844.

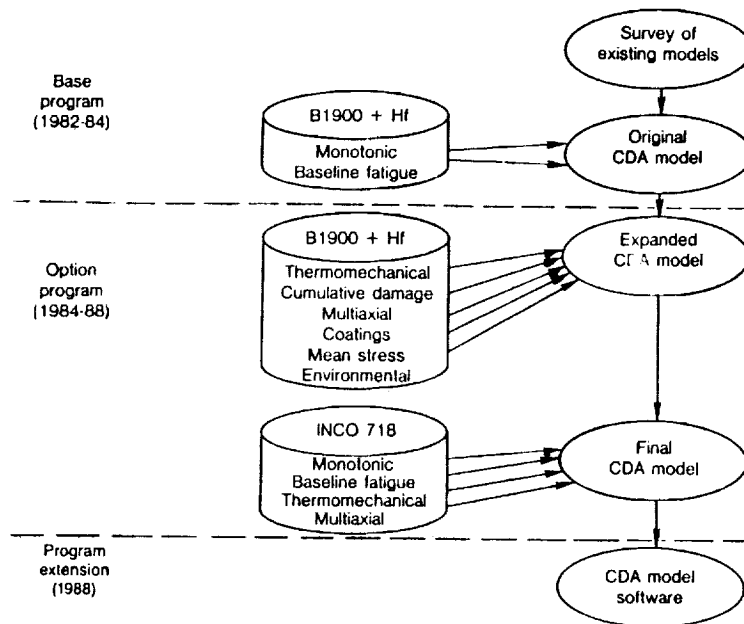
Nelson, R. S., Schoendorf, J. F., and Lin, L. S., 1986, "Creep Fatigue Life Prediction for Engine Hot Section Materials (Isotropic) Interim Report," NASA CR-179550.

Swanson, G. A., Linask, I., Nissley, D. M., Norris, P. P., Meyer, T. G., and Walker, K. P., 1987, "Life Prediction and Constitutive Models for Engine Hot Section Anisotropic Materials Program," NASA CR-179594.

OVERVIEW

- Summary of Contract Activities
- Features of CDA Life Prediction Model
- Application to High Temperature Components
- Future Research

THE CDA METHOD IS BASED ON EXTENSIVE HIGH TEMPERATURE SPECIMEN TESTING



CDA MODEL BEGINS WITH INTEGRATION OF DAMAGE RATES FOR MULTIPLE MODES

For use as a practical design method, "Damage = 1" is defined as initiation of a 0.030 in. (0.76 mm.) surface length crack

- The basic equation for CDA is simply an integration of damage rate from 0 to 1:

$$1 = \int_0^1 \frac{dD}{dN} dN \quad (1)$$

- This same calculation is performed simultaneously for multiple modes of damage, as required for a given material. Currently defined modes include:

1. Transgranular fatigue
2. Intergranular fatigue
3. Oxidation / environmental damage
4. Interactions of the above

TRANSGRANULAR DAMAGE MODEL UTILIZES A STRESS AND STRAIN RATIO CONCEPT

Absolute inelastic strains can be small and difficult to predict reliably for many nickel-base superalloys

- The damage rate is calculated using the ratio of current parameters to reference values:

$$\frac{dD}{dN} = \left(\frac{1}{N_{REF}} \right) \left(\frac{\Delta \epsilon_T}{\Delta \epsilon_{T, REF}} \right)^{\eta_1} \left(\frac{\Delta \sigma}{\Delta \sigma_{REF}} \right)^{\eta_2} \left(\frac{\epsilon_{P, REF}}{\epsilon_P} \right) \quad (2)$$

- A loading history parameter derived from primary creep data is also included:

$$\left(\frac{\epsilon_P}{\epsilon_{P, REF}} \right) = f_{\epsilon_P} \left(\frac{\sigma_{MAX}}{\sigma_{\epsilon_P, REF}} \right)_{MAX, HISTORY} \quad (3)$$

TWO ADDITIONAL TERMS WERE NECESSARY TO PREDICT BASELINE FAST RATE DATA

- The first predicts mean stress and R-ratio effects using a ratio based on maximum tensile stress:

$$\frac{dD}{dN_{\text{BASIC}}} = \frac{dD}{dN} e^{\left(\frac{\sigma_{\text{MAX}}}{\sigma_{\text{MAX,REF}}}\right)} \quad (4)$$

- A threshold strain range was necessary to predict the high life, low strain data for both B1900+Hf and INCO 718:

$$\Delta\epsilon_T = \Delta\epsilon_{\text{TACTUAL}} - \Delta\epsilon_{\text{TTHRESHOLD}} \quad (5)$$

STRAIN RATE EFFECTS CAN BE PREDICTED FOR ANY ARBITRARY WAVEFORM

Permits direct application of CDA to practical component cycles

- The basic transgranular damage rate (product of the previous terms) is modified by a time & temperature dependent term:

$$f_{\text{TD}} = 1 + \int A_1 e^{B_1 \sigma} e^{-\left(\frac{Q_1}{RT}\right)} dt \quad (6)$$

- This eliminates the need to estimate hold time, average frequency, or other similar parameters for complex loading cycles typically experienced by modern high temperature components

CLASSICAL CUMULATIVE DAMAGE EFFECTS ARE ALSO PREDICTED BY THE CDA MODEL

Real components see a spectrum of loads during their service life

- Non-linear damage accumulation is included in a modifying function for the basic transgranular damage rate:

$$G(D) = (1-f_L) (\beta+1) D^\beta + f_L \quad (7)$$

$$\text{where } \beta = \left(\frac{B_{NL}}{dD/dN_{BASIC}} \right)^\alpha \quad (8)$$

- Subcycles are computed using the rainflow cycle counting method based on reversals of stress range ratio
- The primary creep ductility term automatically reduces the damage done by subcycles when their maximum stress is lower than that of the major cycle

THE RATIO CONCEPT PERMITS CDA TO HANDLE NON-ISOTHERMAL LOADING

Many practical applications involve varying temperature

- The reference stresses and strains are functions of temperature for each material in the CDA library

This is sufficient for variable temperature components below the range where TMF is a concern

- For TMF, an additional strain due to thermal expansion coefficient mismatch was necessary to correlate the data:

$$\epsilon_{TMF} = \int_0^t \Delta \alpha(T) \dot{T} dt \quad (9)$$

THE SECOND DAMAGE MODE PREDICTS INTERGRANULAR FAILURE MECHANISMS

Often components fail by cyclic loads which result in failure by creep mechanisms, not fatigue

- The damage rate for this mode is based on an Arrhenius function, but with constants which are different from those used for the transgranular mode:

$$\frac{dD}{dN} = \int A_2 e^{B_2 \sigma} e^{-\left(\frac{Q_2}{RT}\right)} dt \quad (10)$$

- This rate is integrated cycle-by-cycle along with the transgranular damage rate (and any other active modes) until some mode reaches a value of unity

ENVIRONMENTAL DAMAGE CAN BE INCLUDED FOR CYCLIC AND STATIC OXIDATION

Certain components can switch between these modes, depending on how they are operated

- For cyclic oxidation, a multiplier factor based on a time-temperature dependent integral is added to the transgranular damage model
- For static oxidation, a separate third damage mode can be calculated which depends only on time and temperature, not cyclic variables such as stress or strain

INTERACTIONS BETWEEN DAMAGE MODES CAN BE EASILY INCORPORATED

- Where interactions are observed among the various damage modes (creep/fatigue/environment), these are handled by combining damage levels from those modes and integrating the result as a separate mode
- Almost any type of interaction may be modeled using this technique:
 1. Linear (additive)
 2. Non-linear
 3. Power law

COATING LIFE PREDICTIONS UTILIZE THE MODEL FROM A COMPANION CONTRACT

Many modern superalloys must be coated for oxidation protection in actual service; this must be accounted for by a practical system

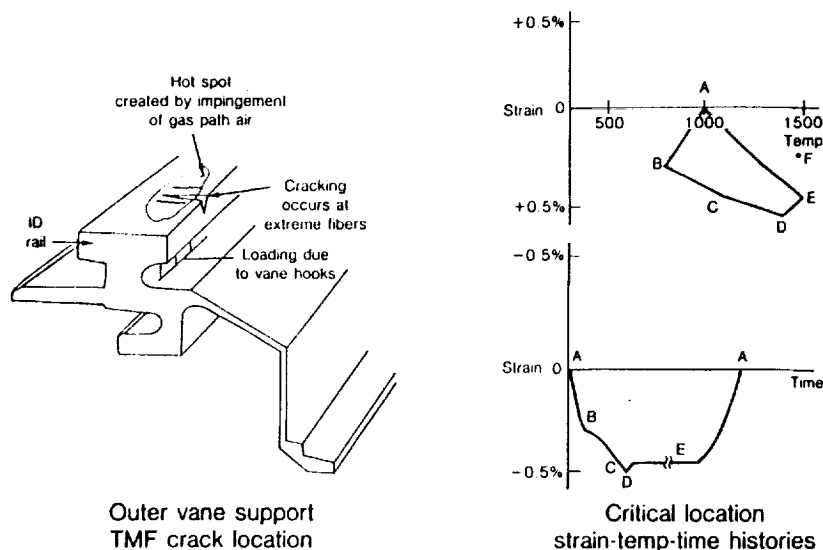
- First, a viscoplastic constitutive model is used to predict the local stress/strain history in the coating itself
- This coating stress/strain history is next used to predict coating cracking life (through the coating thickness)
- Finally, this life is converted to an equivalent damage rate which can be integrated along with the other active damage modes for the substrate material

MULTIAXIAL STRESS/STRAIN STATES ARE CONVERTED TO EQUIVALENT CDA VALUES

Many actual components are analyzed using 3-D methods which produce full tensors; these must be interpreted by a practical life system

- The applied stress/strain tensors are transformed into 100 different axis orientations in the plane of the component surface to search for the crack plane (with the "worst" orientation)
- Two different algorithms are currently implemented for choosing the plane which experiences the worst damage:
 1. Maximum normal strain range
 2. Socie parameter (combination of shear and normal)
- New materials may use these or choose some other appropriate parameter

THE EFFECTS OF COMPLEX STRAIN AND TEMPERATURE HISTORIES MUST BE DETERMINED FOR ACCURATE LIFE PREDICTIONS



CDA USES THE GIVEN STRESS/STRAIN HISTORY DIRECTLY TO PREDICT LIFE

- The CDA program accepts as input one or many "defined cycles" for which a full stress/strain history is known. These may come from many sources:
 1. Actual rig data taken during specimen testing
 2. Simplified methods using elastic input
 - a. Neuber's rule
 - b. Integrated energy density
 3. Full inelastic analysis methods
 - a. Finite element
 - b. Boundary integral equation
- The program performs semi-log interpolation of damage rates to determine intermediate values between the defined cycles

THE CDA PROGRAM CAN BE EASILY EXPANDED FOR NEW MATERIALS OR METHODS

"The only thing constant is change ..."

- The current CDA equations are sufficient for most current nickel-base alloys; a new set of constants can be generated for materials other than B1900+Hf or INCO 718
- The program is modular so that new equations, damage modes, or even completely different life prediction methods can be added if desired
- The program is written in standard FORTRAN-77 and has run on machines from PC's to mainframes; source code will be available for distribution soon

FUTURE RESEARCH

Practical methods must undergo continuous improvement and continue to adapt to new materials and analytical methods

- The extensive database for B1900+Hf, including both constitutive and creep-fatigue data, provides an excellent opportunity for evaluating new prediction methods
- TMF cycle path effects (such as CW vs. CCW elliptical cycles) are not fully explained by the current CDA formulation; possible new methods include:
 1. Equilibrium stress/strain methods
 2. Micromechanical models
- The CDA model could be applied to the constituent materials in advanced systems such as metal matrix composites



NOTCHED FATIGUE OF SINGLE CRYSTAL PWA 1480
AT TURBINE ATTACHMENT TEMPERATURES

53-39
19860

T. G. MEYER, UNITED TECHNOLOGIES RESEARCH CENTER
D. M. NISSLEY AND G. A. SWANSON, PRATT & WHITNEY
EAST HARTFORD, CONNECTICUT

This paper presents results obtained under Option 1 of NASA contract NAS3-23939, "Life Prediction and Constitutive Models for Engine Hot Section Anisotropic Material". The Option 1 portion of this contract is focused on the lower temperature, uncoated and notched features of gas turbine blades. Constitutive and fatigue life prediction models applicable to these regions are being developed. This paper will present fatigue results obtained thus far. The program will continue throughout the current year.

Fatigue tests are being conducted on PWA 1480 single crystal material using smooth strain controlled specimens and three different notched specimens. The smooth fatigue specimens have a circular cross section and a one inch gage length. The notched specimen configurations are shown in Figure 1. The threaded ends of the thick specimen are not shown in Figure 1. The relative orientation of the geometric and crystallographic axes are uniquely defined by a specimen's primary orientation, \underline{P} , (corresponding to the loading direction and also to the crystal growth direction of the bars from which the specimen is machined) and its secondary orientation, \underline{S} , (corresponding to the direction normal to the notch). Six different notched specimen orientations will be tested in the program. Thus far, notched fatigue tests have been conducted on three of these orientations: $\langle 001 \rangle$, $\langle 100 \rangle$, $\langle 001 \rangle$, $\langle 210 \rangle$, and $\langle 111 \rangle$, $\langle 011 \rangle$.

Isothermal fatigue tests have been conducted at 1200°F, 1400°F and 1600°F. The bulk of the tests have been conducted at 1200°F and are presented here. The strain controlled tests were conducted at 0.4% per second strain rate and the notched tests were cycled at 1.0 cycle per second. Previous tests have shown no material rate dependence at 1200°F. A clear orientation dependence is observed in the smooth strain controlled fatigue results as shown in Figure 3. Figure 4 indicates that much of this apparent orientation dependence is reduced when the life data is plotted versus stress range. The fatigue lives of the thin, mild notched specimens agree fairly well with this smooth data as shown in Figure 5 when elastic stress range is used as a correlating parameter. Finite element analyses were used to calculate notch stresses. The finite element meshes used in the analyses are shown in Figure 1.

In the notched specimens, the locations of maximum principal stress, maximum principal strain and maximum octahedral slip system shear stress do not always coincide.

Fatigue cracks initiate at micropores at the maximum principal stress location and the crack plane is normal to the principal stress. Final fracture occurs along a $\langle 111 \rangle$ crystal plane. Figure 6 shows the initiation site and final crack planes for a thin, mild notched specimen. In this specimen, the maximum principal strain occurs at the minimum cross section while the maximum principal stress is calculated to occur 26 degrees from the minimum section point. In the smooth specimens, cracks initiate at pores near the surface on planes perpendicular to the applied stress.

Even though the data shown in Figure 5 appears to be fairly well correlated, a closer examination shows that some orientation dependence is still manifested. This can be seen clearly in the statistical distribution of the data about the mean trend line as shown in Figure 7; all $\langle 111 \rangle$ specimens have lives greater than the mean trend line. This indicates that the fatigue models being developed cannot depend solely upon stress range.

Two of the notched specimens being tested can be considered to be thick in that the ratio of actual thickness to notch radius is greater than or equal to 1.0. Figure 8 shows that these specimens exhibit a somewhat different life trend from the thin specimens. These results indicate that correlating parameters should include the effect of the transverse stress.

When the material is hot isostatically pressed (HIP) to remove casting micropores, a clear improvement in fatigue life is observed as shown in Figure 9. The initiation sites are again at the maximum principal stress location with the crack plane normal to the principal stress.

Fatigue testing will continue to further explore the trends observed thus far. Constitutive and life prediction models are being developed.

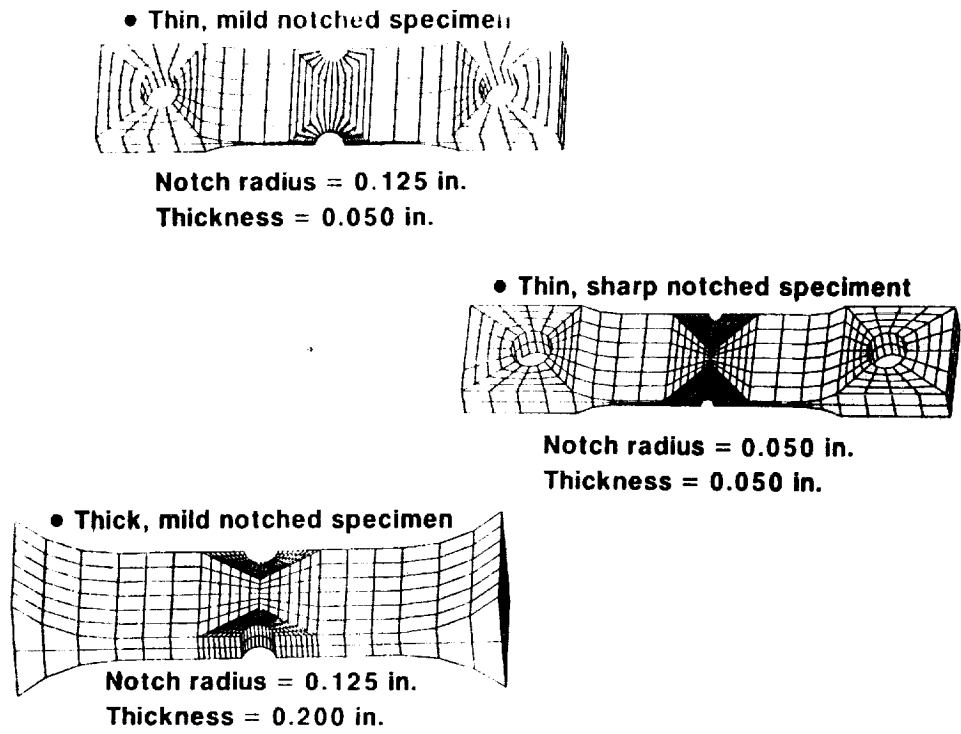


Figure 1. Notched fatigue specimen geometries and finite element meshes used to determine notch stresses.

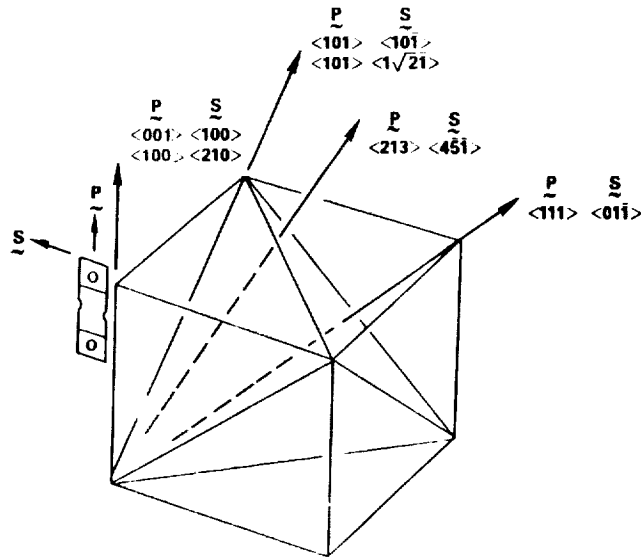


Figure 2. Notched specimen orientations that will be tested.

1200F PWA 1480 STRAIN CONTROLLED FATIGUE

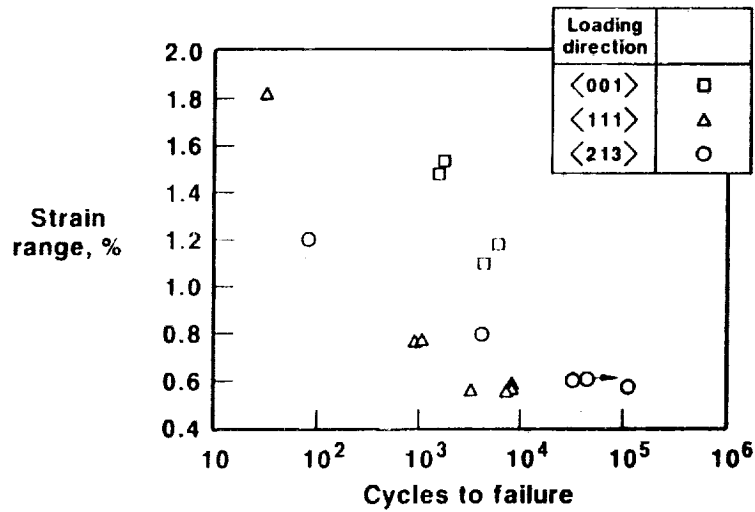


Figure 3. A clear orientation dependence is seen in the smooth strain controlled fatigue lives when plotted versus strain range.

1200F PWA 1480 STRAIN CONTROLLED FATIGUE

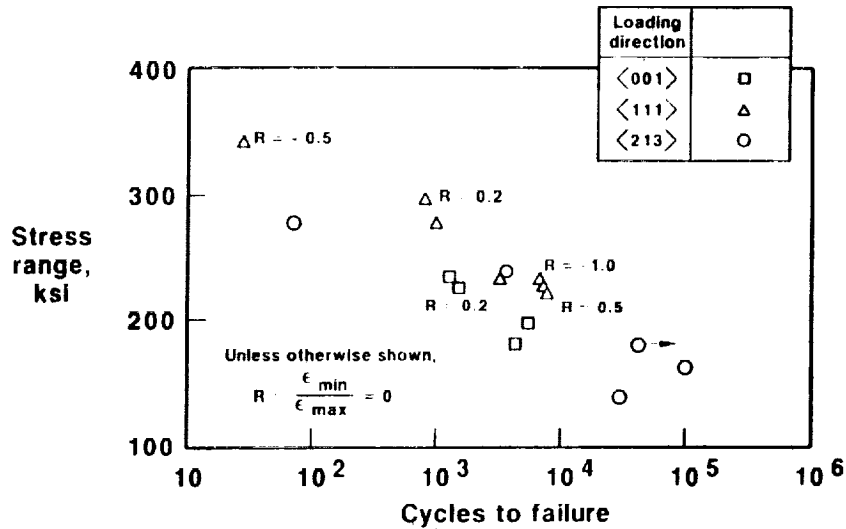


Figure 4. Stress range is a better life correlating parameter.

1200F PWA 1480 FATIGUE
Uniaxial and mild notched specimens

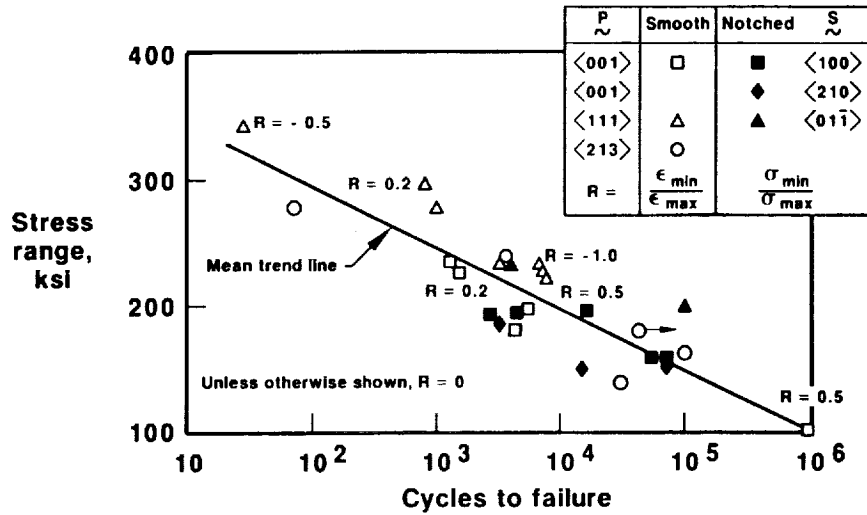


Figure 5. Mild notched and smooth strain controlled lives follow the same trend line.

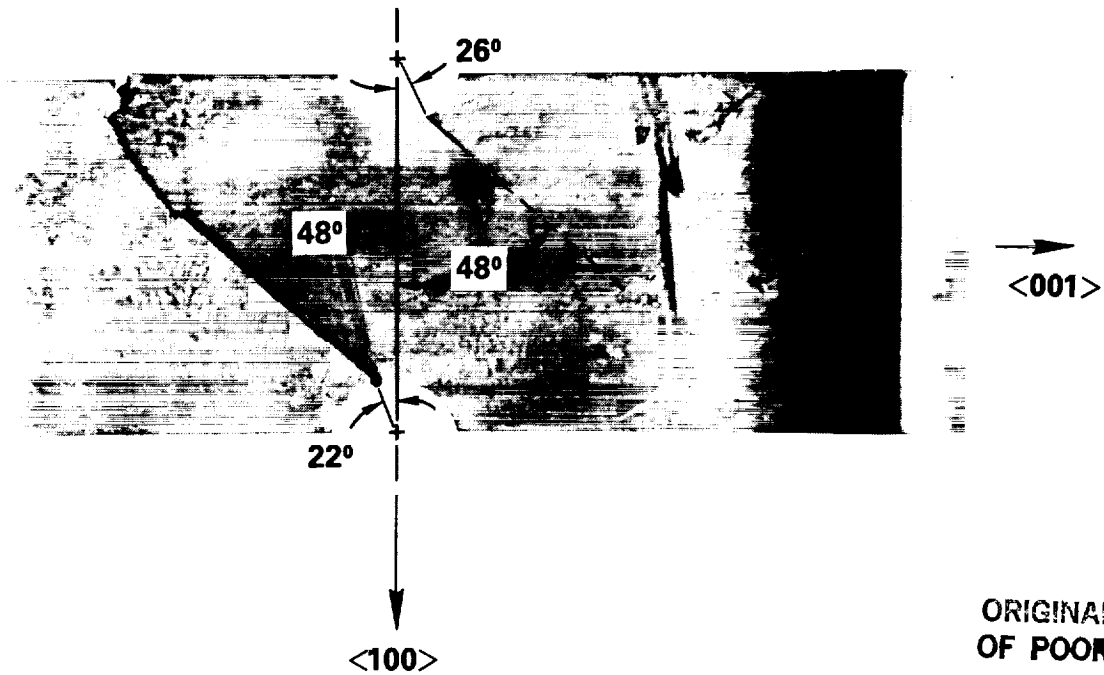


Figure 6. Fatigue cracks initiate at the maximum principal stress location with crack planes perpendicular to the principal stress. Cracks progress along $\langle 111 \rangle$ planes in the final stages of crack growth.

STATISTICAL DISTRIBUTION ABOUT MEAN TREND LINE

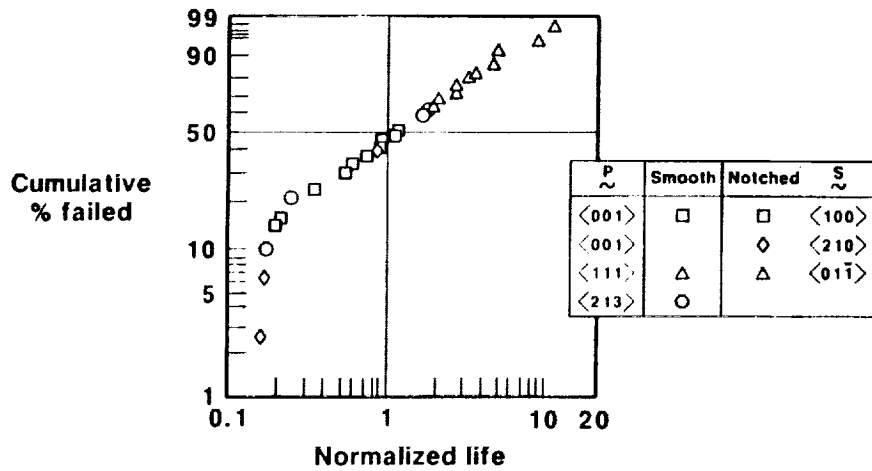


Figure 7. The statistical distribution of failure lives relative to the mean trend line shows that all <111> specimens have lives greater than the mean trend.

1200F PWA 1480 FATIGUE
Effect of thickness

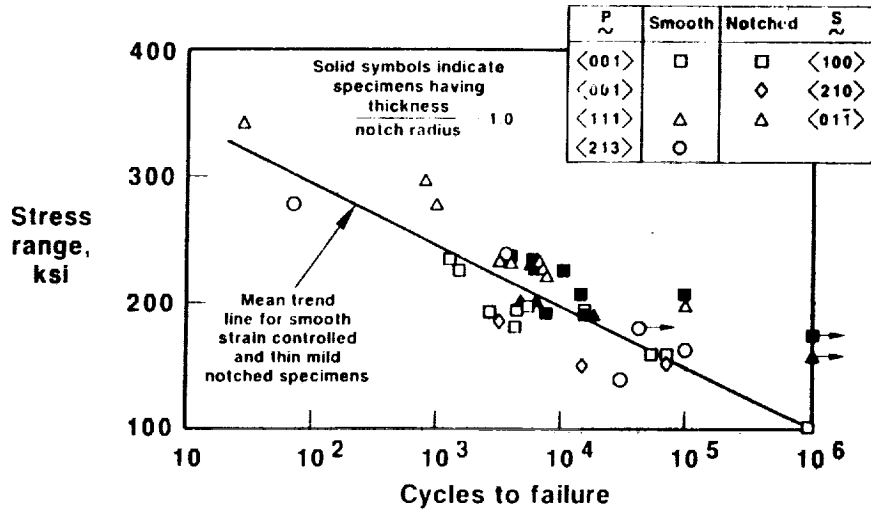


Figure 8. Thin, sharp notched and thick, mild notch specimens display a life trend different than the thin mild notch and smooth specimens.

1200F PWA 1480 FATIGUE
Effect of HIP on thin and smooth specimens

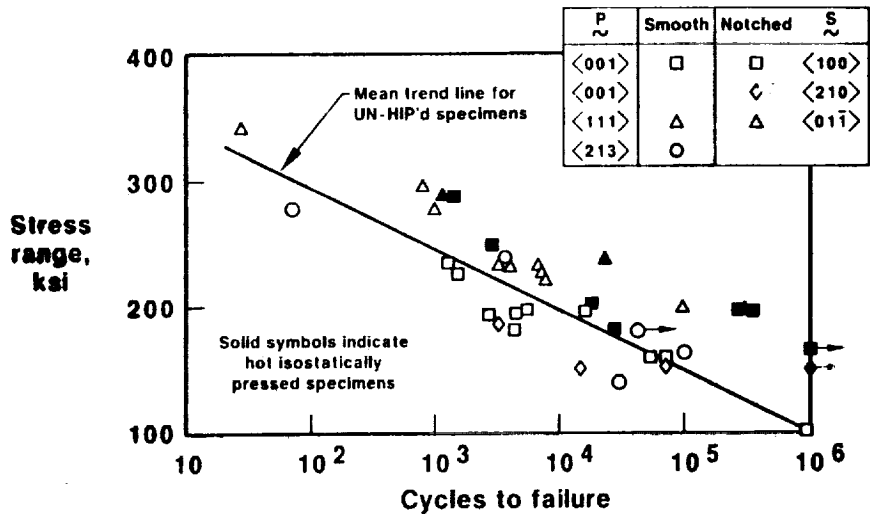


Figure 9. Fatigue life is improved by hot isostatic pressing.



54-24
19861**TENSILE AND FATIGUE BEHAVIOR OF TUNGSTEN/
COPPER COMPOSITES****M.J. Verrilli, T.P. Gabb, and Y.S. Kim
NASA Lewis Research Center**

Work on W/Cu unidirectional composites was initiated to study the behavior of this ductile-ductile composite system under thermomechanical fatigue and to examine the applicability of fatigue-life prediction methods for thermomechanical fatigue of this metal matrix composite.

The first step has been to characterize the tensile behavior of four ply, 10 vol.% W/Cu plates at room and elevated temperatures. Since it is envisioned that unidirectional composites in service will likely see off-axis stresses, the tensile behavior of four fiber orientations are being studied: 0°, 5°, 15°, and 90° (where fiber orientation is the angle between the applied stress and the fiber direction). The 0° and 90° tests are the upper and lower bounds of tensile strength and modulus. The 5° and 15° tests are intermediate cases. Strain-controlled experiments at 25 and 260 °C have been performed to date. At 25 °C the tensile strength, yield strength, and modulus of the 0°, 5°, and 15° specimens were about the same. The 90° specimen had lower strengths and modulus. At 260 °C the strengths and the modulus were largest for the 0° specimen and decreased as the orientation angle increased. These properties were consistent with the rule of mixtures at both temperatures. The yielding behavior of the 0°, 5°, and 15° specimens was discontinuous at 25 °C but was smooth at 260 °C.

The fracture surfaces of the 0°, 5°, and 15° specimens had the same predominant features. Fiber pullout predominated, but, because of a very strong fiber-matrix bond, the W fiber surfaces have tightly adhered Cu matrix scales, covering about 20 to 25 percent of the fiber surface. Ductile microvoid coalescence predominates in the copper matrix. Longitudinal sections of the failed specimens reveal that the fibers each have multiple breaks, up to 25 to 50 mm from the fracture surface. Upon closer examination, each individual fiber break is found to be two closely spaced fiber fractures.

The 90° specimens fail by transverse splitting of the fibers. The matrix between the fibers fails by ductile microvoid coalescence. The fibers remain very well bonded to the matrix, with no significant debonding even on the fracture surface. The fibers are all split up to 35 mm away from the fracture surface. Some of these splits start inside the fibers, away from the machined surface, although most of the observed fibers had at least one wide split, which extended across the width of the specimen.

Fatigue experiments were conducted in load control on 0° specimens at 260 °C. The maximum cyclic stress was varied but the minimum cyclic stress was kept constant. Cycle frequency was about 3 cpm, which gave strain rates similar to those used in the tensile tests. All tests were performed in vacuum.

The cyclic mean strain increased throughout the fatigue tests, suggesting that there may be a creep fatigue process controlling the failure. The elastic modulus remained constant until just before failure. The strain at failure increased with increasing maximum cyclic stress.

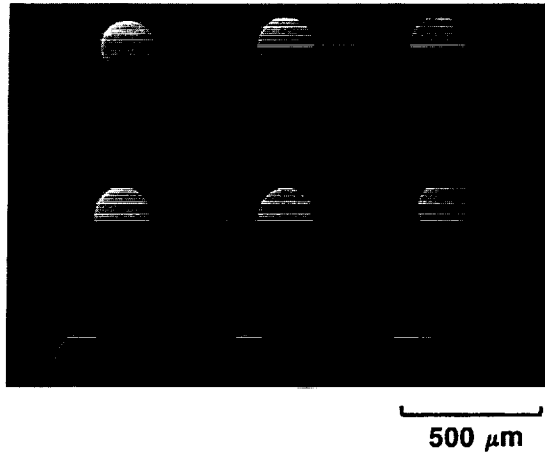
Future experimental work will include fatigue at 550 °C and thermomechanical fatigue between 260 and 550 °C. In addition, the availability of a 12-ply composite plate should enable fully reversed, strain-controlled fatigue to be performed. The applicability of currently available life prediction techniques to the data generated will be examined.

OUTLINE

- 1. MATERIAL AND TEST PROCEDURES**
- 2. TENSILE BEHAVIOR**
- 3. FATIGUE BEHAVIOR**
- 4. SUMMARY**
- 5. FUTURE WORK**

CD-89-39162

TUNGSTEN-FIBER-REINFORCED COPPER



9 VOLUME PERCENT UNIDIRECTIONAL W FIBERS, 4 PLYS
MATRIX: OFHC COPPER, ASTM GRAIN SIZE #8-9
FIBERS: G.E. 218 W WIRE (0.008 in. DIAM.)

CD-89-39163

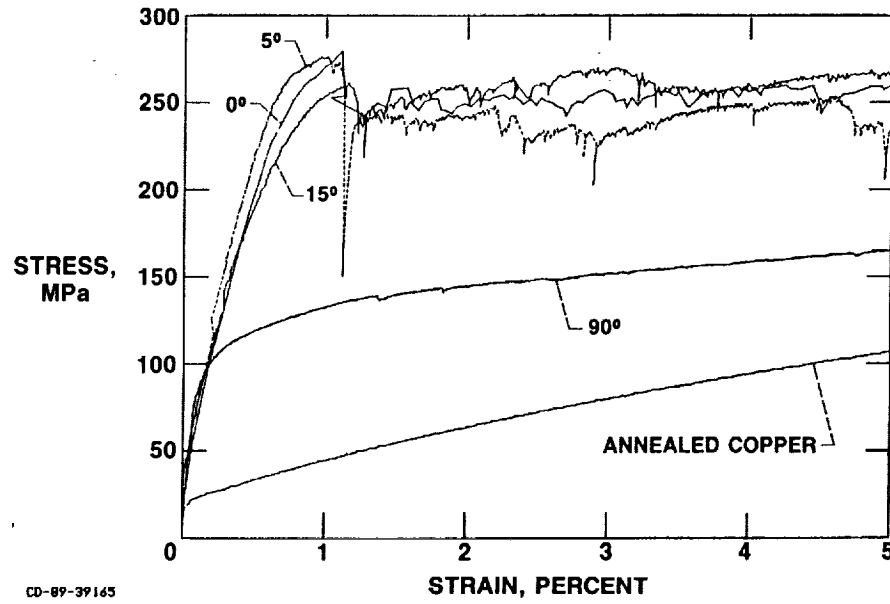
TEST CONDITIONS

	TENSILE	FATIGUE
TEMPERATURE, °C	25, 260	260
FIBER ORIENTATIONS	0°, 5°, 15°, 90°	0°
TEST CONTROL	STRAIN	LOAD
TEST RATE	2.0×10^{-4} /SEC	3 CPM
ENVIRONMENT	VACUUM	VACUUM

CD-89-39164

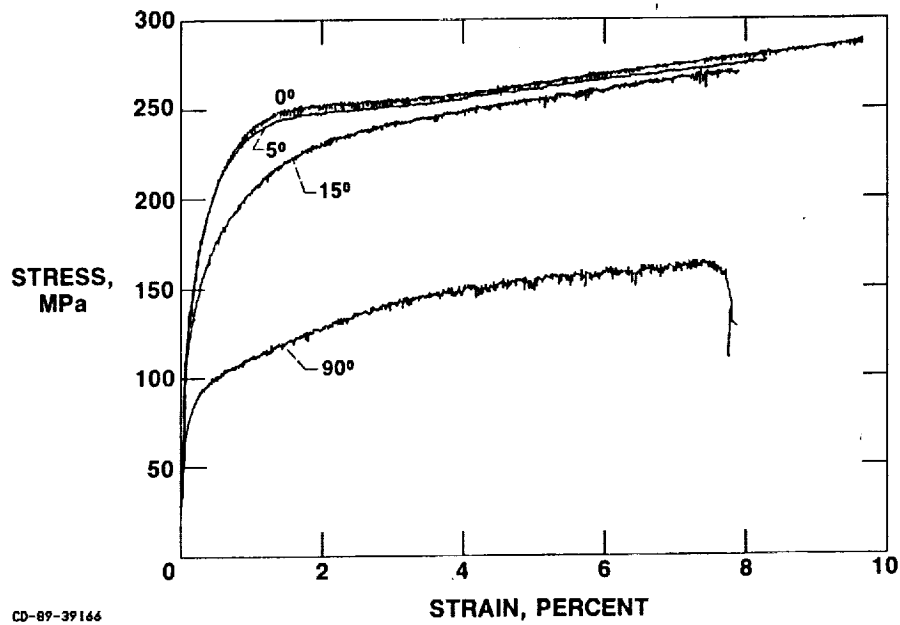
TENSILE DATA FOR 9 VOLUME PERCENT W/Cu

T = 25 °C



TENSILE DATA FOR 9 VOLUME PERCENT W/Cu

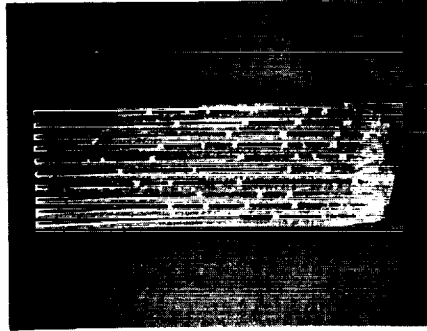
T = 260 °C



ORIGINAL PAGE
BLACK AND WHITE PHOTOGRAPH

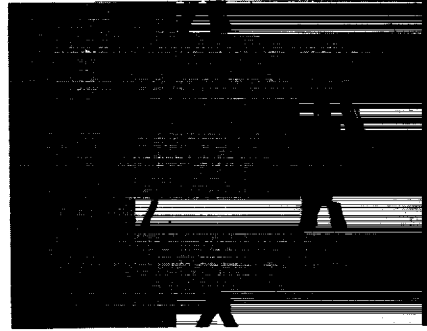
**TENSILE FAILURE BEHAVIOR FOR W/Cu AT 25 °C
0°, 5°, AND 15° SPECIMENS**

FIBER FRACTURES



5.6 X

PAIRS OF FIBER BREAKS

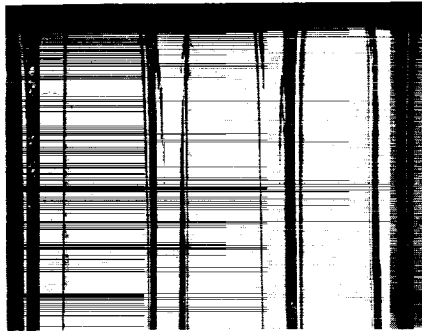


50 X

CD-89-39147

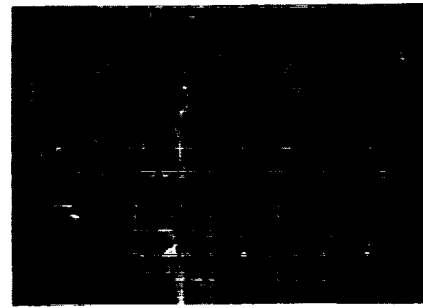
**TENSILE FAILURE BEHAVIOR FOR W/Cu AT 25 °C
90° SPECIMEN**

FIBER SPLITTING



50 X

INTERGRANULAR FIBER SPLIT

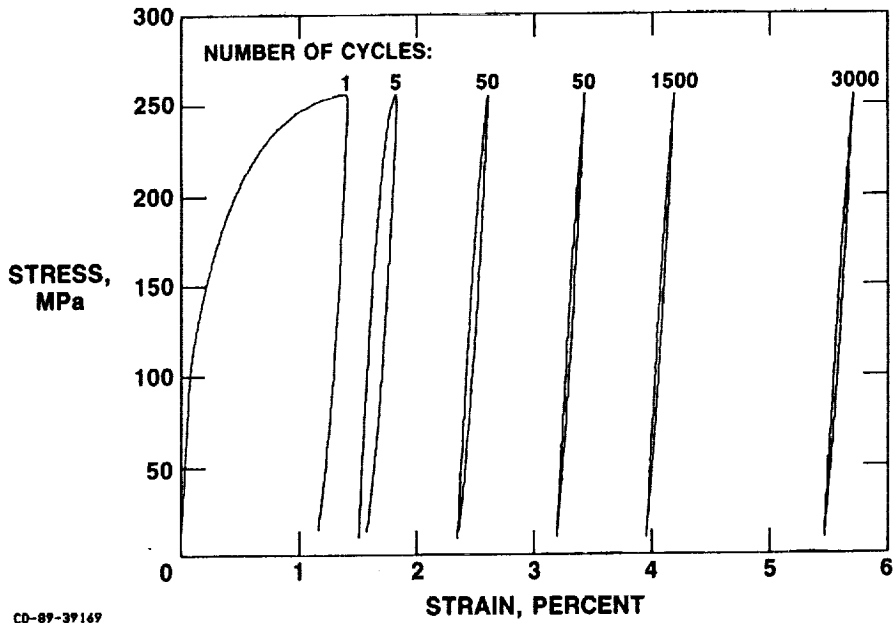


20 μm

CD-89-39148

FATIGUE DATA FOR 9 VOLUME PERCENT W/Cu

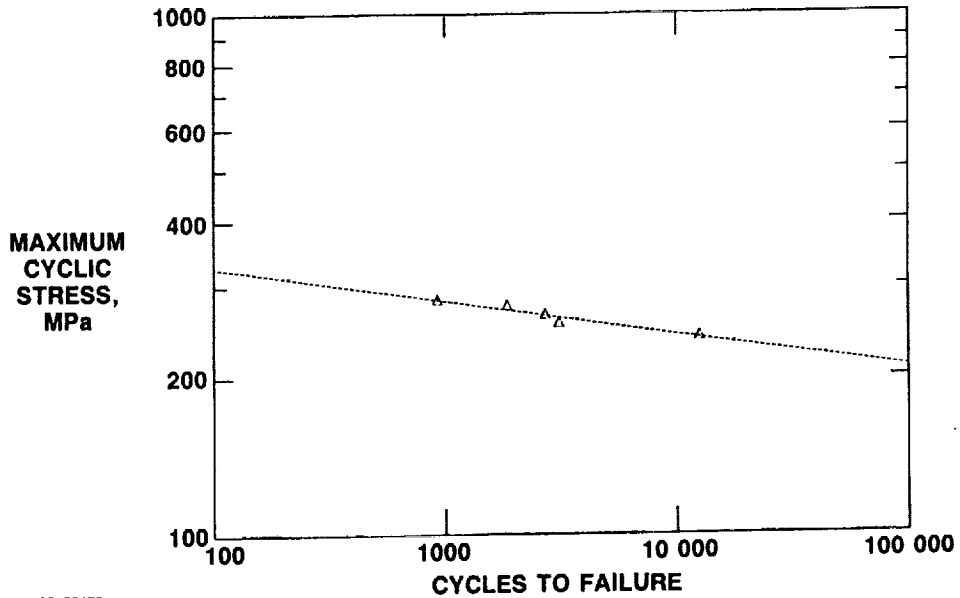
T = 260 °C



CD-89-39169

MAXIMUM CYCLIC STRESS VERSUS LIFE FOR FATIGUE OF 9 VOLUME PERCENT W/Cu

T = 260 °C



CD-89-39170

SUMMARY

TENSILE BEHAVIOR

- 1. AT 25 °C, 0°, 5°, 15° SPECIMENS HAD THE SAME TENSILE PROPERTIES. THESE VALUES WERE CONSISTENT WITH RULE OF MIXTURES.**
- 2. THESE SPECIMENS HAD DISCONTINUOUS YIELDING CAUSED BY PROGRESSIVE FIBER FAILURE.**
- 3. AT 25 AND 260 °C THE TRANSVERSE (90°) SPECIMEN HAD THE LOWEST PROPERTIES. FAILURE AT 25 °C WAS CAUSED BY FIBER SPLITTING.**

FATIGUE BEHAVIOR

- 1. CYCLIC MEAN STRAIN INCREASED CONTINUOUSLY TO FAILURE.**
- 2. ELASTIC MODULUS REMAINED CONSTANT UNTIL FAILURE.**
- 3. STRAIN AT FAILURE INCREASED WITH INCREASING MAXIMUM CYCLIC STRESS.**

CD-89-39171

FUTURE WORK

- 1. ISOTHERMAL FATIGUE AT 550 °C**
- 2. THERMOMECHANICAL FATIGUE**
- 3. FULLY REVERSED FATIGUE**
- 4. LIFE PREDICTION**

CD-89-39172



CUMULATIVE CREEP FATIGUE DAMAGE IN 316 STAINLESS STEEL

**Michael A. McGaw
NASA Lewis Research Center**

The cumulative creep-fatigue damage behavior of 316 stainless steel at 1500 °F has been experimentally established for the two-level loading cases of fatigue followed by fatigue, creep fatigue followed by fatigue, and fatigue followed by creep fatigue. The two-level loadings were conducted such that the lower life (high strain) cycling was applied first for a controlled number of cycles and the higher life (low strain) cycling was conducted as the second level, to failure. The target life levels in this study were 100 cycles to failure for both the fatigue and creep-fatigue low life loading, 5000 cycles to failure for the higher life fatigue loading and 10 000 cycles to failure for the higher life creep-fatigue loading. Results of the fatigue followed by fatigue loading experiments follow the behavior predicted by the double linear damage rule and damage curve approach of Manson and Halford (ref. 1), while the remainder of the two-level experiments produced results that were inadequately predicted by this approach. These experiments all involved creep-fatigue loading and likely introduced a different damage mechanism from a cumulative damage standpoint. The failed specimens are being examined both fractographically and metallographically to ascertain the nature of the damaging mechanisms that produced failure. Models of creep-fatigue damage accumulation are being evaluated and knowledge of the various damaging mechanisms is necessary to ensure that predictive capability is instilled in the final failure model.

EXPERIMENTAL RESULTS AND DISCUSSION

A strainrange partitioning (SRP) characterization of this material was performed for the PP and CP damage modes at 1500 °F. While a complete SRP characterization for this material at this temperature has been established by Kalluri (ref. 2), the emphasis in that work was on the effect of exposure time on the low-cycle fatigue life; the life data so developed are over a range that was considered too narrow for the purposes of the present cumulative creep-fatigue damage study. Since, in fatigue, the nonlinear cumulative effects depend strongly on the relative life levels involved in the loading, the present study is focused on obtaining failure data at two widely separated life levels, both under pure fatigue and creep-fatigue loading. To this end, baseline SRP experiments were performed to establish the inelastic strain range levels for 100 and 5000 cycles to failure in PP and 100 and 10000 cycles to failure in CP. Results of these baseline characterization experiments are shown in figure 1. The resulting life relationships expressed in terms of inelastic strain range versus cyclic life are substantially different in the lower life regime and appear to approach each other in the longer life regime.

These life relationships were used to determine the life levels corresponding to the loading levels applied in the two-level loading experiments.

The results of the two-level loading experiments involving PP followed by PP loadings are shown in figure 2. Substantial cyclic hardening was observed at the low life level, which served to influence the cyclic behavior observed at the (subsequent) high life level. The material response at the second loading level was different from that observed for experiments involving that loading level alone, in the respect that it exhibited much higher stresses for the applied strains. As the second level cycling progressed, the material cyclically softened and tended to approach the stabilized cyclic response observed in the baseline fatigue characterization experiments. The failure data in figure 2 are well represented by the damage curve approach of Manson and Halford (ref. 1), and are unconservatively represented by the linear damage rule of Miner (ref. 3).

The results of the two-level loading experiments involving PP followed by CP loadings are shown in figure 3. In this case as well, the influence of the substantial amount hardening induced by the first level, lower life cycling manifested itself in terms of a somewhat different cyclic response at the second, higher life level, CP loading. In the second level the material exhibited much higher cycle times, which, as the cycling went on, tended to approach the cycle times observed in the baseline CP behavior. The data in figure 3 show a trend that is reasonably represented by the linear damage rule. A prediction based on the damage curve approach is also shown, which, while providing a very conservative estimate for the results, does not adequately represent the observed behavior. The presence of creep damage in the second loading level appears to influence the cumulative damage behavior, implying that another damage mechanism is operative. Fractographic and metallographic analysis of the fractured specimens is currently underway to ascertain the nature of the damaging mechanisms operative in this type of cumulative fatigue loading.

The results of the two-level loading experiments involving CP followed by PP are shown in figure 4. In this series of tests the effect of the CP low life level cycling on the second, high life level PP cycling was to introduce a significant tensile mean stress as well as to produce a "harder", cyclic stress strain response than was observed in the baseline PP experiments at the same applied total strain range. This mean stress tended to relax somewhat as the second load level cycling progressed, but a significant mean stress was nevertheless maintained throughout the test. The life data shown in figure 4 were calculated assuming $R = -1$, and the results of these experiments indicate that the influence of the earlier CP cycling on the subsequent PP cycling is, at worst, virtually insignificant, and, at best, an enhancer of fatigue resistance at the second level. These results also indicate the possibility of another damage mechanism. Fractographic and metallographic analyses are in progress.

The results obtained thus far indicate that for this material in cumulative creep fatigue loading, the interaction between PP and CP loadings is not as deleterious as the interaction that occurs between PP and PP loading. This result suggests that another cumulative damage mechanism is operative when CP loading is followed by PP loading or vice versa. While this is not surprising (the SRP approach is predicated on the possibility of different damaging modes of straining), the direction of the influence in the cumulative case, is an

unexpected experimental result. Future work will include characterization of the PP and PC and the PP and CC cumulative damage behaviors so that the development of a physically based model that describes the general cumulative damage behavior for this material under conditions of fatigue and creep-fatigue loading is achieved.

REFERENCES

1. Manson, S.S.; and Halford, G.R.: Practical Implementation of the Double Linear Damage Rule and Damage Curve Approach for Treating Cumulative Fatigue Damage, *Int. J. Fract.*, vol. 17, 169-192, 1981.
2. Kalluri, S.: Generalization of the Strainrange Partitioning Method for Predicting High Temperature Low Cycle Fatigue Life at Different Exposure Times, Ph.D. Dissertation, Case Western Reserve University, Cleveland, Ohio, 1987.
3. Miner, M.A.: Cumulative Damage in Fatigue, *J. Appl. Mech.*, vol. 67, A159-A164, 1945.

SRP PP AND CP CHARACTERIZATIONS

316 SS AT 1500 °F

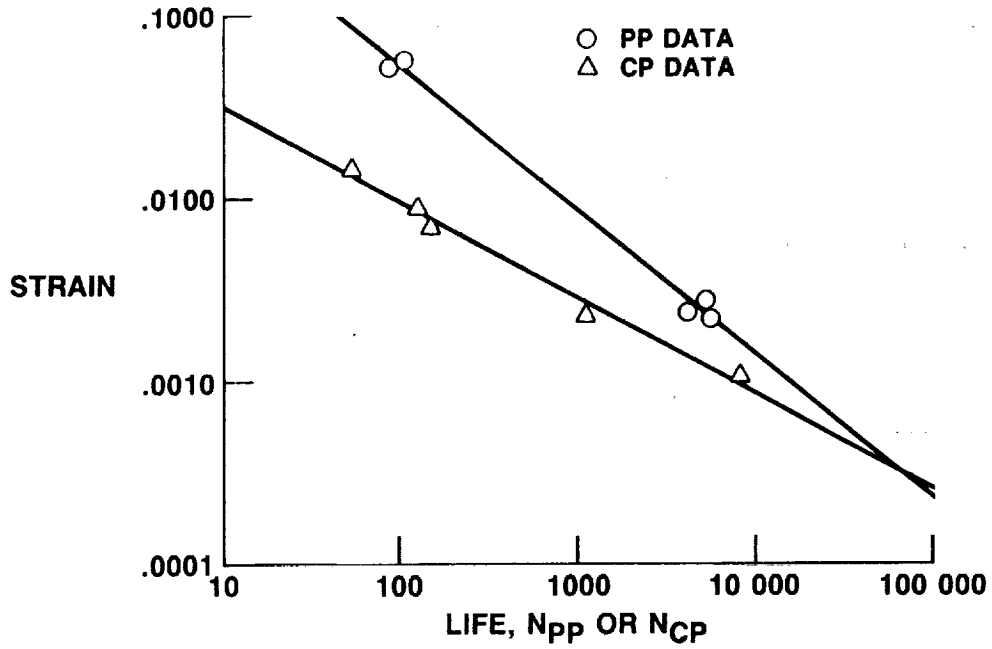


Figure 1

CD-89-39293

PP PLUS PP INTERACTION

316 SS AT 1500 °F

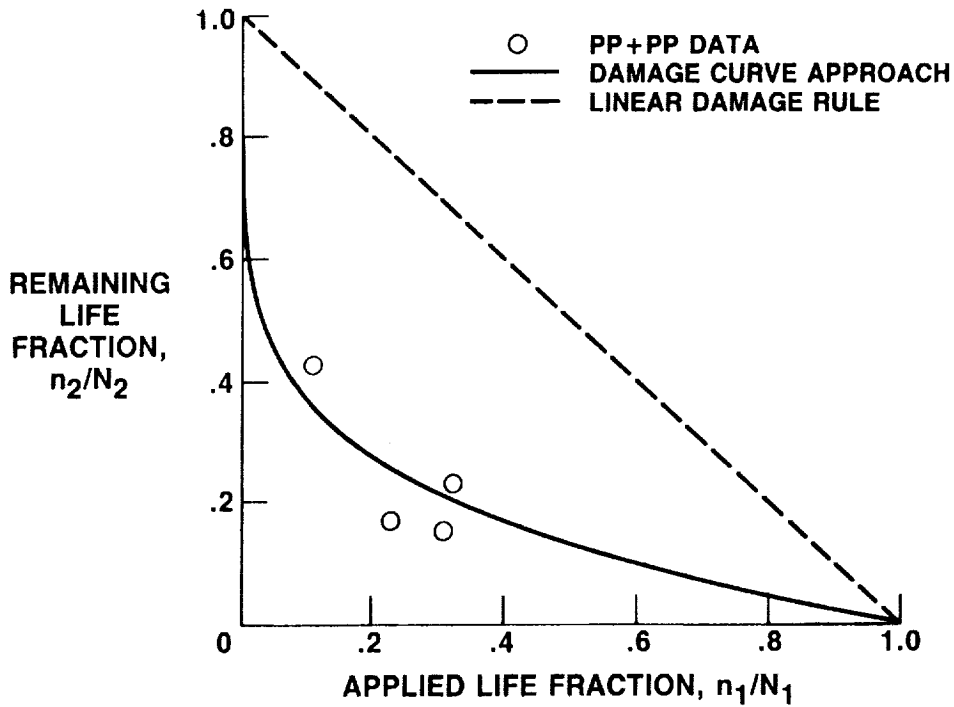
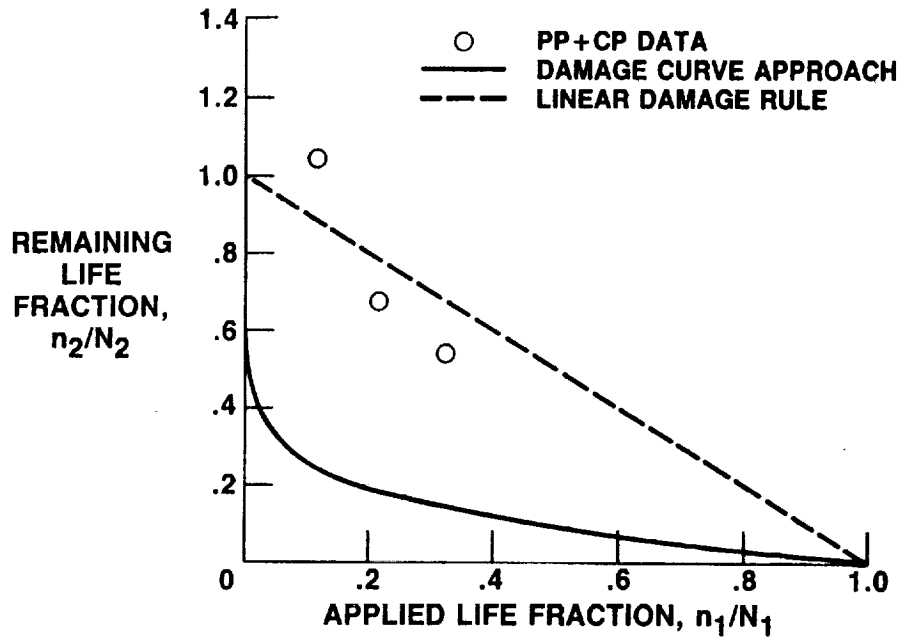


Figure 2

CD-89-39294

PP PLUS CP INTERACTION

316 SS AT 1500 °F

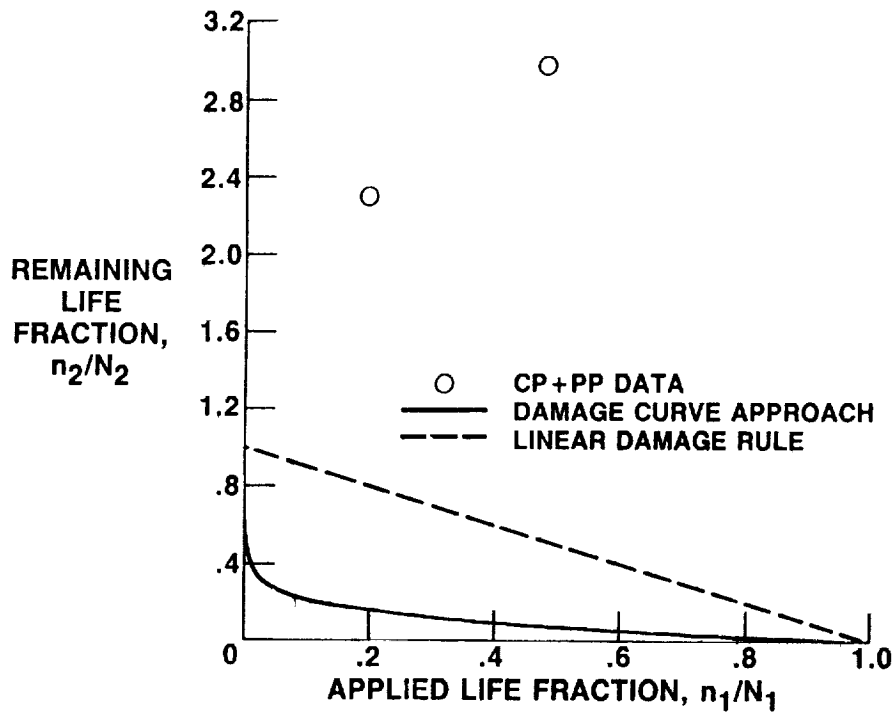


CD-89-39295

Figure 3

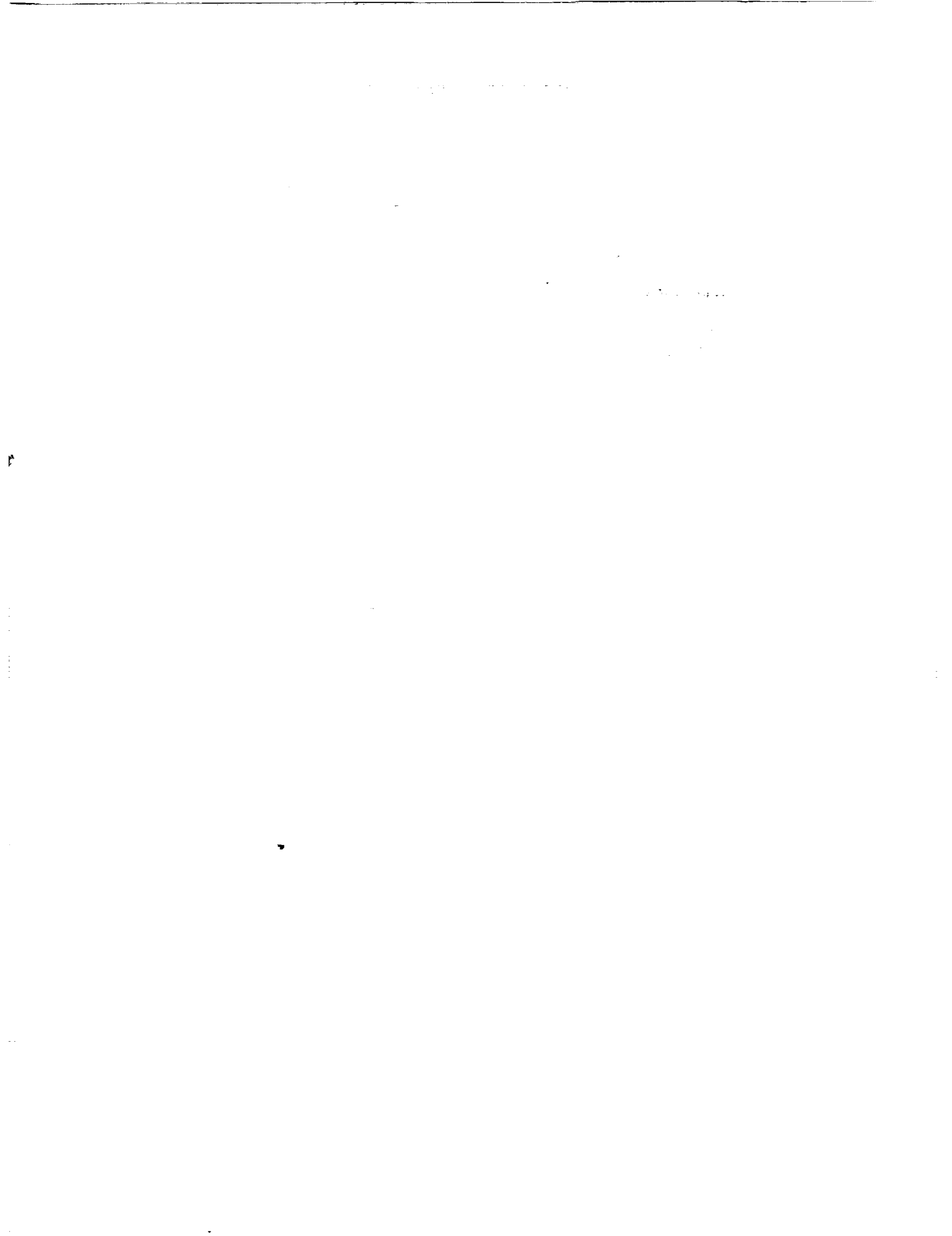
CP PLUS PP INTERACTION

316 SS AT 1500 °F



CD-89-39294

Figure 4



FATIGUE BEHAVIOR OF A SINGLE-CRYSTAL SUPERALLOY

Sreeramesh Kalluri
Sverdrup Technology, Inc.
NASA Lewis Research Center Group

56-26
19863

and

Michael A. McGaw
NASA Lewis Research Center

Single-crystal superalloys have been used extensively during the past decade in the manufacture of turbine blades of aircraft engines. At the present time, a single crystal superalloy, PWA 1480 is under consideration as a replacement material for the turbine blades of the high pressure fuel turbopump (HPFTP) of the space shuttle main engine (SSME). It is necessary to characterize the fatigue behavior of this material for the safe and reliable operation of the SSME. In order to achieve this goal, NASA Lewis Research Center purchased during the early 80's cast single crystal PWA 1480. The material was cast by TRW, Inc., both in the form of cylindrical bars (11/16 in. diam. and 6 in. long) and slabs (6.5 by 2.5 by 0.5 in.) along the (001) orientation. Even though each bar and slab was cast individually, all nominally had the same chemical composition (table I). The cast single crystal PWA 1480 material was observed to contain microporosity, especially between the dendrites (refs. 1 and 2).

Three separate experimental programs were conducted to characterize the fatigue behavior of this alloy at two laboratories (refs. 1 to 3). Fatigue tests were conducted at room temperature (in air) and at 1000 °F (in vacuum) on smooth specimens machined from both the cast bars and slabs. In this study the data from all of these programs are consolidated to provide a broader characterization of the fatigue behavior of the single crystal PWA 1480. The zero-mean-stress fatigue life relationships are expressed in terms of stress range versus cyclic life lines on log-log plots (figs. 1 and 2). At room temperature the slope of the life relationship of this single-crystal superalloy is larger than that observed typically in polycrystalline alloys. For a polycrystalline alloy, the slope of this line is usually between -0.07 and -0.14, whereas for PWA 1480 single crystal the slope is -0.17. A large amount of scatter was observed in the room temperature fatigue data generated at NASA Lewis Research Center. This scatter is attributable to the porosity observed both within the material and on the surface of the fatigue specimens (ref. 1). However, it is interesting to note that the data generated from both the cast bars and slabs are within the same scatter band (fig. 1). Also, the fact that two different laboratories and three separate test systems that were involved in generating the data does not appear to have affected the scatter in the data to a significant extent. Only two fatigue data points were available for the zero mean stress condition in vacuum at 1000 °F. The life relationship at this temperature was determined by using the slope of the room temperature zero-mean-stress fatigue data (fig. 2).

Characterization of the fatigue behavior of $\langle 001 \rangle$ oriented PWA 1480 single crystal under conditions of tensile mean stress was an objective of the work done at Argonne National Laboratory (ANL) (ref. 3). Fatigue data with tensile mean stresses were also generated by Rockwell International on this material (ref. 4). The material tested at ANL had the same chemical composition as the NASA Lewis material, while the Rockwell material had a chemical composition that was not significantly different from the material used at NASA Lewis (table I). In the current study an attempt was made to characterize the effect of tensile mean stress on the fatigue life of PWA 1480 single crystal by using the unified approach proposed by Heidmann (ref. 5). In this approach the fatigue life is modified by a mean stress parameter so that a single life relationship can be used to represent both zero and tensile mean stress data. A better correlation of the fatigue data was obtained by modifying the functional form proposed originally in reference 5. When tensile mean stresses are properly accounted for, the data with and without mean stress collapse to a single line (figs. 3 and 4). The implications of this type of treatment of mean stress effects, in terms of the conventional approach, are shown in figure 5 (room temperature in air) and Figure 6 (1000 °F in vacuum). These plots indicate that tensile mean stresses are likely to be more detrimental in low-cycle fatigue than in high-cycle fatigue for PWA 1480 single crystal. However, this type of behavior is exactly the opposite of the behavior exhibited by most polycrystalline alloys (ref. 6). The effect of tensile mean stress on the fatigue life appears to diminish at 1000 °F compared with room temperature. This result may be due to the differences in the deformation mechanisms at these two temperatures and environmental conditions. Additional experimental fatigue data on PWA 1480 single-crystal superalloy with different levels of mean stress and cyclic lives are necessary to confirm the trends of mean stress effects observed in this analysis.

REFERENCES

1. McGaw, M.A.: The Fatigue Damage Behavior of a Single Crystal Superalloy. M.S. Thesis, Case Western Reserve University, Cleveland, Ohio, 1987.
2. Gayda, J.; Gabb, T.P.; and Dreshfield, R.L.: The Effect of Hydrogen on the Low Cycle Fatigue Behavior of a Single Crystal Superalloy. Paper submitted for the Fourth International Conference on Hydrogen Effects on Material Behavior, September 1989.
3. Majumdar, S.; and Kwasny, R.: Effects of a Mean Stress on the High-Cycle Fatigue Life of PWA 1480 and Correlation of Data by Linear Elastic Fracture Mechanics. Report prepared by Argonne National Laboratory for NASA Lewis Research Center, NASA CR-175057, 1985.
4. Fritzemeier, L.G.: Advanced Single Crystal for SSME Turbopumps. Report prepared by Rocketdyne Division of Rockwell International for NASA Lewis Research Center, NASA CR-182244, 1988.
5. Heidmann, K.R.: Technology for Predicting the Fatigue Life of Grey Cast Iron. Ph. D. Thesis, Case Western Reserve University, 1985.
6. Manson, S.S., and Heidmann, K.R.: A New Formulation of Mean Stress Effects in Fatigue. Proceedings of the Conference on Structural Integrity and Durability of Reusable Space Propulsion Systems, NASA CP-2471, May 1987.

**CHEMICAL COMPOSITION OF CAST
PWA 1480 SINGLE CRYSTAL
[WEIGHT PERCENT]**

ELEMENT	NASA LEWIS BARS AND SLABS (REF. 1)	ROCKETDYNE MATERIAL (REF. 4)
CHROMIUM	10.40	10.16
COBALT	5.30	5.35
TUNGSTEN	4.10	4.13
TANTALUM	11.90	11.95
ALUMINUM	4.80	4.91
TITANIUM	1.30	1.35
NICKEL	BALANCE	BALANCE

Table I

CD-89-39510

**PWA 1480 SINGLE CRYSTAL ZERO-MEAN-STRESS
(R = -1) FATIGUE DATA
ROOM TEMPERATURE IN AIR**

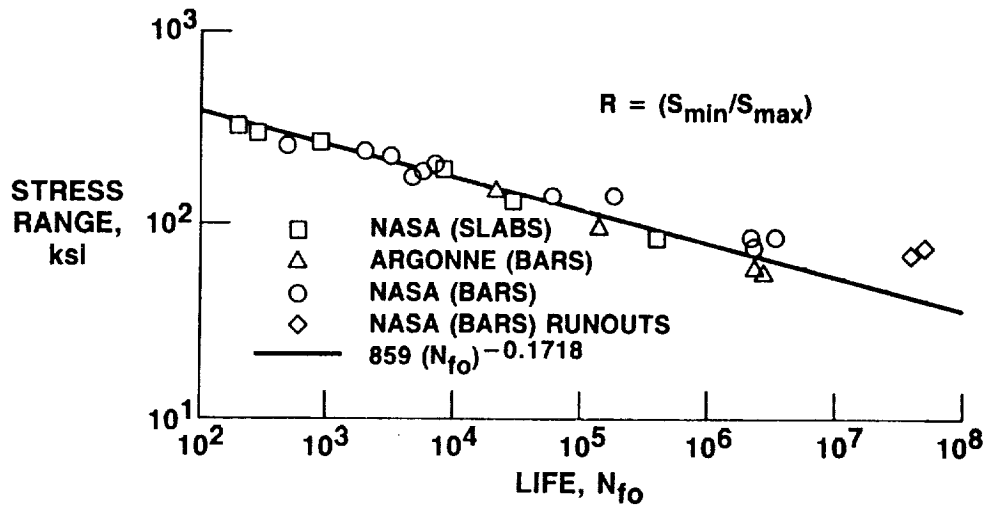


Figure 1

CD-89-39284

**PWA 1480 SINGLE CRYSTAL ZERO-MEAN-STRESS
(R = -1) FATIGUE DATA
1000 °F IN VACUUM**

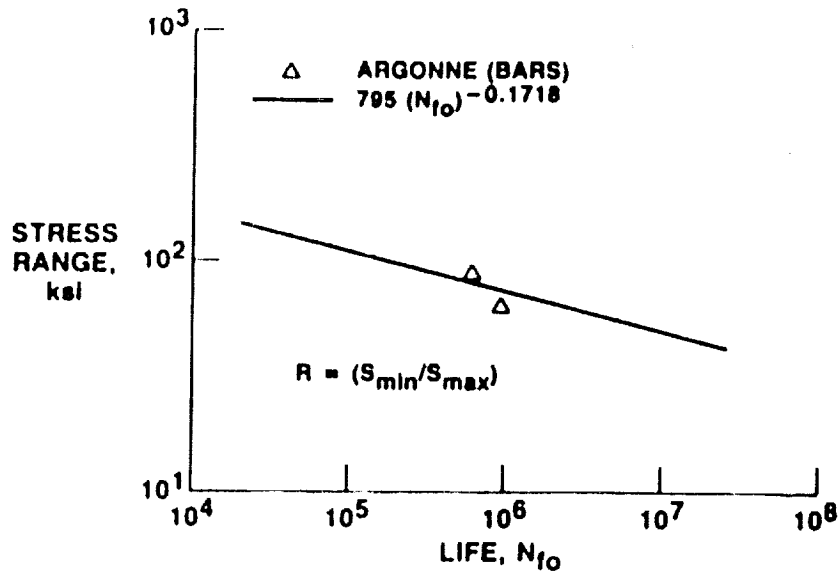
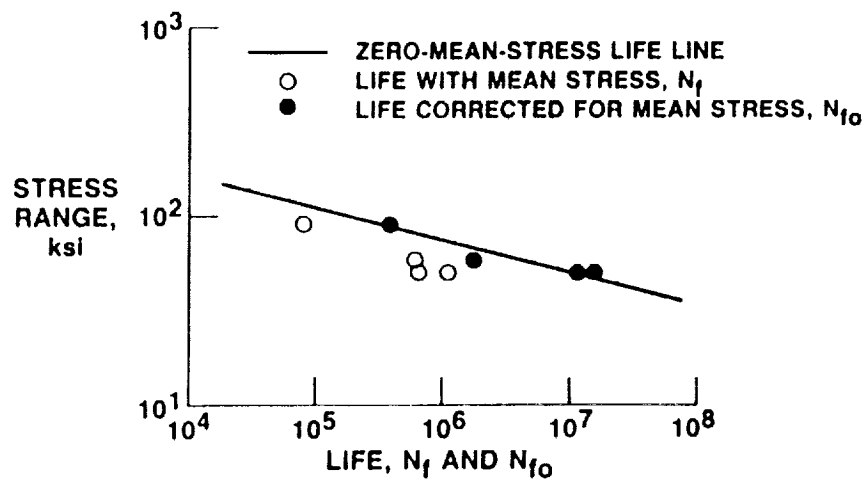


Figure 2

CD-87-39785

**PWA 1480 SINGLE CRYSTAL
TENSILE-MEAN-STRESS FATIGUE DATA
1000 °F, IN VACUUM; ARGONNE**



$$N_{f0} = N_f \left[1 - \left(\frac{S_m}{S_f} \right)^G(N_f) \right]^{1/b}$$

$$G(N_f) = 0.087 (\log N_f)^2 - 0.583 (\log N_f) + 2.0$$

WHERE

S_m TENSILE MEAN STRESS

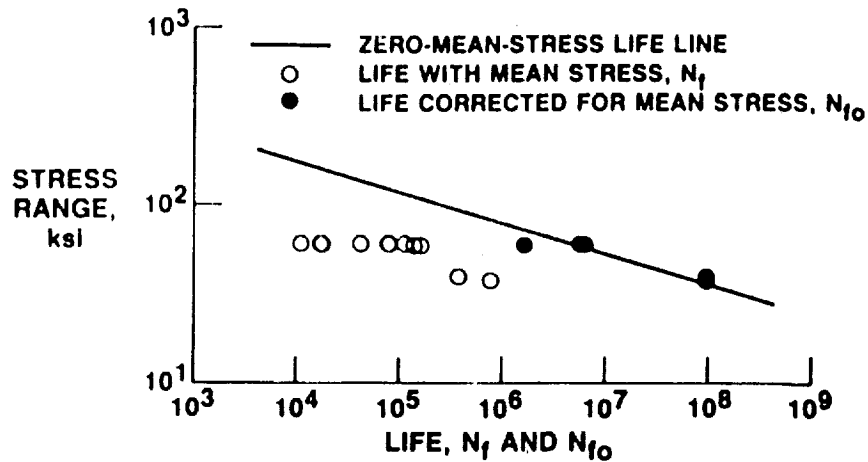
S_f TRUE FRACTURE STRENGTH

b FATIGUE STRENGTH EXPONENT

CD-87-39787

Figure 3

**PWA 1480 SINGLE CRYSTAL
TENSILE-MEAN-STRESS FATIGUE DATA
ROOM TEMPERATURE, IN AIR; ARGONNE AND ROCKETDYNE**



$$N_{f0} = N_f \left[1 - \left(\frac{S_m}{S_f} \right)^{G(N_f)} \right]^{1/b}$$

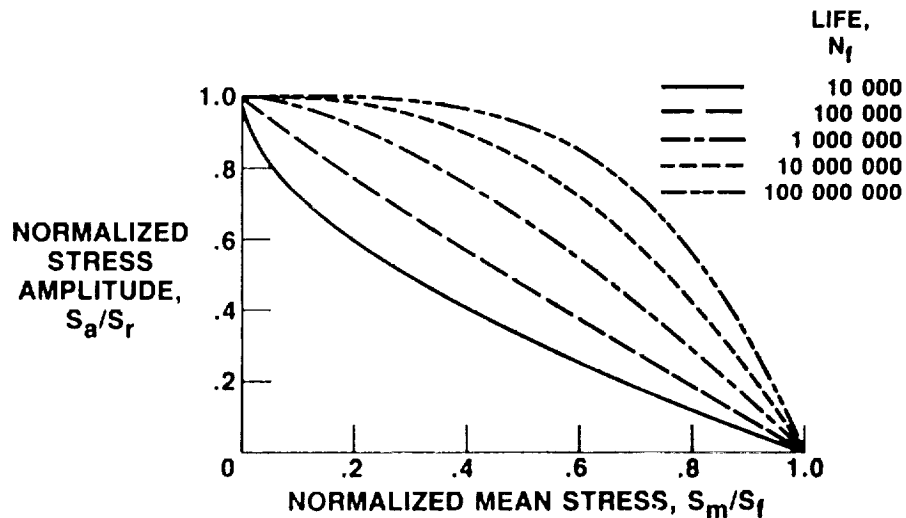
$$G(N_f) = 0.142 (\log N_f)^2 - 0.928 (\log N_f) + 2.0$$

WHERE
 S_m TENSILE MEAN STRESS
 S_f TRUE FRACTURE STRENGTH
 b FATIGUE STRENGTH EXPONENT

CD-89-39286

Figure 4

**EFFECT OF TENSILE MEAN STRESS ON
FATIGUE LIFE OF PWA 1480 SINGLE CRYSTAL
ROOM TEMPERATURE, IN AIR**

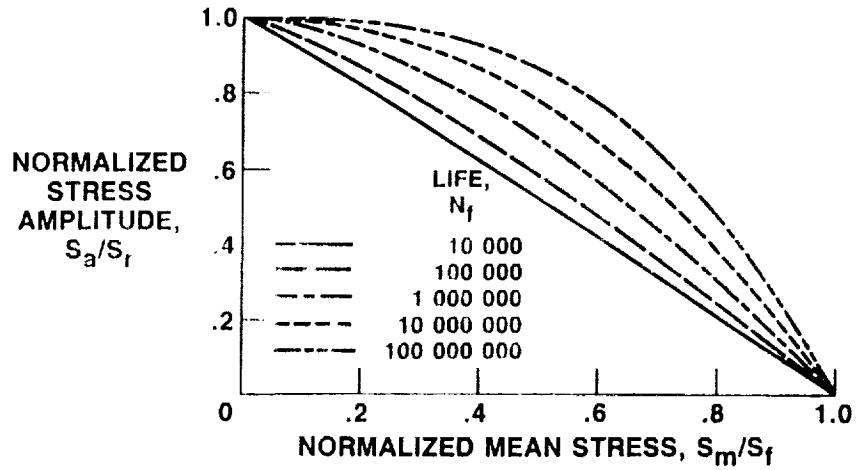


S_m TENSILE MEAN STRESS
 S_f TRUE FRACTURE STRENGTH
 S_a ALTERNATING STRESS AMPLITUDE
 S_r FULLY REVERSED STRESS AMPLITUDE WHICH PRODUCES THE SAME
 FATIGUE LIFE AS A COMBINED MEAN AND ALTERNATING STRESS

CD-89-39288

Figure 5

**EFFECT OF TENSILE MEAN STRESS ON
FATIGUE LIFE OF PWA 1480 SINGLE CRYSTAL
1000 °F, IN VACUUM**



S_m TENSILE MEAN STRESS
 S_f TRUE FRACTURE STRENGTH
 S_a ALTERNATING STRESS AMPLITUDE
 S_r FULLY REVERSED STRESS AMPLITUDE WHICH PRODUCES THE SAME
 FATIGUE LIFE AS A COMBINED MEAN AND ALTERNATING STRESS

CD-89-39289

Figure 6

ELEVATED TEMPERATURE CRACK GROWTH

K.S. KIM AND R.H. VAN STONE

57-39
19864

LIFE ASSESSMENT AND METHODS TECHNOLOGY
GE AIRCRAFT ENGINES
CINCINNATI, OHIO 45215

The propagation of a crack in hot path components such as combustor liners can occur under complicated thermo-mechanical loading histories which may include substantial inelastic deformation. Current methods of predicting crack growth behavior utilizes linear elastic fracture mechanics (LEFM) which is not accurate for these circumstances. Therefore, it is desirable to determine suitable non-linear fracture mechanics parameters. The most likely parameters appear to be path-independent (P-I) integrals, several of which can be applied to high temperature inelastic crack growth problems. A combined analytical and experimental evaluation of these parameters is being performed at elevated temperatures under isothermal and thermo-mechanical loading, both with and without thermal gradients and hold times.

Several path-independent (P-I) integrals have been reviewed to determine their limitations under thermo-mechanical loadings. The basis for selecting candidate P-I integrals was that they were path-independent for these complex loading conditions. Based on these results, the following integrals were selected for more extensive evaluations

1. Blackburn's J^* -Integral and its rate form \dot{J}^*
2. Kishimoto's \hat{J} -Integral and its rate form $\hat{\dot{J}}$
3. Atluri's ΔT^* - and \dot{T}^* -Integral

Alloy 718 crack growth experiments were conducted to assess the ability of the selected P-I integrals to describe the elevated temperature crack growth behavior. These tests were performed on single edge notch (SEN) specimens under displacement control with multiple extensometers to monitor the specimen and crack mouth opening displacement (CMOD). The displacements in these tests were sufficiently high to

induce bulk cyclic inelastic deformation of the specimen. Under these conditions, the LEFM parameter K does not correlate the crack growth data. The experimentally measured displacements gradient at the end of specimen gage length were used as the boundary conditions in elastic-plastic finite element method (FEM) analyses. These analyses were performed with a node release approach using CYANIDE, a GEAE FEM code, which included a gap element which is capable of efficiently simulating crack closure. Excellent correlation was obtained between the experimentally measured and predicted variation of stress and CMOD with crack length and the stress-CMOD loops for Alloy 718 tests conducted at 538°C. This confirmed the accuracy of the FEM crack growth simulation approach. The experimentally measured crack growth rate data correlated well the three selected P-I integrals. The selection of the most accurate parameter will be based on analysis of temperature gradient and thermal mechanical fatigue crack growth experiments performed using Alloy 718.

It is currently planned to model crack growth under time dependent deformation using the superposition of the crack growth from cyclic or time-independent deformation and that from static or time-dependent deformation. The latter crack growth may be described using rate integrals (\dot{J}^* , $\dot{\hat{J}}$, and \dot{T}^*). The software for computation of these P-I integrals from FEM analyses has been developed. The P-I integrals in an SEN specimen have been calculated for both uniform load and uniform strain under isothermal conditions and for uniform load with a linear temperature gradient. The FEM analyses showed the relaxation and redistribution of the normal stress which occurs as a result of the time-dependent deformation. The three rate P-I integrals (J^* , \hat{J} , and ΔT^*) and their rate integrals (\dot{J}^* , $\dot{\hat{J}}$, and \dot{T}^*) were obtained with reasonable accuracy and showed path-independence for the conditions evaluated.

These investigations have produced significant progress in developing P-I integrals as non-linear fracture mechanics parameters. The analytical and experimental results to date suggests that this methodology has the potential of accurately describing elevated temperature crack growth behavior under the combined influence of thermal cycling and bulk elastic-inelastic deformation states.

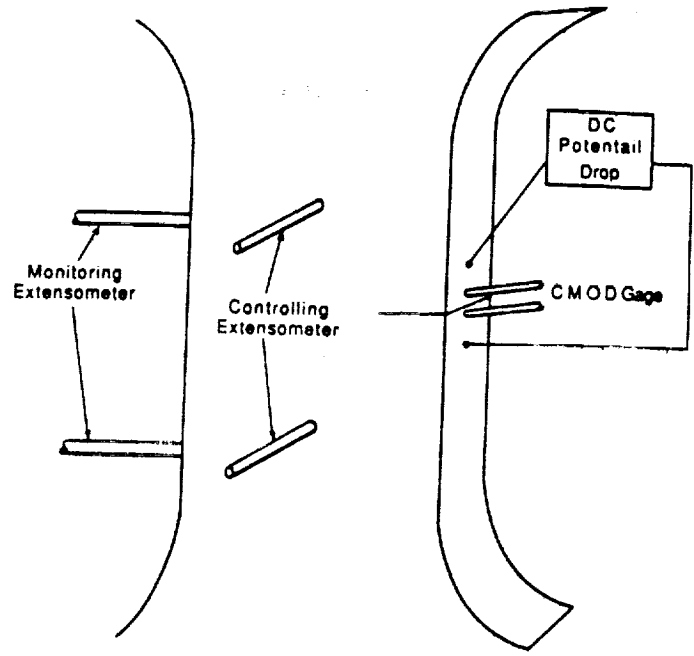
This work was performed under contract NAS3-23940 with the NASA-Lewis Research Center. T.W. Orange is the Program Manager.

TIME INDEPENDENT P-I INTEGRALS

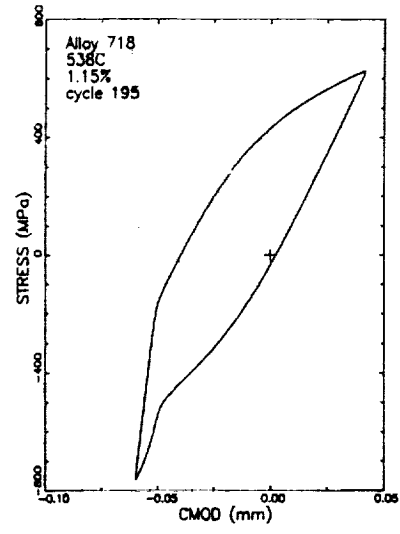
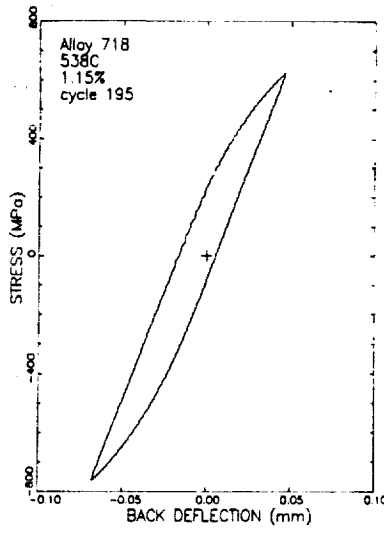
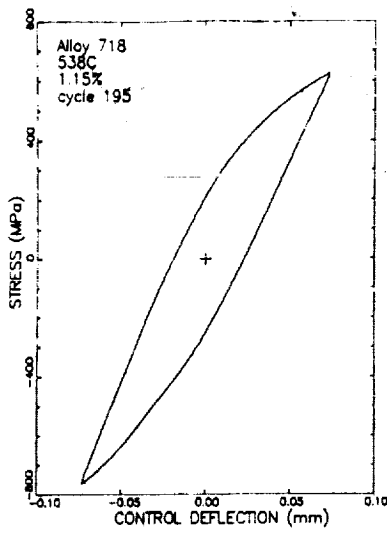
<u>P-I INTEGRAL</u>	<u>NON-PROPORTIONAL CYCLIC LOADING</u>	<u>TEMPERATURE GRADIENT</u>	<u>MATERIAL INHOMOGENEITY</u>	<u>ELASTIC-PLASTIC STRAINS</u>
RICE	NO	NO	NO	YES
AINSWORTH	NO	YES	NO	YES
WILSON & YU	NO	YES	NO	NO
GURTIN	NO	YES	NO	NO
BLACKBURN	YES	YES	YES	YES
KISHIMOTO	YES	YES	YES	YES
ATLURI	YES	YES	YES	YES

TIME DEPENDENT P-I INTEGRALS

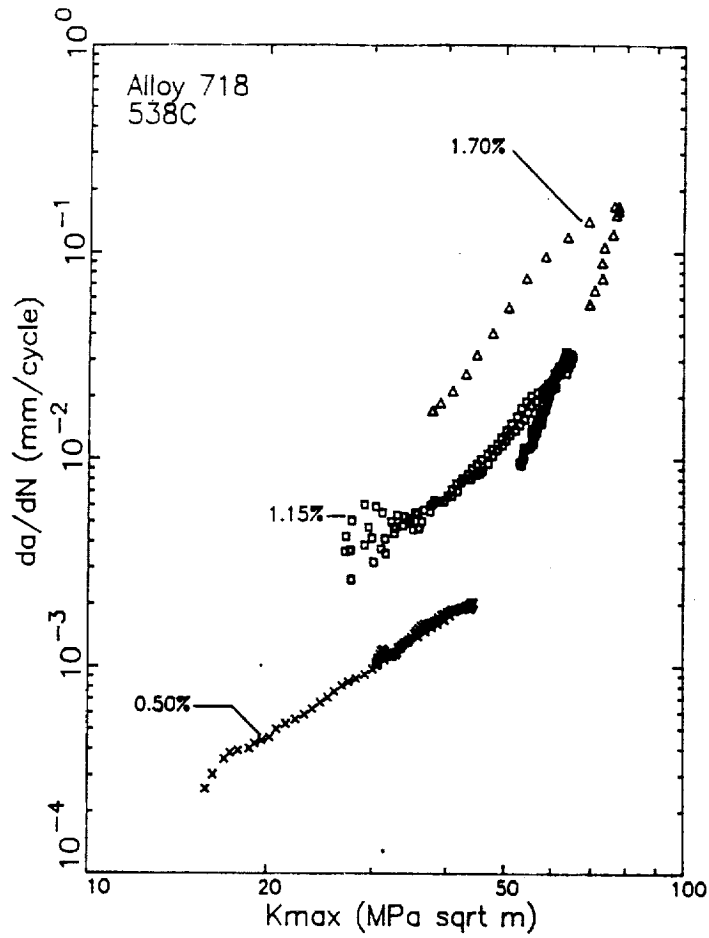
<u>P-I INTEGRAL</u>	<u>NON-PROPORTIONAL CYCLIC LOADING</u>	<u>CREEP DEFORMATION</u>	<u>TEMPERATURE GRADIENT</u>	<u>MATERIAL INHOMOGENEITY</u>
BLACKBURN	YES	YES	YES	YES
KISHIMOTO	YES	YES	YES	YES
ATLURI	YES	YES	YES	YES
HUTCHINSON GOLDBERG LANDES & BEGLEY	NO	STEADY STATE ONLY	NO	NO



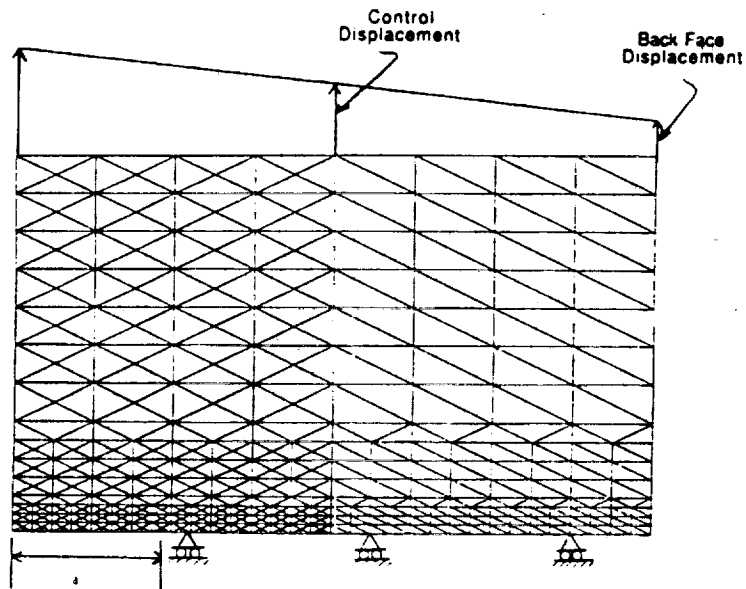
SCHEMATIC DIAGRAM OF TESTING METHOD



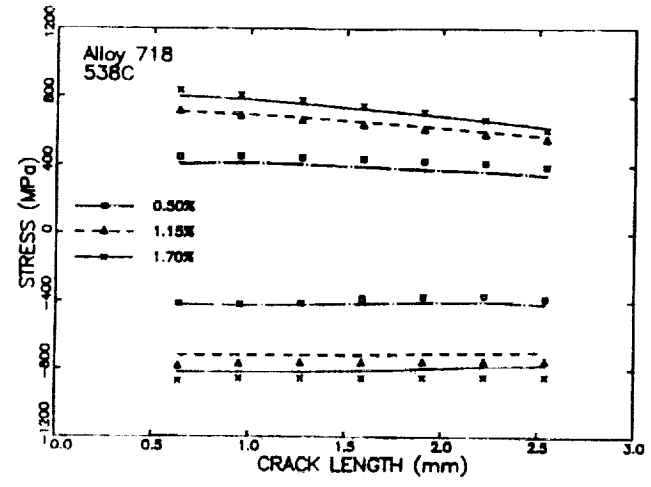
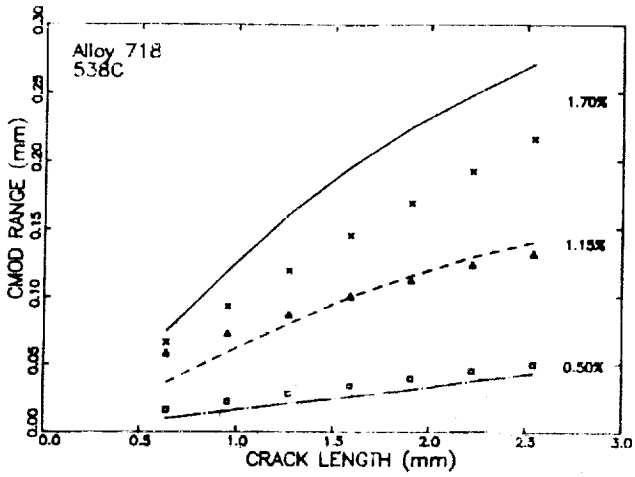
**HYSTERESIS LOOPS FROM
538C ALLOY 718 TEST WITH
A STRAIN RANGE OF 1.15%
AND A MEAN STRESS OF ZERO**



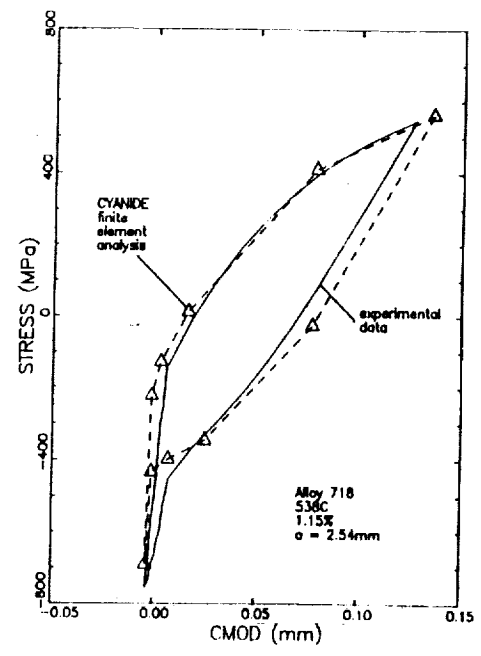
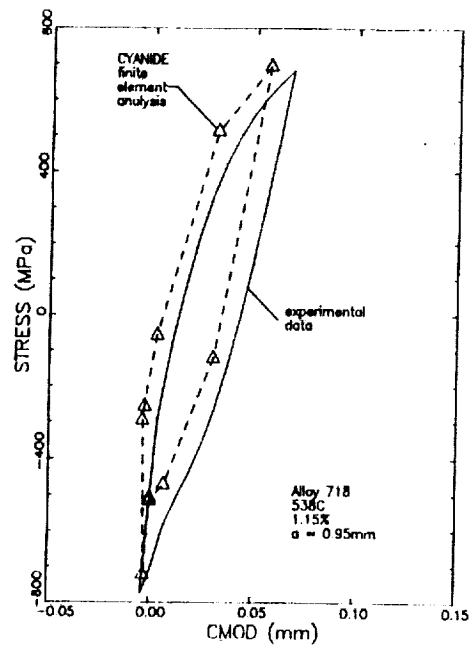
VARIATION OF CRACK GROWTH RATE WITH K_{MAX} IN 538C ALLOY 718 TESTS



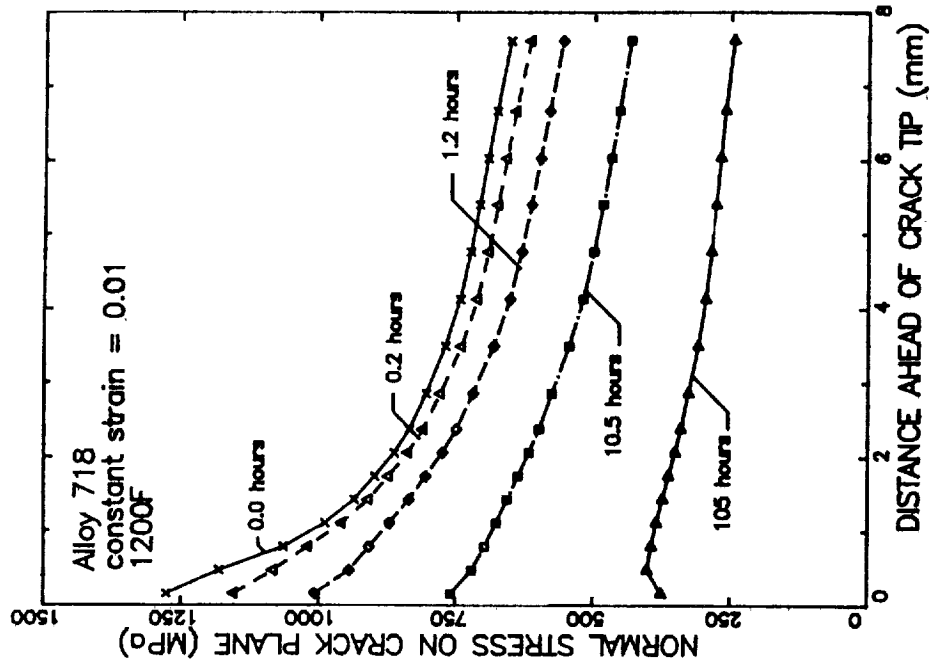
FINITE ELEMENT MESH AND LINEAR DISPLACEMENT BOUNDARY CONDITIONS



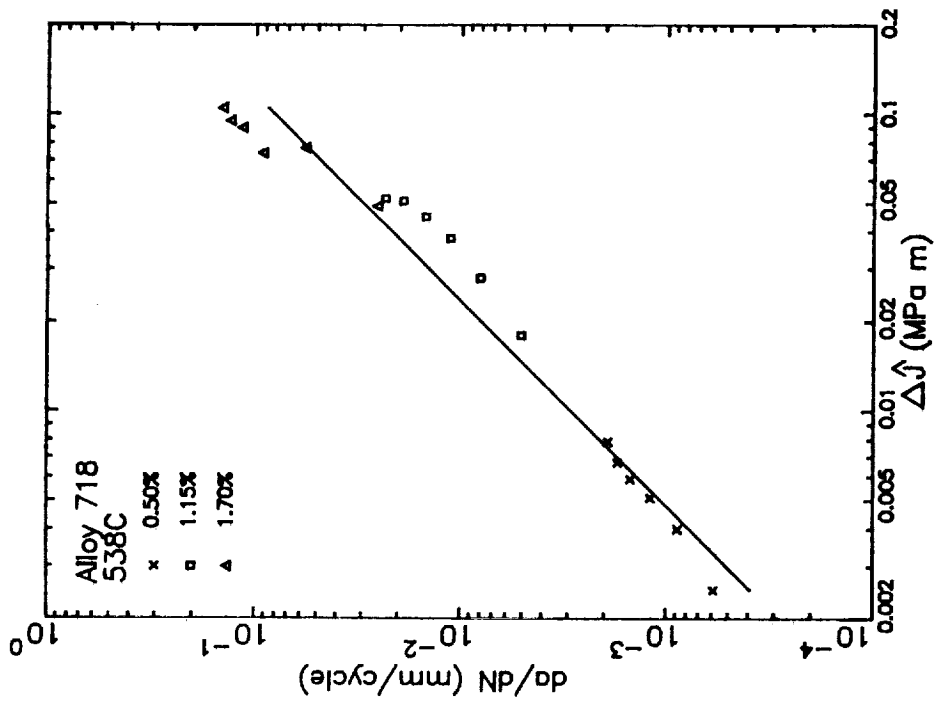
COMPARISON OF EXPERIMENTALLY MEASURED AND PREDICTED VARIATION OF STRESS AND CMOD WITH CRACK LENGTH IN 538C ALLOY 718 CRACK GROWTH TESTS



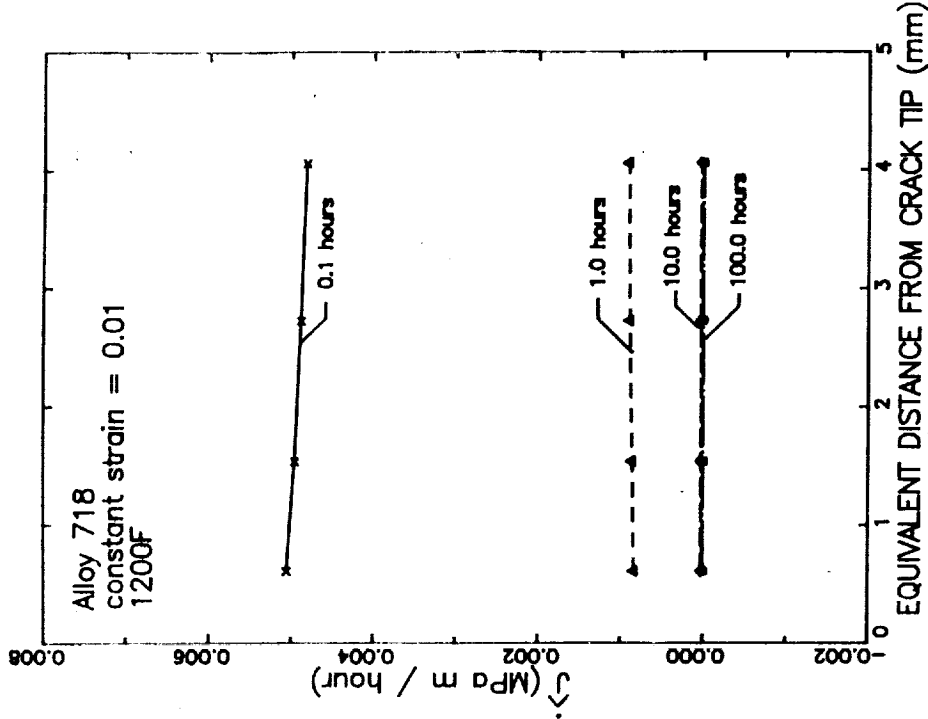
COMPARISON OF EXPERIMENTALLY MEASURED AND PREDICTED STRESS - CMOD HYSTERESIS LOOPS FOR TWO CRACK LENGTHS IN 538C ALLOY 718 CRACK GROWTH TESTS



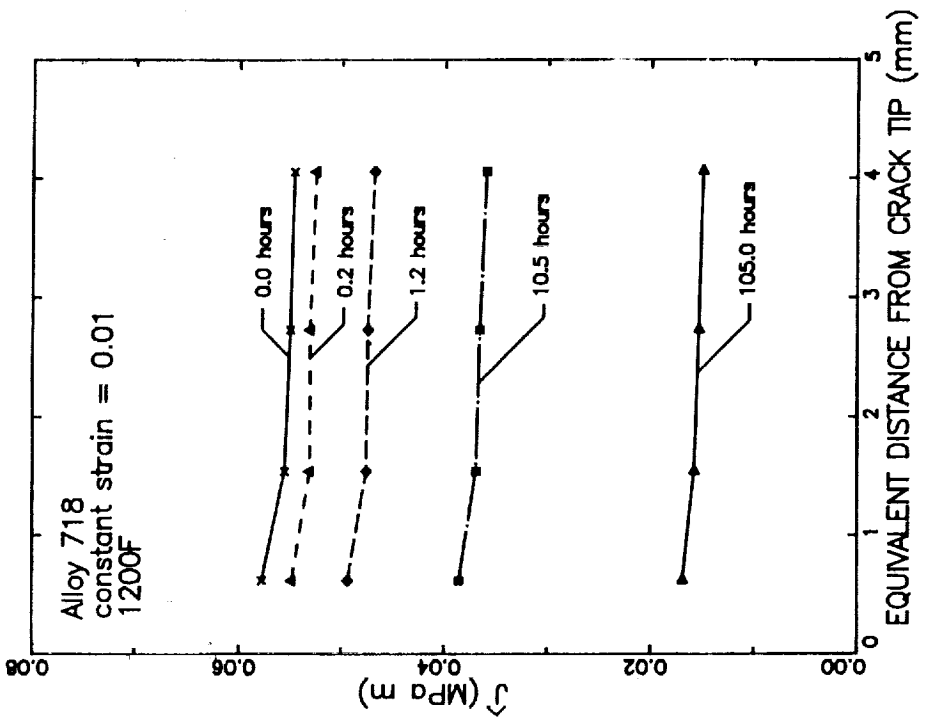
NORMAL STRESS REDISTRIBUTION AHEAD OF CRACK TIP IN A SEN SPECIMEN WITH A CRACK LENGTH OF 2.54 MM AT DIFFERENT TIMES FOR A CONSTANT STRAIN OF 0.01



VARIATION OF CRACK GROWTH RATE WITH \hat{J} IN 538C ALLOY 718 TESTS



VARIATION OF \hat{J} WITH DISTANCE FROM CRACK TIP IN A SEN SPECIMEN WITH A CRACK LENGTH OF 2.54 MM AT DIFFERENT TIMES FOR A CONSTANT STRAIN OF 0.01



VARIATION OF \hat{J} WITH DISTANCE FROM CRACK TIP IN A SEN SPECIMEN WITH A CRACK LENGTH OF 2.54 MM AT DIFFERENT TIMES FOR A CONSTANT STRAIN OF 0.01

58-39
19865

ANALYSIS OF DAMAGE IN MMC COMPONENTS USING
AN INTERNAL STATE VARIABLE MODEL

V.K. Arya
University of Toledo

The need to model the rate dependence and observed creep and plasticity interactions exhibited by materials, particularly at elevated temperatures, has greatly stimulated the development of numerous viscoplastic models. These models, in general, provide a better description of high-temperature time-dependent inelastic behavior of materials.

Owing to their lightweight and enhanced strength, the metal-matrix composite (MMC) materials are attracting considerable attention for high-temperature applications. As a result of concerted and leading efforts in this direction at NASA Lewis, a metal-matrix composite model was developed by Robinson and Duffy (1989). (See figs. 1 and 2.) The concept of damage evolution has recently been included by Robinson (personal communication) in the above model. The evolution of damage is assumed to be governed by a Kachanov-type equation. (See fig. 3.)

The highly nonlinear and mathematically "stiff" nature of the constitutive equations of viscoplastic models renders analytical solutions of problems, in general, intractable. It, therefore, becomes mandatory to develop suitable finite element or other numerical solution technologies to be able to use these models in component design. With this objective in mind, the above viscoplastic damage model was implemented in the finite element code, MARC. Both uniaxial (creep) and multiaxial (an internally pressurized thick-walled cylinder) problems were analyzed using this implementation. Some preliminary results are presented here. These results consider monotonic (constant) loadings. The study of damage accumulation under variable (cyclic) loadings is being undertaken. The results of this study will be presented later.

Figure 4 shows the experimental data (Cooper, 1966) utilized to determine the values of anisotropic parameters that appear in the model.

The creep curves including damage for four fiber orientations are depicted in figure 5. As expected, the minimum creep occurs when load is applied in a direction parallel to the fibers.

The tangential strains at the inner radius of a thick-walled MMC-cylinder for four fiber orientations are plotted in figure 6. The damage is included. The cylinder exhibits the maximum creep resistance when the fibers are oriented in the circumferential direction, perpendicular to the axis of cylinder.

Figure 7 shows the time-to-failure for the thick-walled cylinder for the same fiber orientation angles. As expected, the life of the cylinder can substantially be increased by orientating the fibers in the circumferential direction, perpendicular to the axis of cylinder.

The results, although qualitative, indicate that significant benefits in creep-resistance and service life can be achieved by using MMC materials as structural materials for high-temperature design.

The finite element technology developed herein is proposed to be applied to aerospace structural components subjected to (cyclic) thermomechanical loadings. The results of these analyses will be reported subsequently.

REFERENCES

- Robinson, D.N.; and Duffy, S.F. (1989): A Continuum Deformation Theory for Metal-Matrix Composites at High Temperature. Journal of Engineering Mechanics, ASCE (under publication).
- Cooper, G.A. (1966): Orientation Effects on Fiber-Reinforced Metals. Journal of Mechanics and Physics of Solids, vol. 14, pp. 103-111.

METAL MATRIX COMPOSITE MODEL INCLUDING DAMAGE

FLOW LAW

$$\dot{\epsilon}_{ij} = \frac{F^n}{2\mu} \Gamma_{ij}$$

WHERE

$$F = \frac{1}{(\psi K_f)^2} (I_1 - \xi I_2 - 12\zeta I_3^2) - 1$$

$$\Gamma_{ij} = \Sigma_{ij} - \xi (d_k d_i \Sigma_{jk} + d_j d_k \Sigma_{ki} - 4I_3 d_i d_j) - 4\zeta I_3 (3d_i d_j - \delta_{ij})$$

$$I_1 = \frac{1}{2} \Sigma_{ij} \Sigma_{ij}$$

$$I_2 = d_i d_j \Sigma_{jk} \Sigma_{ki} - 4I_3^2$$

$$I_3 = \frac{1}{2} d_i d_j \Sigma_{ij}$$

$$\xi = \frac{\eta^2 - 1}{\eta^2}$$

$$\zeta = \frac{4(\omega^2 - 1)}{4\omega^2 - 1}$$

AND WHERE

d_i = A UNIT VECTOR ALONG THE PREFERRED DIRECTION AT A POINT OF THE MATERIAL

ω AND η = ANISOTROPIC PARAMETERS

CD-89-39299

Figure 1

METAL MATRIX COMPOSITE MODEL INCLUDING DAMAGE

EVOLUTION LAW

$$\dot{\alpha}_{ij} = \frac{H}{G^\beta} \dot{\epsilon}_{ij} - RG^{m-\beta} \Pi_{ij}$$

WHERE

$$G = \frac{1}{K_f^2} [l'_1 - \xi l'_2 - 12\zeta l'_3{}^2]$$

$$\Pi_{ij} = \alpha_{ij} - \xi (d_k d_j \alpha_{jk} + d_j d_k \alpha_{ki} - 4l'_3 d_i d_j) - 4\zeta l'_3 3d_i d_j - \delta_{ij}$$

$$l'_1 = \frac{1}{2} \alpha_{ij} \alpha_{ij} \quad l'_2 = d_i d_j \alpha_{jk} \alpha_{ki} - 4l'_3{}^2 \quad l'_3 = \frac{1}{2} d_i d_j \alpha_{ji}$$

$$\xi = \frac{\eta^2 - 1}{\eta^2} \quad \zeta = \frac{4(\omega^2 - 1)}{4\omega^2 - 1}$$

AND WHERE

d_i = A UNIT VECTOR ALONG THE PREFERRED DIRECTION AT A POINT OF THE MATERIAL

ω AND η = ANISOTROPIC PARAMETERS

CD-89-39300

Figure 2

METAL MATRIX COMPOSITE MODEL INCLUDING DAMAGE

DAMAGE LAW

$$\dot{\psi} = -A \bar{\sigma}^p / \psi^q$$

$$\bar{\sigma} = \chi (N, S)$$

IN WHICH DAMAGE VARIABLE,

$$D = 1 - \psi$$

WHERE

N = MAXIMUM TENSILE STRESS TO THE FIBER DIRECTION

S = MAXIMUM LONGITUDINAL SHEAR STRESS ALONG FIBER DIRECTION

FORM OF FUNCTION χ USED:

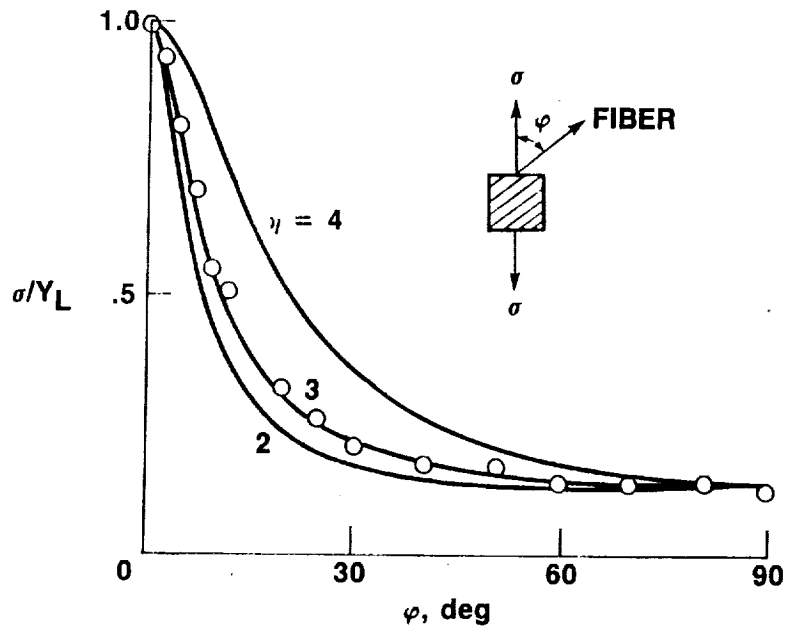
$$\bar{\sigma} = \lambda \langle N \rangle + (1 - \lambda) S \quad (0 \leq \lambda \leq 1)$$

CD-89-39301

Figure 3

YIELD STRESS OF TUNGSTEN/COPPER FOR VARIOUS FIBER ORIENTATION ANGLES

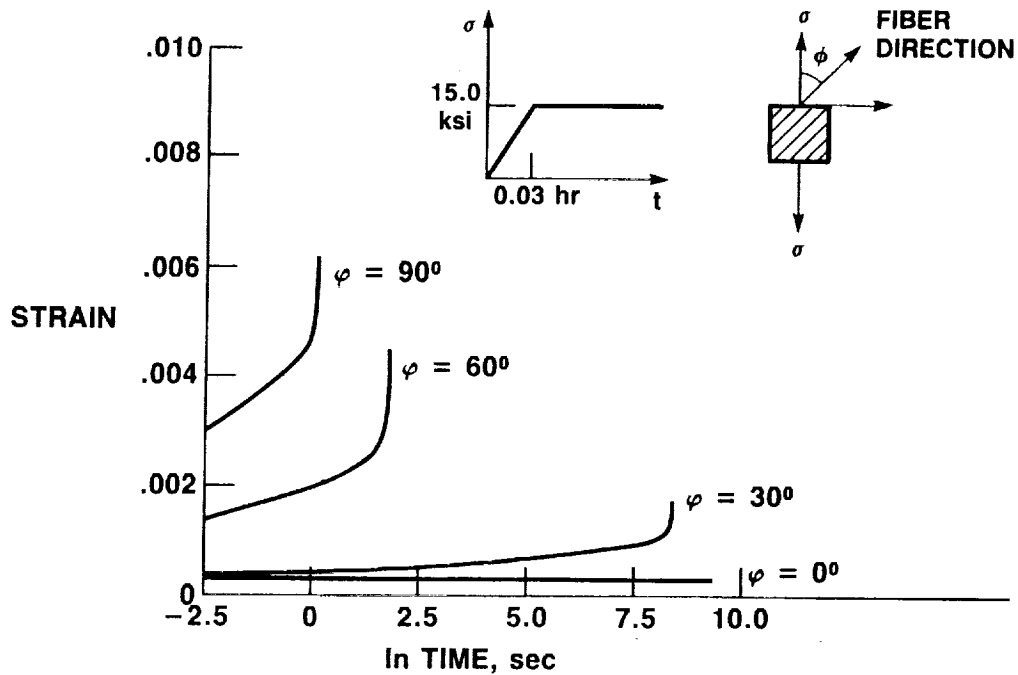
$\omega = 7$; EXPERIMENTAL DATA FROM COOPER (1966)



CD-89-39302

Figure 4

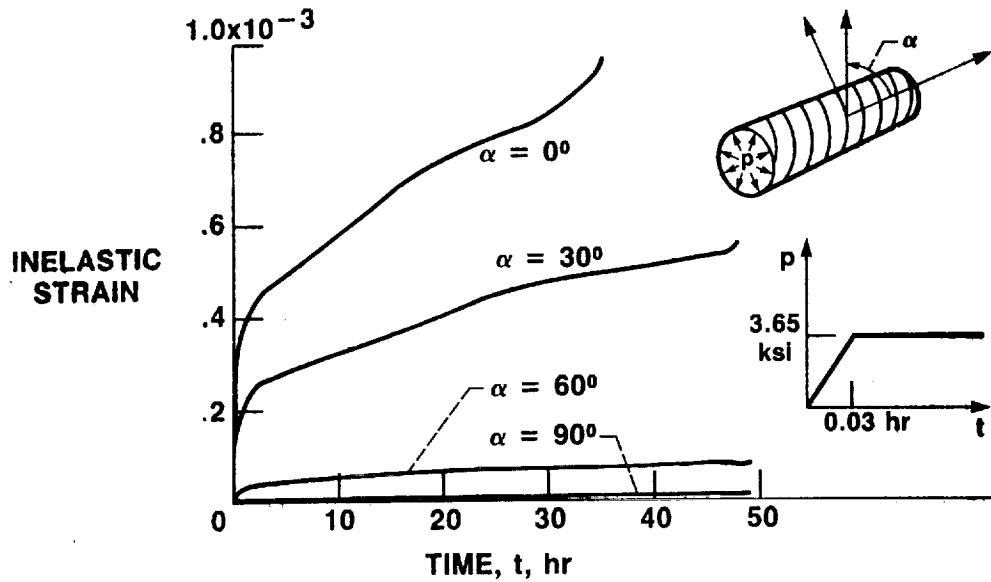
CREEP CURVES INCLUDING DAMAGE



CD-89-39303

Figure 5

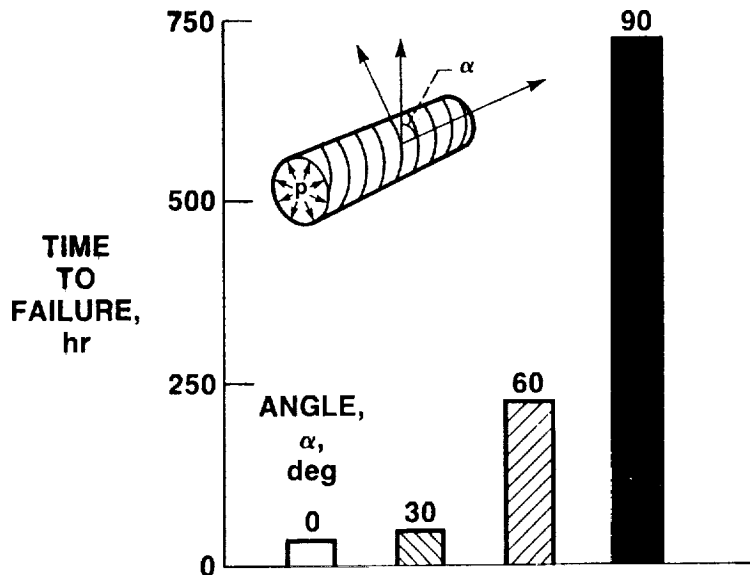
TANGENTIAL STRAIN AT INNER RADIUS OF METAL-MATRIX COMPOSITE CYLINDER (INCLUDING DAMAGE)



CD-89-39304

Figure 6

ROBINSON'S METAL-MATRIX COMPOSITE VISCOPLASTIC DAMAGE MODEL THICK-WALLED CYLINDER (800 °F, $p = 3.65$ ksi)



CD-89-39305

Figure 7

100

100

100

100

100

100

100

100

100

100

100

100

100

THE EFFECT OF HYDROGEN ON THE DEFORMATION BEHAVIOR OF A SINGLE
CRYSTAL NICKEL-BASE SUPERALLOY

W.S. Walston and A.W. Thompson
Carnegie Mellon University
Pittsburgh, PA 15213

59-26
19866

I.M. Bernstein
Illinois Institute of Technology
Chicago, IL 60616

The major goal of this study is to determine how hydrogen affects the deformation and fracture behavior of PWA 1480. Tensile tests, hydrogen-induced crack growth and fracture toughness tests are being performed in order to meet this goal. The role of hydrogen trapping sites is also being incorporated by varying the levels of porosity and eutectic γ . This presentation will concentrate mainly on the effect of hydrogen on the tensile deformation behavior.

All tensile samples tested were within 5° of [001]. The samples were given the normal heat treatment resulting in a cuboidal γ size of approximately $0.5 \mu\text{m}$. Samples were gas-phase charged for 15 days at 350°C and 20 kpsi resulting in a uniform hydrogen concentration of 300 ppm by weight (17500 appm). The concentration in the samples was analyzed by vacuum hot extraction at 900°C . Tensile tests were interrupted at different plastic strain levels to observe the development of the dislocation structure. TEM foils were cut perpendicular to the tensile axis to allow the deformation of both phases to be simultaneously observed as well as parallel to [111] to show the superdislocations on their slip planes. TEM observations were performed on a JEOL 120 CX operating at 120 KeV.

Similar to other nickel-base superalloys, hydrogen was detrimental to the room temperature tensile properties of PWA 1480. There was little effect on strength, however the material was severely embrittled. Even without hydrogen, the elongation-to-failure was only approximately 3%. The tensile fracture surface was made up primarily of ductile voids with regions of cleavage fracture. These cleavage facets are the eutectic γ in the microstructure. It was shown by quantitative fractography that hydrogen embrittles the eutectic γ and causes the crack path to seek out and fracture through the eutectic γ . There was two to three times the amount of cleavage on the fracture surface of the hydrogen-charged samples than on the surface of the uncharged samples.

The effect of hydrogen can also be seen in the dislocation structure. There is a marked tendency for dislocation trapping in the γ matrix with and without hydrogen at all

This work is supported by NASA Lewis Research Center

plastic strain levels. Without hydrogen there is a high dislocation density in the γ matrix leading to strain exhaustion in this region and failure through the matrix. The dislocation structure at failure with hydrogen is slightly different. TEM foils cut parallel to [111] showed dislocations wrapping around γ precipitates. This is in contrast to other observations on high γ V_f superalloys which report long straight screw dislocations cutting through the γ precipitates.¹ [001] foils show that there is a lower dislocation density in the γ matrix which can be linked to the effects of hydrogen on the fracture behavior. By seeking out the eutectic γ and preferentially failing through this phase, it is possible that the maximum accommodating strain in the γ matrix is not reached. This suggests that removing the eutectic γ through heat treatment would result in less hydrogen embrittlement. Preliminary results indicate that this is true and also that eliminating the eutectic γ results in a significantly higher ductility in all specimens.

The primary activity in the γ precipitates is in the form of superlattice intrinsic stacking faults (SISFs). These faults have been reported in other ordered alloys and superalloys.^{2,3} It is not believed that these SISFs play a large role in the deformation of this alloy. In hydrogen-charged samples, "extended Z" configurations have been observed in the γ precipitates similar to those in superalloys at high temperatures.⁴ This suggests that solute hydrogen promotes the cross-slip of superdislocation segments at room temperature. This phenomena was observed in previous work at Carnegie Mellon on a similar superalloy,¹ and recently room temperature cross-slip has been reported in Ni₃Al.⁵

References

1. M. Dollar and I.M. Bernstein, *Acta Met.*, **36**, 2369, (1988)
2. D.P. Pope and S.S. Ezz, *Int. Met. Rev.*, **29**, 136, (1984)
3. W.W. Milligan, *priv. comm.*
4. A. Huisein't Veld, et. al., *Scr. Met.*, **19**, 105, (1985)
5. A. Korner, *Phil. Mag. A*, **58**, 507, (1988)

Table I. Effect of Hydrogen on <001> Room Temperature Tensile Properties.

	σ_{ys} (MPa)	σ_{UTS} (MPa)	e_t (%)	R.A. (%)
uncharged	1001	1120	2.9	3.1
charged	1014	1060	0.38	2.7

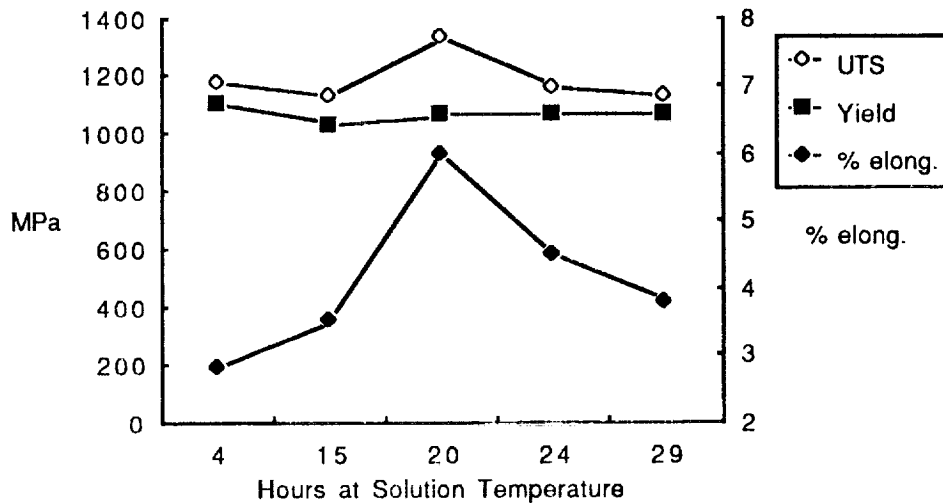
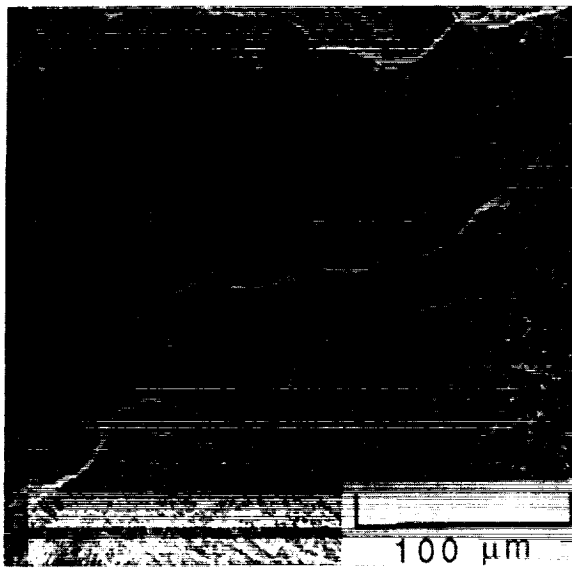
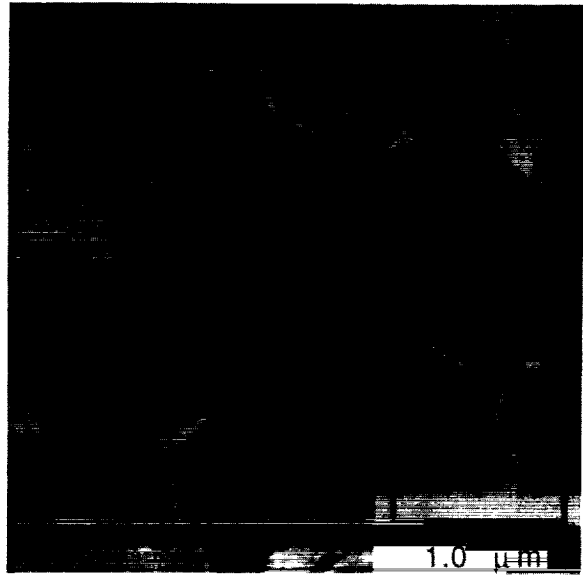


Figure 1. Effect of heat treatment solutionizing time on tensile properties. At 20 hours all of the eutectic γ is removed, and at longer times incipient melting becomes a factor. This shows that removing the eutectic γ can significantly increase ductility.



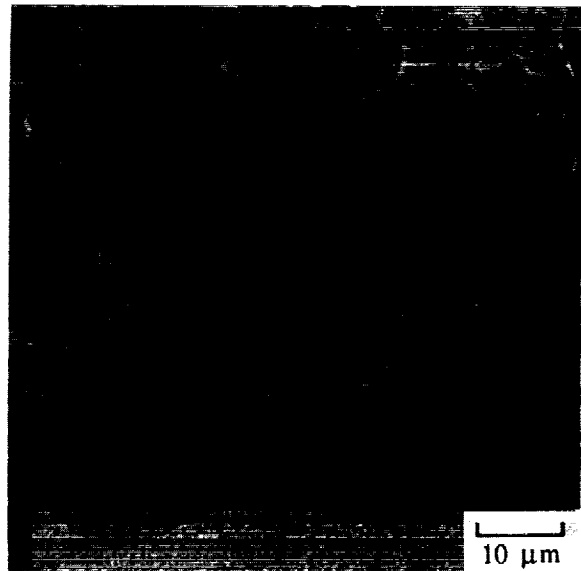
a



b



c

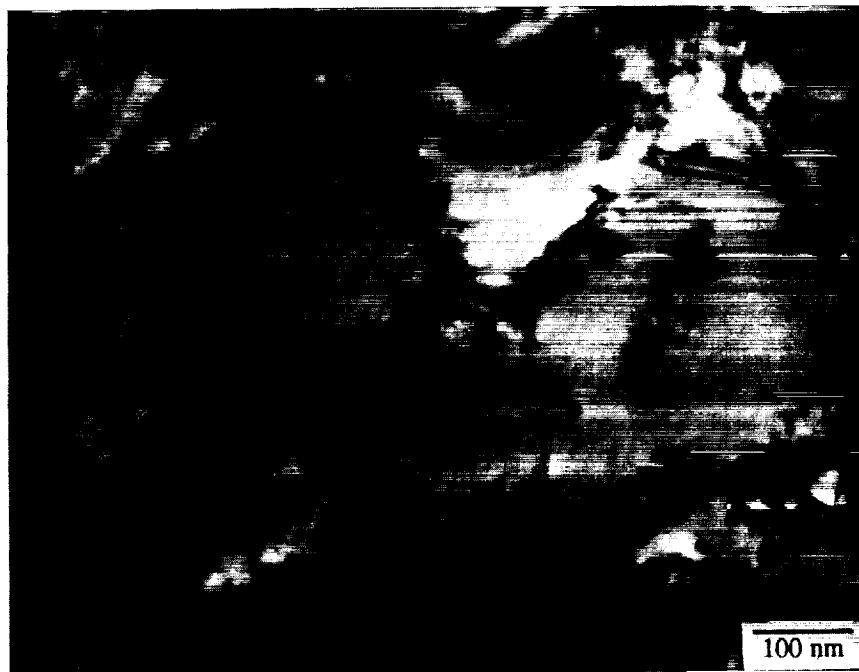


d

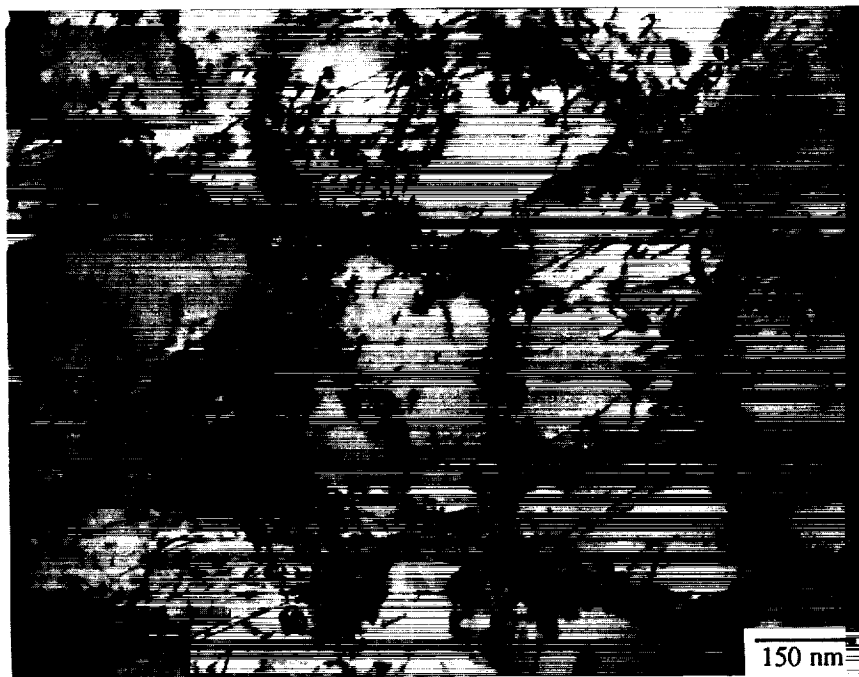
Figure 2. (a) Overall [001] tensile fracture (b) small ductile voids (c) cleavage facet (d) plateau etch showing cleavage on fracture surface and eutectic γ in microstructure.

ORIGINAL PAGE
BLACK AND WHITE PHOTOGRAPH

ORIGINAL PAGE
BLACK AND WHITE PHOTOGRAPH

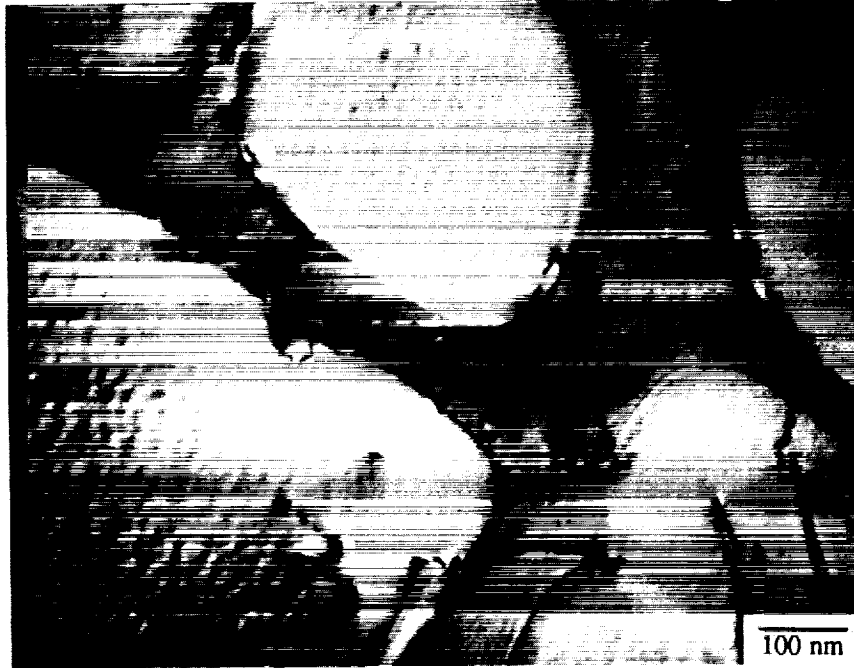


a

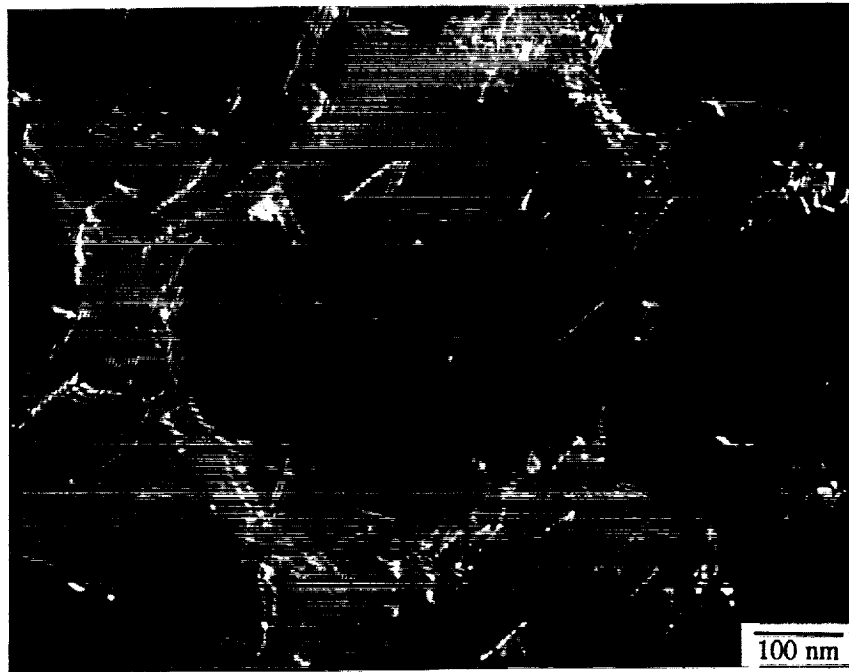


b

Figure 3. [001] micrographs of uncharged sample (a) $\epsilon_p = 1.2\%$ (b) $\epsilon_f = 3.0\%$.



a



b

Figure 4. [001] micrographs of charged sample (a) $\epsilon_p = 0.15\%$ (b) $\epsilon_f = 0.4\%$, weak-beam dark field (WBDF).

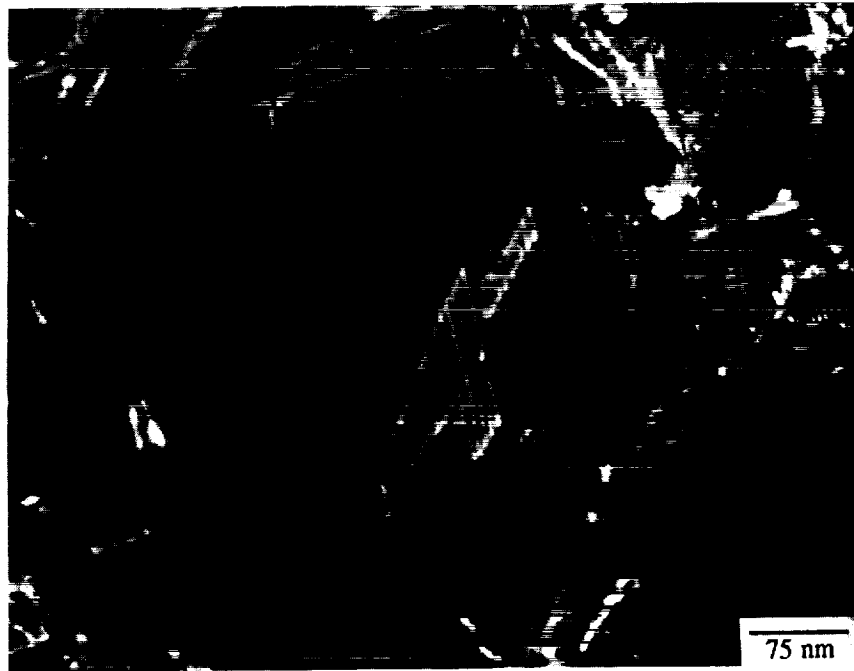


Figure 5. WBDF of superlattice intrinsic stacking faults (SISFs) in γ precipitate.



Figure 6. Room temperature cross-slip in hydrogen charged samples.

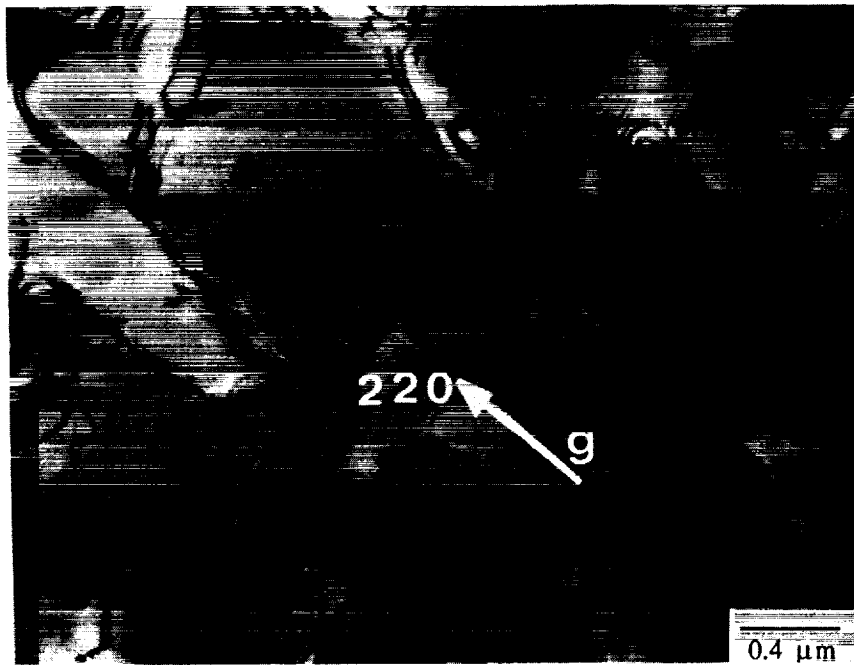


Figure 7. [111] micrograph showing superdislocations bowing around γ' precipitates.

ORIGINAL PAGE
BLACK AND WHITE PHOTOGRAPH

The Influence of Advanced Processing on PWA 1480

L. G. Fritzemeier and G. D. Schnittgrund
Rocketdyne Division
Rockwell International

Single crystal nickel base superalloys have been evaluated for potential application in the Space Shuttle Main Engine (SSME) high pressure turbopump turbines. Single crystals exhibit low cycle and high cycle fatigue life improvements over directionally solidified, hafnium modified, MAR-M246 (DS MAR-M246), the current SSME turbine blade alloy. The extreme start and stop thermal transients, high rotational speeds and high frequency vibrational modes dictate that these properties are life limiting in the SSME. In contrast, the long time creep and stress rupture behavior in gas turbine engines, for which the turbine blade alloys were developed, are not of concern for the SSME application. Although the fatigue life improvements due to a direct material substitution are significant, additional gains are possible through the application of advanced processing techniques to the single crystal production sequence. The primary initiation sites for fracture in single crystal superalloys, especially under cyclic loads, are internal casting pores. This casting porosity is inherent due to the dendritic solidification of these two phase systems. Pores are caused by shrinkage of the interdendritic liquid during final solidification. The primary objective of this program was to evaluate the potential improvements in microstructures and material properties due to the reduction in size and density of these casting defects due to the application of high thermal gradient casting and hot isostatic pressing.

PWA 1480 was chosen as the alloy to be evaluated for this program. The alloy had previously been chosen for the SSME application after screening of the commercially available single crystal alloys. PWA 1480 exhibited superior hydrogen environment embrittlement resistance relative to other candidate single crystal superalloys. In addition, a significant data base of material properties had been compiled for this alloy. Baseline tests for this program were conducted on standard commercial thermal gradient cast and standard PWA 1480 heat treated material. High thermal gradient casting was evaluated as an avenue for reducing the size of casting porosity. Hot isostatic pressing (HIP) was also employed for the elimination of casting pores. An alternate to the standard PWA 1480 coating plus diffusion bonding aging heat treatment cycle was also evaluated for potential improvements in the properties of interest to the SSME application. Microstructural changes associated with the high thermal gradient casting process were quantified by measurement of the size and density of the casting porosity, amount of retained casting eutectic and dendrite arm spacings. Tensile tests were conducted in air at 760°C. Stress rupture tests were conducted in air at 871°C at an initial applied stress of 620 MPa. Statistically determined numbers of low cycle and high cycle fatigue tests were conducted, for each material condition, to quantify changes in life due to process improvements. Three low cycle fatigue tests were conducted at 538°C and 2.0% total strain range and eight high cycle fatigue tests were conducted at room temperature and at 871°C, at a stress ratio of 0.47.

High thermal gradient casting was found to reduce both the size and density of the internal casting porosity relative to the standard thermal gradient process. The smaller pore size is a result of the decreased dendrite arm spacing afforded by the higher casting thermal gradient. Elemental segregation between the dendritic and interdendritic regions is also reduced. The reduced pore size provided an increase in both low cycle and high cycle fatigue lives relative to the standard gradient material. In addition, the high thermal gradient material exhibited a superior combination of tensile strength and ductility, though with a reduction in short time stress rupture life. These results are

complicated somewhat due to the introduction of the alternate heat treatment schedule along with the high gradient casting process. The high cycle fatigue life improvement should be more sensitive to the initiating flaw (pore) size, while the low cycle fatigue, tensile and stress rupture behaviors are more generally related to the morphology and character of the strengthening gamma prime precipitates.

Test results from the high gradient cast and HIP material were poor due to post-HIP heat treatment problems. HIP of the standard thermal gradient material was followed by the alternate heat treatment cycle. The combination of strength and ductility was improved somewhat, especially at 760°C. Stress rupture life was again found to be reduced relative to the standard process material. Low cycle fatigue life was approximately doubled, by the application of HIP and the alternate heat treatment relative to the baseline material. High cycle fatigue lives were conducted at stress levels different from the baseline material so a direct statistical comparison is difficult. An increase in life is indicated.

The results of the program have shown an improvement in material microstructure due to high thermal gradient casting. Improved homogeneity of PWA 1480 is advantageous in providing an improved solution heat treatment window and, potentially, easier HIP. High thermal gradient casting improves fatigue life by reducing casting pore size. The alternate heat treatment improves the balance of strength and ductility which appears to improve low cycle fatigue life, but with a reduction in short time stress rupture life. Based upon the testing from this program, hot isostatic pressing appears to afford further improvements in cyclic life, though additional evaluation is suggested. Development of the alternate heat treatment is not recommended due to the reduced stress rupture capability and the need to develop a new properties data base. High thermal gradient casting and HIP are recommended for application to single crystal castings.

Improving Properties of Rocket Engine Turbine Blades

<u>Technical Change</u>	<u>Property Benefit</u>
<ul style="list-style-type: none"> • Substitute single crystal for columnar grained alloy 	<ul style="list-style-type: none"> • Eliminate carbides as fatigue initiation sites
<ul style="list-style-type: none"> • High gradient single crystal casting • Hot isostatically pressed single crystal • Alternate heat treatment 	<ul style="list-style-type: none"> • Improve homogeneity, increase fatigue life • Eliminate porosity as fatigue initiation site • Improve hydrogen environment embrittlement resistance
<ul style="list-style-type: none"> • Crystallographic orientation control 	<ul style="list-style-type: none"> • Improve hydrogen environment embrittlement resistance, control dynamic response
<ul style="list-style-type: none"> • Rocket engine turbine blade alloy development 	<ul style="list-style-type: none"> • Hydrogen resistant, fatigue capable alloy



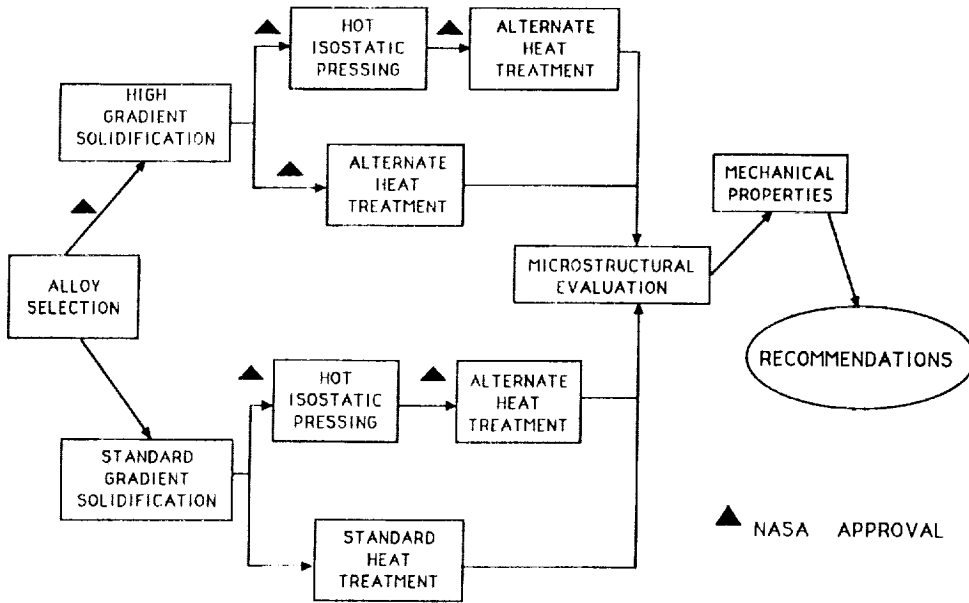
88D-32-2
102-75

ADVANCED PROCESSING OF PWA 1480 PROGRAM OBJECTIVE

EVALUATE THE INFLUENCE OF HIGH THERMAL GRADIENT CASTING, HOT ISOSTATIC PRESSING AND ALTERNATE HEAT TREATMENT ON THE MICROSTRUCTURE AND MECHANICAL PROPERTIES OF A SINGLE CRYSTAL NICKEL BASE SUPERALLOY

D1-89-2-2

ADVANCED PROCESSING OF PWA 1480 PROGRAM LOGIC

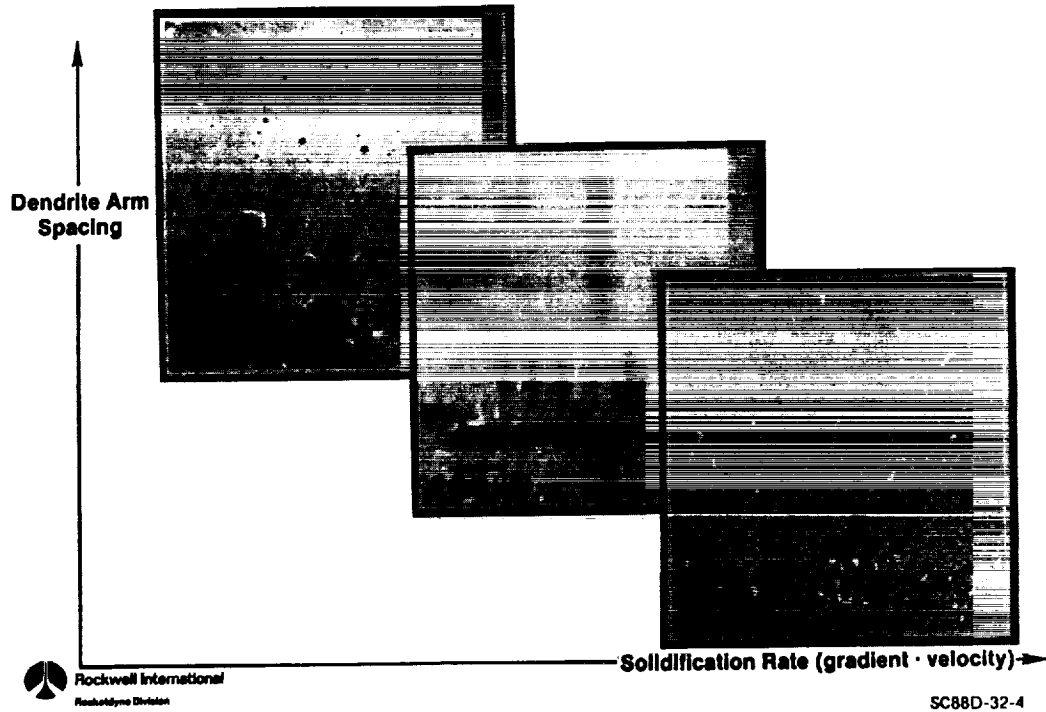


ADVANCED PROCESSING OF PWA 1480 ALLOY SELECTION CRITERIA

- HYDROGEN ENVIRONMENT EMBRITTLEMENT RESISTANCE SUPERIOR TO DS MAR-M246
- EXISTING DATA BASE
- PWA 1480 HAD BEEN SELECTED FOR SSME TURBINE BLADE DEVELOPMENT

D1-89-2-4

Influence of Casting Process on Microstructure of PWA 1480



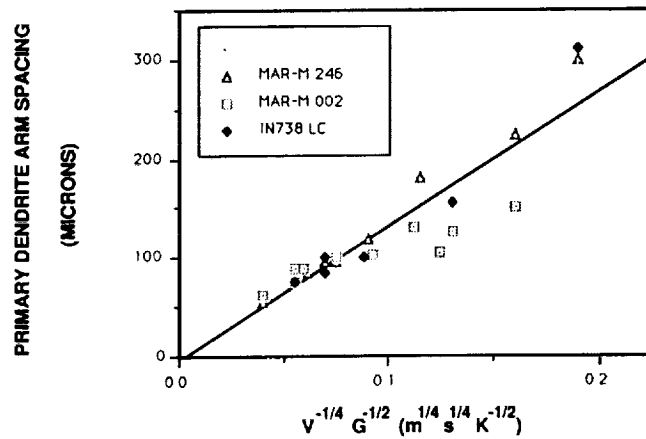
ADVANCED PROCESSING OF PWA 1480 CASTING THERMAL GRADIENT

CASTING PROCESS	AVERAGE DAS (MICRONS)	CALCULATED GRADIENT (C/CM)
STANDARD	445	12
HIGH	220	50

ORIGINAL PAGE IS
OF POOR QUALITY

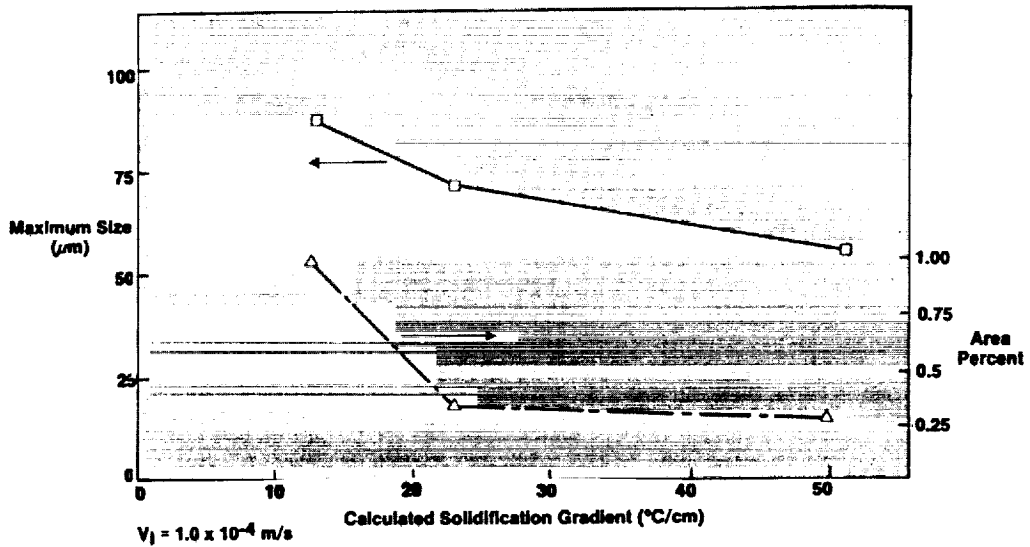
ADVANCED PROCESSING OF PWA 1480

DENDRITE ARM SPACINGS

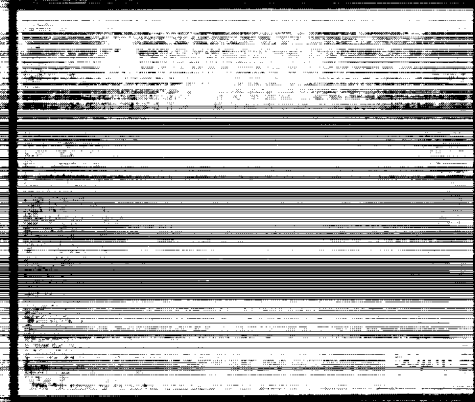


D1-89-2-7

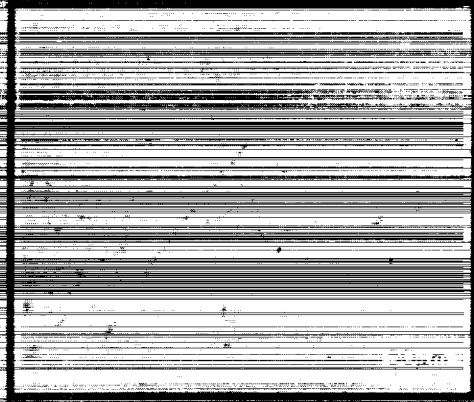
Influence of Thermal Gradient on Size and Distribution of Pores in PWA 1480



Hot Isostatic Pressing



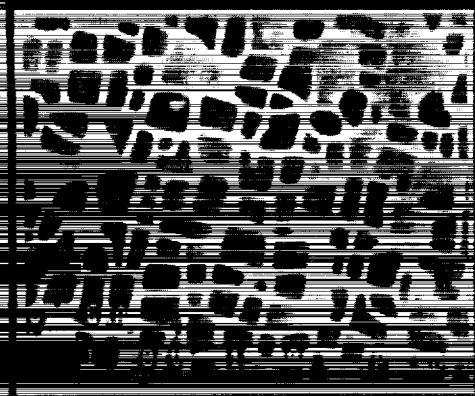
Internal Recrystallization
HIP Cycle = 103.5 MPa/1128°C/4 h



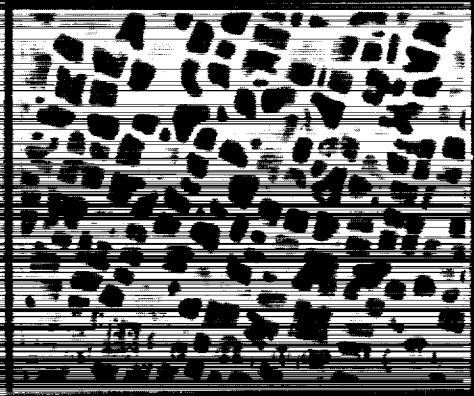
Surface Carburization

ORIGINAL PAGE IS
OF POOR QUALITY

Heat Treated Microstructures



Standard Heat Treatment:
Solution Heat Treat
Plus: 1,080°C/ 4 h
Plus: 871°C/32 h



Alternate Heat Treatment:
Solution Heat Treat
Plus: 1,010°C/ 2 h
Plus: 871°C/48 h

**ADVANCED PROCESSING OF PWA 1480
AVERAGE TENSILE TEST RESULTS**

CASTING GRADIENT	HEAT TREATMENT	TEMPERATURE (C)	YIELD STRENGTH (MPa)	ULTIMATE STRENGTH (MPa)	REDUCTION OF AREA (%)	ELONGATION (%)
STANDARD	STANDARD	24	1024	1075	12.5	11.7
STANDARD	HIP/ALT.	24	989	1219	9.2	9.8
HIGH	ALTERNATE	24	1080	1209	10.3	10.3
HIGH	HIP/ALT.	24	973	1003	3.8	NA
STANDARD	STANDARD	760	1149	1273	7.6	5.0
STANDARD	HIP/ALT.	760	1067	1240	12.9	13.2
HIGH	ALTERNATE	760	1110	1303	12.6	NA
HIGH	HIP/ALT.	760	972	1136	24.8	12.5

D1-89-2-8

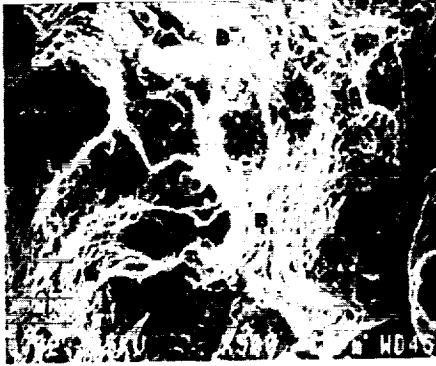
**ADVANCED PROCESSING OF PWA 1480
AVERAGE STRESS RUPTURE TEST RESULTS**

CASTING GRADIENT	HEAT TREATMENT	TIME TO RUPTURE (HOURS)	ELONGATION (%)
STANDARD	STANDARD	14	NA
STANDARD	HIP/ALT.	4	22
HIGH	ALTERNATE	9.4	15
HIGH	HIP/ALT.	2.8	6.2

D1-89-2-9

ORIGINAL PAGE
BLACK AND WHITE PHOTOGRAPH

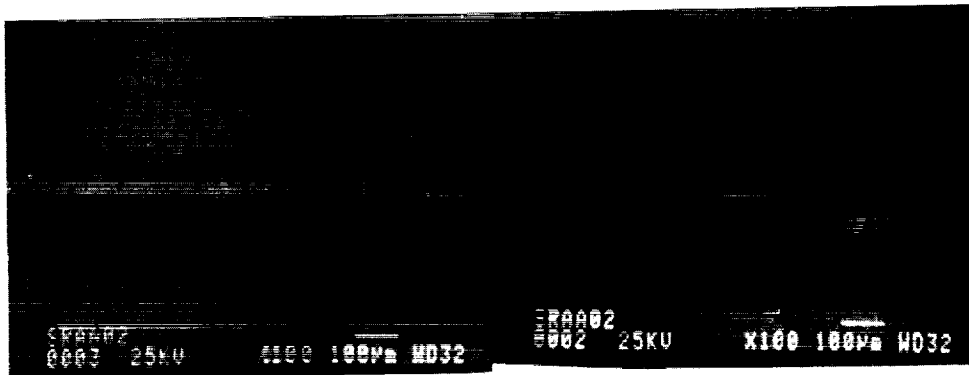
ADVANCED PROCESSING OF PWA 1480 STRESS RUPTURE FRACTOGRAPHY



FRACTURE SURFACE OF NON-HIP, HIGH
GRADIENT STRESS RUPTURE BAR.
FRACTURE INITIATES AT INTERNAL CASTING
POROSITY AT 'A' AND LINKS UP BY DUCTILE
TEARING AT 'B'.

D1-89-2-10

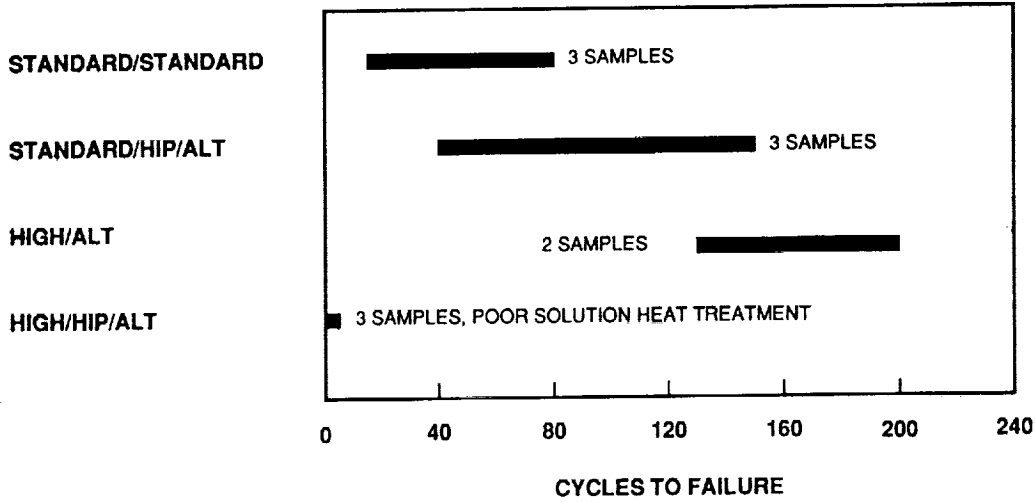
ADVANCED PROCESSING OF PWA 1480 STRESS RUPTURE FRACTOGRAPHY



LONGITUDINAL SECTION THROUGH FAILED STRESS RUPTURE BAR SHOWS
CRACK INITIATION AT INTERNAL CASTING POROSITY (ARROWS)

D1-89-2-11

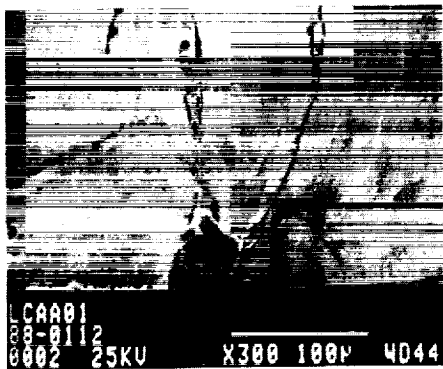
ADVANCED PROCESSING OF PWA 1480 LOW CYCLE FATIGUE TEST RESULTS



538C, 2.0% STRAIN RANGE

D1-89-2-12

ADVANCED PROCESSING OF PWA 1480 LOW CYCLE FATIGUE FRACTOGRAPHY



CRACK INITIATION IS AT THE SPECIMEN SURFACE OR AT NEAR SURFACE DEFECTS

PROPAGATION IS STAGE I ON {111} TYPE PLANES

R = -1.0, 538C

D1-89-2-14

ADVANCED PROCESSING OF PWA 1480 HIGH CYCLE FATIGUE TEST RESULTS

(R = 0.47)

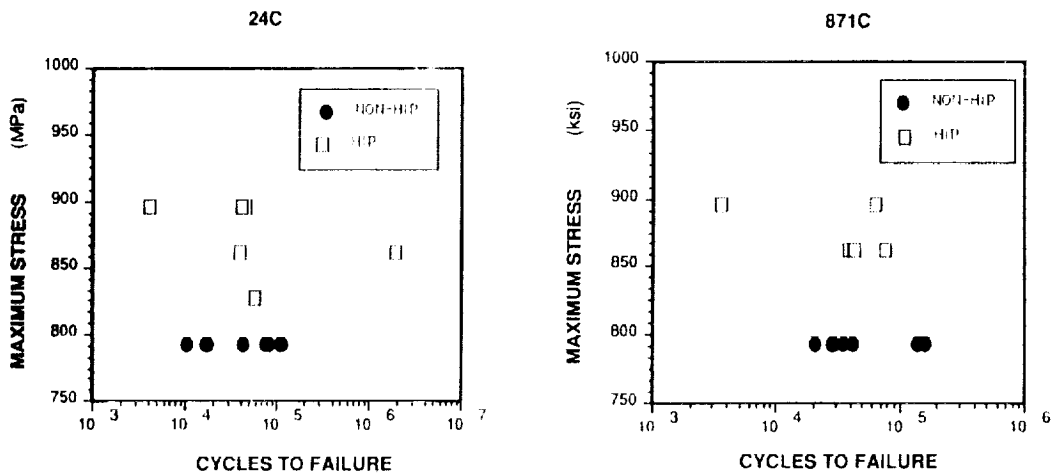
CASTING GRADIENT	HEAT TREATMENT	TEMPERATURE (C)	NUMBER OF TESTS	AVERAGE CYCLES TO FAILURE	STANDARD DEVIATION
STANDARD	STANDARD	24	8	58881	42528
STANDARD	HIP/ALT.	24	-	-	- *
HIGH	ALTERNATE	24	4	3.13×10^6	4.6×10^6
HIGH	HIP/ALT.	24	1	4.3×10^6	-
STANDARD	STANDARD	871	8	74320	60163
STANDARD	HIP/ALT.	871	-	-	- *
HIGH	ALTERNATE	871	5	1.18×10^6	594000
HIGH	HIP/ALT.	871	6	71246	72817

* TESTED AT DIFFERENT STRESS LEVELS

D1-89-2-15

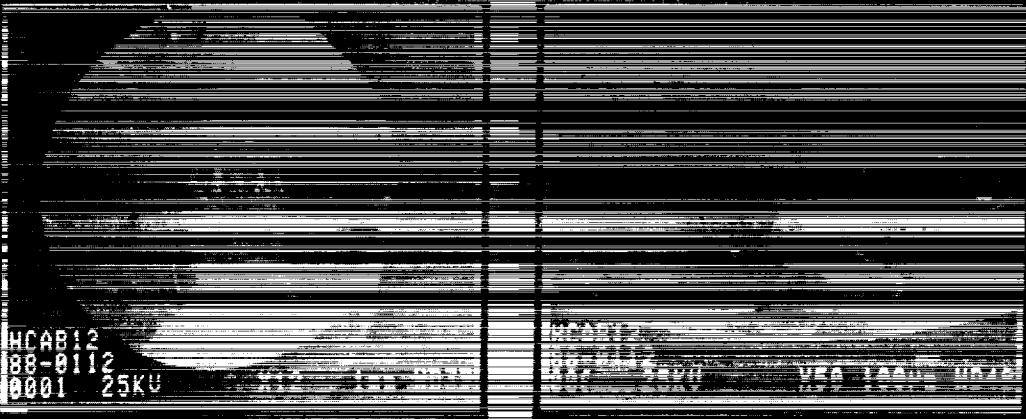
ADVANCED PROCESSING OF PWA 1480 STANDARD GRADIENT HCF RESULTS

R = 0.47



D1-89-2-13

High Cycle Fatigue Failure Analysis
20°C, R = 0.47, Maximum Stress = 793 MPa
 $N_f = 7.69 \times 10^6$ Cycles



Rockwell International
Rockwell Division

SC88D-32-15

High Cycle Fatigue Failure Analysis
871°C, R = 0.47, Maximum Stress = 793 MPa
 $N_f = 9.97 \times 10^6$ Cycles



Rockwell International
Rockwell Division

SC88D-32-16

ORIGINAL PAGE IS
OF POOR QUALITY

ORIGINAL PAGE
BLACK AND WHITE PHOTOGRAPH

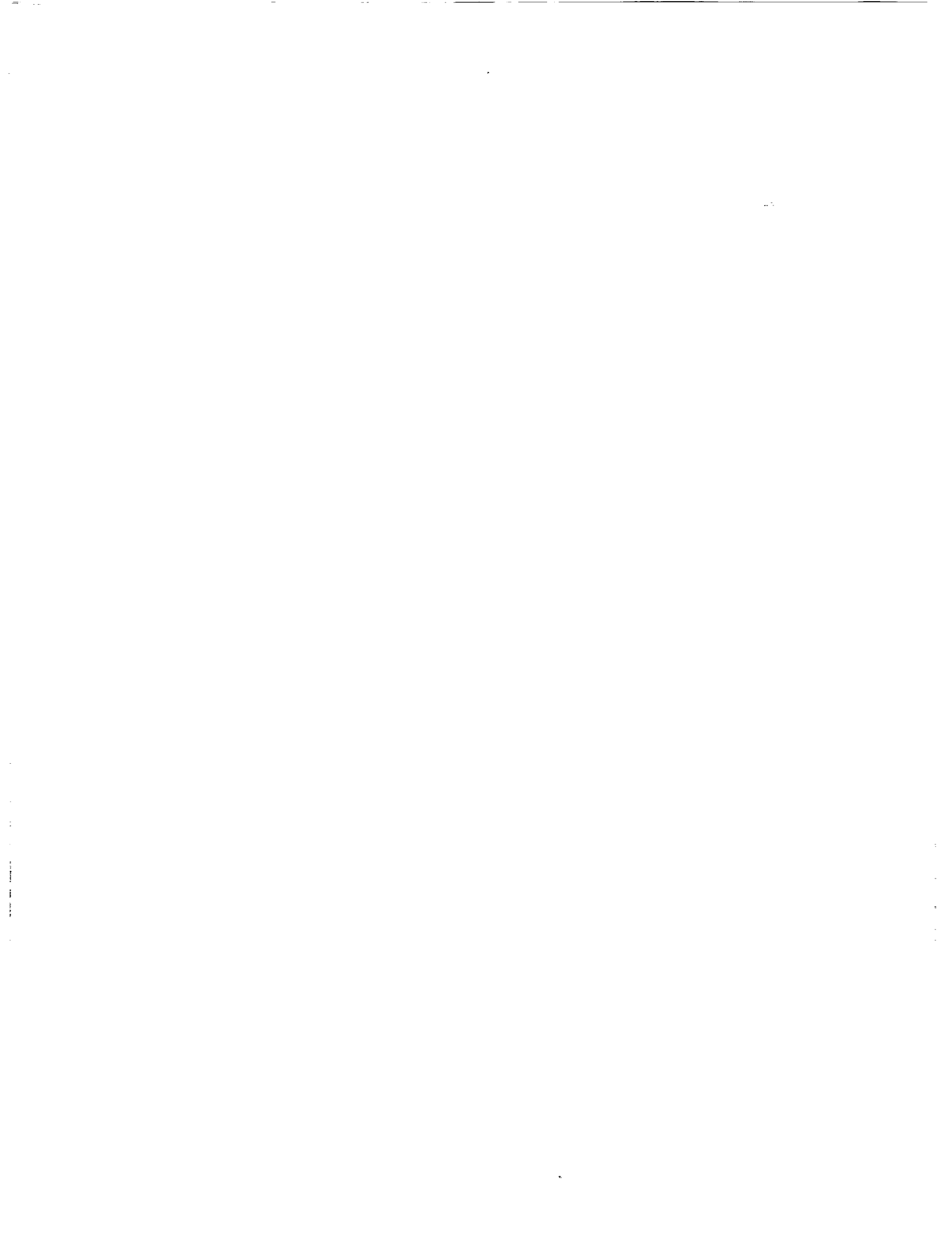
ADVANCED PROCESSING OF PWA 1480 CONCLUSIONS AND RECOMMENDATIONS

- **HIGH THERMAL GRADIENT CASTING**
 - **PRODUCES LESS SEGREGATED, FINER MICROSTRUCTURE**
 - **REDUCES PORE SIZE**
 - **RECOMMENDED FOR POTENTIAL IMPROVED HEAT TREATMENT AND HIP**

- **HOT ISOSTATIC PRESSING**
 - **REMOVES INTERNAL CASTING POROSITY**
 - **SIGNIFICANT CYCLIC LIFE IMPROVEMENT**
 - **RECOMMENDED FOR APPLICATIONS INVOLVING FATIGUE LIMITED LIFE**

- **ALTERNATE HEAT TREATMENT**
 - **SOME TENSILE PROPERTY IMPROVEMENT**
 - **BENEFIT IS NOT SIGNIFICANT ENOUGH TO WARRANT APPLICATION**

D1-89-2-4



511-35
19868**OVERVIEW OF THE INSTRUMENTATION PROGRAM****William C. Nieberding
NASA Lewis Research Center**

As you have heard or will hear in the rest of this conference, one of the major goals of the durability program is to develop computational models of the structural behavior, the fatigue life, and the environmental conditions pertinent to advanced reusable space propulsion systems. In many cases, however, there is very little experimental data available either to verify these models or to use as input conditions to the models.

The instrumentation portion of this durability program is thus aimed primarily at developing sensors and measurement systems capable of obtaining the data necessary for the verification of computational models. Indeed, some of these sensor systems may and probably will find their way into the test bed engine and possibly even into flight engines. This is increasingly likely because of the recent rise in the importance of instrumentation for health monitoring purposes. The major effort, though, is to develop what is needed for bench mark experiments in research rigs to more fully define the actual conditions experienced in such an engine. In some cases the only research rig available will turn out to be the test bed engine simply because the conditions cannot be adequately simulated in less extensive facilities.

One of the characteristics of measurement systems needed to verify codes is that the sensors must be nonintrusive or at least minimally intrusive so as not to significantly perturb the conditions being measured. The reason for this is that the computer codes do not take into account the perturbations that would be caused by an intrusive probe. This leads to a heavy emphasis on laser optical techniques and on thin-film sensors.

Another characteristic of such instruments is that they must be highly accurate and produce very high spatial and temporal resolution of the parameter being measured. Verifying codes demands this because the codes usually calculate highly resolved maps of such things as velocity, strain, temperature, etc.

The measurement systems needed generally fall into a number of broad categories. First there are the measurements needed on the surfaces of components such as turbine blades and vanes. Some of the desired parameters are temperature, strain, and heat flux. In this session the significant progress made in these measurement areas since the last durability conference will be discussed.

Another broad category encompasses those measurements needed in the flow environment around these components. Here, the desired results are high resolution maps of such parameters as flow velocity, temperature, density, pressure, and species concentration. One of the papers in this session deals with this type of measurement.

The remaining category deals with measurements necessary for monitoring

the health of the engine. This category, not reported at the last conference, has loomed ever more important since the Challenger disaster. One paper deals with an optical method for determining the characteristics of the plume. Another looks at holographic measurement of structural damage.

In summary, the instrumentation program is aimed at high accuracy, high resolution, minimally intrusive measurements on space propulsion system components and on the environment that surrounds these components. The primary goal is code verification, but some of the results may apply to later flight instruments. A more recently added goal is that of health monitoring.

N91-24319
SI-39
19869

TWO-DIMENSIONAL HIGH TEMPERATURE STRAIN MEASUREMENT SYSTEM

Christian T. Lant
Sverdrup Technology, Inc.
Lewis Research Center Group

and

John P. Barranger
NASA Lewis Research Center

The Instrumentation and Control Technology Division of the Lewis Research Center has developed the in-house capability to make two-dimensional optical strain measurements on high temperature test specimens. The first phase of this effort demonstrated one-dimensional strain measurement at temperatures to 450 °C, with a resolution of 18 microstrain (ref. 1). The phase II effort expands the phase I system to provide a two-dimensional strain measurement capability. This two-dimensional capability is implemented through a rotatable sensitive strain axis. Three components of surface strain can be measured automatically, from which the first and second principal strains are calculated. The phase II system demonstrated one- and two-dimensional strain measurements at temperatures beyond 750 °C with a resolution of 15 microstrain.

The system is based on the one-dimensional speckle shift technique of I. Yamaguchi (ref. 2). Some of the features of the technique include noncontact measurements, automatic cancellation of rigid body motion, no surface preparation requirement, and near-real time results. The Lewis system also features a short gauge length (<1 mm) and a programmably rotatable sensitive axis.

The speckle shift technique makes use of the linear relationship between surface strain and the differential shift of laser speckle patterns in the diffraction plane. Laser speckle is a phase effect that occurs when spatially coherent light interacts with an optically rough surface. Since speckle is generated by any diffusely reflecting surface, no specimen preparation is needed to obtain a good signal. Speckle shift is measured from a laser beam incident on a test specimen at 30° from the surface normal. By also measuring the speckle shift from a beam incident at an equal and opposite angle, potential errors due to rigid body motions are eliminated.

Figure 1 shows a schematic of the phase II optical system. An argon-ion laser beam is directed onto a test specimen at an angle. The Pockels cell and beamsplitting cube combination switches the beam from -30° to +30° by rotating the polarization of the beam. The acousto-optic modulator controls the exposure time of the line scan camera. The rotating assembly allows the plane of incidence of the beams onto the specimen to rotate, changing the sensitive axis of the instrument. A pair of 1/4-wave retardation plates maintains the polarization state of the beam going into the rotating assembly. Waist positioning lenses locate the laser beam waist at the specimen surface, improving

the error cancellation of the system. It is suspected that a planar wave front at the specimen surface also stabilizes the speckle patterns in the presence of nonuniform heating. The optical pallet can be easily mounted on a multiaxis positioning table.

Figure 2 is a view of the actual test setup. The rotating assembly is shown mounted on a goniometer. The optical axis is coincident with the goniometer's axis of rotation. The test specimen is located within a thermal enclosure in order to decrease the temperature gradients near the specimen surface.

Testing was done on a flat specimen of Inconel 600 mounted in a fatigue testing machine. A load cell measured the stress on the specimen before and after acquiring the speckle data. Figure 3 shows one-dimensional strain data at room temperature. The coincidence of the data loading up and loading down demonstrates the repeatability of the instrument. Figure 4 shows a two-dimensional run at room temperature. Strain components were measured at 0° (parallel to the load axis) and at $\pm 45^\circ$, and the plots indicate the calculated values of the first and second principal strains. The measured values of Young's modulus and Poisson's ratio are in good agreement with handbook values.

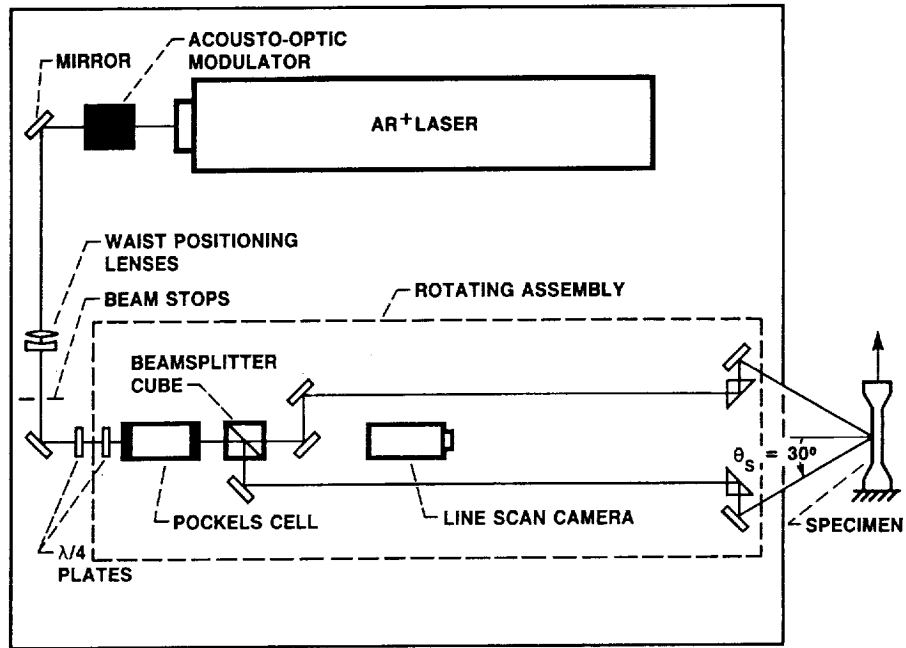
An RF induction heater was used to heat the specimen in the high-temperature runs. Good linearity of the principal strain moduli at high temperatures indicate precision and stability of the system. However, a systematic error in the high-temperature test setup introduced a scale factor in the slopes of the two-dimensional stress-strain curves. The scale factor is due to a gradual load relaxation during the retrieval of the three components of strain. The load relaxation occurred because, due to the spacing of the induction heating coils, the ends of the specimen were hotter than the test section; although the test section behaved linearly, the specimen ends were under plastic deformation. This result underscored the need for the load to be static during the system's data acquisition time of about 10 sec per two-dimensional strain point. No high temperature effects, however, have been observed to degrade speckle correlation.

Future efforts will include reading two-dimensional speckle patterns with an area array camera. This will allow the correlation peak to be maximized and will extend the range of tolerable rigid body motion. Dedicated correlation hardware will reduce the correlation times to the point that true real time measurements can be made.

REFERENCES

1. Lant, C.T.; and Qaqish, W.: Optical Strain Measurement System Development - Phase I. (Sverdrup Technology, Inc.; NASA Contract NAS3-24105) NASA CR-179619, 1987.
2. Yamaguchi, I.: A Laser-Speckle Strain Gauge. J. Phys. E. Sci. Instrum., vol. 14, no. 11, Nov. 1981, pp. 1270-1273.

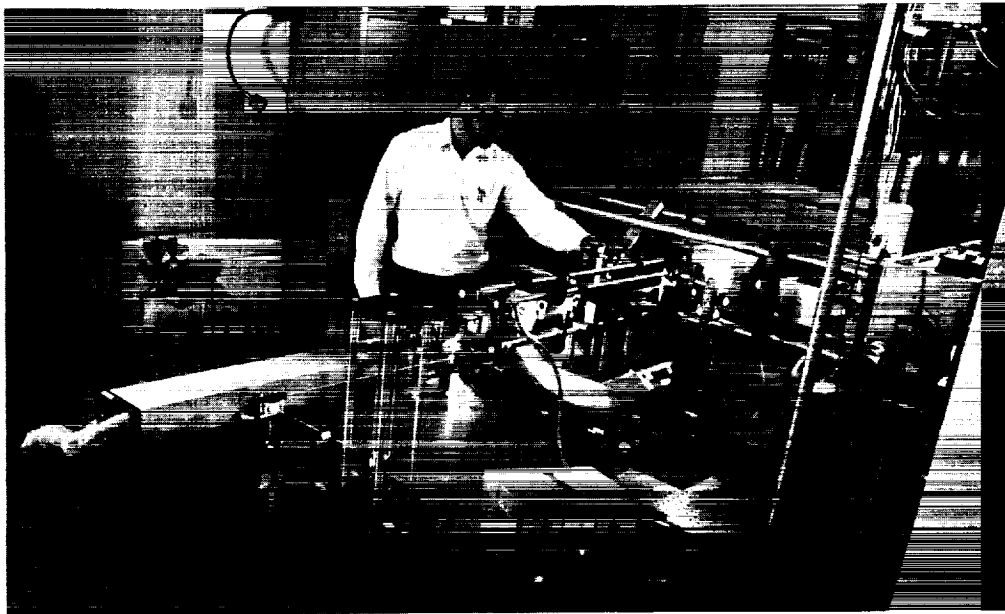
PHASE II OPTICAL DESIGN



CD-89-39279

Figure 1

PHASE II TEST SETUP



CD-89-39280

Figure 2

ONE-DIMENSIONAL STRESS/STRAIN DATA

25 °C

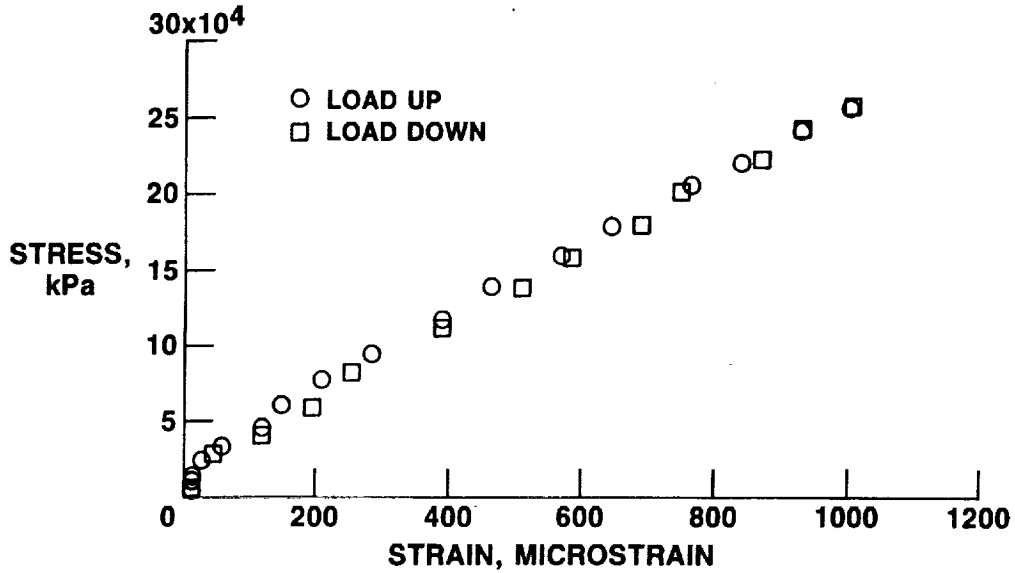


Figure 3

TWO-DIMENSIONAL STRESS/STRAIN DATA

25 °C

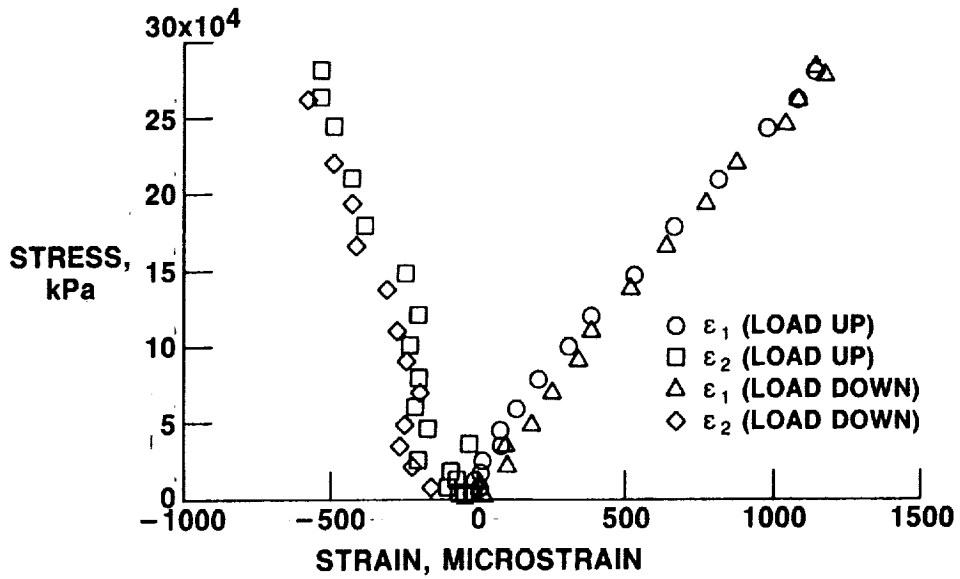


Figure 4

OPTICAL INSPECTION OF SPACE-PROPULSION COMPONENTS
USING AN INJECTION SEEDED Nd:YAG LASER SYSTEM

Arthur J. Decker
National Aeronautics and Space Administration
Lewis Research Center
Cleveland, Ohio 44135

513-36
19870

A dual-beam, injection-seeded, Nd:YAG laser has been demonstrated for detecting structural defects. This demonstration was part of an ongoing project¹ to use dual-reference-beam holographic interferometry to inspect space propulsion components for cracks, defects, structural failures, structural changes, and gas leaks. Potential subjects for inspection include welds, duct work, casings, turbopumps, blades, composites, and ceramics. The maximum dimension of an inspected area ranges from a few centimeters to a meter. The entire optical inspection system is now ready for a demonstration application.

Dual-reference-beam holographic interferometry overcomes the most significant limitation of holographic interferometry: interpretation of the recorded fringe patterns. Measurement and analysis of the fringe pattern are fully computerized and automated. There is also a factor of 10 to 100 increase in sensitivity and dynamic range over other holographic methods. The electronic detection and computerized analysis of an interference fringe pattern can be accomplished by optical heterodyning, quasiheterodyning, or phase shifting. Optical heterodyning was selected as the most sensitive.

Pulsed lasers are needed for inspections in the field between tests and during tests of components or engines. The short pulse of the laser (7 nanoseconds) makes the hologram recording process insensitive to vibration and motion of the subject. A double exposure records the vibration or load-induced deflection of the subject. The deflection is encoded in the interference fringe pattern reconstructed from the hologram. The term "dual reference beam" means that geometrically distinct reference beams are used for each of the two exposures of the double-exposure hologram.

Both pulsed-laser and continuous-wave-laser holograms are interpreted by the same computerized, automated, readout facility. The recorded scene is reconstructed in that facility with duplicates of the two reference beams originally used to record the hologram. In optical heterodyning, an acoustooptic frequency shifter shifts the frequency of one duplicate relative to the other. A 125 kHz frequency shift is used in our facility. A lens forms an image of the fringe pattern and subject. The intensity of the fringe pattern varies sinusoidally at 125 kHz, and the phase of this signal contains the interference phase $\Delta\phi$. The interference phase, in turn, depends upon the structural-deflection field $\delta(\mathbf{r})$ occurring between the two exposures. The signal is detected at each point of the fringe pattern by a photodetector positioned by a computer controlled, precision, XYZ, positioning system. The signal is sent to a phase sensitive detector which measures the interference phase $\Delta\phi$ relative to a reference.

We note that the interference phase $\Delta\varphi$ in holographic interferometry is most sensitive to deflections along the optical axis or viewing direction. Therefore, we orient the surface of the subject as nearly perpendicular to the viewing direction as possible for an optical inspection. We also evaluate numerically one or more of the second derivatives of interference phase

$$\frac{\partial^2 \Delta\varphi}{\partial x^2} \quad \frac{\partial^2 \Delta\varphi}{\partial y^2} \quad \frac{\partial^2 \Delta\varphi}{\partial x \partial y}$$

These quantities depend primarily on the deflection-induced change of curvature (bending) of the surface or on the spatial rate of twist (torsion) of the surface.

The bending distribution is sensitive to structural defects such as cracks. The use of heterodyne holographic interferometry to monitor the formation of a fatigue-induced crack in a blade of composite material has been reported.¹ We used the same kind of fatigue failure test to evaluate the performance of the pulsed laser system for recording dual-reference-beam holograms for heterodyne readout.

The pulsed laser system, intended for field inspections of propulsion components, contains two injection seeded, frequency doubled, Nd:YAG lasers. There is a 1-to-1000 microsecond adjustable delay between laser firings, so that double-exposure holograms with different time separations can be recorded. A single injection seeder assures that the Nd:YAG lasers operate in a single longitudinal mode. The laser system will produce two pulses of green light (532 nm) where each pulse has an energy equal to 500 mJ. The spectroscopic line-width of the pulses is 0.005 cm^{-1} . Consequently, good holograms can be recorded of subjects having a projected size up to about a meter and a surface relief (scene depth) of about half a meter.

The pulsed laser was compared with a continuous wave laser (argon-ion) for detecting fatigue cracking in a blade of composite material 8 cm long and 2 cm wide. The blade was vibrated at a large amplitude in a shaker to induce cracking. Periodically, this destruction was interrupted and optical inspections performed. The pulsed-laser optical inspections were performed by recording double-exposure holograms of the blade as it vibrated in its first bending mode at a small amplitude. The laser firing was synchronized with an accelerometer attached to the blade. The two laser beams were each divided, routed into two separate reference-beam channels, and combined carefully in a single object-beam channel. The argon-ion inspections were performed by accurately displacing the blade tip between exposures of the double-exposure hologram.

The Nd:YAG laser and argon-ion laser performed equally well for detecting cracking in the blade using the procedures above. Both lasers were used with a small angle between reference beams (about 0.015 degree). The small angle makes it easy to form detectable fringes from holograms recorded in the field.

Optical inspections of the bending induced by a carefully excited vibrational mode, with the laser accurately synchronized with the phase of an accelerometer output, have the advantage of being repeatable. Hence changes in complex structures should

be easier to recognize. This method is suitable between runs of a component or for acceptance testing. It may be desirable to inspect a component during a run or other test. The Nd:YAG laser is able to record up to 10 double-exposure holograms per second of such a time varying component. Using film to record the holograms, one could conceive of performing 100 optical inspections of a time varying and changing component from holograms recorded during a 10 second run.

The conclusion is that the combination of automated, computerized fringe measurement system and injection seeded Nd:YAG laser is both suitable and ready for a field demonstration of an optical inspection of a propulsion component based on dual-reference-beam holographic interferometry. The detailed inspection procedure will depend on the component and conditions.

1 Decker, A.J.; Krasowski, M.J.; and Krogulec, M.A.: Optical Inspection of Propulsion System Components Using Heterodyne Holographic Interferometry. in *Advanced Earth-To-Orbit Propulsion Technology 1988*, vol. II, NASA Conference Publication 3012.

TALK AND PROGRAM OBJECTIVES

- DISCUSS PROGRESS IN USING NEW Nd:YAG LASER FOR OPTICAL INSPECTION OF SPACE PROPULSION COMPONENTS
- INSPECT FOR CRACKS, DEFECTS, STRUCTURAL FAILURES, STRUCTURAL CHANGES, GAS LEAKS
- INSPECT WELDS, DUCT WORK, CASINGS, TURBOPUMPS, BLADES, COMPOSITES, CERAMICS
- INSPECT STRUCTURES WITH MAXIMUM PROJECTED DIMENSIONS PER INSPECTION FROM A FEW CENTIMETERS TO A METER

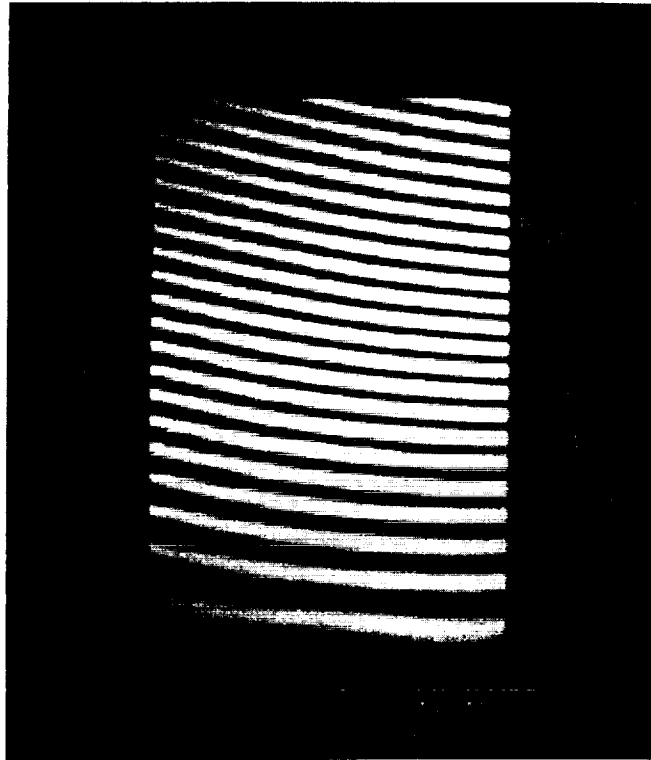
CD-89-39394

METHOD OF INSPECTION

- DUAL-REFERENCE-BEAM HOLOGRAPHIC INTERFEROMETRY
- AUTOMATED FRINGE MEASUREMENTS USING OPTICAL HETERODYNING
- CW LASER IMPLEMENTATION DISCUSSED AT EARTH-TO-ORBIT PROPULSION TECHNOLOGY CONFERENCE, MARSHALL, MAY, 1988
- PULSED LASERS NEEDED FOR INSPECTIONS IN FIELD BETWEEN TESTS AND DURING TESTS OF COMPONENTS OR ENGINES

CD-89-39395

**COSINE INTERFERENCE-FRINGE PATTERN
BETWEEN BENT AND UNBENT STATES
OF CANTILEVER**



CD-89-39396

**PHASE CHANGE FOR DEFLECTION
OF STRUCTURE**

$$\Delta\phi(\vec{r}) = \frac{4\pi}{\lambda} \frac{(\vec{k}_i - \vec{k}_r) \cdot \vec{\delta}(\vec{r})}{2}$$

CD-89-39397

ORIGINAL PAGE
BLACK AND WHITE PHOTOGRAPH

Nd:YAG LASER LAYOUT



CD-89-39398

HETERODYNE HOLOGRAPHY

$$I = I_0 + I_1 \cos [\Delta\Phi \pm \omega t]$$

CD-89-39399

ORIGINAL PAGE
BLACK AND WHITE PHOTOGRAPH

STRUCTURAL PROPERTIES FROM HOLOGRAPHY

STRAIN

$$\epsilon_{xx} = \frac{\partial \delta_x}{\partial x} \quad \epsilon_{xy} = \frac{1}{2} \left(\frac{\partial \delta_x}{\partial y} + \frac{\partial \delta_y}{\partial x} \right)$$

$$\epsilon_{yx} = \frac{1}{2} \left(\frac{\partial \delta_y}{\partial x} + \frac{\partial \delta_x}{\partial y} \right) \quad \epsilon_{yy} = \frac{\partial \delta_y}{\partial y}$$

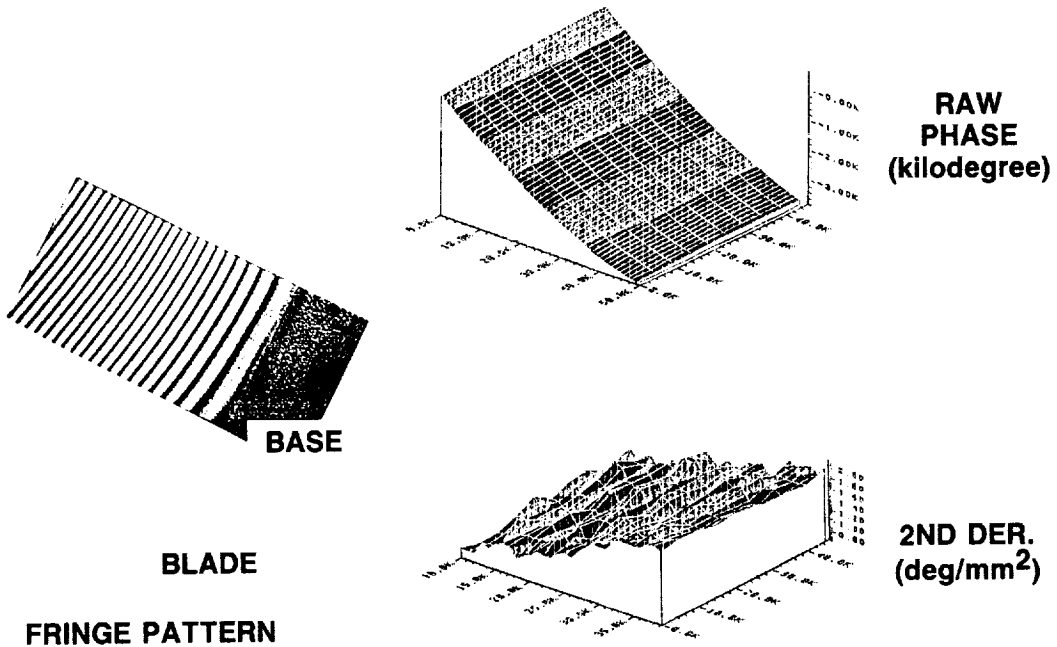
BENDING

$$\Delta K_\alpha = \frac{\partial^2 \delta_z}{\partial x^2} \cos^2 \alpha + 2 \frac{\partial^2 \delta_z}{\partial x \partial y} \cos \alpha \sin \alpha + \frac{\partial^2 \delta_z}{\partial y^2} \sin^2 \alpha$$

TORSION

$$\frac{d\Omega}{dS} = \frac{\partial^2 \delta_z}{\partial x \partial y} \cos^2 \alpha + \frac{1}{2} \left(\frac{\partial^2 \delta_z}{\partial y^2} - \frac{\partial^2 \delta_z}{\partial x^2} \right) \sin^2 \alpha$$

CD-89-39400

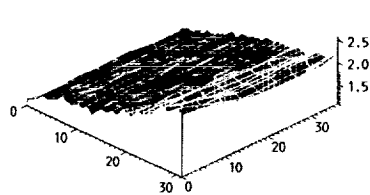


**RAW
PHASE
(kilodegree)**

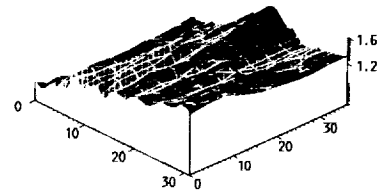
**2ND DER.
(deg/mm²)**

CD-89-39401

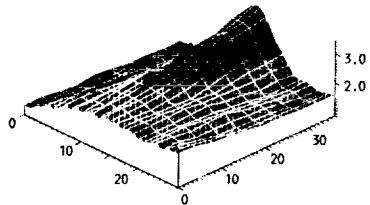
OPTICAL INSPECTIONS OF COMPOSITE BLADE



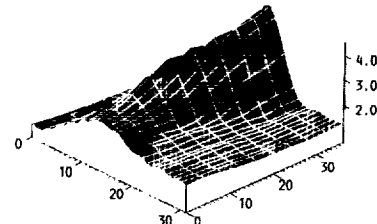
(a) COMPOSITE, VIBRATED 0 SEC.



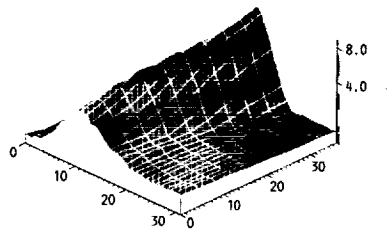
(b) COMPOSITE, VIBRATED 60 SEC AT 50 HZ.



(c) COMPOSITE, VIBRATED 120 SEC AT 50 HZ.



(d) COMPOSITE, VIBRATED 1200 SEC AT 50 HZ.



(e) COMPOSITE, VIBRATED 2400 SEC AT 50 HZ.

CD-89-39402

TESTS IN THE FIELD

- NEED DOUBLE-PULSE, PULSED-LASER SYSTEM (INJECTION-SEEDED Nd:YAG)
- CAN USE EXISTING AUTOMATED FRINGE MEASUREMENT SYSTEM USED FOR CW LASER APPLICATIONS
- NEED WAY TO CREATE INTEREXPOSURE DISPLACEMENT FIELD (VIBRATION)
- NEED PROCEDURES FOR INSURING REPEATABILITY OF TEST CONDITIONS

CD-89-39403

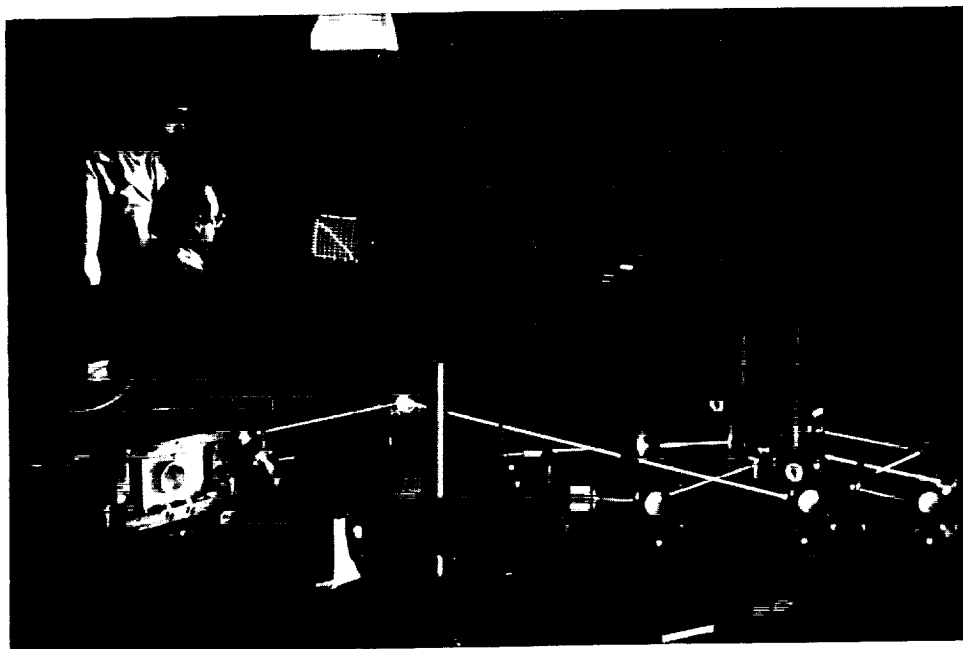
ORIGINAL PAGE
BLACK AND WHITE PHOTOGRAPH

INJECTION SEEDED Nd:YAG LASER SYSTEM

- TWO INDEPENDENT, Q-SWITCHED, Nd:YAG, OSCILLATOR, AMPLIFIER, FREQUENCY DOUBLER COMBINATIONS (QUANTEL YG 580 SERIES LASERS)
- ONE INJECTION SEEDER
- 500 mJ PER LASER OF 532 nm LIGHT
- 0.005 cm^{-1} LINE-WIDTH (2 m COHERENCE LENGTH)
- 1 TO 1000 MICROSECONDS BETWEEN PULSES FOR DOUBLE EXPOSURE
- 10 PULSE PAIRS PER SECOND

CD-89-39404

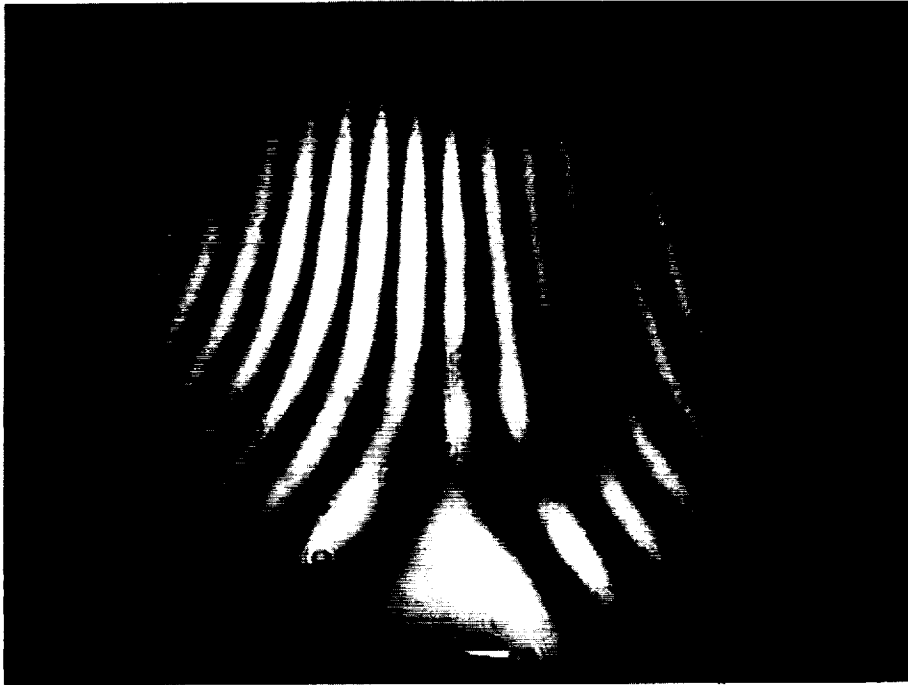
SAMPLE LAYOUT DUEL REFERENCE-BEAM HOLOGRAPHIC INTERFEROMETRY



CD-89-39405

FRINGE PATTERN

SIZE ABOUT 1 m



CD-89-39406

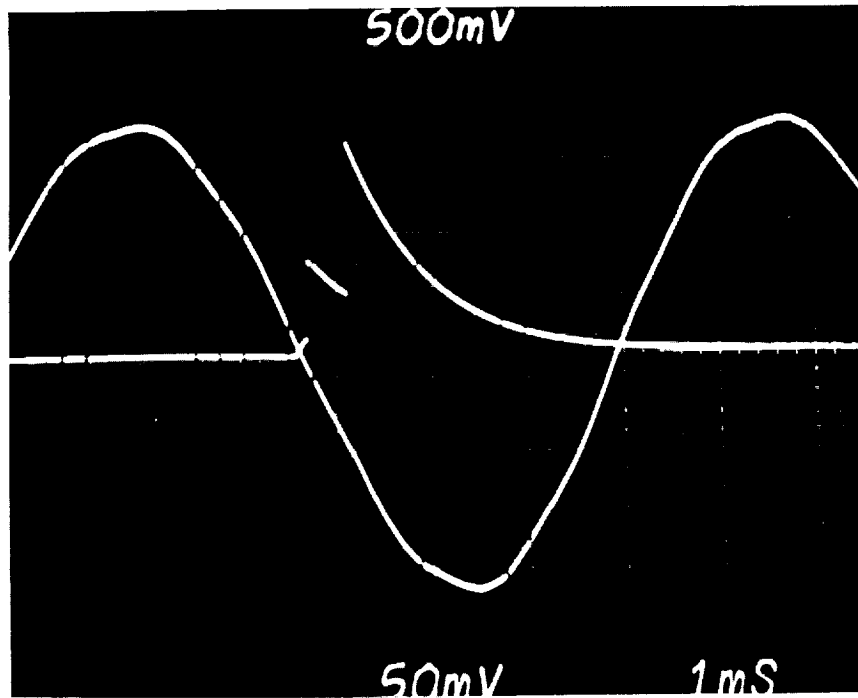
INTEREXPOSURE DISPLACEMENT

- SYNCHRONIZE LASER TO VIBRATIONAL MODE
- COMPONENT OR ENGINE INSPECTION BETWEEN RUNS:
EXCITE VIBRATIONAL MODE NONDESTRUCTIVELY

CD-89-39407

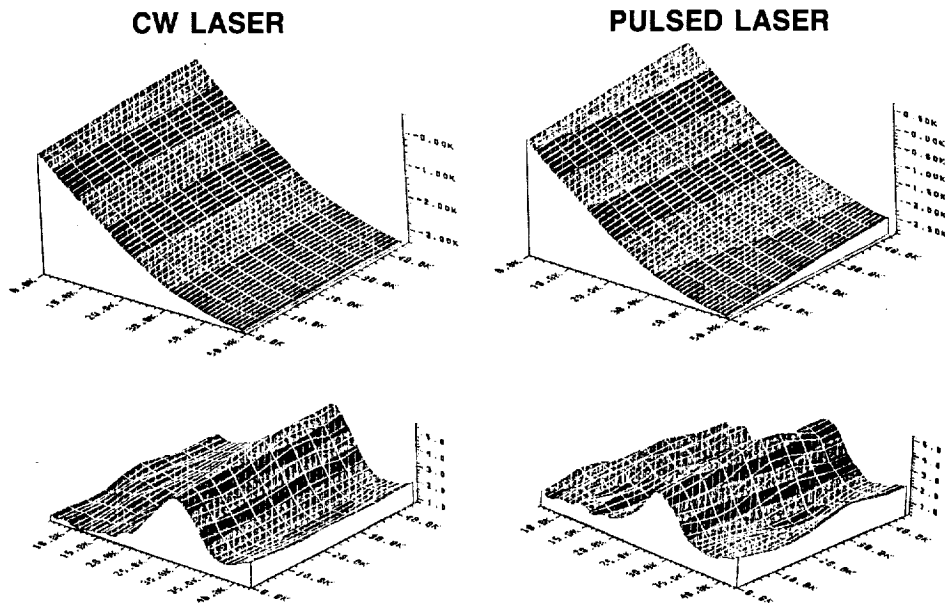
ORIGINAL PAGE
BLACK AND WHITE PHOTOGRAPH

ORIGINAL PAGE
BLACK AND WHITE PHOTOGRAPH
**TWO LASER PULSES SYNCHRONIZED WITH
ACCELEROMETER OUTPUT**



CD-89-39408

COMPOSITE AT 21 000 FATIGUE CYCLES



CD-89-39409

STATUS

- INJECTION SEEDED Nd:YAG LASERS ARE SUITABLE FOR DUAL-REFERENCE-BEAM HOLOGRAPHIC INTERFEROMETRY
- SENSITIVITY OF CW AND PULSED LASER INSPECTIONS SIMILAR FOR THE SAME REFERENCE BEAM INTERANGLE
- 3 STANDARD DEVIATIONS:
1/300 FRINGE, CW, LARGE ANGLE
1/100--1/60 FRINGE, CW AND PULSED LASER, SMALL ANGLE
- CW AND PULSED LASER METHODS CAN NOW BE DELIVERED TO SPECIFIC PROJECTS

CD-89-39410

514-35
19871

CALIBRATOR TESTS OF HEAT FLUX GAUGES MOUNTED IN SSME BLADES

Curt H. Liebert
NASA Lewis Research Center

Measurements of heat flux to space shuttle main engine (SSME) turbine blade surfaces are being made in the Lewis heat flux calibration facility. This facility was described at the 1987 Structural Integrity and Durability of Reusable Space Propulsion Systems Conference (ref 1). Surface heat flux information is obtained from transient temperature measurements taken at points within the gauge (refs. 2 to 4). A 100-kW Vortek arc lamp (ref. 5) is used as a source of thermal radiant energy. Figure 1 shows a gauge that has been placed at the external focus of an elliptical reflector in a lamp head attached to the side of a service module in the lamp system.

The schematic drawing of figure 2 details the miniature plug-type heat flux gauges being developed for measurement and study of blade surface heat flux. An annulus is electrical discharge machined (trepanned) into MAR M 246 (Hf)(DS) blade material creating a post, or thermoplug. The annulus is machined only part way through the blade thickness. This fabrication method is advantageous because a joining process (welding) is not required between the thermoplug and the gauge. Therefore, no seams are formed between the thermoplug and blade surface; seams can disturb boundary layer flow and heat transfer on the gauge surface. Figure 3 shows the rear of a gauge with the cover removed. Chromel-Alumel thermocouple wires (not shown) with diameters of 0.00254 cm are attached to the front surface of the gauge and along the sides and on the rear of the thermoplug. These wires are routed through the annulus to the back of the blade where they are attached to electrically insulated extension wires. The extension wires are mounted in grooves machined into the airfoil pressure surface (fig. 3), then routed through holes machined into the platform and finally fastened to the blade shank.

Thermoplugs, with diameters of about 0.190 cm and lengths varying from about 0.190 to 0.320 cm, are being investigated. The thermoplug is surrounded on all surfaces except the active surface by a pocket of air located in the circular annulus and under the back cover. Since the thermoplug is insulated, it is assumed that heat is conducted in a one-dimensional manner from the hot active surface to the cooler back side of the thermoplug. A one-dimensional relationship for obtaining surface heat flux is then (ref 2):

$$\dot{q}_s = \int_0^L (\rho C_p \partial T / \partial t) dz, \quad \text{w/m}^2 \quad (1)$$

where \dot{q}_s is the surface heat flux, L is the thermoplug length, and ρ and C_p are the density and specific heat of MAR-M-246(Hf)(DS), $\partial T / \partial t$ is the partial derivative of temperature with respect to time, and z is a distance along the thermoplug axis.

Values of specific heat as a function of temperature for MAR-M-246(Hf)(DS)

and a similar alloy (MAR-M-200) are shown in figure 4. These data were obtained from reference 6. The density of MAR-M-246(Hf)(DS) is 8442 kg/m^3 (ref. 6). Unfortunately, no indication of experimental error associated with property measurement is given in reference 6. Experimental errors of specific heat and density data are assumed as ± 20 percent and ± 5 percent. These uncertainties of measured property data are typical for many alloys. The curve of specific heat versus temperature used herein to solve equation (1) is shown as a solid curve in figure 4. The solid curve and literature data correspond within experimental error.

The suction surface of an instrumented SSME blade mounted on the calibrator is shown in figure 5. A heat flux gauge is mounted on both the suction and pressure surfaces at midspan and midchord. In figure 5 radiation is incident on the active surface of the suction surface gauge, and radiation is also incident on the back of the pressure surface gauge. Both this and the reverse orientation are being investigated. Welds attaching a cover plate (304 stainless steel) to the suction surface of the blade and a cover plate welded over extension wires buried in grooves machined into the airfoil are discernible in figure 5. Because there is no airflow over the airfoil surface tested in the calibrator, these welds were not machined flush to the surface.

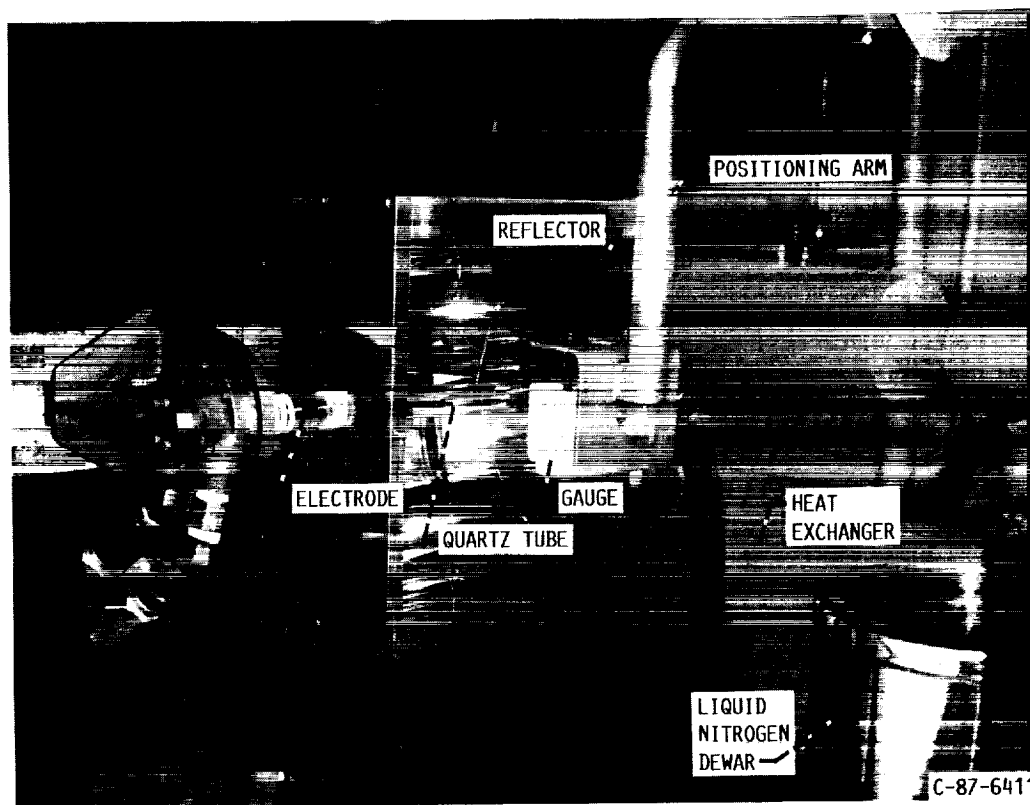
The heat flux gauge mounted on the suction surface below the cover is not discernible in figure 5 because the thermoplug and blade at this location are one piece. Thermoplug temperature history measured within the suction surface gauge is plotted in figure 6, and the corresponding heat flux history is shown in figure 7. Blade heat flux data are measured over a temperature range of about 100 to 1100 K at a lamp current of 400 A. This data are compared in figure 7 with data previously obtained with other gauges: (1) four miniature plug-type gauges mounted in MAR-M-246(Hf)(DS) coupons, (2) two commercial factory-calibrated Hy-Cal gauges, and (3) a photocell. The photocell millivolt data show that the lamp intensity rises rapidly during startup (time = 0.3 to 0.6 sec) and then becomes relatively constant at longer times. This trend was also observed when the two Hy-Cal gauges and the four miniature plug-type gauges mounted in the coupons were investigated in the calibrator. Furthermore, the plug-in-coupon data compare reasonably well (-6%) with the Hy-Cal gauge data. Surface heat flux measured on the blade instrumented with a miniature plug-type gauge compares well with both the Hy-Cal and gauge-in-coupon data (fig 7).

Because these comparisons are reasonable, it is concluded that the miniature plug-type gauge concept is feasible for measurement of blade surface heat flux. Reference 7 suggests that it is important to measure heat flux near the hub on the suction surface and at the throat on SSME blades rotating in engines because stress and heat transfer coefficients are high in this region. Nonrotating tests in the calibrator on gauges mounted at this throat location are being planned. Also, tests on gauges with lower thermal conductivity insulation (compared with air) around the thermoplug are planned in the calibrator. Use of insulation with lower thermal conductivity will minimize heat conduction between the plug, the surrounding annulus, and the cover plate. Furthermore, designs for locating heat flux gauges at the leading edge of SSME blades have been started. Finally, plans to test heat flux gauges mounted on nonrotating SSME blades inserted into the Marshall Space Flight Center turbine blade tester are being formulated. The results, in terms of measured gas-side heat transfer coefficients, will be compared with calculations (ref. 7).

REFERENCES

1. Liebert, C.H.: Heat Flux Calibration Facility Capable of SSME Conditions. Structural Integrity and Durability of Reusable Space Propulsion Systems. NASA CP-2471, 1987, pp. 47-49.
2. Liebert, C.H.: Measurement of Local, High Level, Transient Surface Heat Flux. NASA TP-2840, 1988.
3. Liebert, C.H.: Study of Transient Heat Flux Measurement. Advanced Earth-to-Orbit Propulsion Technology, NASA CP-3012, Vol. II, 1988, pp. 396-407.
4. Liebert, C.H.; and Weikle, D.H.: Heat Flux Measurements. NASA TM-101428, 1989.
5. 100,000-W Arc Lamp (Model 107, Vortek Industries, Ltd.) Industrial Research and Development, vol 25, no. 10, Oct. 1983, p. 107.
6. Aerospace Structural Metals Handbook, Metals and Ceramics Information Center, Battelle Labs, Columbus OH, 1988.
7. Civinskas, K.C.; Boyle, R.J.; and McConnaughey, H.V.: Impact of ETO Propellants on the Aerothermodynamic Analyses of Propulsion Components. AIAA Paper 88-3091, July 1988 (also NASA TM 101303).

LAMPHEAD AND POSITIONING ARM



CD-89-39223

ORIGINAL PAGE
BLACK AND WHITE PHOTOGRAPH

Figure 1

ORIGINAL PAGE IS
OF POOR QUALITY

**PLUG-TYPE HEAT FLUX GAUGE
(DIMENSIONS IN CENTIMETERS)**

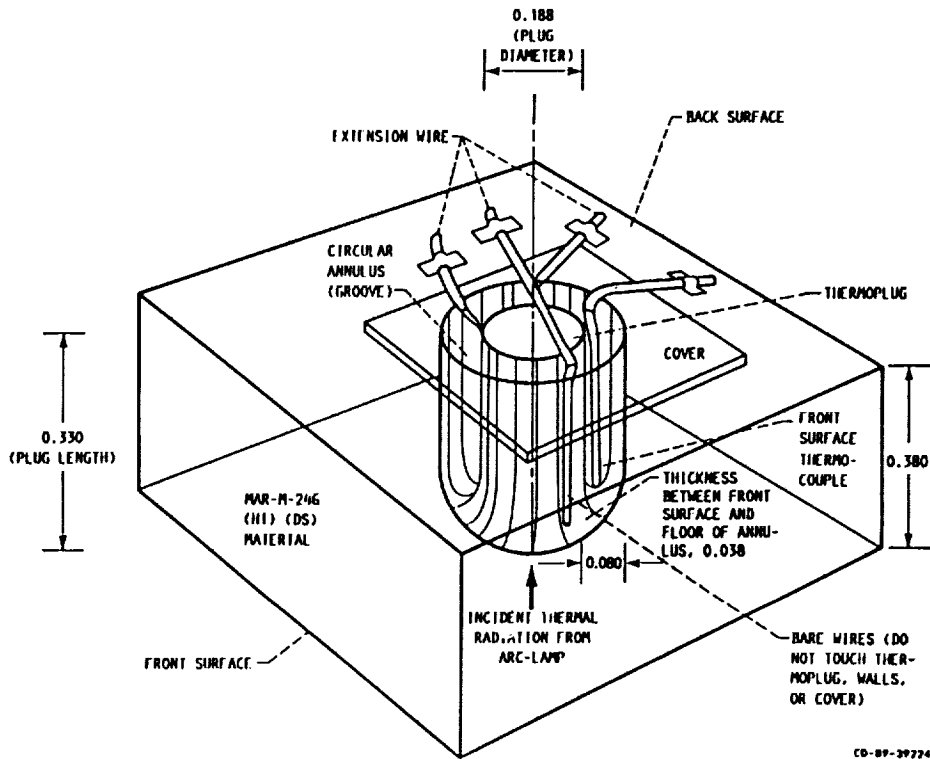
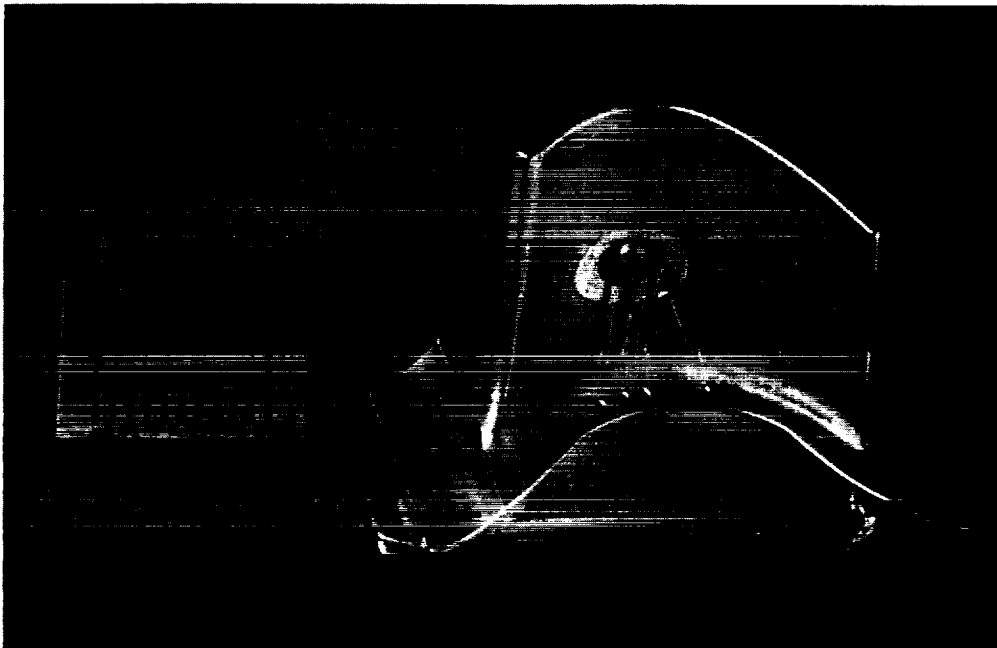


Figure 2

**MINIATURE HEAT FLUX GAUGE BEFORE
THERMOCOUPLE INSTALLATION**



CD-89-39725

Figure 3

SPECIFIC HEAT VERSUS SPECIMEN TEMPERATURE

DENSITY = 8442 kg/m³; ref. 6

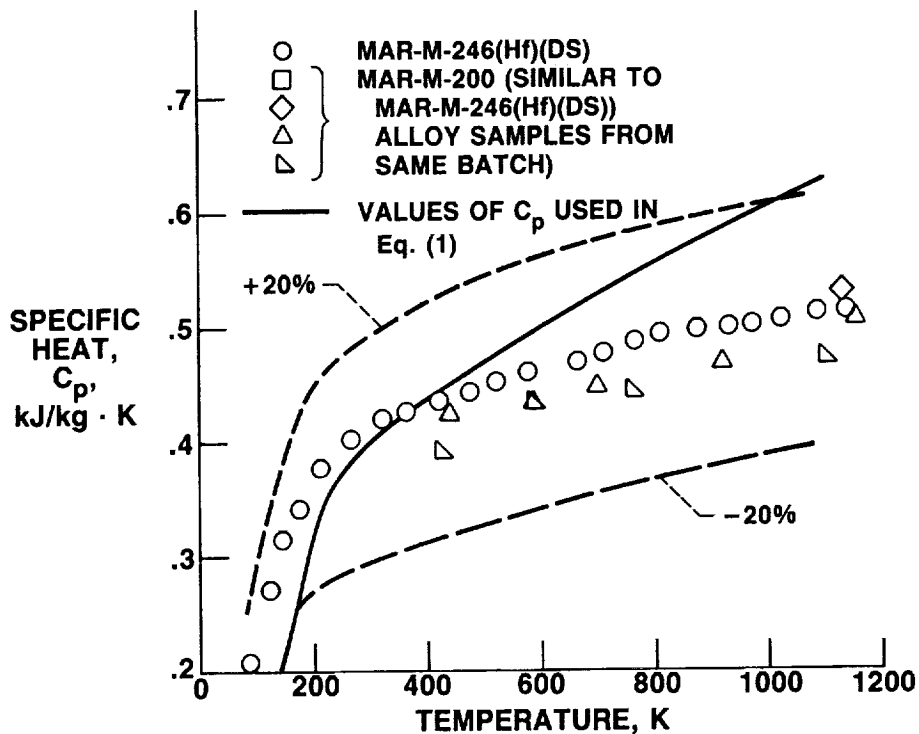


Figure 4

CD-89-39226

INSTRUMENTED SSME BLADE MOUNTED IN CALIBRATOR

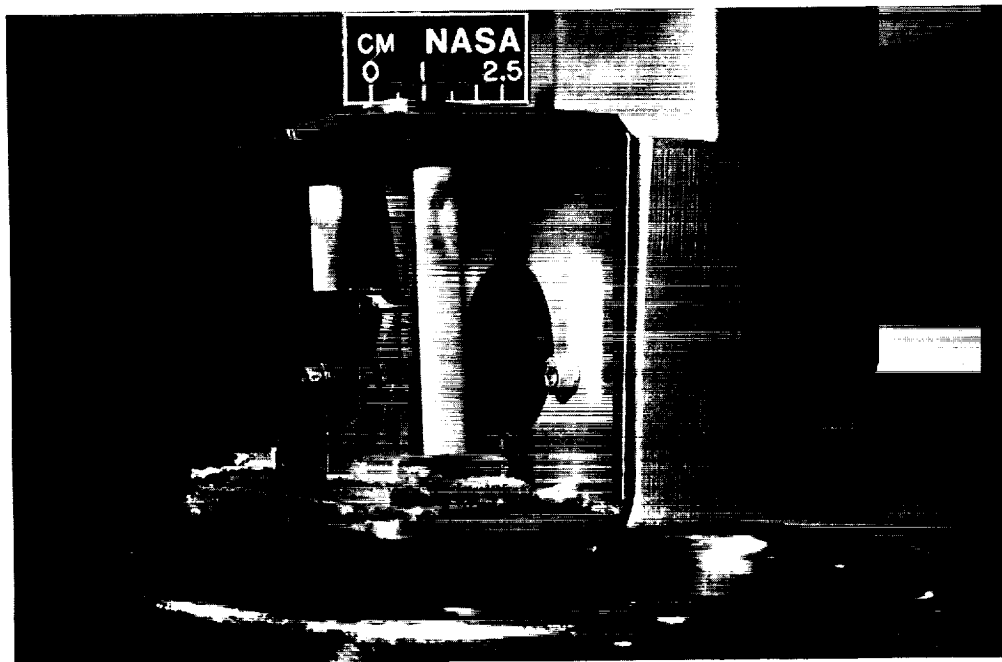
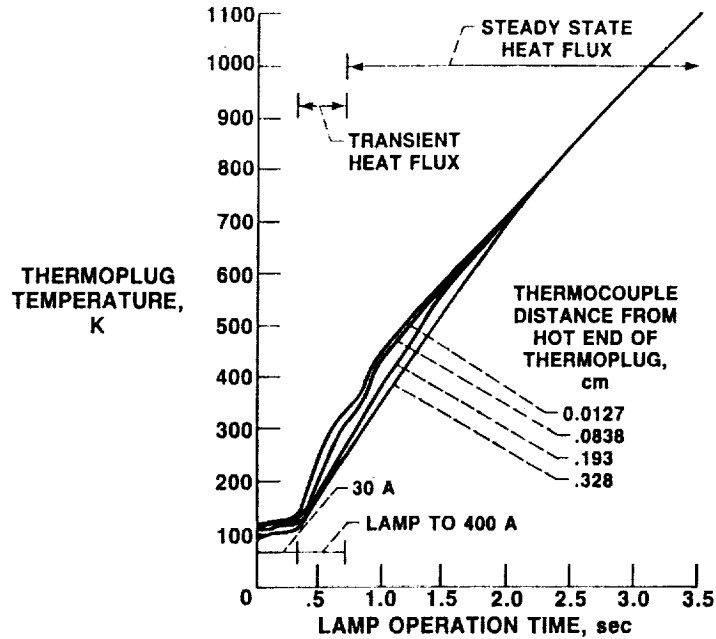


Figure 5

CD-89-39227

ORIGINAL PAGE IS
OF POOR QUALITY

TEMPERATURE HISTORY OF GAUGE MOUNTED IN SSME BLADE

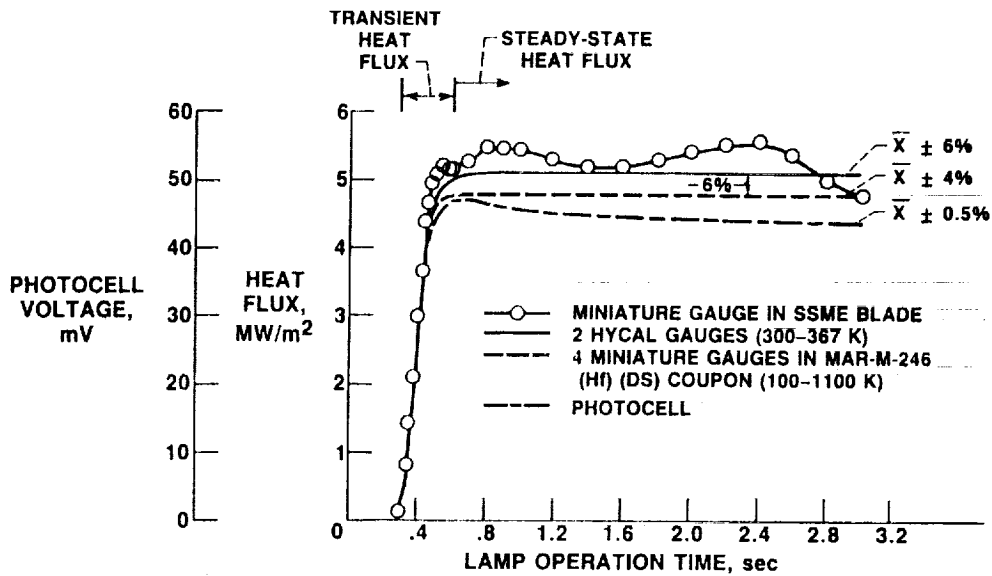


CD-89-39228

Figure 6

HEAT FLUX MEASUREMENTS WITH GAUGE MOUNTED IN SSME BLADE

LAMP CURRENT, 400 A



\bar{X} EVALUATED AT 95 PERCENT CONFIDENCE INTERVAL:

- STEADY-STATE IS 100 DATA POINTS MEASURED AT $t=0.6 - 3.0$ sec
- TRANSIENT IS 10 DATA POINTS MEASURED AT SELECTED TIMES

CD-89-39229

Figure 7

**DEVELOPMENT OF FIBER-BASED LASER ANEMOMETER FOR
SSME APPLICATION**

**Dariush Modarress and Robert Fan
Physical Research, Inc.**

*515-35
19872*

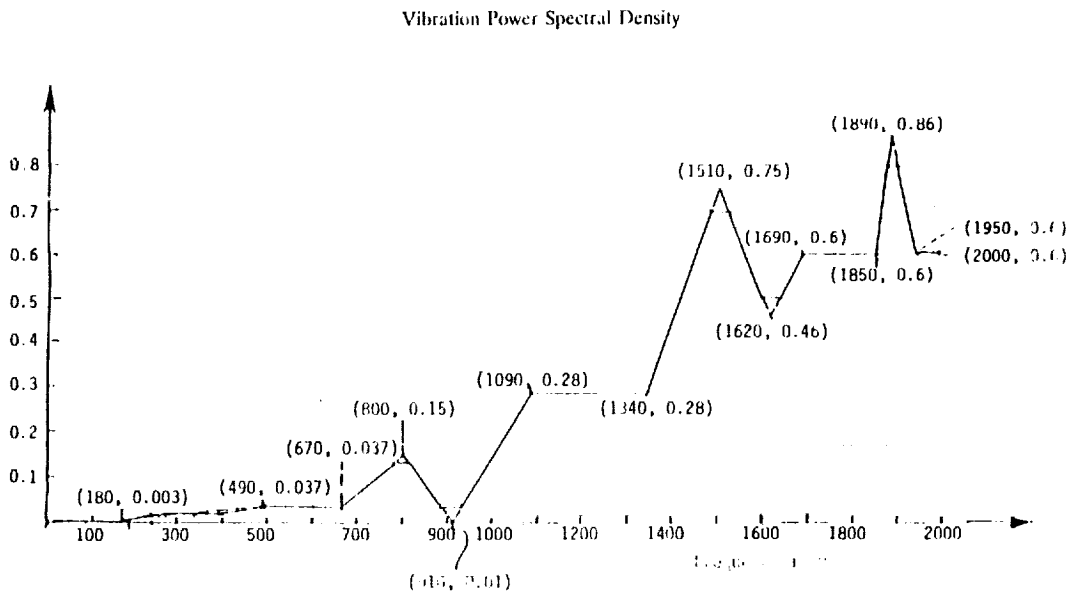
SUMMARY

During the past twenty years, laser Doppler anemometry has become an important non-intrusive diagnostic tool. It has been used for detailed and accurate measurement of fluid flows in wind tunnels, air-breathing engines, rocket motors, shock tubes, etc. A recent study by Rocketdyne for NASA identified laser anemometry, using a compact optical head, as a feasible diagnostic instrument for the SSME Model Verification experiments. PRi is presently under contract from NASA Lewis to develop and deliver such a laser anemometer system. For this application, it is desired to place the laser at a remote distance from the engine, and use single mode polarization preserving fiber optics for the transmission of the laser light to and from the measurement head. Other requirements for the instrument include:

1. Two simultaneous components
2. Flow velocity: -300 to 300 m/s
3. Flow angle: 0 to 360°
4. Severe vibration and temperature environments as specified
5. Measurement resolution: 1 mm (normal to the flow)
6. Optical probe dimensions: 25 mm diameter; 15 cm length
7. Total run time: 500 seconds
8. Accuracy: 5% velocity magnitude, 3 degree in angle

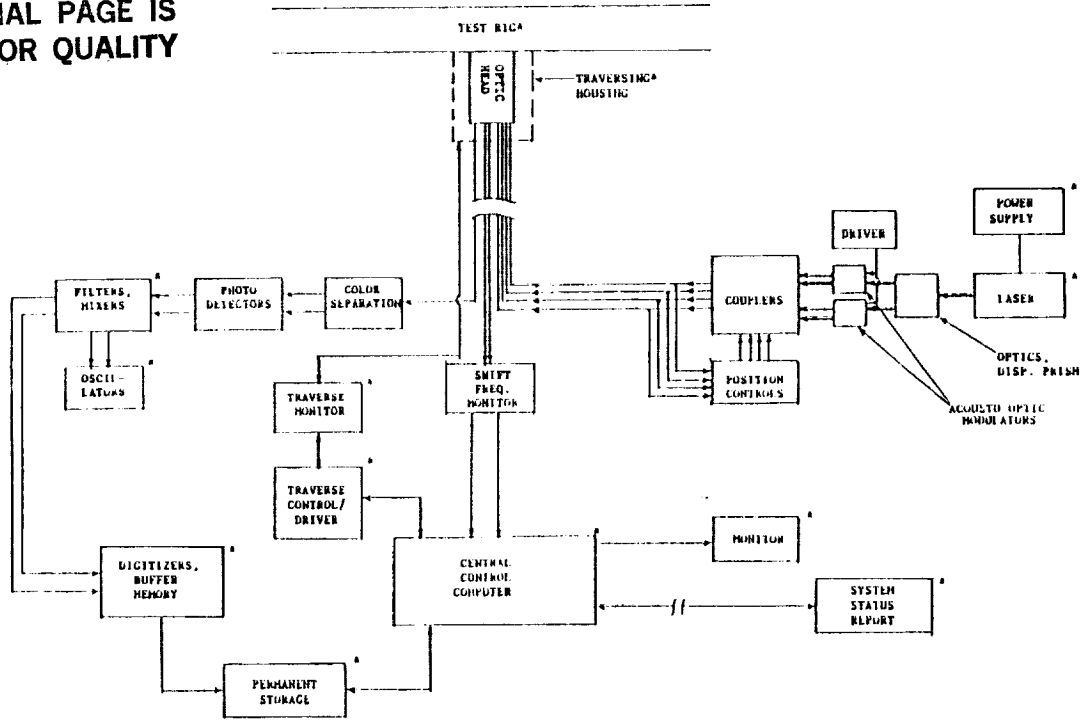
Analytical and experimental tools are being used to develop the technologies required for the laser anemometer. These include finite element analysis of the optical head and vibration tests for various optical and mechanical components. Design of the optical head and the fiber optic connectors are driven by the temperature and vibration requirements for the measurement environment. Results of the finite element analysis and the vibration tests of the components are included. Conceptual design of the fiber optic launcher and the optical probe has also been complete. Detailed design of the probe as well as the fabrication and assembly of the components is in progress.

It is anticipated that the anemometer will be fabricated and its performance evaluated through a series of vibration and environmental tests before the delivery of the optical system to NASA for further evaluation.



ORIGINAL PAGE IS
OF POOR QUALITY

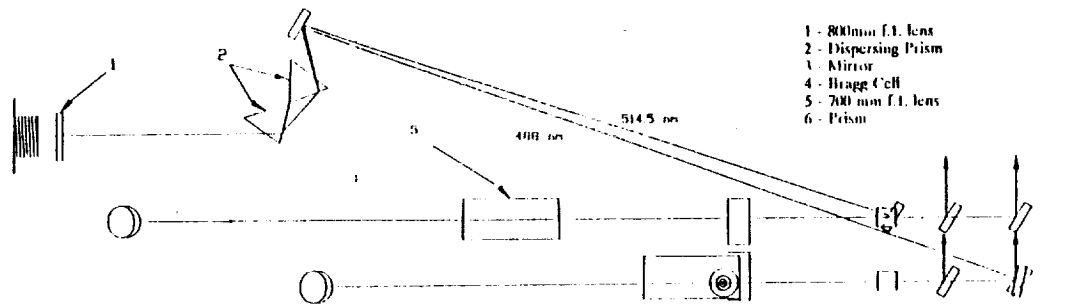
Component System Diagram



*Not included in the deliverables.

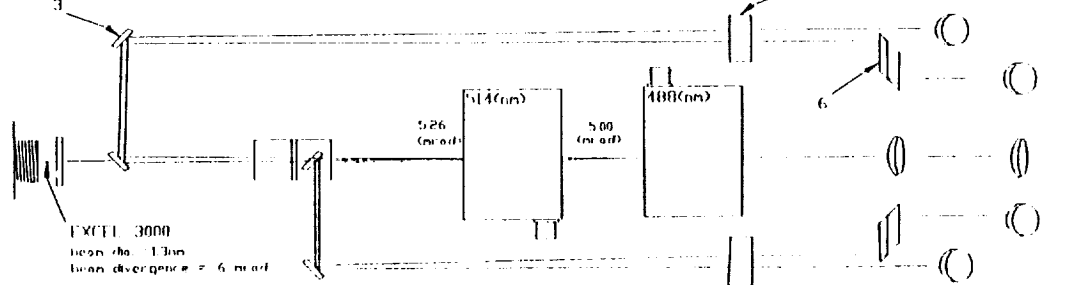
Optical Configuration of the Source System

sideview



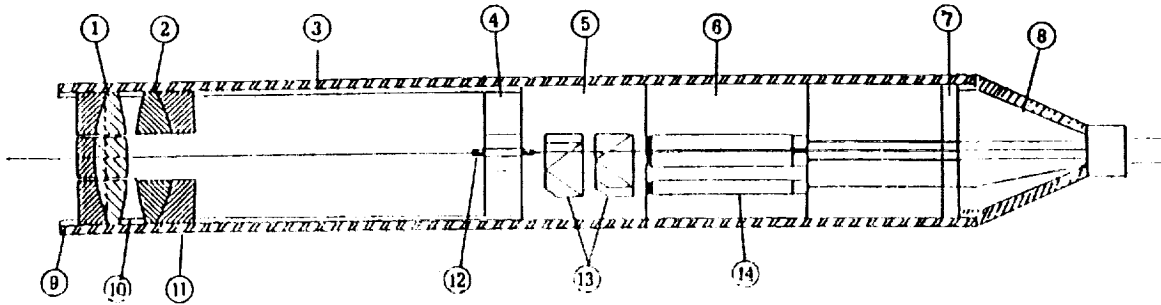
- 1 - 800mm f.l. lens
- 2 - Dispersing Prism
- 3 - Mirror
- 4 - Bragg Cell
- 5 - 700 mm f.l. lens
- 6 - Prism

bottom view



ORIGINAL PAGE IS
OF POOR QUALITY

Optical Head Design

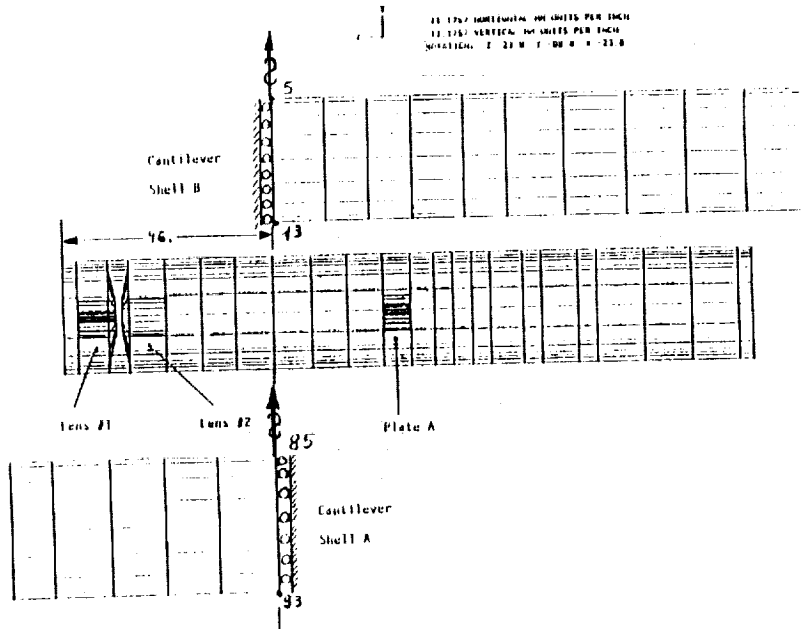


Description

- | | |
|--|--------------------|
| 1. Transmitter Lens | 8. Backshell |
| 2. Focus Lens | 9. Cap |
| 3. Spacer | 10. Spacer |
| 4. Receiver Fiber Stage | 11. Shell |
| 5. Prism Carrier | 12. Receiver Fiber |
| 6. Collimating Lenses Alignment Assembly | 13. Prism |
| 7. Spider Ring | 14. Feedback |

/RPT88-1/DURABILITY. 104-7/

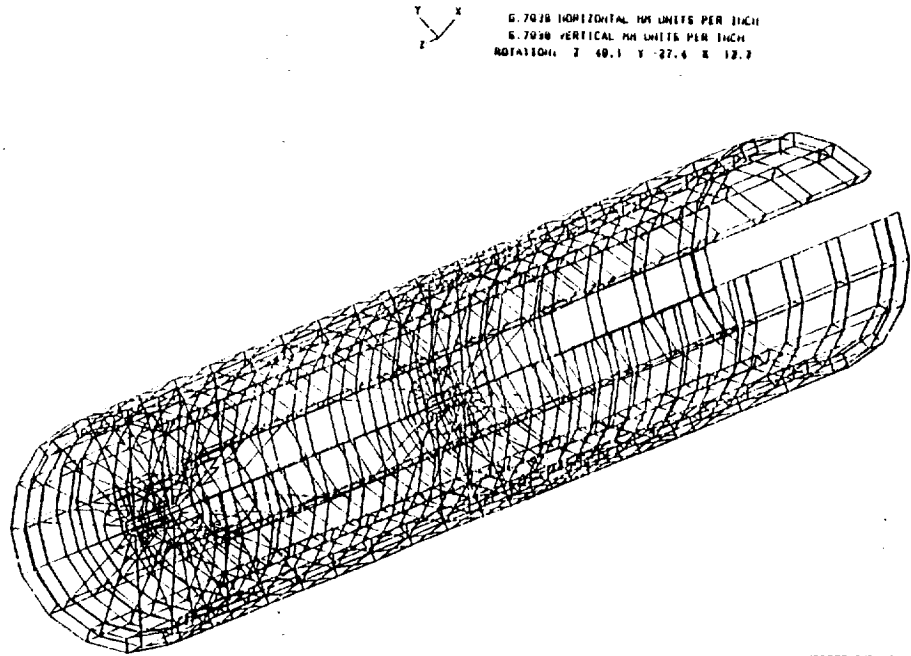
Division of the Probe into Two Cantilevers for Independent Analysis



/RPT89-1/DURABILITY. 104-8/

ORIGINAL PAGE IS
OF POOR QUALITY

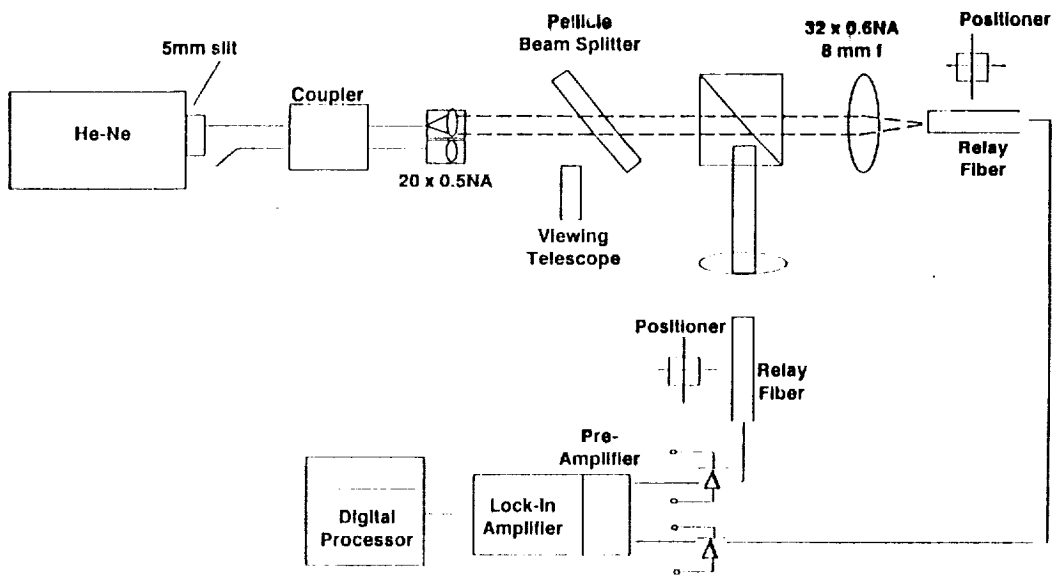
Finite Element Model of the Probe, Including the Lenses and Fiber Holders



G. 7038 HORIZONTAL MM UNITS PER INCH
G. 7038 VERTICAL MM UNITS PER INCH
ROTATION: Z 49.1 Y -27.4 X 12.2

/RPT88-1/DURANI ET AL. 104-97

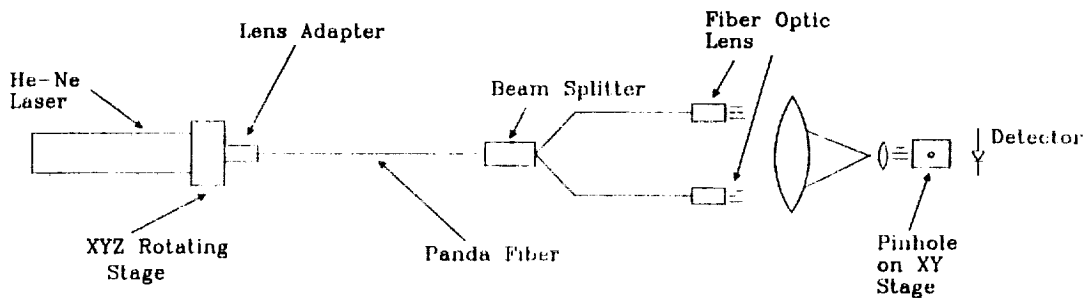
Beam Quality Test Set-Up



/RPT88-1/DURANI ET AL. 104-107

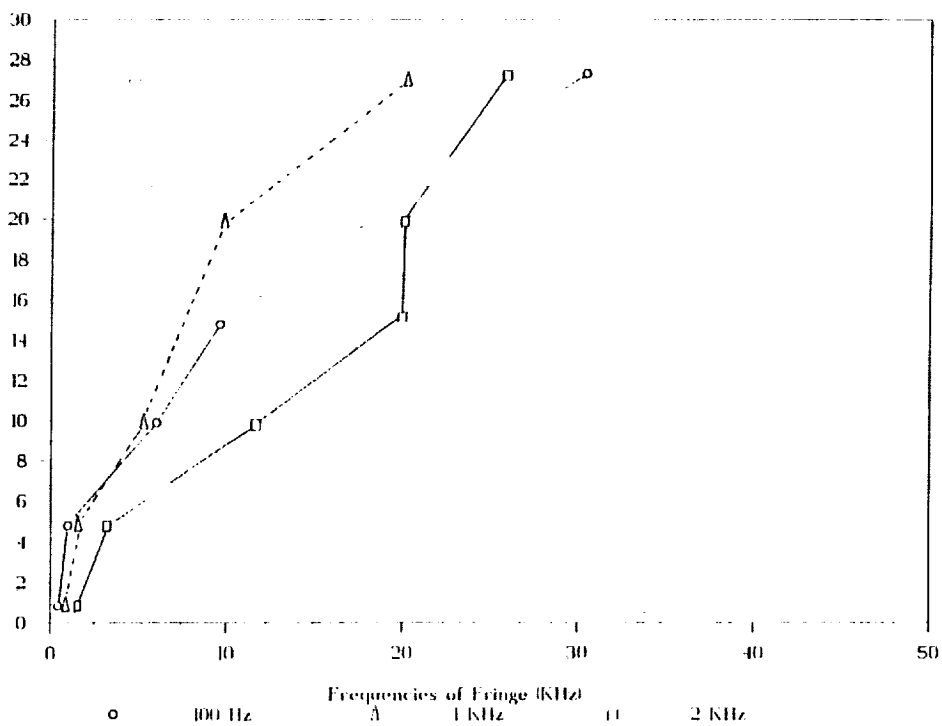
ORIGINAL PAGE IS
OF POOR QUALITY

Fiber Vibration Test Setup

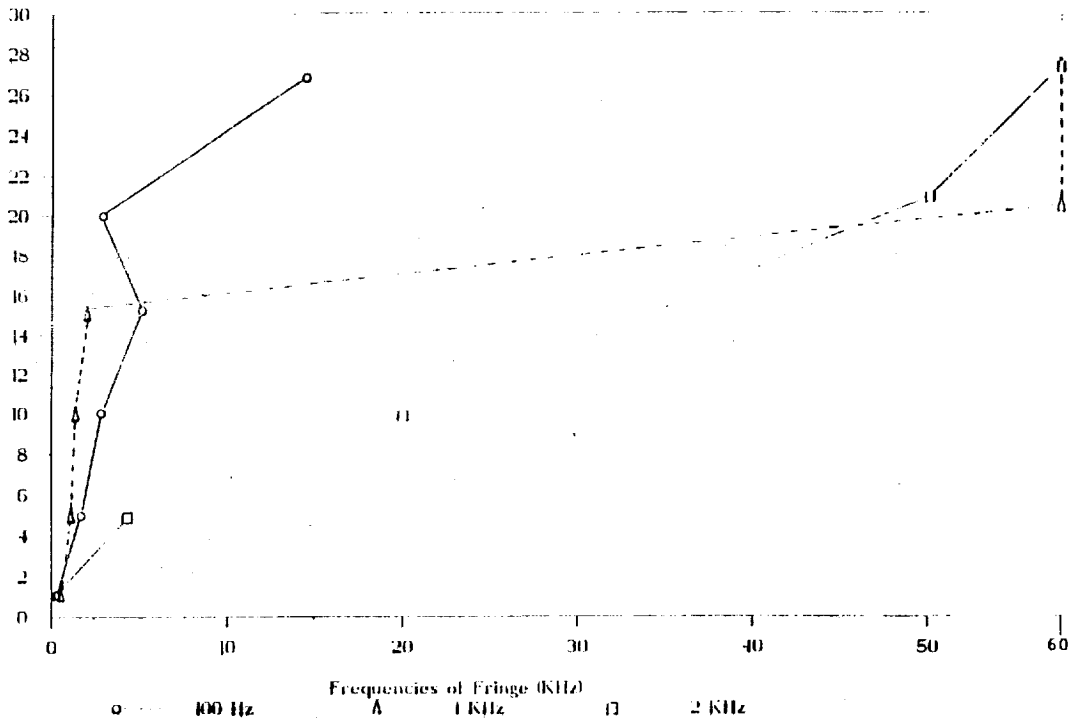


/RPT88-1/DURABILITY.104-11/

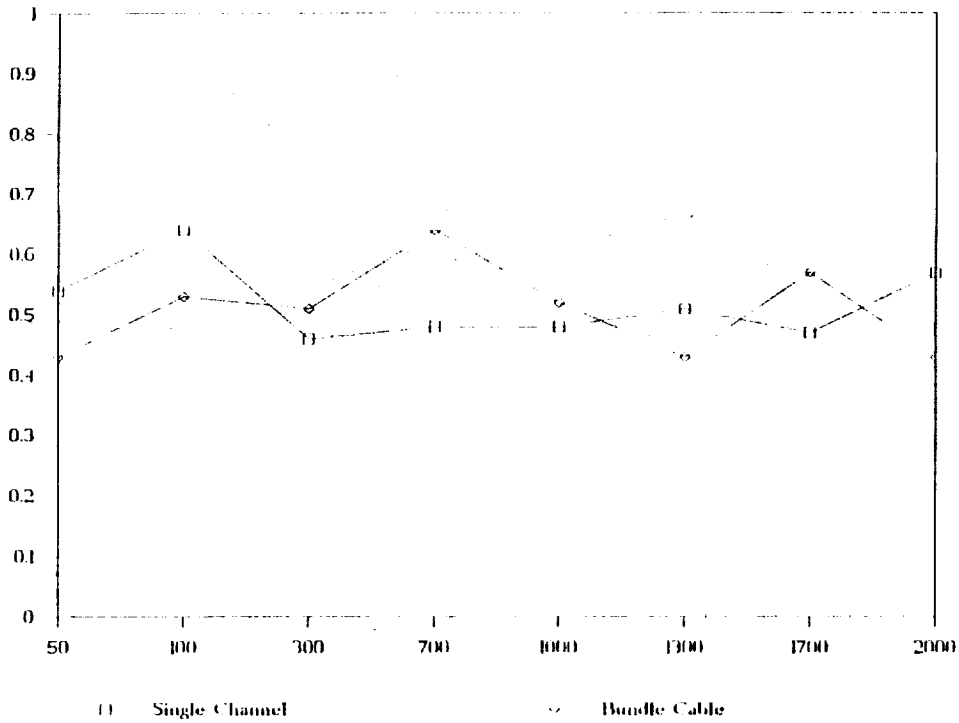
Vibration Test (Single Cable)



Vibration Test (Bundle Cable)

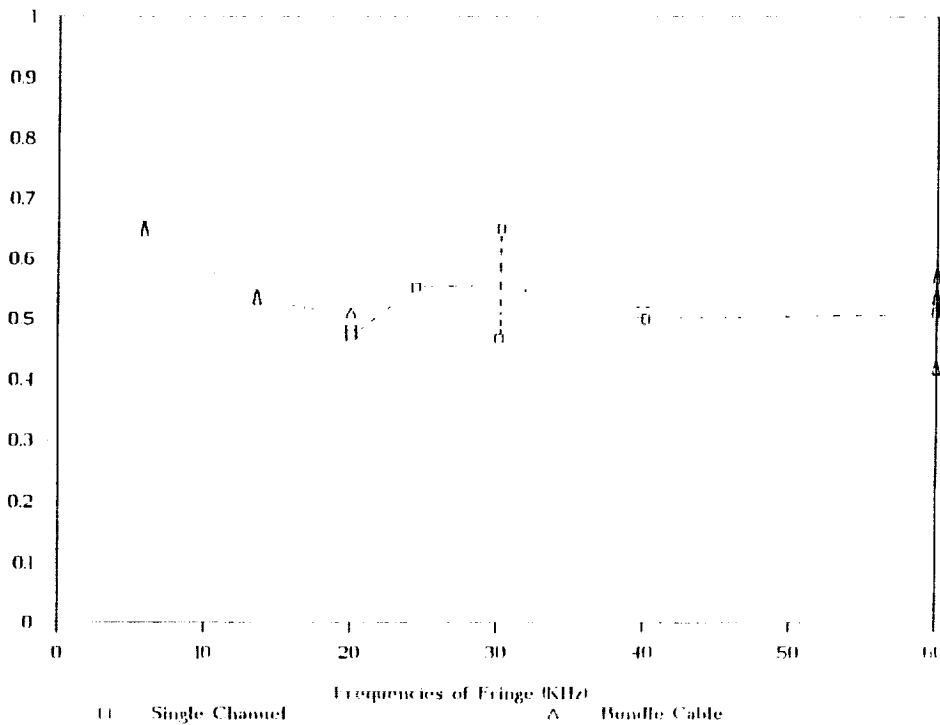


Visibility vs Cable Vibration Frequency

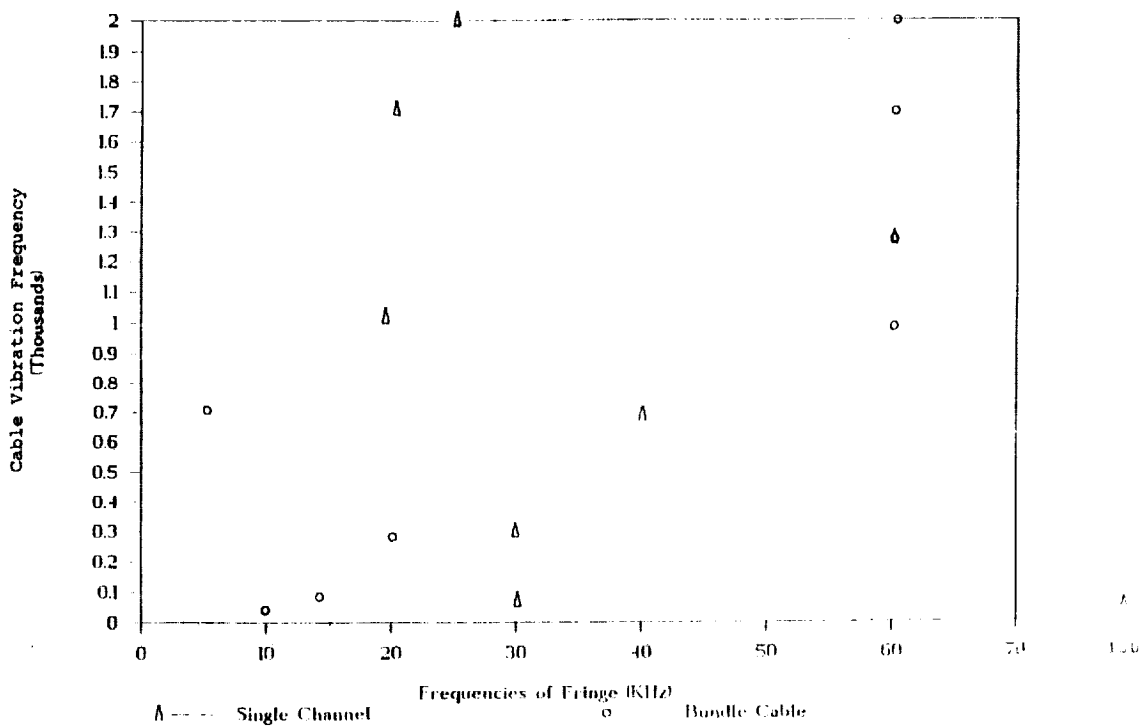


ORIGINAL PAGE IS
OF POOR QUALITY

Visibility vs Frequencies of Fringes



Cable Vibration Frequency vs. the Frequency of the Fringes at 27 G



56-35
19873

Analysis of the Transient Calibration of Heat Flux

Sensors – one Dimensional Case

A. Dybbs and J. X. Ling

Case Center for Complex Flow Measurements, C³FM
Department of Mechanical Engineering
Case Western Reserve University
Cleveland, Ohio 44106

ABSTRACT

The purpose of this analysis is to determine the effect of transient heat flux on heat flux sensor response and calibration.

We have begun this work by studying a one dimensional case. This was done to elucidate the key parameters and trends for the problem. It has the added advantage that the solutions to the governing equations can be obtained by analytical means. The analytical results obtained to date indicate that the transient response of a heat flux sensor depends on the thermal boundary conditions, the geometry and the thermal properties of the sensor. In particular it was shown that if the thermal diffusivity of the sensor is small, say for a material such as Nichrome, then the transient behavior must be taken into account.

INTRODUCTION

The purpose of this analysis was to determine the effect of transient heat flux on sensor response and calibration.

Consider the case of a heat flux sensor mounted in a wall subjected to both radiative and convective heat transfer on the top side and purely convective heat transfer on the bottom side as shown in Fig. 1, where x and r are the axial and radial coordinates, respectively; L and ℓ , D and d are the thicknesses and diameters of the two layers; k is the thermal conductivity, α is the diffusivity, T is temperature, h_1 and h_2 are the convective heat transfer coefficients, q_0 is the radiant incident heat flux, and T_∞ is the ambient temperature. The subscripts 1 and 2 refer to the different materials of the sensor.

In this analysis we make the following simplifying assumptions

- (1) neglect re-radiation;
- (2) constant thermal properties;
- (3) constant, uniform ambient temperatures;
- (4) constant, uniform convection coefficients;
- (5) constant, uniform radiant incident heat flux;
- (6) perfect thermal contact between the regions of different k ;
- (7) the equations are one-dimensional;

Steady - State Solution To determine a base line case we first solve for the steady-state case.

For this case, the governing equations and corresponding boundary conditions are, under the above assumptions.

$$\frac{d^2 T_1}{dx^2} = 0 \quad 0 \leq x \leq \ell \quad (1)$$

$$\frac{d^2 T_2}{dx^2} = 0 \quad \ell \leq x \leq L \quad (2)$$

$$-k_1 \frac{dT_1}{dx} + h_1 (T_1 - T_\infty) - q_0 = 0 \quad \text{at } x = 0 \quad (3)$$

$$\left. \begin{aligned} T_1 &= T_2 \\ k_1 \frac{dT_1}{dx} &= k_2 \frac{dT_2}{dx} \end{aligned} \right\} \text{ at } x = \ell \quad (1)$$

$$k_2 \frac{dT_2}{dx} = h_2 (T_2 - T_{\infty 2}) \quad \text{at } x = L \quad (5)$$

(3) and (5) are rearranged as:

$$-k_1 \frac{\partial T_1}{\partial x} + h_1 T_1 = h_1 f_1 \quad \text{at } x = 0 \quad (3-a)$$

$$k_2 \frac{\partial T_2}{\partial x} + h_2 T_2 = h_2 f_2 \quad \text{at } x = L \quad (5-a)$$

where $f_1 = T_{1\infty} + \frac{q_0}{h_1}$

$$f_2 = T_{2\infty}$$

The solutions to equs. (1) and (2) are

$$T_1 = A_1 x + B_1$$

$$T_2 = A_2 x + B_2$$

The coefficients A_1 , B_1 , A_2 , B_2 can be determined in terms of the boundary conditions (3-a), (4), and (5-a).

The sensor output is based on the temperature difference between two fixed points where the two alumel wires are attached. Assume that the coordinates of these two points are x_1 and x_2 respectively (they are usually at different layers), then

$$T_1(x_1) = A_1 x_1 + B_1$$

$$T_2(x_2) = A_2 x_2 + B_2$$

Hence,

$$\Delta T^S = T_1(x_1) - T_2(x_2) \quad (6)$$

where

$$\begin{aligned} A_1 &= \frac{k_2}{k_1} A_2, \quad B_1 = (k_1 A_1 + h_1 f_1)/h_1 \\ B_2 &= B_1 + \ell (A_1 - A_2) \\ A_2 &= \frac{k_1 h_1 h_2 (f_2 - f_1)}{k_1 k_2 h_1 + k_1 h_1 h_2 L + k_2 h_1 h_2 \ell + k_1 k_2 h_2 - k_1 h_1 h_2 \ell} \end{aligned} \quad (7)$$

Note that ΔT^S is independent of time.

Unsteady - State Solution

For unsteady state case, we have

$$\begin{aligned} \alpha_1 \frac{\partial^2 T_1}{\partial x^2} &= \frac{\partial T_1}{\partial t} & 0 \leq x \leq \ell, \quad t > 0 \\ \alpha_2 \frac{\partial^2 T_2}{\partial x^2} &= \frac{\partial T_2}{\partial t} & 0 \leq x \leq L, \quad t > 0 \end{aligned} \quad (8)$$

with

$$\begin{aligned} -k_1 \frac{\partial T_1}{\partial x} + h_1 T_1 &= h_1 f_1 & \text{at } x = 0, \quad t > 0 \\ T_1 &= T_2 & \text{at } x = \ell, \quad t > 0 \\ k_1 \frac{\partial T_1}{\partial x_1} &= k_2 \frac{\partial T_2}{\partial x_2} & \text{at } x = \ell, \quad t > 0 \\ k_2 \frac{\partial T_2}{\partial x} + h_2 T_2 &= h_2 f_2 & \text{at } x = L, \quad t > 0 \end{aligned} \quad (9)$$

and

$$T_1(x, 0) = T_2(x, 0) = T_0 \quad (10)$$

The solutions to equs. (7) and (8) with nonhomogeneous boundary conditions (9) and (10) can be expressed in the form

$$\begin{aligned} T_i(x, t) &= \theta_i(x, t) + \varphi_i(x) f_1 + \psi_i(x) f_2 \\ i &= 1, 2 \end{aligned} \quad (11)$$

where the functions $\varphi_i(x)$, $\psi_i(x)$, and $\theta_i(x, t)$ are the solutions of the following subproblems:

$$(a) \frac{d^2 \varphi_1}{dx^2} = 0$$

$$\frac{d^2 \varphi_2}{dx^2} = 0$$

$$\text{with } -k_1 \frac{d\varphi_1}{dx} + h_1 \varphi_1 = h_1 f_1$$

$$\text{at } x = 0$$

$$\varphi_1 = \varphi_2$$

$$\text{at } x = \ell$$

$$k_1 \frac{d\varphi_1}{dx} = k_2 \frac{d\varphi_2}{dx}$$

$$\text{at } x = \ell$$

$$k_2 \frac{d\varphi_2}{dx} + h_2 T_2 = 0$$

$$\text{at } x = L$$

Therefore,

$$\varphi_1(x) = C_1 x + D_1$$

$$\varphi_2(x) = C_2 x + D_2$$

$$(b) \frac{d^2 \psi_1}{dx^2} = 0$$

$$\frac{d^2 \psi_2}{dx^2} = 0$$

$$\text{with } -k_1 \frac{d\psi_1}{dx} + h_1 \psi_1 = 0$$

$$\text{at } x = 0$$

$$\psi_1 = \psi_2$$

$$\text{at } x = \ell$$

$$k_1 \frac{d\psi_1}{dx} = k_2 \frac{d\psi_2}{dx}$$

$$\text{at } x = \ell$$

$$k_2 \frac{d\psi_2}{dx} + h_2 x_2 = h_2 f_2$$

$$\text{at } x = L$$

we have

$$\psi_1(x) = E_1 x + F_1$$

$$\psi_2(x) = E_2 x + F_2$$

In this case, the sensor output will be dependent on time. To determine the sensor output we calculate the temperature difference to be

**ORIGINAL PAGE IS
OF POOR QUALITY**

$$\begin{aligned}\Delta T^u(t) &= T_1(x_1, t) - T_2(x_2, t) \\ &= \theta_1(x_1, t) - \theta_2(x_2, t) + [\varphi_1(x_1) - \varphi_2(x_2)]f_1 \\ &\quad + [\psi_1(x_1) - \psi_2(x_2)]f_2\end{aligned}$$

Computational results show that

$$[\varphi_1(x_1) - \varphi_2(x_2)]f_1 + [\psi_1(x_1) - \psi_2(x_2)]f_2 = \Delta T^s$$

Therefore,

$$\Delta T^u(t) = \theta_1(x_1, t) - \theta_2(x_2, t) + \Delta T^s \quad (12)$$

(c) $\theta_1(x, t)$ and $\theta_2(x, t)$ are determined from the following homogeneous problem:

$$\begin{aligned}\alpha_1 \frac{\partial^2 \theta_1}{\partial x^2} &= \frac{\partial \theta_1}{\partial t} \\ \alpha_2 \frac{\partial^2 \theta_2}{\partial x^2} &= \frac{\partial \theta_2}{\partial t}\end{aligned}$$

$$\text{Subject to } -k_1 \frac{\partial \theta_1}{\partial x} + h_1 \theta_1 = 0 \quad \text{at } x = 0$$

$$\theta_1 = \theta_2 \quad \text{at } x = \ell$$

$$k_1 \frac{\partial \theta_1}{\partial x} = k_2 \frac{\partial \theta_2}{\partial x} \quad \text{at } x = \ell$$

$$k_2 \frac{\partial \theta_2}{\partial x} + h_2 \theta_2 = 0 \quad \text{at } x = L$$

$$\text{and } \theta_i(x, 0) = T_0 - \varphi_i(x)f_1 - \psi_i(x)f_2$$

$$\text{let } \theta_i(x, t) = X_i(x) \Gamma(t)$$

$$\Rightarrow \Gamma(t) = e^{-j_n^2 t}$$

where β_n are eigenvalues which will be determined later.

$$X_{1n}(x) = A_{1n} \sin\left(\frac{\beta_n}{\sqrt{\alpha_1}} x\right) + B_{1n} \cos\left(\frac{\beta_n}{\sqrt{\alpha_1}} x\right)$$

$$X_{2n}(x) = A_{2n} \sin\left(\frac{\beta_n}{\sqrt{\alpha_2}} x\right) + B_{2n} \cos\left(\frac{\beta_n}{\sqrt{\alpha_2}} x\right)$$

Without loss of generality, we choose $A_{1n} = 1$, B_{1n} , A_{2n} , and B_{2n} can be determined with the corresponding boundary conditions (and several pages of algebra).

Finally,

$$\Delta T^u(t) = \sum_{n=1}^{\infty} C_n [X_{1n}(x_1) - X_{2n}(x_2)] e^{-\beta_n^2 t} + \Delta T^s \quad (13)$$

where C_n is determined by the initial conditions. The equation for the determination of the eigenvalues β_n is

$$\begin{array}{ccc} \sin \gamma + H_1 \gamma \sin \gamma & -\sin \eta & -\cos \eta \\ K \cos \gamma - KH_1 \gamma \sin \gamma & \cos \eta & -\sin \eta \\ 0 & H_2 \eta \cos\left(\frac{L}{\sqrt{\alpha_2}} \eta\right) + \sin\left(\frac{L}{\sqrt{\alpha_2}} \eta\right) & \cos\left(\frac{L}{\sqrt{\alpha_2}} \eta\right) - H_2 \eta \sin\left(\frac{L}{\sqrt{\alpha_2}} \eta\right) \end{array} = 0$$

where $\gamma = \frac{\beta_n}{\sqrt{\alpha_1}} \ell$, $\eta = \frac{\beta_n}{\sqrt{\alpha_2}} \ell$, $H_1 = \frac{k_1}{h_1 \ell}$

$$K = \frac{k_1}{k_2} \sqrt{\frac{\alpha_1}{\alpha_2}}, \quad H_2 = \frac{k_2}{h_2 \ell}$$

Some additional algebra will lead to the following transcendental equation for the determination of the eigenvalues β_n :

$$\operatorname{tg}\left(\frac{\ell}{\sqrt{\alpha_1}} \beta_1\right) = K \frac{h_2}{h_1} \frac{\ell}{L} \operatorname{tg}\left(\frac{L-\ell}{\sqrt{\alpha_2}} \beta_1\right) \quad (14)$$

Rewrite equation (13) as:

$$\Delta T^u(t) = \sum_{n=1}^{\infty} C_n^* e^{-\beta_n^2 t} + \Delta T^S \quad (15)$$

where

$$C_n^* = C_n [X_{1n}(x_1) - X_{2n}(x)]$$

Numerical example shows that $\beta_1^2 \ll \beta_2^2 \ll \beta_3^2 \ll \dots$, so we can just take the first term to approximate the result. In other words, we have:

$$\Delta T^u = c_1 e^{-\beta_1^2 t} + \Delta T^S$$

$$\text{but } \Delta T^u = 0 \quad \text{at } t = 0$$

$$\text{Therefore, } c_1 = -\Delta T^S$$

$$\text{Then, } \frac{\Delta T^u}{\Delta T^S} = 1 - e^{-\beta_1^2 t} \quad (16)$$

where β_1 can be determined from Equation (11). The following observations can be made by examining Eqs. (14) and (16):

- (1) $\Delta T^u(t) = \Delta T^S$ as $t \rightarrow \infty$;
- (2) The transient process depends on the boundary conditions (h_1, h_2), the geometry (ℓ, L) and the properties ($k_1, k_2, \alpha_1, \alpha_2$) of the sensor.
- (3) The transient term ($e^{-\beta_1^2 t}$) may be very important if β_1 is small.

ORIGINAL PAGE IS
OF POOR QUALITY

Typical Example

To illustrate the impact of these results consider a typical example. Assume that $D = 0.8$ cm, $l = 0.02$ cm, $L = 0.11$ cm, choose $h_2/h_1 = 1.0$. See Fig. 1. The material of the sublayer is alumel whose properties are $k_2 = 237$ w/m·k, $\alpha_2 = 9.7 \times 10^{-5}$ m²/s. If the materials of the foil are pure nickel and nichrome (80% Ni, 20% Cr), respectively. The results are shown in Table I.

Table I

Foil Material	α_1 (m ² /s)	β_1	$e^{-\beta_1^2 t}$ (at $t = 0.05$ second)
Nickel (pure)	2.3×10^{-5}	16.745	8.15×10^{-7}
Nichrome (80% Ni, 20% Cr)	3.4×10^{-6}	6.438	1.26×10^{-1}

As can be seen from Table I, if we choose Ni-Cr alloy as the foil material, the transient term " $e^{-\beta_1^2 t}$ " would be important.

SUMMARY

We have initiated a study of the transient heat flux response of heat flux sensors. This paper presents a one dimensional analysis of the problem. This was done to elucidate the key parameters and trend for the problem. The results of a heat flux sensor depends on the thermal boundary conditions, the geometry and the thermal properties of the sensor. In particular, it was shown that if the thermal diffusivity of the sensor is small, say for a material like Nichrome, then the transient behavior must be taken into account.

**ORIGINAL PAGE IS
OF POOR QUALITY**

REFERENCES

1. Atkinson, W.H. and Strange, R.R.: "Development of Advanced High Temperature Heat Flux Sensors," NASA CR-165618, NASA Lewis Research Center, September, 1982.
2. Atkinson, W.H., Cyr, M.A., and Strange, R.R.: "Turbine Blade and Vane Heat Flux Sensor Development Phase I - Final Report," NASA CR-168297, NASA Lewis Research Center, August, 1984.
3. Holman, J.P.: Heat Transfer, Mc-Graw-Hill Book Company, 1982.
4. Atkinson, W.H., Cyr, M.A., and Strange, R.R.: "Turbine Blade and Vane Heat Flux Sensor Development Phase II - Final Report," NASA CR-174995, NASA Lewis Research Center, October, 1985.
5. Woodruff, L.W., Hearne, L.F., and Keliher, T.J.: "Interpretation of Asymptotic Caorimeter Measurements," AIAA Journal, Vol. 5, No. 4, April, 1967, pp. 795-797.

Schematic of Transient Analysis

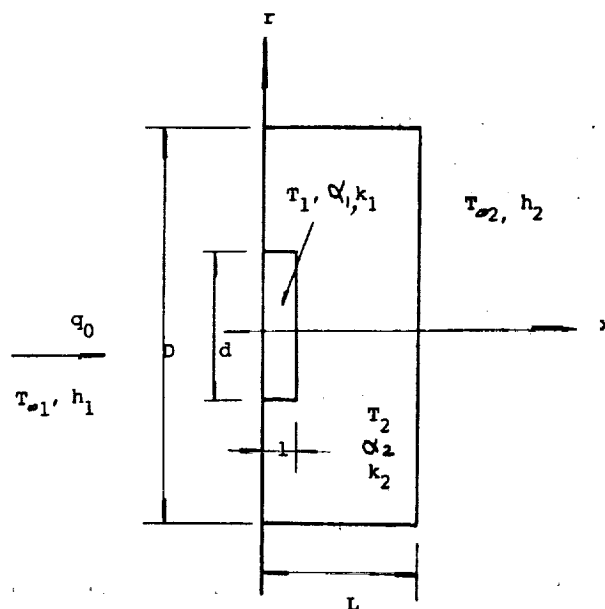


Fig. 1

517-20
19874**THIN-FILM SENSORS FOR SPACE PROPULSION TECHNOLOGY:
FABRICATION AND PREPARATION FOR TESTING****Walter S. Kim and Aloysius F. Hepp
NASA Lewis Research Center**

The goal of this work is to develop and test thin-film thermocouples for space shuttle main engine (SSME) components. Thin-film thermocouples have been developed for aircraft gas turbine engines and are in use for temperature measurement on turbine blades up to 1800 °F (refs. 1 to 3). Established aircraft engine gas turbine technology is currently being adapted to turbine engine blade materials and the environment encountered in the SSME, especially severe thermal shock from cryogenic fuel to combustion temperatures. Initial results using coupons of MAR M-246(+Hf) and PWA 1480 have been followed by fabrication of thin-film thermocouples on SSME turbine blades. Current efforts are focused on preparing for testing in the Turbine Blade Tester at the NASA Marshall Space Flight Center (MSFC). Future work will include testing of thin-film thermocouples on SSME blades of single crystal PWA 1480 at MSFC.

Successful fabrication and testing of thin-film thermocouples on a coupon of SSME high-pressure fuel turbopump (HPFTP) material (DS MAR M-246(+Hf)) was discussed previously (ref. 4). The same procedure, adapted from aircraft technology (ref. 3), was used on an HPFTP blade. The test specimen was coated with 120 μm of NiCoCrAlY (PWA 270 Spec. - Chromalloy Corp.). An adherent, electrically insulating Al_2O_3 film was then grown for 50 hr. This thermally grown film was followed by a sputtered Al_2O_3 film. Finally, the thin-film thermocouple of Pt/Pt(13% Rh) was deposited. A typical fabrication process on a plasma jet sprayed NiCrAlY-coated SSME blade is shown along with that for a jet aircraft gas turbine blade in figure 1. An example of a recently fabricated device is shown in figure 2.

Currently work is underway to prepare for testing of the SSME blade in MSFC's turbine blade tester (shown schematically in fig. 3). We anticipate completing at least one round of testing during the next 5 months. The instrumented blade will be inserted into a blade holder, supplied by MSFC (fig. 4), in the middle position and will be surrounded by two other SSME blades with or without instrumentation, depending on the test requirements. The test will be conducted with the instrumented blades in a wired holder installed in the turbine blade tester at either blade position A or B. Since only the middle blade experiences close to SSME conditions, only one blade per holder assembly will model SSME conditions during a run on the turbine blade tester. A mockup is being prepared with wiring to the installed instrumentation on the blades. Final qualification at MSFC will precede final design and building of a holder to accommodate the wiring and instrumented blades.

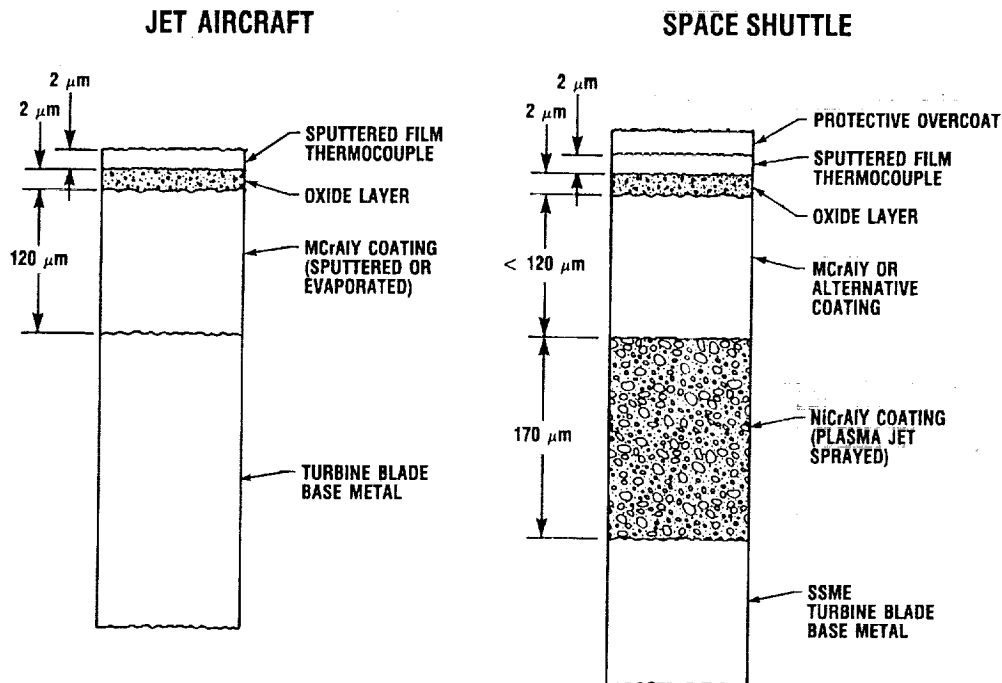
In a related development, we have successfully instrumented coupons of single-crystal PWA 1480. It is anticipated that this material will eventually replace the current MAR M-246(+Hf). Thermal cycling data (fig. 5) show the

thin-film thermocouple on single-crystal PWA 1480 to be of comparable survivability with thin-film thermocouple on coupons of MAR M-246 (ref. 4). Successful application of this technology to this blade material will allow rapid response to testing needs in the future for single-crystal PWA 1480 blades. A further enhancement of our ability to respond to future testing needs is our recent improvement of our in-house capability to fabricate, test, and characterize devices. We have expanded our analytical capability (ref. 4) with an energy dispersive x-ray spectroscopy instrument (which allows elemental identification of materials).

REFERENCES

1. Dils, R.R.; and Follansbee, P.S.: Superalloy Sensor. *Superalloys: Metallurgy and Manufacture*, Kear, B.H.; Muzyka, D.R.; Tien, J.K.; and Wlodek, S.T., eds., (Claitor, Baton Rouge, LA, 1976) pp. 37-44.
2. Kreider, K.G.; Semanicik, S.; and Olson, C.: Advanced Thin Film Thermocouples. (National Bureau of Standards; Interagency Agreement C-54715-D, NBSIR-84-2949), NASA CR-175541, 1984.
3. Grant, H.P.; Przybyszewski, J.S.; Claing, R.G.; and Anderson, W.L.: Thin Film Temperature Sensors, Phase III. (United Technologies Corp., Pratt & Whitney Aircraft Group, NASA Contract NAS3-22002) NASA CR-165476, 1982.
4. Kim, W.S.: Progress on Thin-Film Sensors for Space Propulsion Technology. Structural Integrity and Durability of Reusable Space Propulsion Systems. NASA CP-2471, 1987, pp. 39-42.

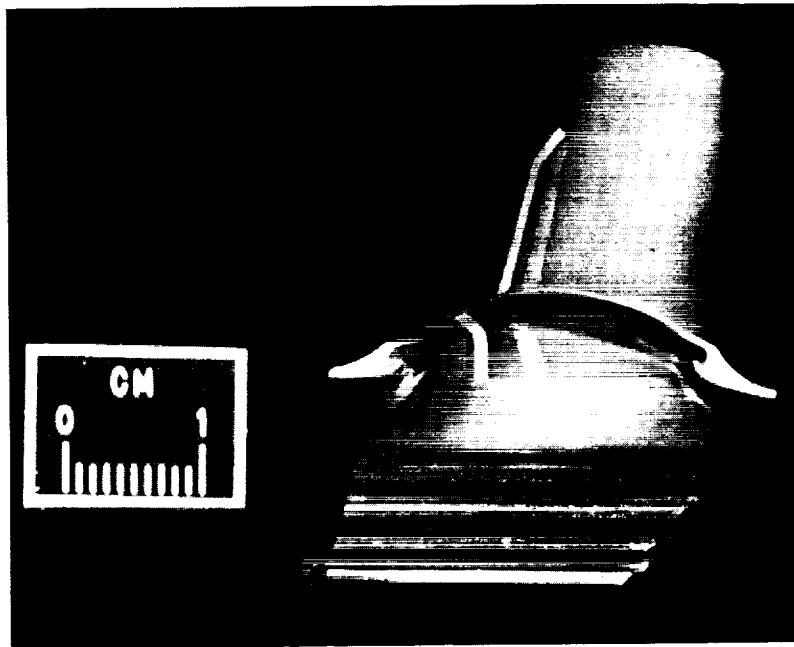
BASIC THIN-FILM THERMOCOUPLE TECHNOLOGY



CD-89-39939

Figure 1

THIN-FILM THERMOCOUPLE ON SSME BLADE



CD-89-39940

Figure 2

SCHEMATIC OF MSFC TURBINE BLADE TESTER

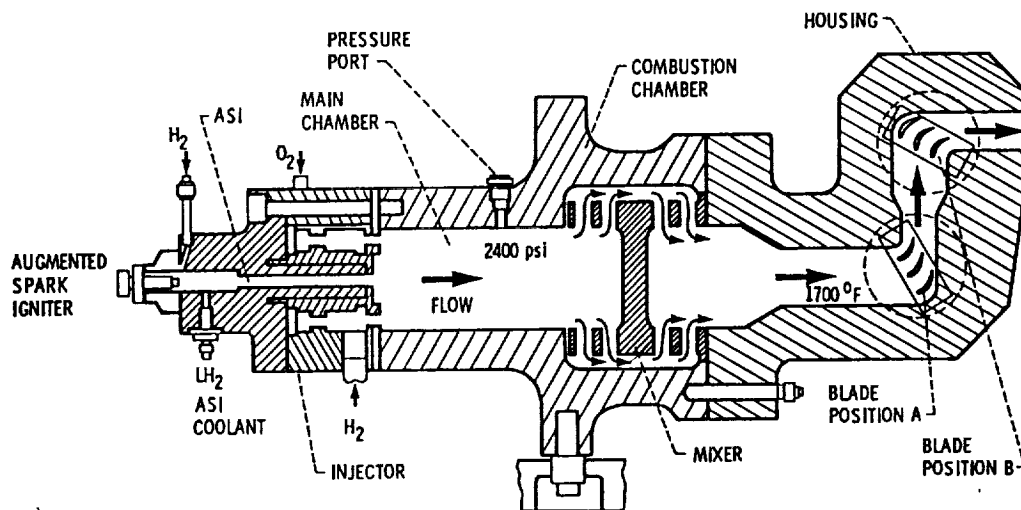
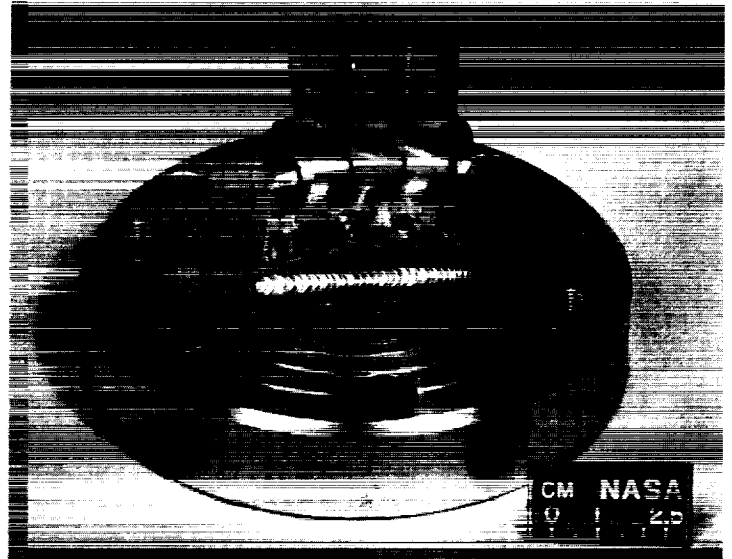
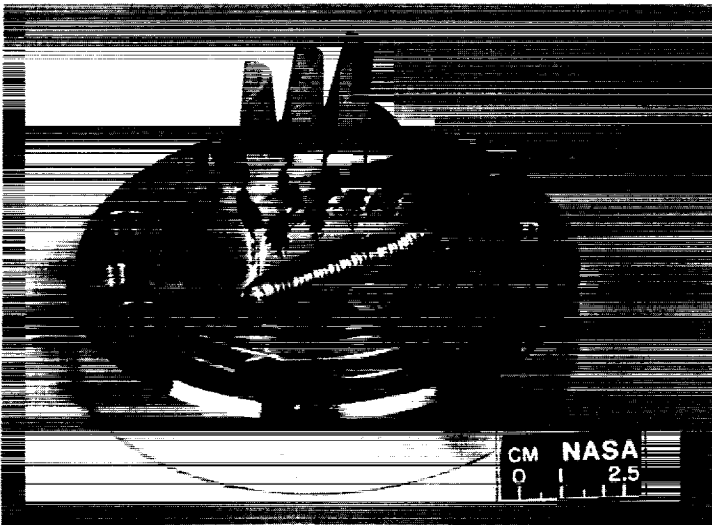


Figure 3

CD-89-39941

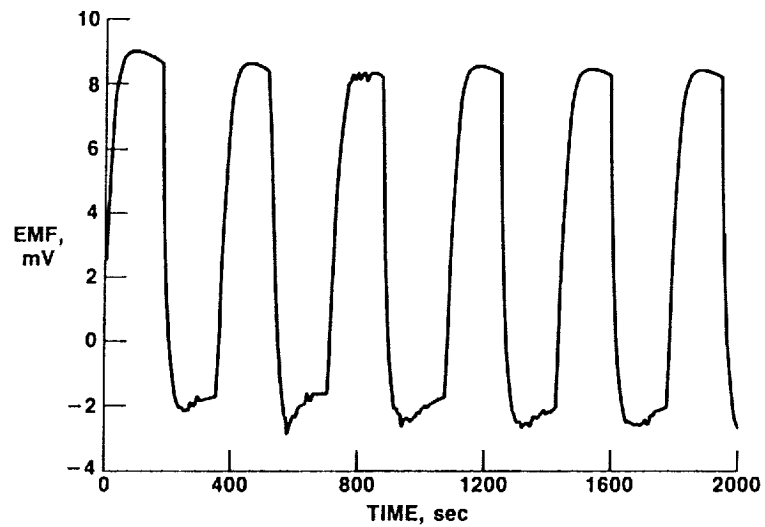
HOLDER FOR TURBINE BLADE TESTER CONTAINING THREE SSME BLADES



CD-89-39942

Figure 4

SIGNAL OUTPUT OF THIN-FILM THERMOCOUPLE DURING THERMAL SHOCK CYCLING BETWEEN LIQUID NITROGEN TEMPERATURE AND 2000 °F THIN FILM THERMOCOUPLE ON SC PWA 1480



CD-89-39943

Figure 5

N91-24325

ROCKET PLUME SPECTROMETRY--A SYSTEM PERMITTING ENGINE
CONDITION MONITORING, AS APPLIED TO THE
TECHNOLOGY TEST BED ENGINE

518-20
19875

BY

W. T. POWERS, MARSHALL SPACE FLIGHT CENTER, AL

ABSTRACT

Visible artifacts have been seen by observers of Space Shuttle Main Engine (SSME) test firings, either directly or on film, prior to several failures, some of which were catastrophic. A program was undertaken to attempt to identify, in the plume of an SSME, anomalous atomic--or molecular--species resulting from wear, normal or excessive, of internal parts, allowing real time monitoring of engine condition or detection of failure precursors. To this end, measurements were taken during test firings on stand A1 at Stennis Space Center and on SSME, and other engines, at the Santa Susanna Facility in California. The results indicated that a system having high spectral resolution, a fast time response, and a wide spectral range was required to meet all requirements, thus two special systems have been designed and built. One is the Optical Plume Anomaly Detector (OPAD) polychromator--a 16 channel spectroradiometer having adjustable optical bandwidth and center wavelength and a time response of 1mS. This instrument has been described elsewhere. The other instrument is the superspectrometer, an optical multichannel analyzer having 8,192 channels covering the spectral band 250 to 1,000 nm. This instrument is described in this paper.

INTRODUCTION

During the process of testing Space Shuttle Main Engines (SSME), movie film surveillance is routinely employed. These films typically form the major source of information available after unusual occurrences. Film is used because rates such as 400 frames-per-second are not uncommon and high frame rates are needed to capture many of the anomalies observed. It is not unusual for "streaking" to occur for one frame only. "Streaking" is a visible (on film) phenomenon thought to result from extraneous material being injected, by some method, into the propellant streams within the engine.

The most commonly observed "streaking" appears to be at the periphery of the plume. It is assumed that anomalies occurring upstream of the Main Combustion Chamber (MCC) will be diffused throughout the plume and, therefore, also in the "mach disc." Anomalies occurring downstream of the injector face plate may appear only at the plume edge.^{1,2}

BACKGROUND

It has been theorized that if such events can be seen on film, and indeed occasionally with the naked eye, then it should be possible to use electronic-optical detection to devise a system allowing automatic engine health monitoring. Such a system might permit the prevention of a catastrophic event. Much effort has been expended in background work in the attempt to build a data base on which such a detection system could be based. Multispectral photometric measurements (Fig 1) were acquired over about a 2-year period at test stands at Stennis Space Center (SSC) in Southern Mississippi^{3,4} and at the SSME development stand (A3)⁵ at the Santa Susanna Test Facility (SSTF) in California. Some data was also obtained from tests of other than SSME.⁹ Using relatively low spectral resolution equipment, several elemental signatures were found in the spectra acquired from tests. The base data acquired showed a very strong continuum from OH emission. That background is sufficient to cover most of the elemental spectra since those lines are very narrow and normally of low amplitude. The nature of the background places demands upon the equipment such that commercially available instruments can be used only to detect the most significant incidences. It would be preferable to be able to follow over a period of time several of the individual elemental or molecular spectral lines so that detectable variations from the norm may be properly interpreted.

RESULTS AND OBSERVATIONS

Calcium (Ca) was identified some time before a bearing cage failure occurred on an SSME; Ca was also seen during the sudden failure of a small H₂/O₂ engine having a compound combustion cycle. The increased level of Ca was detected as an erratic and significant increase in the normally observed level (believed to come from the H₂). During another SSME test at SSTF an injector face plate carrying intentionally plugged LOX tubes suffered some damage and that damage

resulted in a "seeded" plume. Spectra indicated the presence of iron (Fe), nickel (Ni), chromium (Cr), and some copper (Cu). Other species were also noted in trace quantities. In truth, this event was a massive failure--the sort which would be extremely serious were the engine a flight unit.

Another unplanned incident occurred at SSTF. Certain shipping procedures for SSMEs at SSC require that minor cracks in the MCC be sealed with a copper foil tape to allow maintenance of an inert dry purge. The tape was not removed at SSTF and when the engine was fired, the copper tape rather handily "seeded" the plume. This event was also detected easily.

INSTRUMENT DESIGN

The basic instrument for the Optical Plume Anomaly Detector (OPAD) program is called a Polychromator (PCM)¹⁰; for further base data a Superspectrometer (SSM) was designed. The PCM provides 16 individually adjustable spectrophotometer channels; the wavelengths are adjustable, the slit-widths are selectable, the amplifiers provide high-speed autoranging, the computers permit setting alarm limits or multichannel complex algorithms for decision-making, and a second computer allows archival storage on removable magnetic disc. This system employs a quartz fiber-optic input system, allowing mounting of the optics and electronics inside the hard-core of the test stand, where the environment is friendly to non-ruggedized equipment. It is this instrument which is the prototype of the safety monitoring system. All the spectral lines accruing from previous failures are monitored as well as OH at 308 nm and two broad banded background channels to observe such things as spurious light and variable occlusions (such as vapor (H₂O)). The spectral band covered ranges from 250 nm to 1,000²nm. This is a continuous device with a digital data system; the sample time is about 1.5 ms.

The system speed is chosen with the fact in mind that the films indicate some events occur within 2.5 ms (400 frame-per-sec film). It is not assumed that these events are individually significant, but rather may be indicative of normal wear. Confounding the ability to see these "streaks" is the fact that they cover a relatively small percentage of the total emitting area of the plume. Edge phenomena are therefore difficult to capture; mach disc inclusions might well be much easier to find, since the higher temperatures of

the disc cause elemental emission strength to increase. Experience with the system will tell more about the area of the plume which should be observed.

The other instrument (the SSM) is intended to provide overall surveillance of the plume perchance some species for which the PCM has not been set appears. It had to have a wide spectral range, high data capability, and high spectral resolution. Since no commercial instrument provides all these features, a special one was designed. It is based upon a 1/2 meter grating spectrometer, uses an input system similar to that of the PCM--telescope and fiber optic cable--, and has at the exit slit folding mirrors directing the dispersed spectrum onto four 2,048 element self-scanning linear silicon diode arrays, for a total of 8,192 elements. The outputs are digitized and processed by computer for display and storage (Fig 3); storage for archiving is by optical disc.

The input system is composed of two telescopes (Fig 2), two quartz multifilament optical fiber cables. The numerical aperture of the fibers, projected onto the plume, does not quite cover the whole plume. The mounting point on the Test Bed Stand is about 63 feet from the "mach disc," and at that distance the viewed field is about 6-1/2 feet across. Two input sets are used because one cable will illuminate only half the entry slit of the spectrograph. Using a direct viewing optic system would eliminate these difficulties of the fiber optics but would also require that the spectrograph and detector set be mounted on the engine deck in some way. All in all, the cable route was considered the most practical. The cables used are round at the telescope end and rectangular at the spectrograph entry slit in order to maximize light transfer at both ends; that scheme also isolates the field of view from the slit shape.

The range of coverage is similar to that of the PCM--250 nM to 1,000 nM, yielding an ultimate resolution of less than 1A (0.1 nM). The sampling technique used, combined with the factory provided service boards (for the arrays), allows at least 10 samples per second. The system normally will display each sample as a line spectrum; several modes would allow detailed examination of selected narrow ranges.

The computer for this system is an "AT" style machine whose prime purpose is to store the data and display it. The archival data is placed on WORM (write once, read many) optical disc; because of the data rates the WORM drive

cannot accept the continuous stream of data, but the internal high capacity hard disc can. Therefore, the processed data is loaded into the hard disc, then on completion of the acquisition run, the hard disc is dumped to the WORM drive. Intensive data processing is done after-the-fact; too much is required of the computer to achieve real-time processing of this data.

SUMMARY

These two instruments should be sufficiently flexible and capable of acquiring spectral data to allow an in-depth study of the plume for most any reason. These systems will be used in an ongoing program wherein the proper algorithms will be determined through experience. At first "simple" redline cuts are envisioned as the operational mode for the PCM, but more complex computations may be necessary. Each channel is presently corrected for background conditions, but multichannel dependence could drive a change to the basic philosophy.

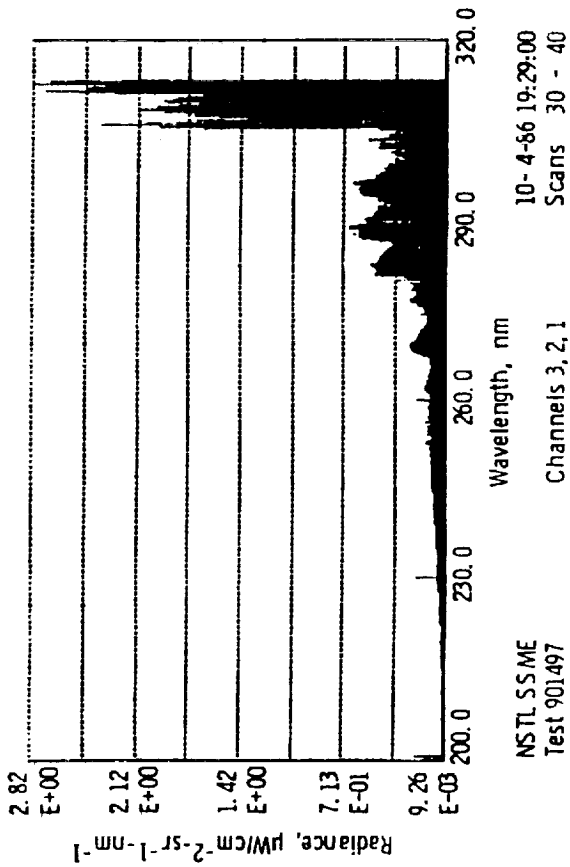
Also, the PCM could be considered a conceptual (from a systems, or scientific, standpoint) prototype for a flight unit. This system, as such, cannot fly--it is much too heavy, bulky, and fragile to put on a shuttle--but the concept is valid, whatever the configuration of a final system. Also, the problem of viewing the proper place in the plume affects the design; the varying nature of the plume with respect to altitude forces considerable compromises on the system. For example, it may be desirable to view the MCC (Main Combustion Chamber) directly by some method. The Technology Test Bed operation should indicate what will be required and how to affect it.

ACKNOWLEDGEMENTS

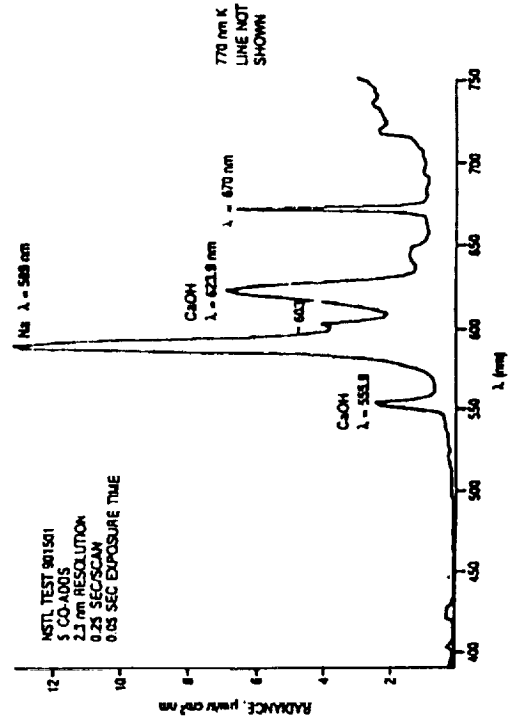
The author wishes to acknowledge the work of Fred Sherrell in the design of the optical system and overall concept of these instruments, Hal Bridges for the electronics, Tim Bratcher for software, and Vince Zaccardi for project overview. Wheeler McGregor is Project Scientist. All the foregoing are on staff at the Arnold Engineering Development Center of the USAF.

REFERENCES

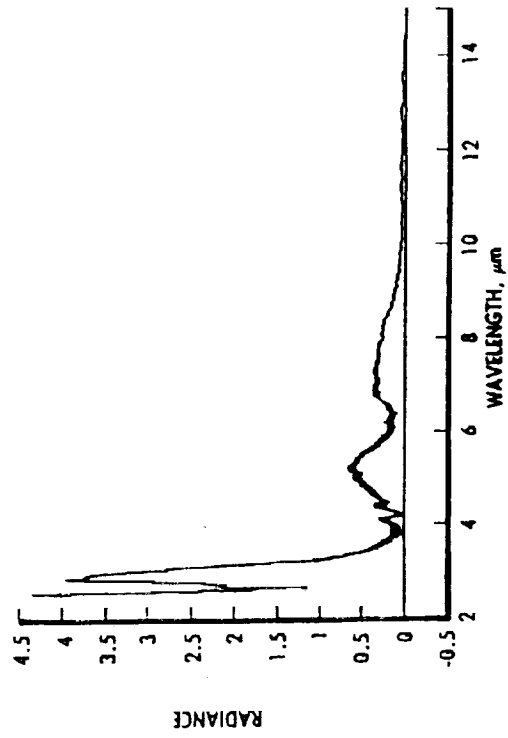
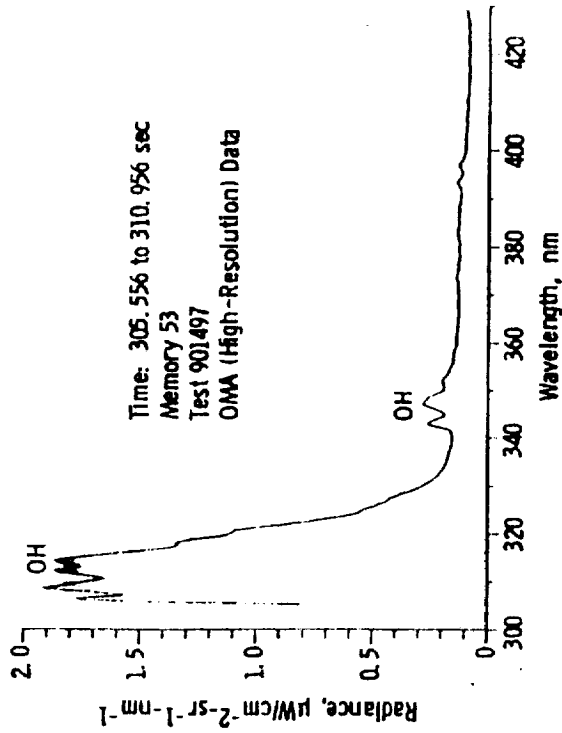
1. Cikanek, H. A. III, "Failure Characteristics of Space Shuttle Main Engine Failures," in Proceedings of the Joint Propulsion Conference, June 1987.
2. Cikanek, H. A. III, Powers, W. T., et al., "Space Shuttle Main Engine Plume Spectral Monitoring - Preliminary Results," in Proceedings of Joint Propulsion Conference, June 1987.
3. McCoy, R. G., Phillips, W. J., McGregor, W. K., Powers, W. T., and Cikanek, H. A., "Analysis of UV-VIS Spectral Radiation From SSME Plume," JANNAF Propulsion Meet, San Diego, December 1987.
4. Limbaugh, C. D., Brown, D. G., Hiers, R. S. III, Gross, K., and Eskridge, R., "Analysis of SSME Plume Images Obtained During Ground Testing," JANNAF Propulsion Meet, San Diego, December 1987.
5. Wyett, L., Maram, J., Barkhoudarian, S., and Reinert, J. J., "Reusable Rocket Engine Optical Condition Monitoring," JANNAF Propulsion Meet, San Diego, December 1987.
6. Sherrell, F. G. and Neese, D. W., "Techniques for Rapid Scanning Spectroradiometry using a Grating Monochromator," AEDC Publication TMR-84-E41, May 1985.
7. Sherrell, F. G., "Autoranging Radiometric System," 33rd International Instrumentation Symposium, Las Vegas, NV, May 1987.
8. Sherrell, F. G. and Neese, D. W., "Circular Variable Filter (CVF) Radiometer Design with Digital Data Processing," AEDC Publication TR-85-11, April 1985.
9. Sherrell, F. G., "Ultraviolet Image Display System for Plume Radiometry," AEDC Publication TR-85-8, March 1985.
10. Powers, W. T., Sherrell, F. G., Bridges, J. H. III, and Bratcher, T. W., "Plume Spectrometry for Liquid Rocket Engine Health Monitoring," AGARD, Propulsion and Energetics Panel, 71st Symposium, May 30-June 3, 1988.



a. Far UV



Detail in the 500-700 nm band.



CVF IR spectrometer response.

Figure 1

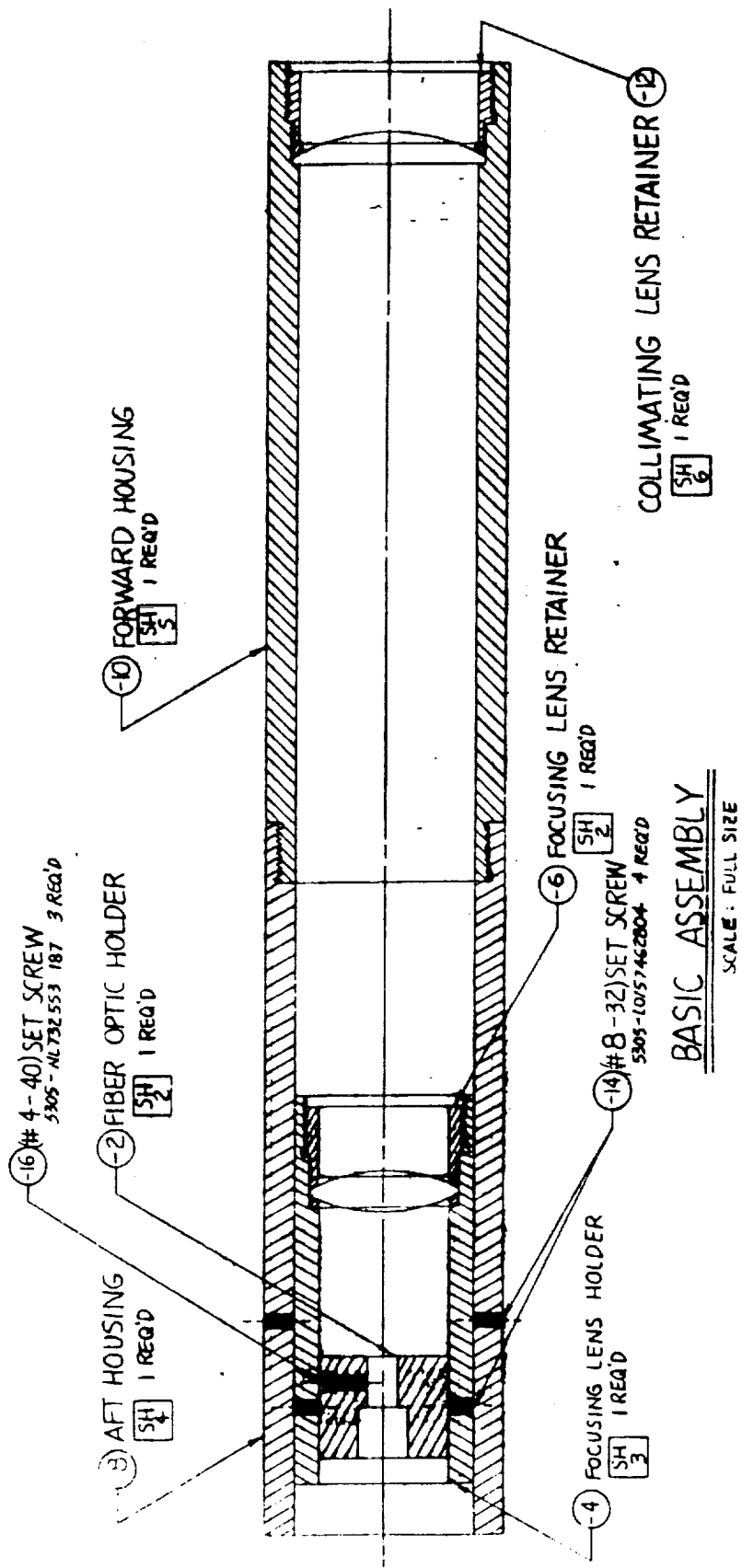
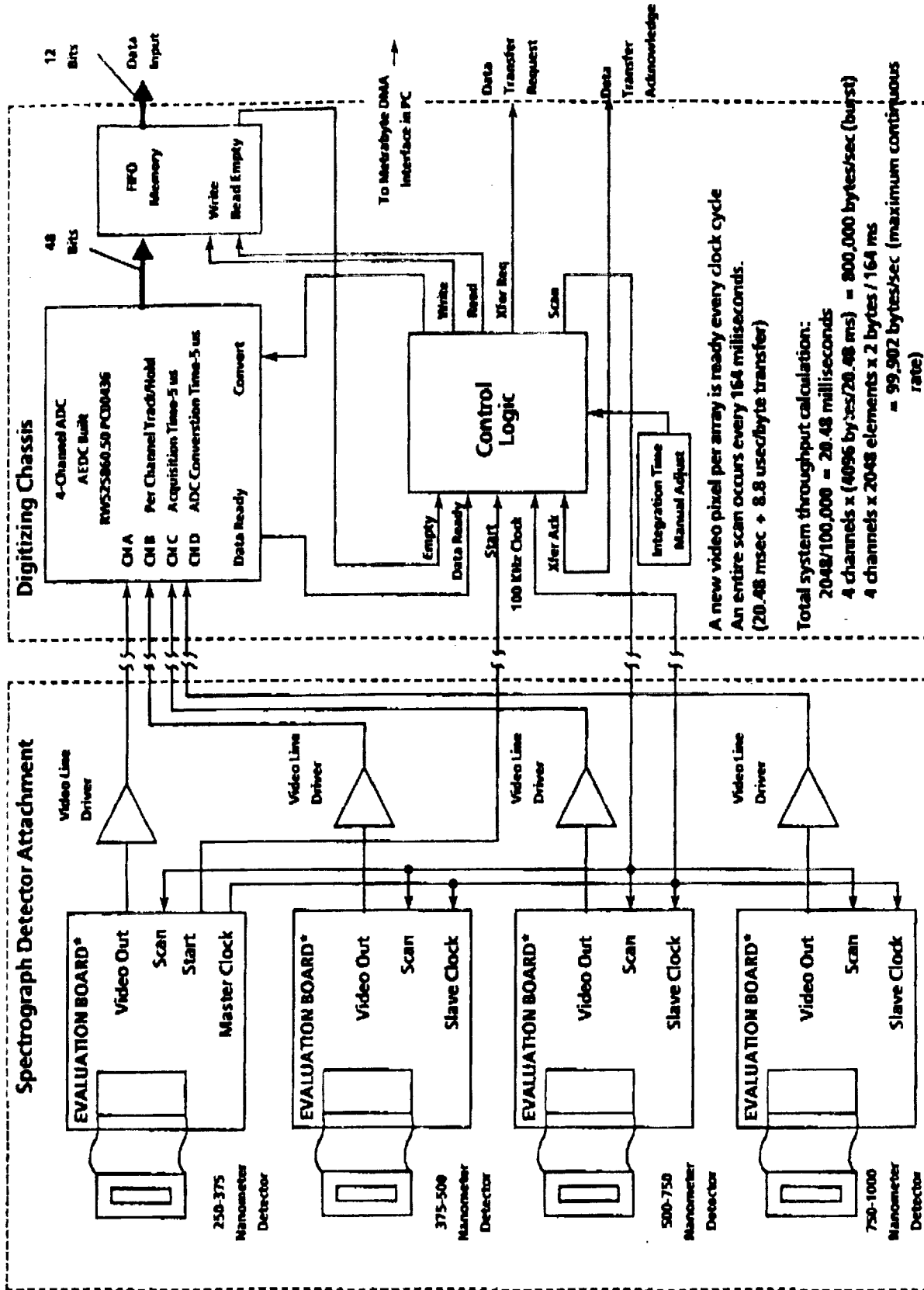


Figure 2



NASA/OPAD Spectrometer Electronics.

Figure 3



519-39
19876

PROBABILISTIC STRUCTURAL ANALYSIS -
INTRODUCTORY REMARKS

Christos C. Chamis
NASA Lewis Research Center

It is becoming increasingly evident that deterministic structural analysis methods will not be sufficient to properly design critical components in hot engine structures. These structural components are subjected to a variety of complex and severe cyclic loading conditions, including high temperatures and high temperature gradients. Most of these are quantifiable only as best engineering estimates. These complex loading conditions subject the material to coupled nonlinear behavior which depends on stress, temperature, and time. Coupled nonlinear material behavior is nonuniform, is very difficult to determine experimentally, and is perhaps impossible to describe deterministically. In addition, hot rotating structural components are relatively small. Fabrication tolerances on these components, which in essence are small thickness variations, can have significant effects on the component structural response. Fabrication tolerances by their very nature are statistical. Furthermore, the attachment of components in the structural system generally differs by some indeterminate degree from that assumed for designing the component. In summary, all four fundamental aspects - loading conditions, material behavior, geometric configuration, and supports - on which structural analyses are based, are of a random nature. The direct way to formally account for all these uncertain aspects is to develop probabilistic structural analysis methods where all participating variables are described by appropriate probability functions (fig. 1).

The development of probabilistic structural analysis methodology consists of the following program elements: (1) composite load spectra models, (2) computational probabilistic structural analysis methods, and (3) probabilistic constitutive relationships. The development of the probabilistic structural analysis methodology is a joint program of NASA Lewis in-house and sponsored research. The objective of this session is to illustrate recent progress on the application of this methodology to determine the reliability of structural components for rocket propulsion systems.

The session contains descriptions of and progress reports on the following specific activities: (1) The NESSUS computer code, (2) approximate methods, (3) advanced methods, (4) composite load spectra applications, (5) probabilistic fracture mechanisms, and (6) probability of failure and risk analysis. Collectively, the progress to date demonstrates that the structural durability of hot engine structural components can be effectively evaluated in a formal probabilistic/reliability framework.

UNCERTAINTIES IN LOAD CONDITIONS AND STRUCTURAL PRIMITIVE VARIABLES ARE INTEGRATED BY PERFORMING MULTIPLE FINITE ELEMENT ANALYSES

GLOBAL: AT ALL NODAL POINTS

$$[M]\{\ddot{u}\} + [c]\{\dot{u}\} + [k]\{u\} = \{F(t)\}$$

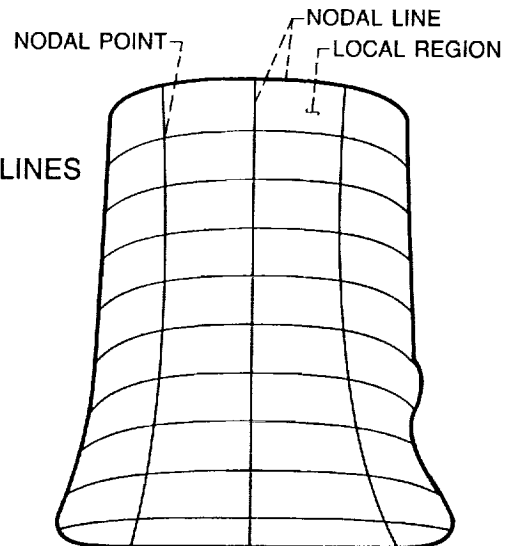
LOCAL: AT EACH REGION BOUNDED BY NODAL LINES

$$[M] = \int_V [B_M]^T [D] [B_M] dv$$

$$[C] = \int_V [B_c]^T [\zeta] [D] [B_c] dv$$

$$[K] = \int_V [B_k]^T [D] [B] dv$$

THE UNCERTAINTIES IN THE
STRUCTURAL RESPONSE VARIABLES
(u , w , σ , ϵ , G) ARE DETERMINED FROM
THE RESULTS OF THE MULTIPLE FINITE
ELEMENT ANALYSES



CD-89-39626

Figure 1

STRUCTURES RESEARCH ACTIVITIES ON SSME STRUCTURAL DURABILITY

	RESEARCH ACTIVITY	TYPE	INSTITUTION
B16	COMPOSITE LOAD SPECTRA	CONTRACT	ROCKETDYNE (PRIME)
B15(A)	PROBABILISTIC STRUCTURAL ANALYSIS METHODS (PSAM)	CONTRACT	SWRI (PRIME)
B15(G)	PROBABILISTIC FINITE ELEMENTS FOR FRACTURE MECHANICS	GRANT	NORTHWESTERN UNIV.
B15(C)	PROBABILISTIC STRUCTURAL ANALYSIS	IN HOUSE	SVERDRUP SUPPORTED

CD-89-39627

Figure 2

PROBABILISTIC STRUCTURAL ANALYSIS METHODS FOR
SELECT SPACE PROPULSION SYSTEM COMPONENTS520-39
19877H.R. Millwater and T.A. Cruse
Southwest Research Institute
San Antonio, Texas

The Probabilistic Structural Analysis Methods (PSAM) project developed at SwRI integrates state-of-the-art structural analysis techniques with probability theory for the design and analysis of complex large-scale engineering structures. PSAM is currently in the fifth year of a five year contract. An advanced efficient software system (NESSUS) capable of performing complex probabilistic analysis has been developed. NESSUS contains a number of software components to perform probabilistic analysis of structures. These components include: an expert system, a probabilistic finite element code, a probabilistic boundary element code and a fast probability integrator. The NESSUS software system is shown in figure 1.

An expert system is included to capture and utilize PSAM knowledge and experience. NESSUS/EXPERT is an interactive menu-driven expert system that provides information to assist in the use of the probabilistic finite element code NESSUS/FEM and the fast probability integrator (FPI). Figure 2 summarizes the expert system menu structure.

The NESSUS system contains a state-of-the-art nonlinear probabilistic finite element code, NESSUS/FEM, to determine the structural response and sensitivities. A broad range of analysis capabilities and an extensive element library is present. A summary of the current analysis capabilities include static, eigenvalue, harmonic, random vibration, and buckling analyses. A variety of random variables are available such as geometry, loads, material properties, temperatures, boundary conditions, harmonic excitation, power spectral density input, etc. In addition, special algorithms have been developed and implemented to efficiently perform sensitivity computations required for probabilistic structural analysis. A summary of the current code capabilities is presented in figure 3.

A fast probability integrator (FPI) has been developed to efficiently perform probabilistic analysis. Fast probability integration is an approximate technique which offers significant advantages over traditional Monte Carlo methods particularly in the low probabilities of failure typically found in structural engineering. FPI contains a number of features and options which are summarized in figure 4.

A probabilistic boundary element analysis program (PBEM) is available in the NESSUS system as an alternative to the finite element code. For many types of analyses, the boundary element method offers significant efficiency and accuracy advantages over finite elements. PBEM is a robust three-dimensional nonlinear boundary element code. The current capabilities of the code are: linear elastic and plastic analyses with temperature dependent materials, time dependent loading, and normal mode vibration.

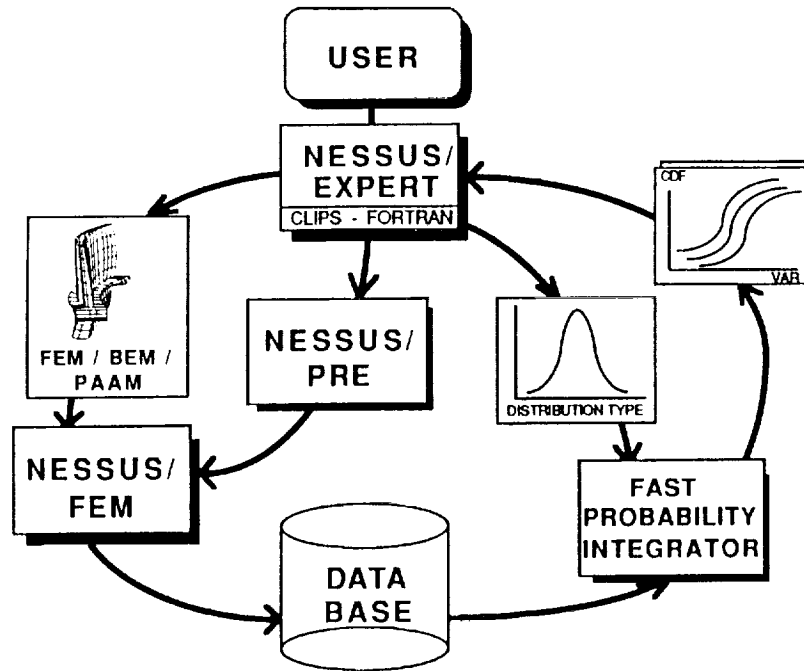
NESSUS has been validated on a number of small-scale problems where the exact solution can be determined. Figure 5 is a finite element model for a notched plate. The primary random variable is the radius of the notch and the response variable is the probabilistic stress concentration. Figure 6 demonstrates the random vibration capabilities of NESSUS. The random variables include the Power Spectral Density acceleration, the structural damping and the PSD cutoff frequency. The response variable is the root-mean-square tip displacement. In both cases, excellent agreement is found between the NESSUS solutions and exact solutions. In general, NESSUS has been validated for a number of capabilities including: static stress analysis, eigenvalue, buckling, harmonic excitation and random vibration.

The application of NESSUS to SSME components is being conducted under the verification phase of PSAM. The four selected components are shown in figure 7. Each component exercises a different capability of NESSUS. Presently, verification studies of the turbine blade and the HPOD have been completed. The turbine blade model exercises the static stress analysis and natural frequency capabilities of NESSUS. The HPOD model exercises the random vibration capabilities.

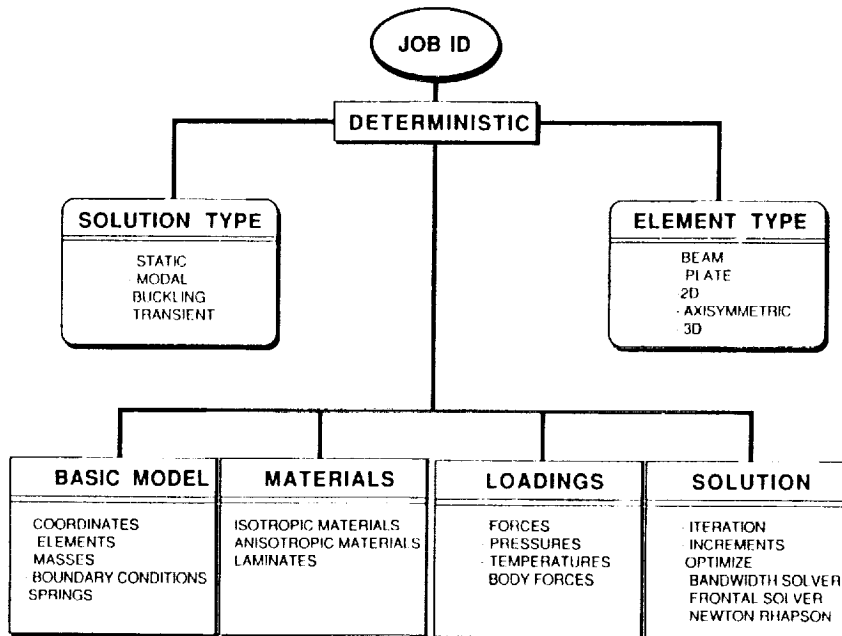
Graphical interfaces between NESSUS and pre- and post-processors have been developed to enhance data interpretation. Figure 8 is a contour plot of the probability of exceeding 80,000 psi stress for the turbine blade. This plot can be used to quickly determine critical areas which can then be examined more accurately with further computations.

NESSUS is currently being extended into transient and nonlinear material and geometric problems. Random variables will include initial accelerations, displacements, velocities and nonlinear parameters such as yield stress and hardening parameters.

Overview of the NESSUS System



NESSUS/EXPERT Menu System



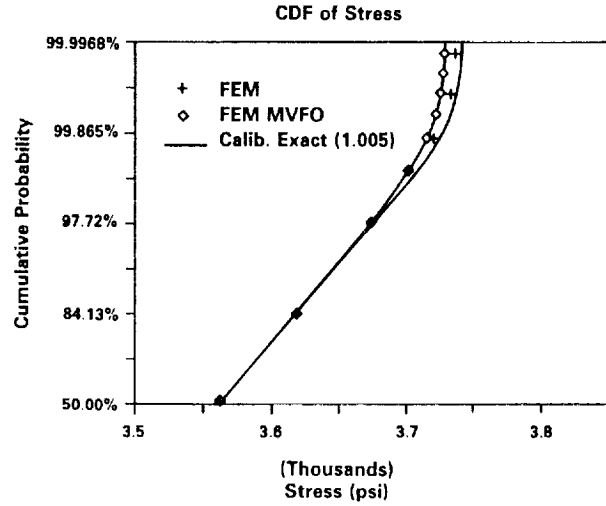
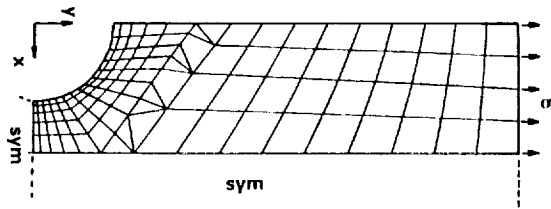
NESSUS/FEM Capabilities

ANALYSIS TYPES	ELEMENT LIBRARY	RANDOM VARIABLES
STATIC	BEAM	
NATURAL FREQUENCY	PLATE	GEOMETRY
BUCKLING	PLANE STRESS	LOADS FORCES PRESSURES TEMPERATURES
HARMONIC EXCITATION	PLANE STRAIN	
RANDOM VIBRATION	AXISYMMETRIC	MATERIAL PROPERTIES ELASTIC MODULUS POISSON'S RATIO SHEAR MODULUS ORIENTATION ANGLE
TRANSIENT DYNAMICS	3D SOLID	
	3D ENHANCED SOLID	
<u>NONLINEAR</u>		
<u>MATERIAL</u>		
<u>GEOMETRY</u>		

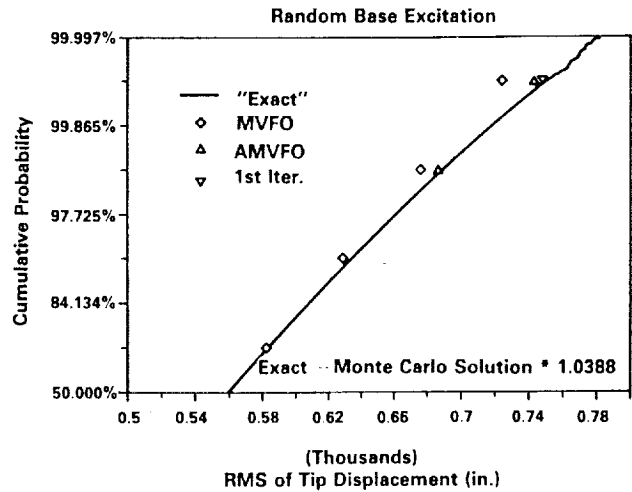
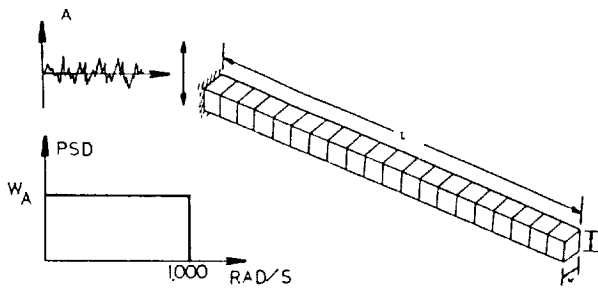
NESSUS/FPI Capabilities

- **Advanced Mean Value First Order Method**
- **Linear and Quadratic G Function Approximation**
- **Confidence Levels**
- **Sensitivity Factors**
- **Empirical Distribution Functions**
- **Full Library of Standard Distribution Functions**
- **Harbitz Method Monte Carlo**

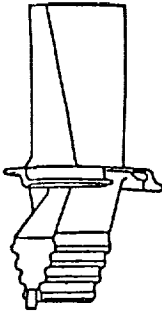
Stress Concentration Analysis



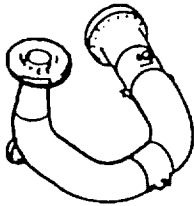
Random Vibration Analysis of Cantilever Beam



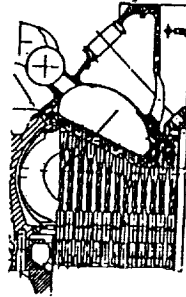
Verification Analyses



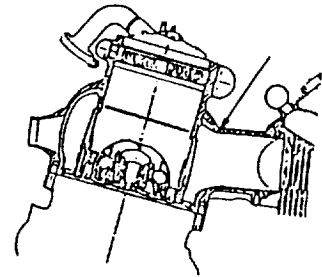
Turbine Blade



High Pressure Duct

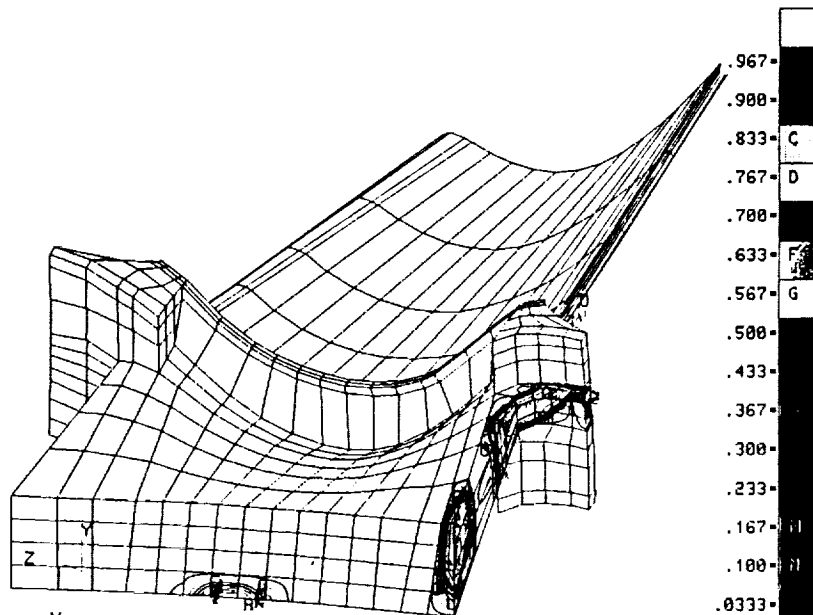


LOX Post



Transfer Tube Liner

Turbine Blade Analysis



PROB. ANALYSIS - MAT. ORIEN, ELASTIC CONSTANTS AND GEOMETRY AS RANDOM
EFFECTIVE STRESS - PROB. OF EXCEEDING 80000 PSI

AN APPROXIMATE METHODS APPROACH TO PROBABILISTIC STRUCTURAL ANALYSIS

R. C. McClung, H. R. Millwater, Y.-T. Wu, B. H. Thacker, and O. H. Burnside
Southwest Research Institute
San Antonio, Texas

521-39
19878

A major research and technology program in Probabilistic Structural Analysis Methods (PSAM) is currently being sponsored by the NASA Lewis Research Center with Southwest Research Institute as the prime contractor [1,2]. This program is motivated by the need to accurately predict structural response in an environment where the loadings, the material properties, and even the structure may be considered random. The heart of PSAM is a software package which combines advanced structural analysis codes with a fast probability integration (FPI) algorithm for the efficient calculation of stochastic structural response.

The most common structural analysis techniques in use today are finite element and boundary element methods. These techniques permit highly accurate three-dimensional modeling of structural geometry, thermal and mechanical load environment, and material properties. Unfortunately, these techniques can also be expensive and time-consuming. In the early stages of design, when geometries, loads, and materials are only tentative, it is not practical to assemble an exact, comprehensive three-dimensional model for every critical component. What is needed, typically, is some means of estimating the nature and rough magnitude of stresses, displacements, natural frequencies, etc. Of further value is the identification of those design parameters which exert the most influence on the total system performance, so that further design evolution is more efficient.

These needs are addressed in the PSAM software by the Probabilistic Approximate Analysis Methods (PAAM) module. The basic idea of PAAM is simple: make an approximate calculation of system response, including calculation of the associated probabilities, with minimal computation time and cost, based on a simplified representation of the geometry, loads, and material. The deterministic solution resulting should give a reasonable and realistic description of performance-limiting system responses, although some error will be inevitable. If the simple model has correctly captured the basic mechanics of the system, however, including the proper functional dependence of stress, frequency, etc. on design parameters, then the response sensitivities calculated may be of significantly higher accuracy. In other words, the calculated probabilistic distribution of the response variable may be in significant error only by some offset of the mean value.

Three factors make up the "approximate" analysis approach. The first is a simplified representation of the part geometry. Complex three-dimensional shapes are replaced by simple beams, shells, etc., with relatively few descriptive parameters. The second factor is a similar simplification of the applied mechanical and thermal loads. Point loads, uniform fields, and linear or parabolic distributions are used to describe these quantities. Often a complex load environment can be approximated through linear superposition of the simple descriptors. The third factor in the PAAM methodology is the solution technique itself. Complex numerical techniques with many degrees of freedom are replaced by simpler computational schemes. In some cases, it is possible to construct a simple mechanics-of-materials model, often in two dimensions. In other cases, more sophisticated closed-form solutions can be derived or (preferably) adapted from previous research results in the literature. These may be based on elasticity or may employ approximate energy methods.

The PAAM code employs the fast probability integration (FPI) algorithm of Wu and Wirsching [3], which has been demonstrated to consistently provide fast and accurate estimates of point probabilities for typical engineering response functions. This algorithm identifies a most-probable-point (or design point) on the response surface, establishes a quadratic polynomial approximation to the response function at that point, and then transforms the quadratic form into a linear one. Input variables are defined using probability distributions. An optimization routine is employed to approximate non-normal variates as equivalent three-parameter normals, thereby approximating the limit state as linear in normally distributed design factors. Solution of this simplified problem is straightforward. The FPI is repeatedly applied to a number of limit states to compute the cumulative distribution function (CDF).

The PSAM code is being demonstrated and validated by analyzing four representative critical components in the current Space Shuttle Main Engine (SSME). The same four components are considered in the PAAM code, which by its very nature is component-specific. It should be noted, however, that the architecture of the PAAM software permits new closed-form expressions for these or other components to be installed and evaluated quickly. In this presentation one of these demonstration components, the liquid oxygen (LOX) post, is used to illustrate typical PAAM solution strategies and results.

Two different simple models are used to analyze the LOX post. The steady temperature and pressure gradients between the internal and external radii are evaluated by modeling the post as an axisymmetric thick cylinder. This is a classic elasticity problem, and exact solutions are readily available in standard textbooks. Other loadings, including the transverse fluid flow, are considered by modeling the post as a beam with hollow circular cross-section and elastically restrained ends (i.e., a mechanics-of-materials approach). Note how this model is used to solve a vibration problem. The basic solutions for free vibration of fixed-fixed and fixed-pinned uniform beams are available in handbooks. Solutions for a limited number of intermediate end conditions are available in tabular form. These results can be fitted with a simple empirical relationship to estimate the frequency factor for any mode and any end condition. Subsequent calculations of mode shapes and stresses for forced vibration follow directly from simple equations.

Several sample PAAM/FPI calculations have been performed in order to validate and further demonstrate the approximate methods approach. Results are given in terms of cumulative distribution functions for critical response variables. FPI and Monte Carlo calculations are shown to agree closely. Also determined are the sensitivity factors of the random variables. These sensitivity factors are a function not only of the mathematical form of the equation, but also of the distribution types and coefficients of variation of each random variable. They are of particular value for guiding improvements in the analytical scheme or component design.

References

1. Burnside, O. H., "Probabilistic Structural Analysis for Space Propulsion System Components," *Advances in Aerospace Structural Analysis*, AD-09, ASME, 1985, pp. 87-102.
2. Cruse, T. A., Wu, Y.-T., Dias, B., and Rajagopal, K. R., "Probabilistic Structural Analysis Methods and Applications," *Computers and Structures*, Vol. 30, No. 1/2, 1988, pp. 163-170.
3. Wu, Y.-T., and Wirsching, P. H., "A New Algorithm for Structural Reliability Estimation," *Journal of Engineering Mechanics*, ASCE, Vol. 113, No. 9, September 1987, pp. 1319-1336.

AN OVERVIEW OF PROBABILISTIC STRUCTURAL ANALYSIS METHODS

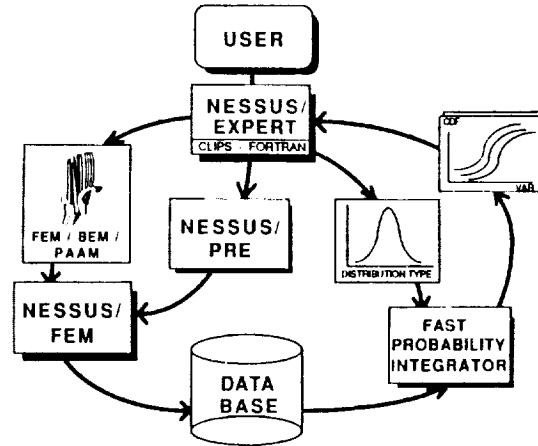
0 PSAM LINKS STRUCTURAL ANALYSIS WITH FAST PROBABILITY INTEGRATION FOR EFFICIENT CALCULATION OF STOCHASTIC STRUCTURAL RESPONSE WHEN LOADS, MATERIALS, AND GEOMETRY ARE RANDOM

0 FEM AND BEM ARE MOST COMMON STRUCTURAL ANALYSIS TECHNIQUES

- DETAILED MODELS
- ACCURATE 3-D SOLUTIONS
- EXPENSIVE, TIME-CONSUMING
- NOT APPROPRIATE FOR EARLY DESIGN/ANALYSIS

0 NEED A RAPID, INEXPENSIVE ESTIMATE OF STRUCTURAL RESPONSE WHICH INCLUDES PROBABILISTIC INFORMATION

0 "PROBABILISTIC APPROXIMATE ANALYSIS METHODS" (PAAM)



WHAT IS AN "APPROXIMATE METHOD" ?

0 SIMPLIFIED REPRESENTATIONS OF

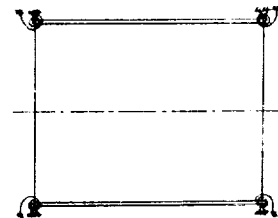
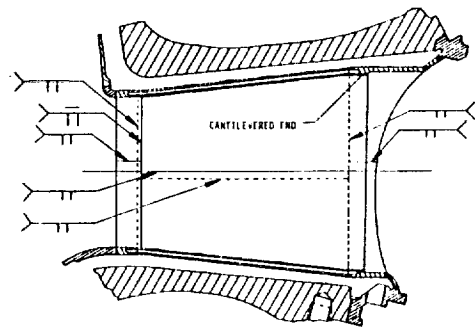
- COMPONENT GEOMETRY
- APPLIED LOADS
- MATERIAL PROPERTIES

0 RAPID, EFFICIENT SOLUTION SCHEME

- MECHANICS-OF-MATERIALS
- SIMPLE ENERGY METHODS
- CLOSED FORM OR TABULATED LITERATURE SOLUTIONS

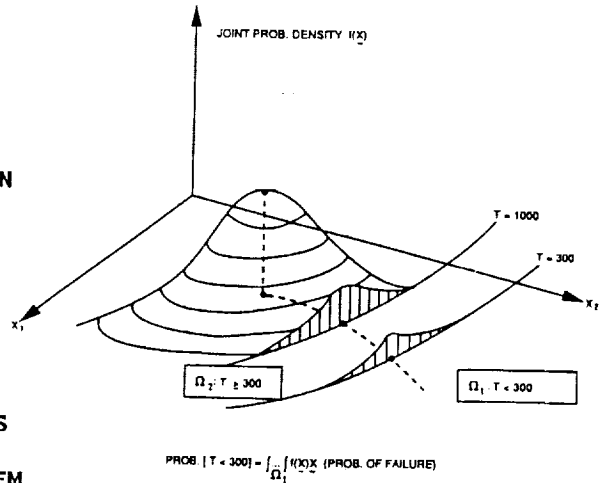
0 CALCULATED MEAN VALUE OF RESPONSE FUNCTION CONTAINS SOME ERROR

0 IF BASIC MECHANICS ARE CORRECT, RESPONSE DISTRIBUTIONS AND PARAMETER SENSITIVITIES WILL BE ACCEPTABLY ACCURATE



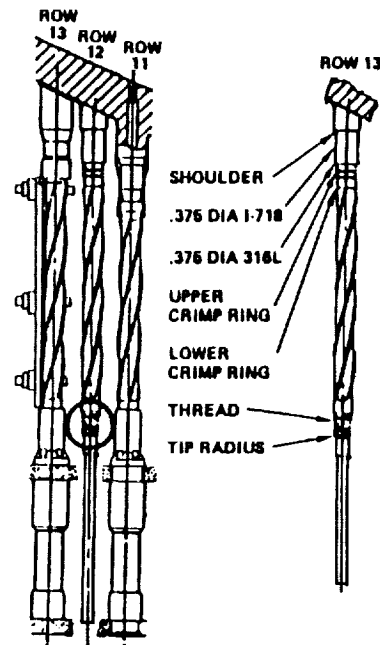
PAAM CODE USES FAST PROBABILITY INTEGRATION ALGORITHM

- 0 WU-WIRSCHING FPI ALGORITHM
- 0 SHARED BY OTHER PSAM MODULES
- 0 IDENTIFY MPP ON RESPONSE SURFACE FOR GIVEN PROBABILITY LEVEL
- 0 ESTABLISH QUADRATIC APPROXIMATION TO THE RESPONSE FUNCTION AT MPP AND TRANSFORM TO A LINEAR FORM
- 0 INPUT VARIABLES DEFINED USING PROBABILITY DISTRIBUTIONS
- 0 APPROXIMATE NON-NORMAL VARIATES AS EQUIVALENT 3-PARAMETER NORMALS
- 0 SOLVE THE RESULTING SIMPLE PROBLEM (LINEAR WITH NORMAL DESIGN FACTORS)



PAAM CODE DEMONSTRATED WITH SSME LOX POST

- 0 ONE OF FOUR SSME DEMONSTRATION COMPONENTS
- 0 A SLENDER, HOLLOW TUBE FIXED AT BOTH ENDS
- 0 IMPORTANT LOADINGS INCLUDE
 - ΔT AND Δp ACROSS TUBE WALL
 - STEADY AND DYNAMIC LOADS DUE TO TRANSVERSE FLUID FLOW
- 0 TWO DIFFERENT PAAM MODELS SHOWN
 - THICK CYLINDER MODEL
 - BEAM MODEL
- 0 ALTHOUGH THESE EQUATIONS ARE COMPONENT-SPECIFIC, THE BASIC PAAM ALGORITHM IS COMPONENT-INDEPENDENT



THICK CYLINDER MODEL USES KNOWN ELASTICITY SOLUTIONS

- 0 THICK CYLINDER SUBJECTED TO DIFFERENT INTERNAL AND EXTERNAL PRESSURES AND TEMPERATURES
- 0 EXACT CLOSED-FORM SOLUTIONS AVAILABLE IN STANDARD TEXTBOOKS

0 CONSIDER THE HOOP STRESS:

- PRESSURE SOLUTION

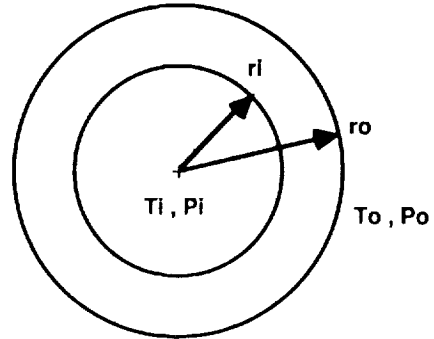
$$\sigma_{\theta} = -\frac{(r_o/r)^2(p_o - p_i)}{k^2 - 1} + \frac{p_i - p_o k^2}{k^2 - 1}$$

- THERMAL SOLUTION

$$\sigma_{\theta} = -\beta \frac{(r_o/r)^2 + 1}{k^2 - 1} + \beta \frac{1 - \ln(r_o/r)}{\ln(k)}$$

$$\beta = \frac{\alpha E (T_i - T_o)}{2(1 - \nu)}$$

$$k = r_o/r_i$$



BEAM MODEL USES A MECHANICS-OF-MATERIALS APPROACH

- 0 SLENDER BEAM WITH HOLLOW CROSS-SECTION
 - FIXED AT ONE END
 - ELASTICALLY RESTRAINED AT THE OTHER
- 0 CONSIDER THE VIBRATION PROBLEM
- 0 BASIC EQUATIONS IN HANDBOOKS IN TERMS OF A FREQUENCY FACTOR λ
- 0 LAMBDA DEPENDS ON END FIXITY AND MODE NUMBER
 - CLOSED FORM EXPRESSIONS FOR FIXED, PINNED
 - TABULATED SOLUTIONS FOR ELASTIC RESTRAINT
 - FIT THESE WITH AN EMPIRICAL EXPRESSION
- 0 SIMPLE TO CALCULATE NATURAL FREQUENCIES, DISPLACEMENTS AND STRESSES DUE TO HARMONIC AND RANDOM FORCED VIBRATION



PAAM INPUT INCLUDES STATISTICAL DESCRIPTIONS OF RANDOM VARIABLES

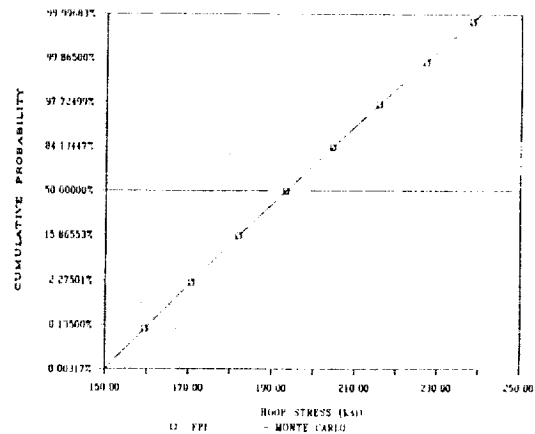
Input Variables for Lox Post Thick Cylinder Model

Variable	Distribution	Mean	COV
r_i	truncated Normal (± 0.003)	0.094 in.	1.06%
r_o	truncated Normal (-0.002, +0.01)	0.110 in.	4.55%
E	Normal	3.40E+7 psi	2%
ν	Normal	0.3594	2%
α	Normal	5.65E-6 /R	5%
p_i	Lognormal	3077 psi	4%
p_o	Lognormal	3232 psi	4%
T_i	Lognormal	194 R	1.55%
T_o	Lognormal	1444 R	1.55%

- 0 USER SUPPLIES MEAN VALUE, DISTRIBUTION TYPE, AND COV FOR EACH RANDOM VARIABLE
- 0 MANY DISTRIBUTION TYPES POSSIBLE (INCLUDING TRUNCATED)
- 0 SET COV=0 FOR DETERMINISTIC VARIABLES
- 0 IF STATISTICAL INFORMATION UNKNOWN, MAKE ESTIMATES FROM DEFAULT SPECIFICATIONS

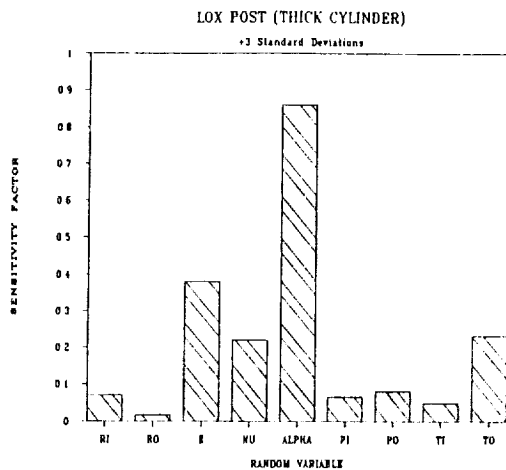
PAAM OUTPUT INCLUDES CDF OF RESPONSE FUNCTION

- 0 FPI CALCULATES CUMULATIVE DISTRIBUTION FUNCTION (CDF) OF RESPONSE VARIABLE
- 0 CDF BASED ON EQUIVALENT NORMAL DISTRIBUTION OF RESPONSE VARIABLE
- 0 EXCELLENT AGREEMENT BETWEEN FPI AND MONTE CARLO
- 0 FPI MUCH FASTER THAN MONTE CARLO



**ORIGINAL PAGE IS
OF POOR QUALITY**

PAAM CALCULATES SENSITIVITY FACTORS OF RANDOM VARIABLES



- 0 SHOWS RELATIVE INFLUENCE OF RANDOM VARIABLES ON THE TOTAL UNCERTAINTY OF THE RESPONSE
- 0 FUNCTION OF BOTH
 - MATHEMATICS OF THE EQUATION
 - DISTRIBUTION TYPE AND COV OF THE RANDOM VARIABLES
- 0 HELPS THE DESIGNER/ANALYST TO DETERMINE REQUIREMENTS FOR FURTHER DESIGN/ANALYSIS
 - MORE ACCURATE INPUT STATISTICS
 - MORE EXACT ANALYSIS MODEL
 - TIGHTER TOLERANCES IN DESIGN
 - BEST OPPORTUNITIES FOR DESIGN IMPROVEMENTS

SUMMARY

- 0 PAAM MAKES A RAPID, INEXPENSIVE ESTIMATE OF THE PROBABILISTIC STRUCTURAL RESPONSE OF A SYSTEM
- 0 REQUIREMENTS:
 - SIMPLIFIED REPRESENTATION OF COMPONENT GEOMETRY AND LOADS
 - CLOSED-FORM SOLUTIONS DERIVED OR ADAPTED FROM THE LITERATURE
 - STATISTICAL DISTRIBUTIONS OF INPUT VARIABLES
- 0 PROBABILISTIC CALCULATION PERFORMED WITH FPI ALGORITHM
- 0 OUTPUT INCLUDES:
 - CDF OF RESPONSE VARIABLE
 - SENSITIVITY FACTORS FOR RANDOM VARIABLES
- 0 PAAM PARTICULARLY USEFUL IN EARLY STAGES OF DESIGN/ANALYSIS



PROBABILISTIC BOUNDARY ELEMENT METHOD

522-39
19879

T.A. Cruse and S.T. Raveendra
Southwest Research Institute
San Antonio, Texas

The purpose of the Probabilistic Structural Analysis Methods (PSAM) project is to develop structural analysis capabilities for the design analysis of advanced space propulsion system hardware. The PSAM effort consists of three major technical thrusts: probabilistic finite element methods (PFEM), probabilistic approximate analysis methods (PAAM), and probabilistic advanced analysis methods (PADAM). The boundary element method is used as the basis of the Probabilistic Advanced Analysis Methods (PADAM) this is discussed in this text. In particular, the BEST3D code developed under NASA/HOST program is modified for inclusion in the PSAM module as NESSUS/BEM.

The probabilistic boundary element method code (PBEM) is used to obtain the structural response and sensitivity results to a set of random variables. As such, PBEM performs analogous to other structural analysis codes such as finite elements in the PSAM system. The probabilistic analysis is performed by coupling PBEM and the Fast Probability Integrator (FPI) using a highly efficient mean based algorithm. Preliminary validation studies have shown PBEM to be an accurate tool for probabilistic analysis.

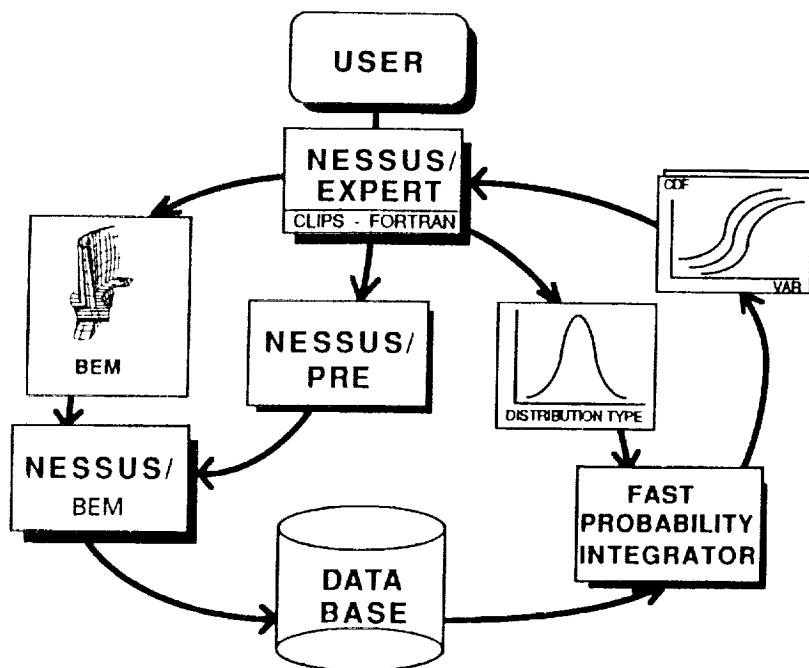
For linear problems, unlike the finite element method (FEM), the BEM governing equations are written at the boundary of the body only, thus, the method eliminates the need to model the volume of the body. However, for general body force problems, a direct condensation of the governing equations to the boundary of the body is not possible and therefore volume modelling is generally required. Since such volume modeling mostly eliminates the advantage of the BEM procedure, a surface transformation technique based on particular integrals is used to replace the volume integral by equivalent surface integrals in the current analysis.

To illustrate the particular integral procedure, consider the solution of thermoelastic problem. The surface transformation technique requires the evaluation of the particular integrals of the inhomogeneous Navier's equilibrium equations. However, in general, the temperature field is not known as a continuous functions, instead, the values of the temperatures are known at selected points at the surface and volume of the body. The procedure assumes that the temperature field then can be expressed in terms of interpolation functions and unknown *densities* associated with each collocation point. Since this procedure replaces the actual temperature field by an approximate field, the resulting integrals equations, while satisfying the equilibrium conditions, are only approximate. A plot of the interpolated temperature field on the surface of a cube subjected to uniform temperature shown in figure 4 indicates that the global interpolation results is in error except at collocation points. Nevertheless, the particular integral solution procedure uses nodal values interpolated by regular isoparametric shape functions in their computations which seems to minimize the interpolation error effect.

PRECEDING PAGE BLANK NOT FILMED

As a first example, consider the free vibration analysis of a cantilever beam. The first five normal modes shown in figure 5 using two BEM models agree well with FEM results, thus, validating the free-vibration analysis procedure. To validate the particular integral procedure for the thermoelastic problem, we considered the solution of hollow sphere with an external radius to internal radius ratio of 2 subjected to linear radial temperature variation. The normalized hoop stress compared to the theoretical results in figure 6 validates the particular integral procedure for thermal problems. To further investigate the accuracy of the procedure for higher temperature variations, we considered the same sphere subjected to cubic radial temperature variation. Again the agreement between the computational the theoretical results for hoop stresses is excellent as shown in figure 7. This shows that while the interpolated temperature field is in error, the solution of the corresponding boundary integral equations even for a higher order temperature field is still very accurate. As a final example, we considered a hollow cylinder subjected to linear temperature variation. We further assumed that the Young's modulus also varied linearly for this case. The resulting hoop stress compared to FEM in figure 8 validates the material inhomogeneity procedure.

Overview of NESSUS/BEM System



BEM Formulation for General Body Force Analysis Does Not Use Domain Modeling

- Regular Domain BIE for Thermoelasticity

$$\underline{c} \underline{u} + \int_s \underline{T} \underline{u} ds = \int_s \underline{U} \underline{t} ds + \int_v \underline{S} \theta dv$$

- BIE for Particular Solution Replaces Domain Integral

$$\underline{c} \underline{u}^P + \int_s \underline{T} \underline{u}^P ds - \int_s \underline{U} \underline{t}^P ds = \int_v \underline{S} \theta dv$$

- Surface-Only BIE Replaces Thermoelastic BIE

$$\underline{c} \hat{\underline{u}} + \int_s \underline{T} \hat{\underline{u}} ds = \int_s \underline{U} \hat{\underline{t}} ds$$

$$\hat{\underline{u}} = \underline{u} - \underline{u}^P(\theta)$$

$$\hat{\underline{t}} = \underline{t} - \underline{t}^P(\theta)$$

Particular Solutions Obtained for Approximating Body Forces

- Navier's Equilibrium Equation (Thermoelastic)

$$\underline{N} \cdot \underline{u}^P = m \nabla \theta$$

- Collocate θ with Boundary Interpolation Functions

$$\tilde{\theta}(\mathbf{q}_m) = \sum_{n=1}^N K(\mathbf{q}_m, \mathbf{Q}_n) \varphi(\mathbf{Q}_n) \quad \mathbf{Q}_n \in S$$

- Particular Solution for Collocated Temperatures Replaces Domain Integral

$$\underline{c} \tilde{\underline{u}}^P + \int_s \underline{T} \tilde{\underline{u}}^P ds - \int_s \underline{U} \tilde{\underline{t}}^P ds = \int_v \underline{S} \tilde{\theta} dV$$

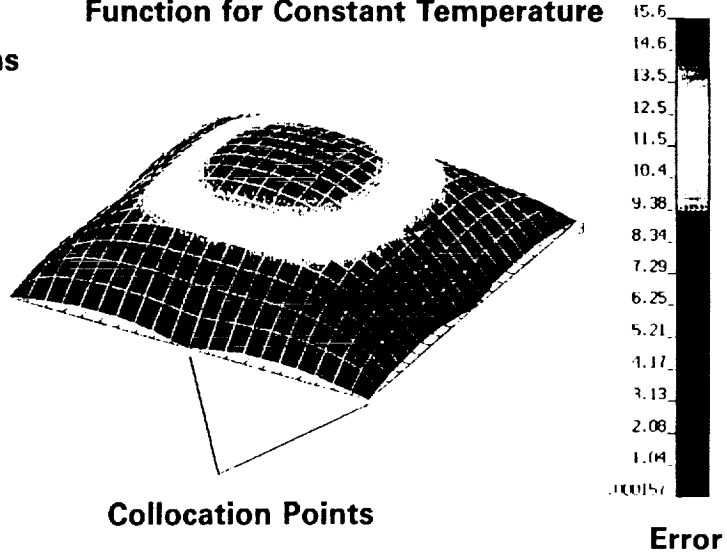
- Surface-Only BIE for Interpolated Temperatures

$$\underline{c} \hat{\hat{\underline{u}}} + \int_s \underline{T} \hat{\hat{\underline{u}}} ds = \int_s \underline{U} \hat{\hat{\underline{t}}} ds + \int_v \underline{S} (\theta - \tilde{\theta}) dV$$

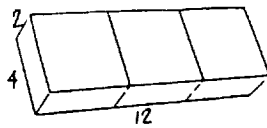
Interpolation Error Within the Domain

- Global Interpolation Functions
- Collocated at User-Defined Points (Surface and Interior)
- Particular Solution Method Minimizes Interpolation Error Effect
- Particular Solution Approximation Uses BIE Shape Functions

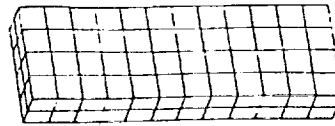
Error in Global Interpolation Function for Constant Temperature



Normal Vibration Modes of BEM and FEM Models Are Compared



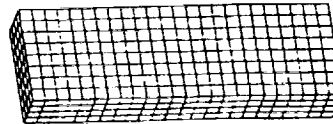
a) BEM Map 1



a) FEM Map 1



b) BEM Map 2



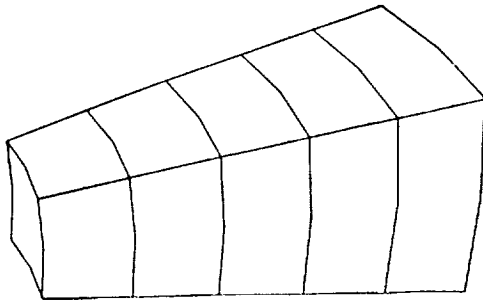
b) FEM Map 2

First Five Modes of Vibration for the Cantilever Models

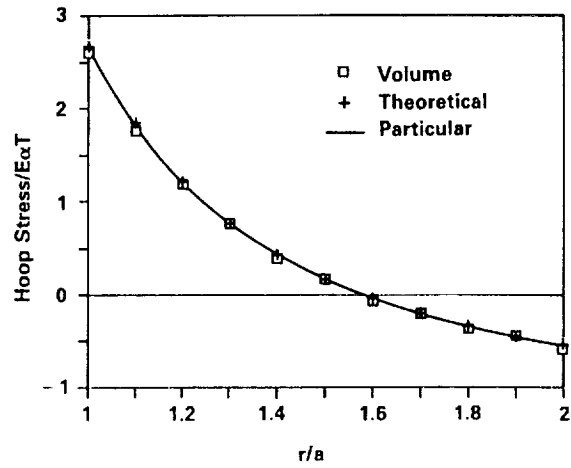
	Mode 1	Mode 2	Mode 3	Mode 4	Mode 5	Nodes/ Elements	CPU (sec) VAX 8700
BEM-1	2686	5441	13485	16810	25382	44/14	352
BEM-2	2810	5333	12736	16255	24523	86/28	1676
FEM-1	3033	5449	13191	17227	25141	195/96	158
FEM-2	2885	5354	12778	16224	24522	1125/768	801

Results Are Accurate Even For Cubic Temperature Variation

Hollow Sphere



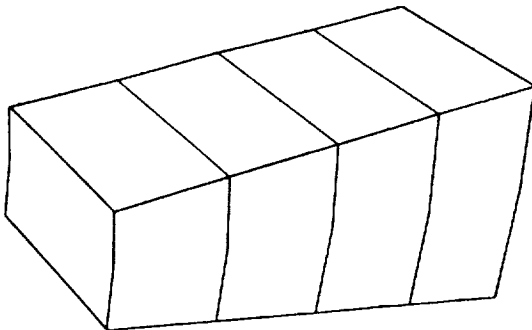
$b/a = 2$
 $a = 10$
 $E = 2600$
 $\nu = 0.3$
 $\alpha = 10^{-4}$



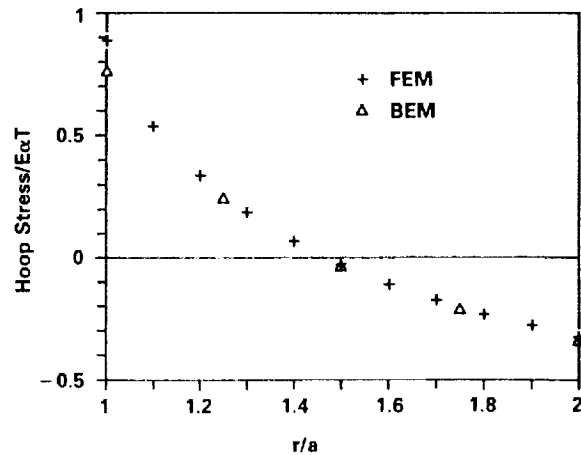
$T = 100 + 10r + r^2 + 0.2r^3$

Temperature-Dependent Thermal Analysis Procedure Validated

Hollow Cylinder



$b/a = 2$
 $a = 10$
 $E_0 = 30 \times 10^6$
 $\nu = 0.3$
 $\alpha = 10^{-4}$



$T = 10r$
 $E = E_0 - 10^4 T$

Current NESSUS/BEM Code Capabilities

- **Linear Elastic Stress Analysis**
- **Centrifugal Loading Analysis**
- **Free-Vibration Analysis**
- **Thermal Analysis**
- **Thermal Analysis with Temperature-Dependent Material Properties**

NESSUS/FEM Future Developments

- **Additional Particular Integrals
(e.g., Steep Thermal Gradient, Linear Temperature Field)**
- **Elastoplastic Analysis**
- **Large Deformation Analysis**
- **Transient Analysis**

Composite Load Spectra
For Select Space Propulsion Structural Components*523-39
19880H. Ho and J. F. Newell
Rockwell International Corporation, Rocketdyne Division
R. E. Kurth
Battell Columbus Laboratory

The objective of the Composite Load Spectra (CLS) project is to build a knowledge-based system to synthesize probabilistic loads for selected space propulsion engine components. The knowledge-based system has a load expert system module and a load calculation module. The load expert system provides load information and the load calculation module generates the probabilistic load distributions.

The engine loads can be divided into four broad classes: the engine independent loads, the engine system dependent load, the component local independent loads and the component loads. The engine independent loads include engine operating conditions and the engine hardware parameters. The engine operating conditions are the O/I mixture ratio, and the engine fuel and oxidizer inlet conditions etc. The engine hardware parameters are for example the HPFIP pump efficiency, the HPOIP turbine efficiency, etc. The engine system dependent loads are the operating conditions of the engine subsystems such as the HPFIP turbine inlet and discharge pressures. The component loads including the local independent loads are loads internal to the engine subsystems. The component loads are evaluated with a multi-level engine model implemented on CLS. The multi-level engine model includes an engine probabilistic influence model and many component load models. The engine subsystem dependent loads are evaluated by the probabilistic influence model and they are in turn fed into the component load models to generate the component loads. Figures 1 and 2 illustrate the loads and the engine models.

The engine probabilistic influence model calculates the engine system dependent load variations from a set of engine influence coefficients as shown in Figure 3. The influence coefficients are dependent of the engine commanded power level. These influence coefficients were derived from the engine flight and test data. The engine model implemented on CLS has 64 independent loads and 99 system dependent loads. The load mean values, coefficient of variations and the influence coefficients are stored in the CLS knowledge base. They can be retrieved by the load expert system when needed. There are many component load models as listed in Figure 4, each of which is for a certain component load. For example, the pressure scaling model is for evaluation the component static pressure for the turbine blade, the transfer duct and other components. The probabilistic thermal load model is for evaluating the temperatures of the components. In many cases, each component has its own geometry model and related parameters. They are stored in a database format in the CLS knowledge base.

* Work performed under NASA Contract NAS3-24382

The four engine components selected for implementation are the turbine blade, the transfer ducts, the LOX posts and the HPOIP discharge duct. The loads for these components important to the probabilistic structural analyses and reliability calculations are listed in Figure 5.

The load calculation module provides three probabilistic methods for generating probabilistic loads. They are the Gaussian moment method, the RASCAL (Random Sampling Condensation Algorithm) method and the Monte Carlo Method. The Gaussian moment method assumes all input loads are normally distributed. The dependent loads are evaluated analytically. The RASCAL is a discrete probability distribution method. It reduces computational time by restricting the sample space as it combines loads. The Monte Carlo method is a standard version of the Monte Carlo sampling method. The probabilistic models implemented on CIS are shown in Figure 6. They include models for calculating the steady state load and the transient state loads. At present, the steady state and the quasi-steady state models are available for duty cycle mission calculations. The other probabilistic models are available for stand alone calculations. Figure 7 shows a comparison of the results of the Gaussian method and the RASCAL method with the HPEIP discharge pressure data at 100% power level. The calculations match reasonably well with the data. Figures 8 and 9 show the confident interval calculations for the HPEIP turbine torque using RASCAL method with various bin numbers and different sampling options. The confident intervals compare well with the Monte Carlo method. Notice that the bin numbers used in RASCAL are much smaller than the Monte Carlo sample size.

The Composite Load Spectra knowledge based system as delineated in Figures 10 and 11 are developed for load syntheses of selected space propulsion engine components. Its domain knowledge includes engine load information and probabilistic engine load models. The knowledge-based system has a built-in database system that can handle the database operations. It provides three basic probabilistic methods and numerous probability models for building models for component load calculations. The load expert system can retrieve the required load data and prepare input files for the load calculations. In an application study, presented separately in this conference, we have demonstrated that using the marginal distribution method the CIS can provide the composite load spectra to a structural analysis program for probabilistic analysis and thus eliminates the need of modeling the loads inside the structural analysis program.

**ORIGINAL PAGE IS
OF POOR QUALITY**

SYSTEM CLASS OF LOADS

- STEADY STATE
 - DIRECT VARIABLES – THRUST, INLET CONDITIONS
 - RANDOM VARIABLES – HARDWARE, TEST VARIATIONS
- TRANSIENTS
 - START AND CUTOFF CONTROLLED
 - LOCAL EFFECTS

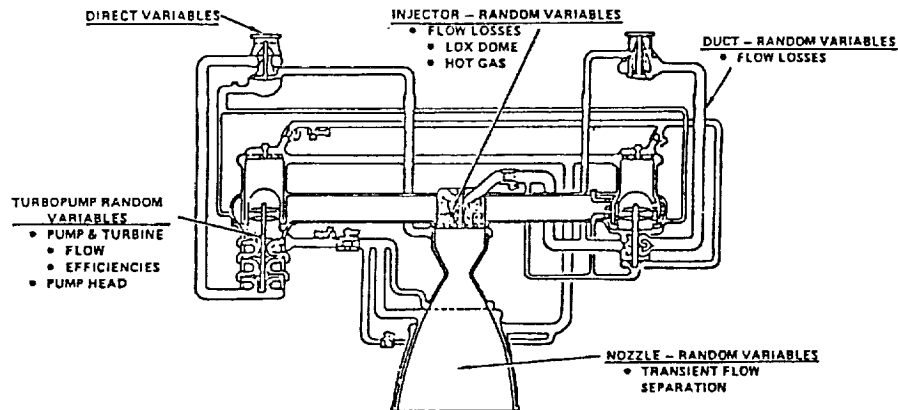


Figure 1 .

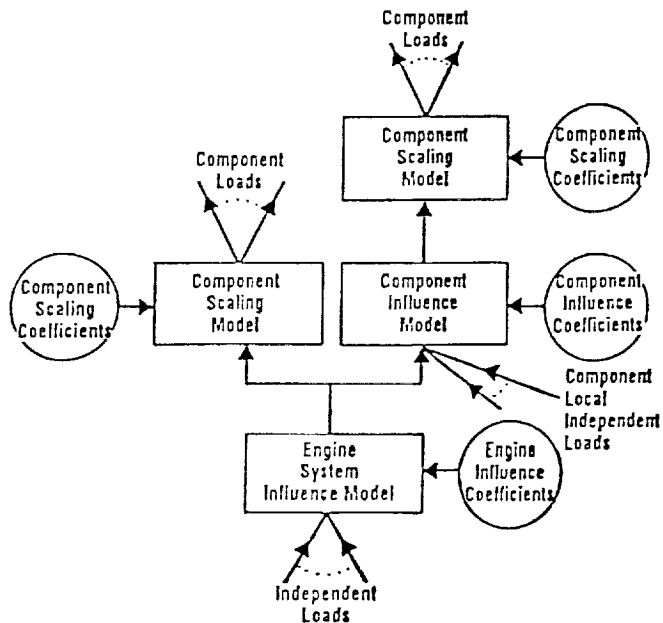


Figure 2.

COMPOSITE LOAD SPECTRA
MULTI-LEVEL ENGINE MODEL

- ENGINE SYSTEM MODEL
 - PROBABILISTIC INFLUENCE MODEL

$$\frac{\Delta Y_j}{Y_{j0}} = \sum_i (IC)_{ji} \frac{\Delta X_i}{X_{i0}}$$

WHERE X_i 's ARE ENGINE INDEPENDENT LOADS

- e.g. ENGINE MIXTURE
 - FUEL AND OXIDIZER INLET PRESSURES AND INLET TEMPERATURES
 - HPFTP & HPOTP PUMP EFFICIENCIES
 - HPFTP & HPOTP TURBINE EFFICIENCIES, ETC.

Y_j 's ARE ENGINE SYSTEM DEPENDENT LOADS

- e.g. HPFTP TURBINE INLET PRESSURE AND DISCHARGE PRESSURE
- HPOTP TURBINE TORQUE, ETC.

$(IC)_{ji}$ ARE THE INFLUENCE COEFFICIENTS
THEY ARE FUNCTIONS OF THE COMMANDED POWER LEVEL

- KNOWLEDGE BASE
 - ENGINE LOAD KNOWLEDGE - MEAN, CV, DISTRIBUTION TYPE
 - INFLUENCE MODEL - INFLUENCE COEFFICIENT SET, GAIN INFORMATION, DUTY-CYCLE DATA

Figure 3.

COMPOSITE LOAD SPECTRA
MULTI-LEVEL ENGINE MODEL

- COMPONENT LOAD MODELS
 - COMPONENT STATIC PRESSURE SCALING MODEL
 - TURBINE BLADE DYNAMIC PRESSURE LOAD MODEL
 - TRANSFER DUCT FLUCTUATION PRESSURE MODEL
 - PROBABILISTIC THERMAL LOAD MODEL
- KNOWLEDGE BASE
 - COMPONENT LOAD MODELS
 - DEPENDENCY ON ENGINE LOADS
 - LOAD PARAMETER DATABASE
 - INFLUENCE AND SCALING COEFFICIENTS
 - COMPONENT GEOMETRY DATABASE

Figure 4.

ORIGINAL PAGE IS
OF POOR QUALITY

SUMMARY MATRIX OF INDIVIDUAL LOADS
VS COMPONENTS

INDIVIDUAL LOAD	TURBINE LOAD	TRANSFER DUCT	LOX POST	HPOT/POD FORMAT	LOAD FORM/ TEST DATA FORMAT
• STATIC PRESSURE	X	X	X	X	DUTY CYCLE
• DYNAMIC PRESSURE					
• CHUGGING (TRANSIENT)	-	X	-	-	AMS, STATOS
• TURBULENCE					
• SINUSOIDAL (REPEATED PULSE)	X				AMS, PSD, STATOS
• RANDOM	-	X	X	X	AMS, PSDS
• CENTRIFUGAL	X	-	-	-	DUTY CYCLE
• TEMPERATURE	X	X	X	X	DUTY CYCLE
• STRUCTURAL VIBRATION					
• TRANSIENT	-	X	X	X	AMS, STATOS
• STEADY STATE	-	X	X	X	AMS, PSD, STATOS

Figure 5.

COMPOSITE LOAD SPECTRA
ANLOAD = THE LOAD CALCULATION MODULE

- PROBABILISTIC METHODS
 - GAUSSIAN MOMENT METHOD
 - RASCAL (A VARIANCE OF DPD METHOD)
 - MONTE CARLO
- PROBABILISTIC MODEL
 - STEADY STATE
 - TRANSIENT STATE
 - QUASI-STEADY STATE
 - POISSON ARRIVAL
 - RARE EVENT
 - PERIODIC MODEL AND PSD

Figure 6.

ORIGINAL PAGE IS
OF POOR QUALITY

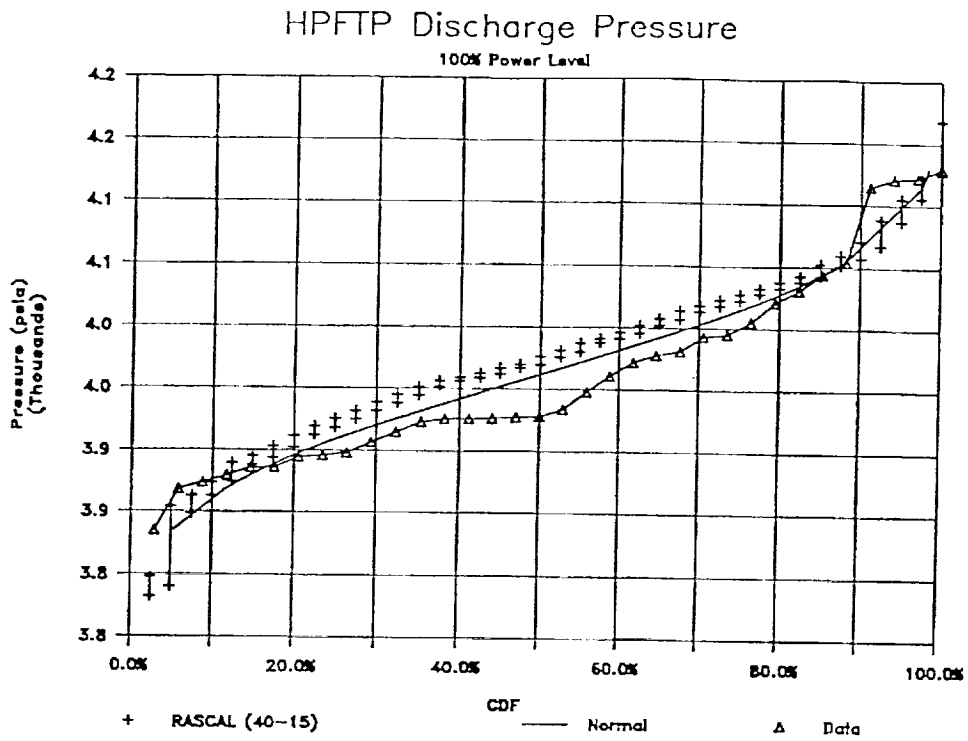


Figure 7.

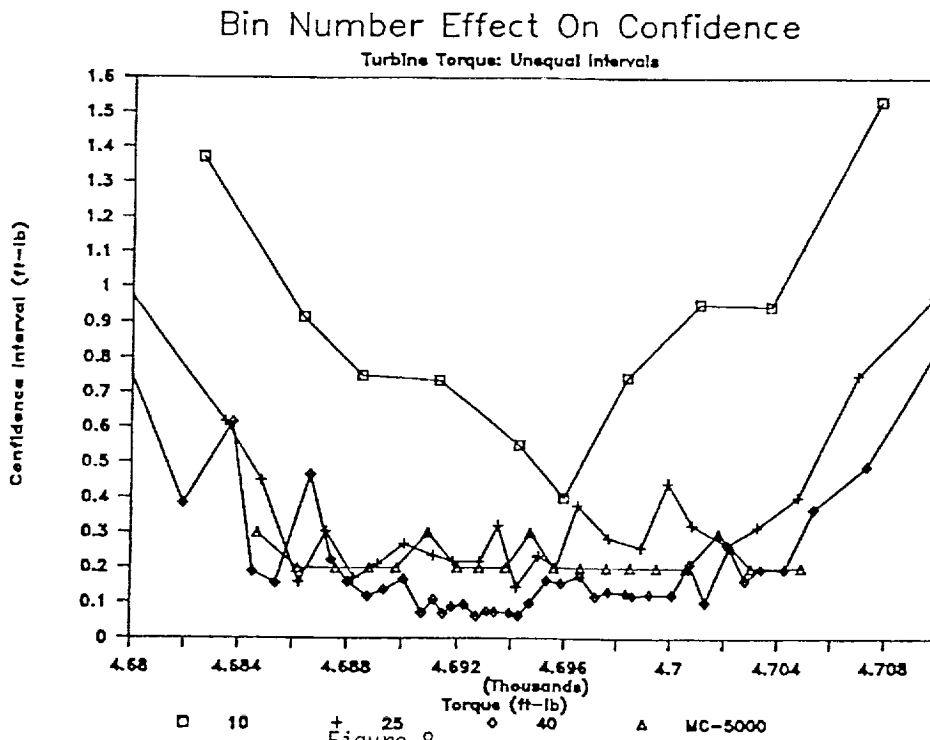
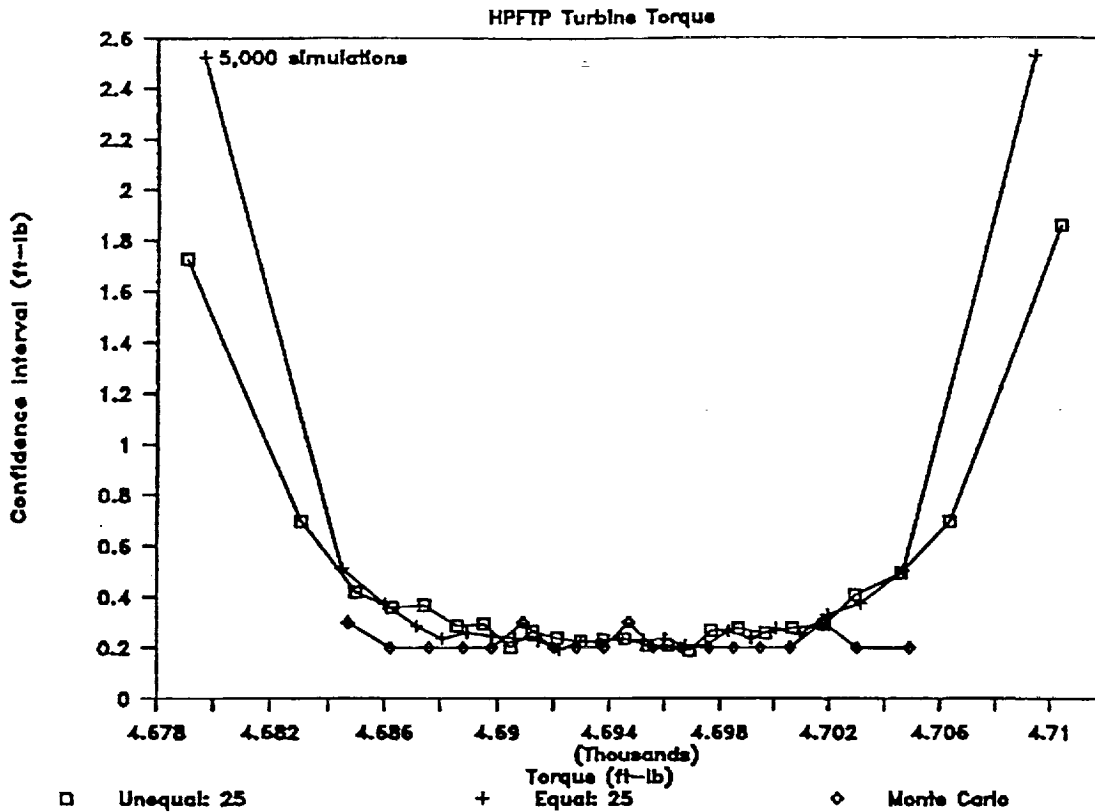


Figure 8.

Initial Interval Effect On Confidence



CONFIDENCE BAND CALCULATIONS

- MONTE CARLO BANDS ARE CALCULATED USING CLASSICAL STATISTICAL RESULTS
- MONTE CARLO CONFIDENCE BAND INTERVALS BECOME SMALLER (I.E. ACCURACY INCREASES) WITH INCREASING NUMBER OF SIMULATIONS
- RASCAL CALCULATIONS INCLUDE THE CONTINUOUS PORTION OF THE PROBABILITY SPACE IN THE CONFIDENCE BAND CALCULATIONS
- THE CONTINUOUS PROBABILITY SPACE THAT IS NOT REPRESENTED IN THE INDIVIDUAL DISCRETE DISTRIBUTIONS CAUSES A DECREASE IN THE POINT ACCURACY BY RASCAL
- THEREFORE, THE CONFIDENCE BAND INTERVALS BECOME SMALLER WITH AN INCREASING NUMBER OF INITIAL DISCRETE INTERVALS

Figure 9.

LDEXPT LOAD EXPERT SYSTEM

- EXPERT SYSTEM DRIVER
 - DECISION TREE INFERENCE
 - QUERY ON THE DATABASE KEY VARIABLES
- LOAD DATABASE SYSTEM
 - STAND-ALONE DATABASE SYSTEM
 - EXPERT SYSTEM INTERFACE
 - KEY VARIABLES ARE ATTRIBUTES OF THE EXPERT SYSTEM
 - USER/EXPERT SYSTEM SELECT OPTIONS ON KEY VALUES
- SIMPLE WORKING MEMORY MODEL
 - PASSING INFORMATION BETWEEN RULE MODULES
- LDEXPT RULE MODULES
 - IMPLEMENTING PROCESS AND CONTROL KNOWLEDGE
 - e.g., RETRIEVING LOAD INFORMATION
 - IMPLEMENTING PROBLEM-SOLVING KNOWLEDGE
 - e.g., SELECTING INDEPENDENT LOADS BASED ON GAINS
- PROBABILISTIC LOAD MODULE – ANLOAD (BATTELLE)

Figure 10.

LDEXPT: LOAD EXPERT SYSTEM

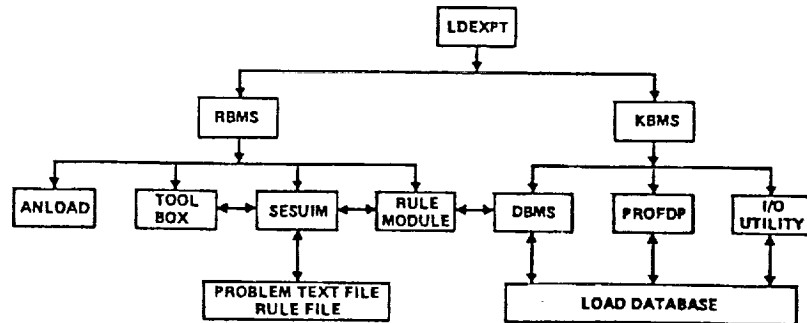


Figure 11.

PROBABILISTIC DESIGN ANALYSIS USING COMPOSITE LOADS SPECTRA (CLS)
COUPLED WITH PROBABILISTIC STRUCTURAL ANALYSIS METHODOLOGIES (PSAM)*524-39
19881J. F. NEWELL, K. R. RAJAGOPAL and H. HO
ROCKWELL INTERNATIONAL CORPORATION, ROCKETDYNE DIVISION

This paper discusses the application of the CLS to generate probabilistic loads for use in the PSAM nonlinear evaluation of stochastic structures under stress (NESSUS) finite element code. The CLS approach allows for quantifying loads as mean values and distributions around a central value rather than maximum or enveloped values typically used in deterministic analysis. NESSUS uses these loads to determine mean and perturbation responses. These results are probabilistically evaluated with the distributional information from CLS using a fast probabilistic integration (FPI) technique to define response distributions. The main example discussed describes a method of obtaining probabilistic (dependent) pressure, temperature and centrifugal steady state load descriptions and stress response of the second-stage turbine blade of the Space Shuttle main engine (SSME) high-pressure fuel turbopump (HPFTP). Additional information is presented on the on-going analysis of the high pressure oxidizer turbopump discharge duct (HPOTP) where probabilistic dynamic loads have been generated and are in the process of being used for dynamic analysis. Example comparisons of load analysis and engine data are furnished for partial verification and/or justification for the methodology.

Figure 1 depicts the component loading analysis. The description of the dependent random variables are obtained from a multilevel physical model that includes an engine system influence model and component load models of the turbine to describe the local conditions on the turbine blade. The independent loads are quantified at the appropriate model - engine or component - to best define the basic variables in the system, as well as maintain the required correlation between the dependent loads on the turbine blade. Both duty cycle and related probabilistic variations are accounted for in these models. The specific turbine blade model, Figure 2, is used both for part of the load modeling-thermal and pressure distribution - as well as the structural analysis. The structural model combines the loads with a probabilistic description of geometry, material property, and material orientations. The work herein discussed is an extension of the analysis performed under the PSAM contract where probabilistic loads were not considered.

Figure 3 is a cross section of the HPFTP turbine showing the overall configuration and the hot gas coolant network. The hot gas flow enters from the fuel preburner at 11 and discharges at 15. The second stage blade and rotor are between 14 and 15. Two geometric variations play a key role in the distribution of the coolant flow around the turbine blade, the interstage seal at 10 and the aft platform seal at 8.

The HPFTP turbine blade loads are dependent to the engine system level major component (turbine) dependent loads. The major component dependent loads are in turn dependent to a set of engine independent loads, including the engine operating parameter loads and the engine hardware parameter loads. A summary and categorization of these loads are listed in figure 4. The independent system level loads and hardware variations are in the first category listed. The major component dependent loads that are calculated in the engine model are the next level. The component level dependent loads are pressure, temperature and centrifugal. Additional local independent loads from the seals are internal to the turbine.

*Work performed under NASA Contract NAS3-24382

Probabilistic methods are built into these models and are described in the CLS discussion in this document. For this analysis, the Gaussian moment method was employed to illustrate the application of the probabilistic methodology. The pressure, temperature and centrifugal loads are correlated with higher level system independent loads. Theoretically, one could obtain correlation fields between pairs of the loads and then decompose them as part of the PSAM solution scheme. These fields are difficult to obtain and decompose. The marginal distribution method is used as a better solution to the load description and interface to the PSAM codes, Figure 5. Figure 6 outlines the process of generating the HPFTP turbine component loads marginal distribution.

At this time, validation of these loads is limited to the standard instrumentation available from engine tests. Pump speed and turbine discharge temperatures are regularly recorded as well as the independent loads at the pump interfaces. Figure 7 has typical plots of test data from a series of tests that can be used to estimate 2 sigma variations of independent loads. Figure 8 has typical dependent pump speed variations. A sample from a flight is also furnished of the 3 pump speeds at 104% power level. The variation in speeds are caused by a combination of hardware and duty cycle variations of primarily the low pressure oxidizer pump inlet pressure and the resulting cavitation of the HPOTP. Table 1 furnishes a correlation of calculated and measured variations of turbine speed and discharge temperature for both high pressure turbopumps. There is excellent correlation with speed and slightly poorer correlation with temperature. Part of the temperature error is attributed to instrumentation error that is not readily accounted for.

Table 2 summarizes the set of random variables, how they affect the structural model and their mean and standard deviation values. Figure 9 shows two points on the structural model where cumulative distributions of effective stress were calculated using NESSUS and FPI codes.

PSAM is performing a series of verification analysis on SSME hardware. CLS is being used to develop the loads for these analyses to furnish realistic input to PSAM and to demonstrate the integrated use of CLS and PSAM. Vibration loads for the HPOTP discharge duct, Figure 10, have been completed. This duct is attached to the HPOTP at two points, Zone G, and at the main injector (MI) at Zone A of the engine. The MI is part of a combustor that generates random vibrations. The pumps generate both random and sinusoidal loads. These vibration loads are dependent on power level of the engine and pump power and speed. The structure of the engine couples the responses of the components such that sinusoidals from the high pressure pumps are found throughout the engine at attenuated levels compared to the point where they are generated. Table 3 summarizes the 38 individual load components that are being applied to the duct. Figure 11 shows one of the six normalized PSD shapes used for the random loading. For this analysis, the random load composite has been modeled as a normalized shape that is scaled by G_{rms}^2 . The sinusoids are depicted in Figure 12. The frequencies generated by a pump are correlated to the synchronous speed, 1N. The 1N, 2N and 3N response levels are typically caused by rotor unbalance and rubbing or nonlinear effects. The 4N is caused by fluid loads on the four primary blades of the inducer. The variations are based on engine test data. The sinusoid amplitude mean levels are correlated with pump speed, but the standard deviation magnitudes are uncorrelated. The sinusoid level distribution is modeled as lognormal, see Figure 13. The variations of the sinusoidal magnitudes have a coefficient of variation of .5 to over 1.0. The high variations are roughly equally caused by component hardware variations and test to test variations. Figure 14 is a recent study of random composite levels coefficients of variations for several environments on the SSME. This information will be used in the development of generic dynamic physical load models.

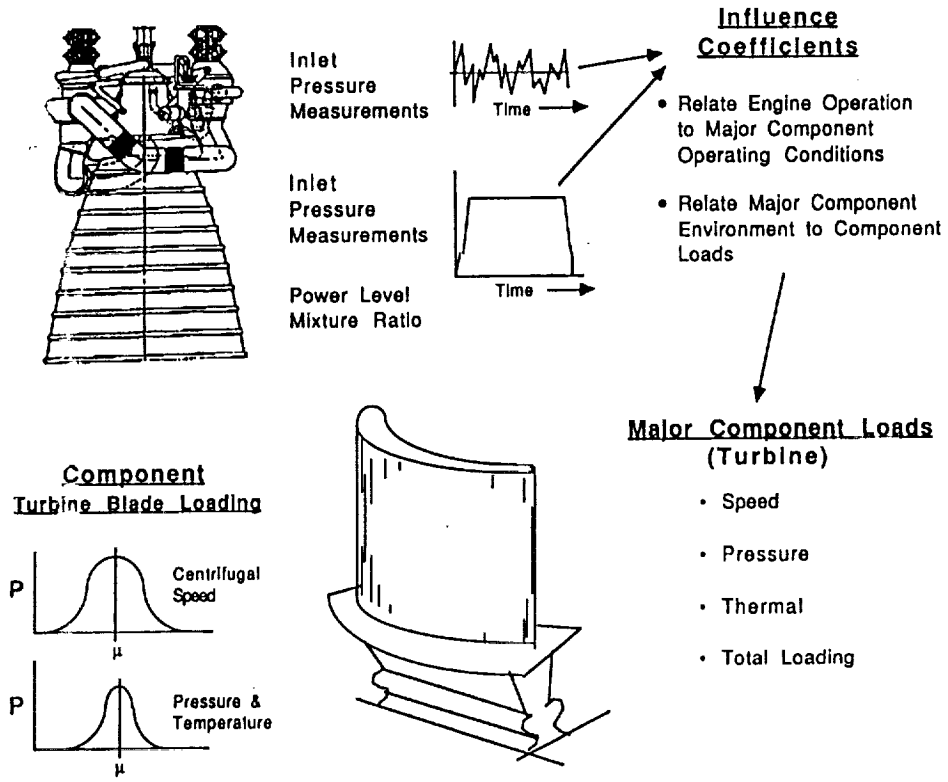


FIGURE 1. COMPONENT LOADS

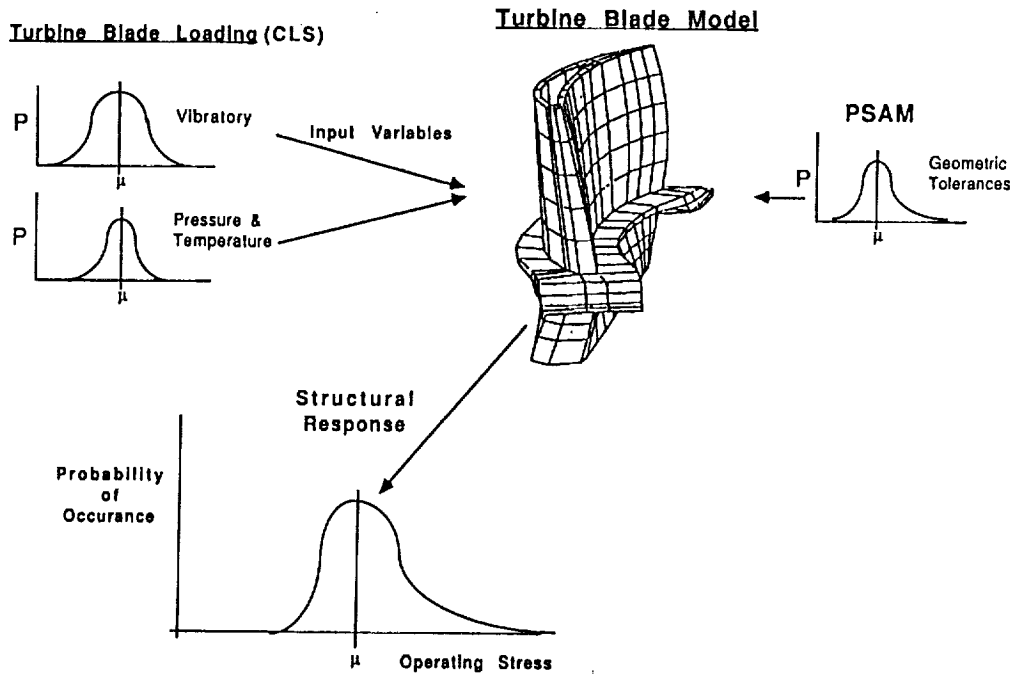


FIGURE 2. COMPONENT MODELS FOR LOADS AND STRUCTURAL ANALYSIS

ORIGINAL PAGE IS
OF POOR QUALITY

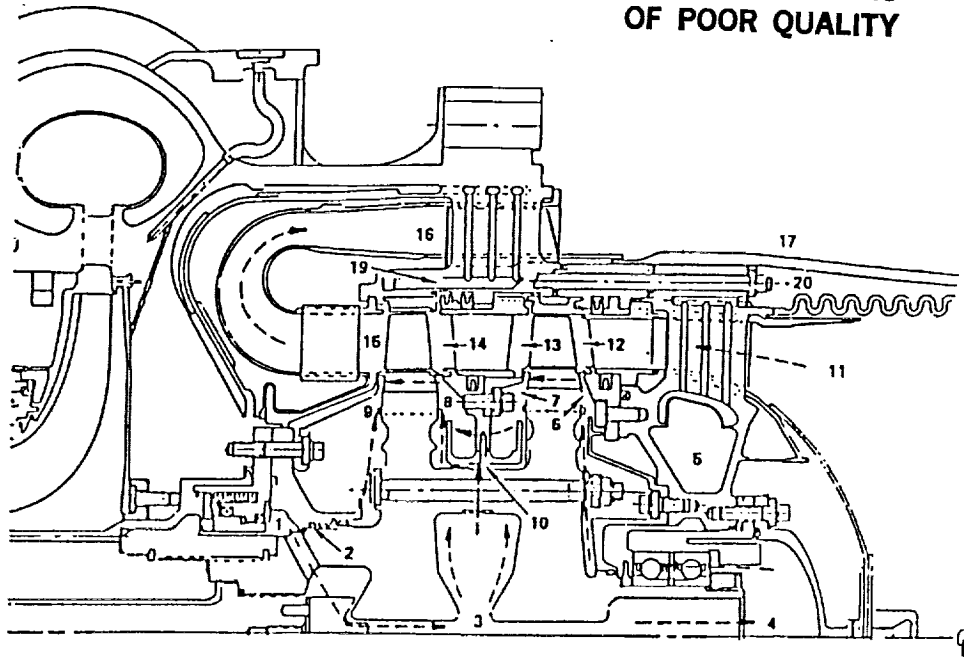


FIGURE 3. SSME HPFTP TURBINE HOT GAS AND COOLANT FLOW NETWORK

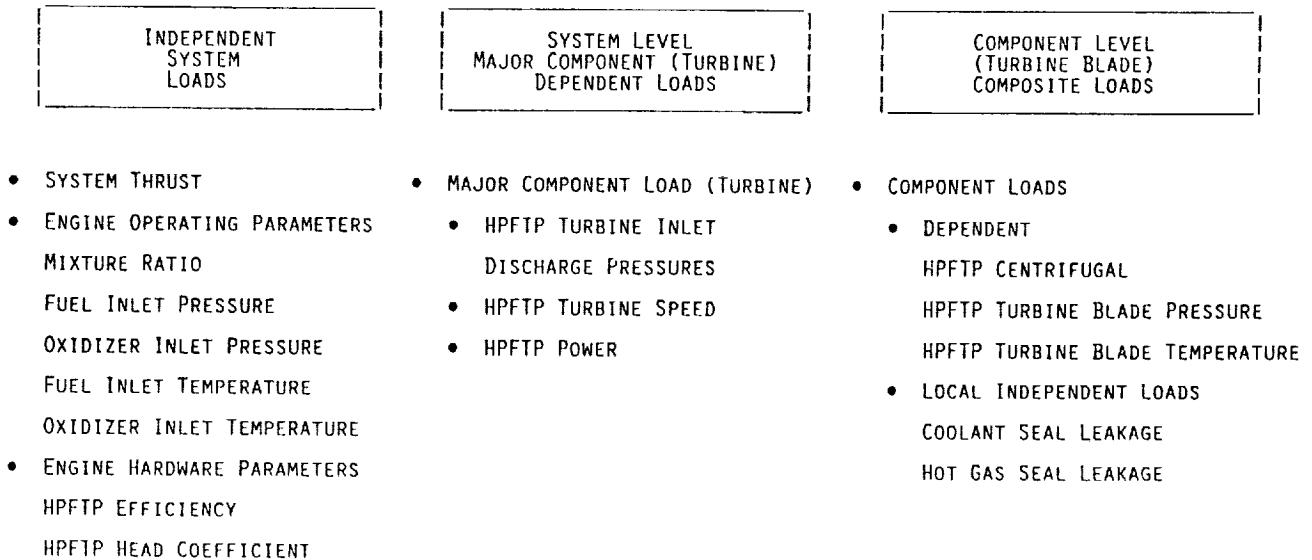


FIGURE 4. COMPOSITE LOADS OF THE HPFTP TURBINE BLADE
FOR THE PROBABILISTIC STRUCTURAL ANALYSIS

- PURPOSE:
 - PREPARING COMPOSITE LOADS FOR STRUCTURAL ANALYSIS.
 - MARGINAL DISTRIBUTION LOADS USED DIRECTLY AS INPUT TO PROBABILISTIC STRUCTURAL ANALYSIS CODES, E.G. NESSUS & FPI.
- ADVANTAGES:
 - MUCH SIMPLER THAN CORRELATION FIELD APPROACH.
 - CORRELATIONS TO THE ENGINE INDEPENDENT LOAD LEVEL AS REQUIRED.
 - DIRECTLY USABLE FOR PERTURBATION LOADING IN PSAM.
- DEFINITION:
 - MARGINAL DISTRIBUTION FOR A COMPONENT LOAD IS A DISTRIBUTION FOR THE COMPONENT LOADS WITH ONLY ONE INDEPENDENT LOAD VARYING AND THE REST OF THE INDEPENDENT LOADS STAYING CONSTANT.
 - FOR A LINEAR SYSTEM

$$\Delta Y = \sum_I B_I \Delta X_I$$

$$\sigma_{Y_I}^{\text{MARGINAL}} = |B_I| \sigma_{X_I}$$

$$\frac{\partial Y}{\partial X_I} = B_I = \frac{B_I}{|B_I|} \frac{\sigma_{Y_I}^{\text{MARGINAL}}}{\sigma_{X_I}}$$

FIGURE 5. MARGINAL DISTRIBUTION METHOD

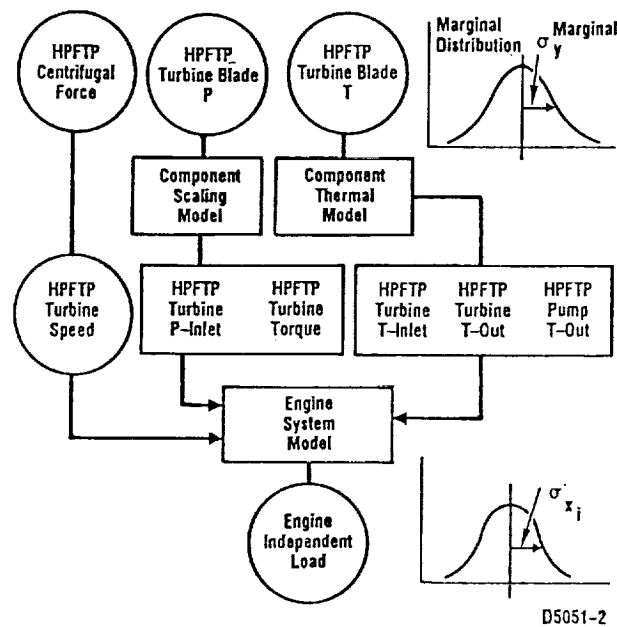
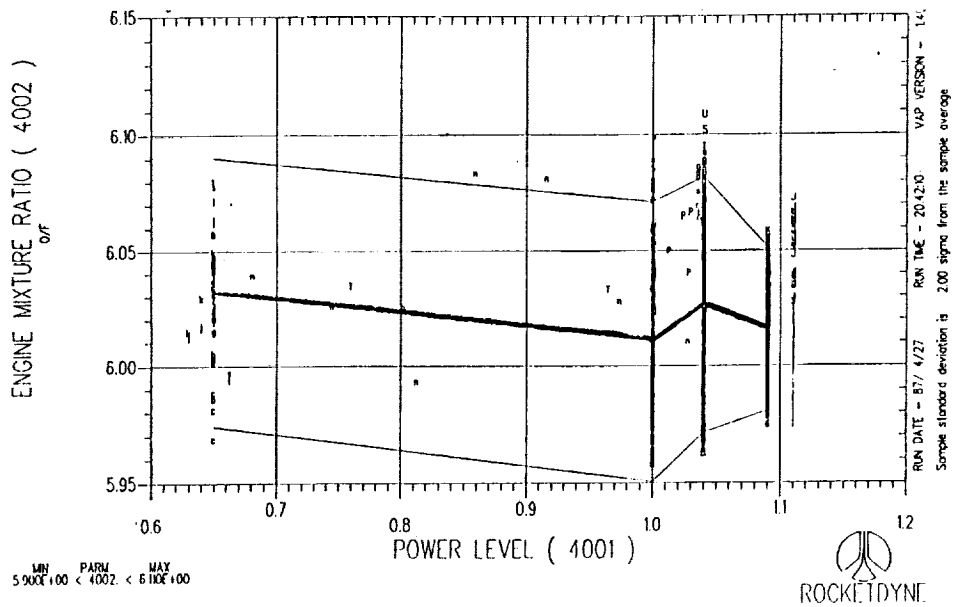
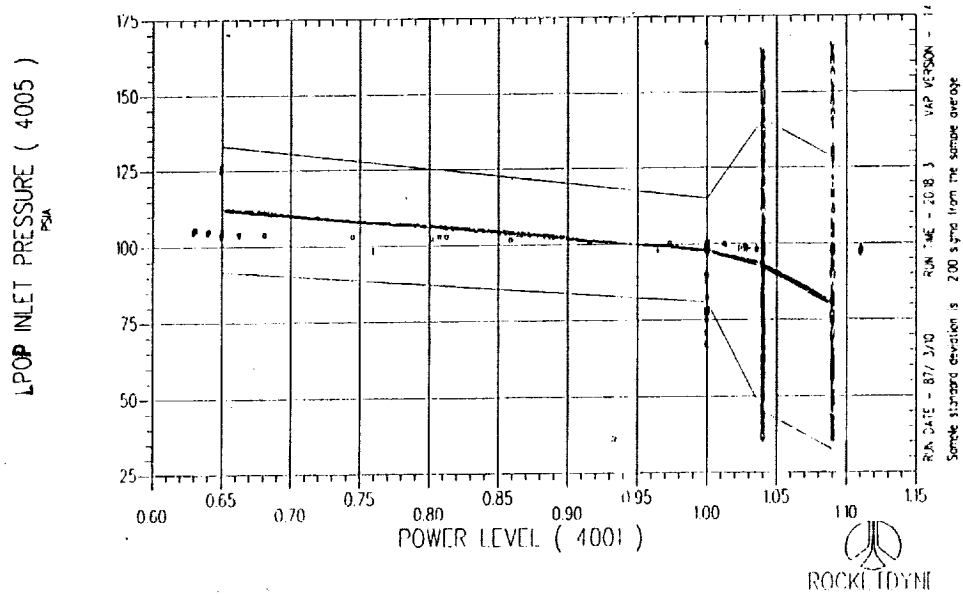


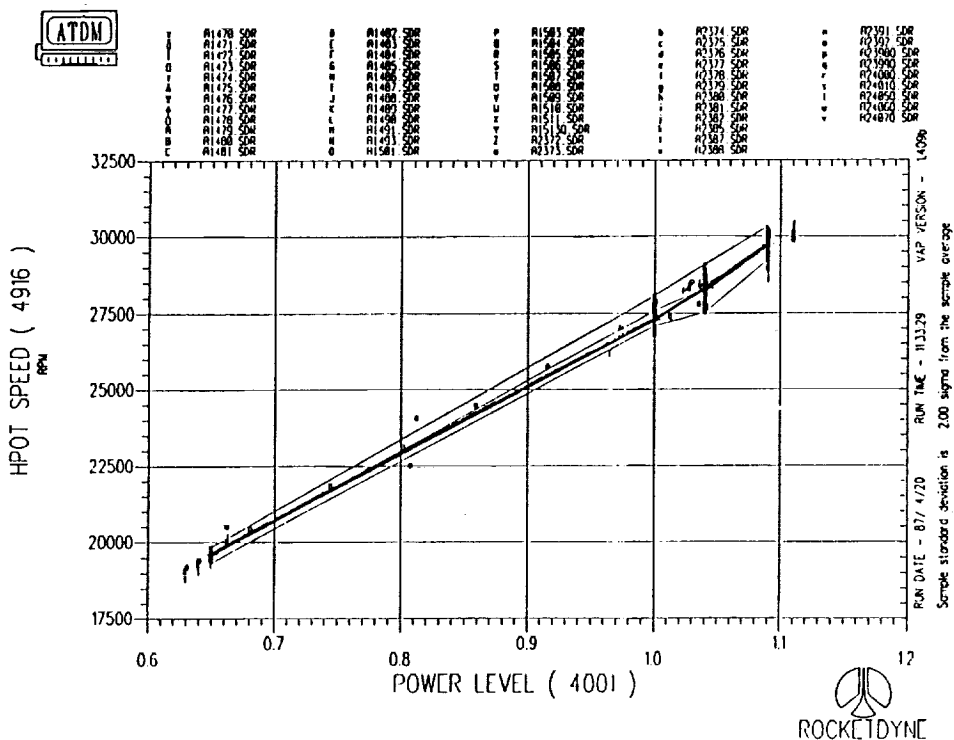
FIGURE 6. MARGINAL LOAD PROCESS



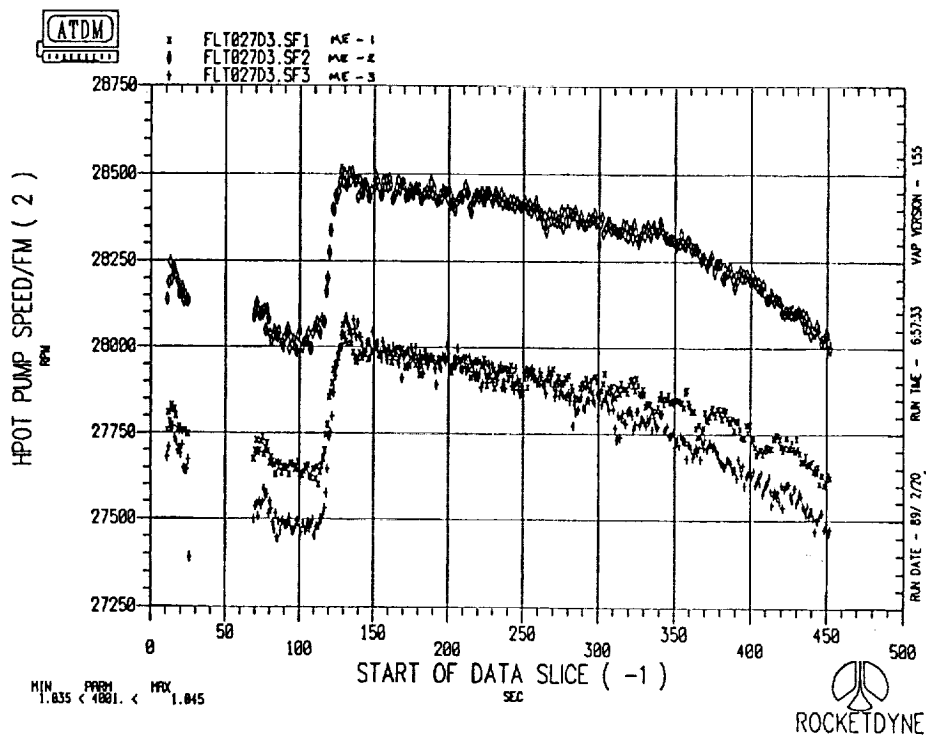
ORIGINAL PAGE IS
 OF POOR QUALITY

FIGURE 7. TYPICAL INDEPENDENT LOAD VARIATIONS
 FOR A PHASE II SSME SERIES OF TESTS

PHASE II TESTS



FLIGHT STS-27



ORIGINAL PAGE IS
OF POOR QUALITY

FIGURE 8. HIGH PRESSURE OXIDIZER TURBOPUMP SPEED

c-3

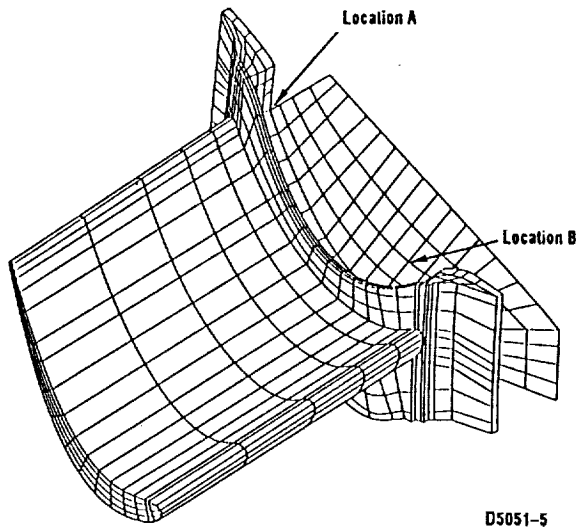
CONDITION	HPOTP				HPFTP			
	SPEED		TURBINE DISCHARGE TEMP		SPEED		TURBINE DISCHARGE TEMP	
	CALC (RPM)	MEASURED (RPM)	CALC °R	MEASURED °R	CALC (RPM)	MEASURED (RPM)	CALC °R	MEASURED °R
HARDWARE - 2σ RANDOM	294	----	53	----	388	----	65	----
TEST - 2σ RANDOM	210	----	157	----	396	----	20	----
TOTAL RANDOM	360	----	165	----	554	----	70	----
LOW NPSP - DET.	620	----	225	----	56	----	52	----
HIGH NPSP - DET.	-317	----	-219	----	-94	----	-62	----
RANGE = RANDOM + DET.	1660	1500	475	400	1260	1000	114	150
MAX	29090	29000	1630	1650	35742	35750	1740	1760
NOM	28100	----	1374	----	35130	----	1688	----
MIN	27430	27500	1155	1250	34482	34750	1625	1610

MEASURED -- MEASURED VARIATION FOR PHASE II TEST SET
 HARDWARE -- VARIATIONS IN ENGINE HARDWARE
 TEST -- INITIAL TEST CONDITIONS -- INLET TEMPERATURES AND MIXTURE RATIO
 DET. -- DUTY CYCLE EFFECTS OF INLET PRESSURES PLUS CORRELATED 2σ VARIATIONS OF CAVITATION

TABLE 1. CALCULATED VS. MEASURED VARIATIONS IN PUMP SPEED AND TEMPERATURE

RANDOM VARIABLE		TYPE	FEM QUANTITIES AFFECTED	MEAN	STANDARD DEVIATION
NO	DESCRIPTION				
1	MATERIAL AXIS ABOUT Z	MATERIAL AXIS VARIATIONS	MATERIAL	-0.087266 RADIANS	0.067544 RADIANS
2	MATERIAL AXIS ABOUT Y		ORIENTATION	-0.034907 RADIANS	0.067544 RADIANS
3	MATERIAL AXIS ABOUT X		ANGLES	+0.052360 RADIANS	0.067544 RADIANS
4	ELASTIC MODULUS	ELASTIC PROPERTY VARIATIONS	ELASTIC CONSTANTS	18.38E6 KSI	0.4595E6 KSI
5	POISSON'S RATIO			0.386	0.00965
6	SHEAR MODULUS			18.63E6 KSI	0.46575E6 KSI
7	GEOMETRIC LEAN ANGLE ABOUT X	GEOMETRY VARIATIONS	NODAL COORDINATES	0.0	0.14 DEGREES
8	GEOMETRIC TILT ANGLE ABOUT Y			0.0	0.14 DEGREES
9	GEOMETRIC TWIST ANGLE ABOUT Z			0.0	0.30 DEGREES
10	MIXTURE RATIO LIQUID HYDROGEN/ LIQUID OXYGEN	INDEPENDENT LOAD		6.00	0.02
11	FUEL INLET PRESSURE	VARIATIONS	PRESSURE	30.00 psia	5.00
12	OXIDIZER INLET PRESSURE	DEPENDENT LOADS ARE	TEMPERATURE	100.00 psia	26.00
13	FUEL INLET TEMPERATURE	TURBINE BLADE	CENTRIFUGAL	38.5° R	0.5
14	OXIDIZER INLET TEMPERATURE	PRESSURE TEMPERATURE	LOAD	167.0° R	1.33
15	HPFP EFFICIENCY	AND SPEED		1.00	0.008
16	HPFP HEAD COEFFICIENT			1.0237	0.008
17	COOLANT SEAL LEAKAGE FACTOR	LOCAL		1.00	0.1
18	HOT GAS SEAL LEAKAGE FACTOR	GEOMETRY FACTORS	TEMPERATURE	1.0	0.5

TABLE 2. LIST OF 2nd STAGE BLADE RANDOM VARIABLES



D5051-5

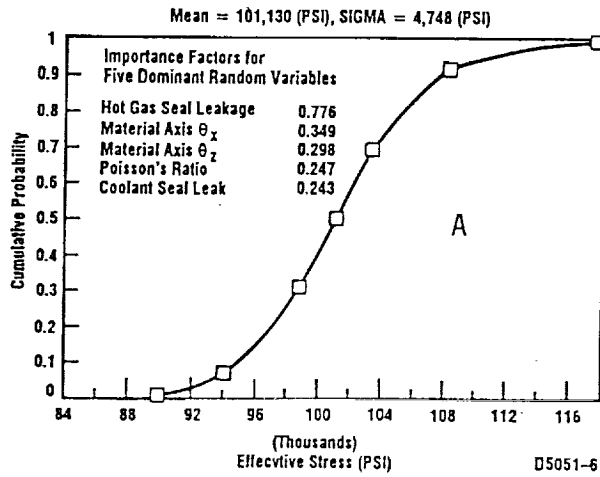
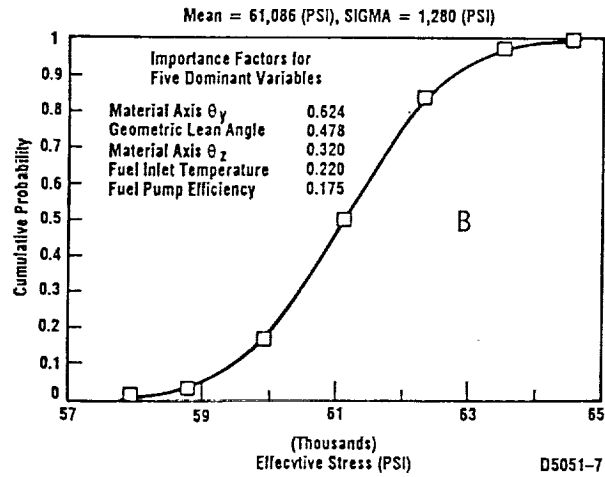


FIGURE 9. STRESS RESPONSE FOR HPFTP TURBINE BLADE

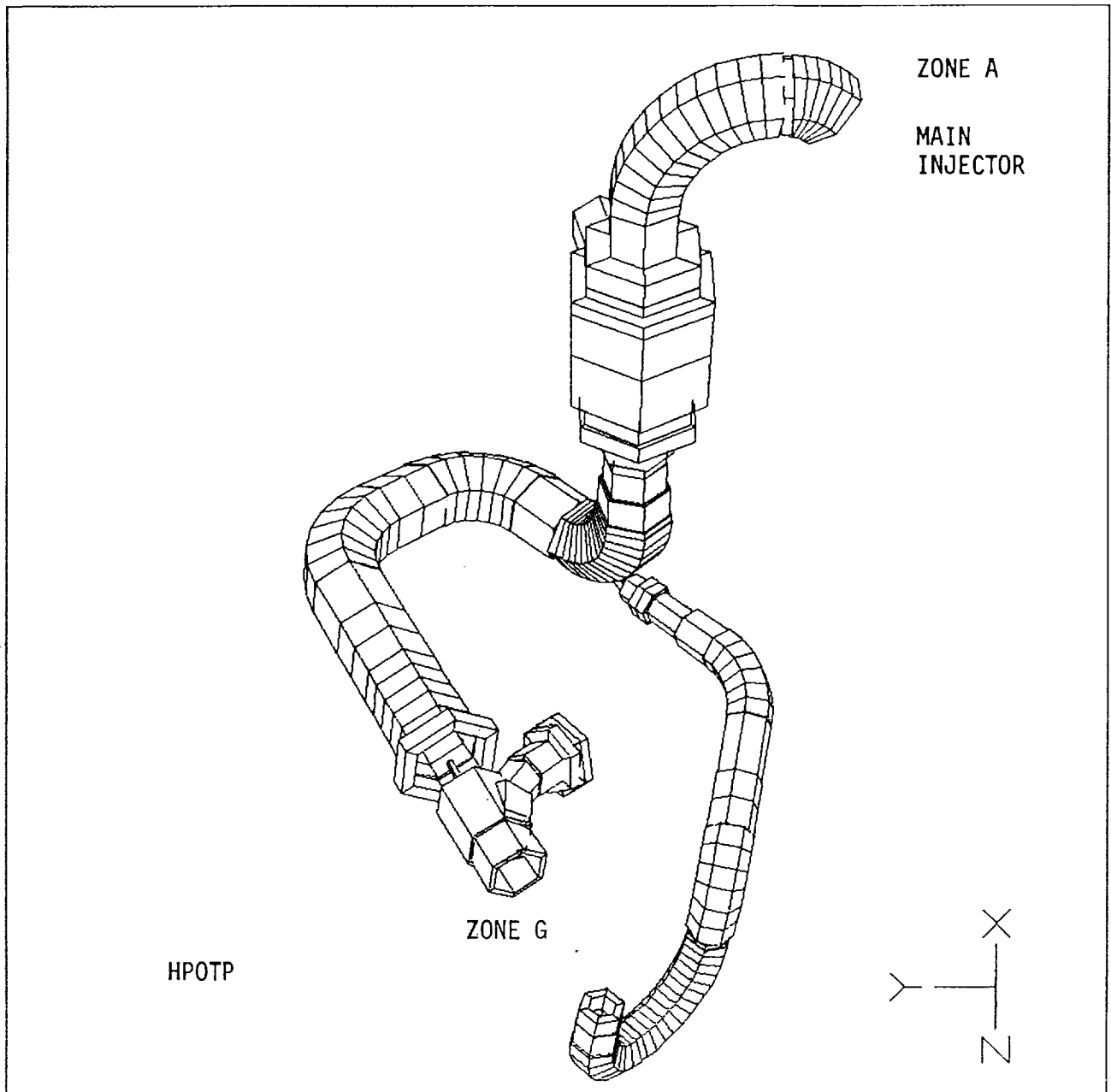


FIGURE 10. HPOTP DISCHARGE DUCT

SEQUENTIAL NO.	RANDOM VARIABLE DESCRIPTION	MEAN	ST. D.	COV
1)	ZONE G - X AXIS, PSD	222.0	163.0	0.73
2)	ZONE G - Y AXIS, PSD	73.5	59.4	0.808
3)	ZONE G - Z AXIS, PSD	73.5	59.4	0.808
4)	ZONE A - X AXIS, PSD	22.5	4.5	0.20
5)	ZONE A - Y AXIS, PSD	54.0	10.8	0.20
6)	ZONE A - Z AXIS, PSD	69.5	13.9	0.2
7)	OXIDIZER PUMP SPEED	2940.53	41.167	0.014
8)	FUEL PUMP SPEED	3707.08	37.07	0.01
9)	DAMPING	0.033	.005	0.15
	ZONE A OXIDIZER TURBOPUMP			
	OXIDIZER PUMP SINE AMPLITUDES			
10)	X DIRECTION 1N	.30	.120	0.4
11)	2N	0.30	.045	0.15
12)	4N	1.5	.45	0.3
13)	Y DIRECTION 1N	0.60	0.30	0.5
14)	2N	0.70	0.28	.40
15)	4N	2.6	.78	.3
16)	Z DIRECTION 1N	0.5	.225	0.45
17)	2N	0.70	.140	0.20
18)	4N	0.70	.140	.20
	FUEL PUMP SINE AMPLITUDES			
19)	X DIRECTION 1N	.35	1.050	.3
20)	Y DIRECTION 1N	0.80	0.280	0.35
21)	Z DIRECTION 1N	1.20	0.96	0.3
	ZONE G - MAIN INJECTOR			
	OXIDIZER TURBOPUMP			
	SINE AMPLITUDES			
22)	X DIRECTION 1N	1.35	1.35	1.0
23)	2N	1.50	0.75	0.5
24)	3N	1.10	0.495	0.45
25)	4N	11.0	2.75	0.25
26, 27)	X-Y DIRECTION 1N	1.9	1.71	0.9
28, 29)	2N	1.6	0.96	0.6
30, 31)	3N	0.75	.225	0.3
32, 33)	4N	5.5	3.30	0.6
	FUEL PUMP SINE AMPLITUDES			
34)	X DIRECTION 1N	0.65	0.2275	0.35
35, 36)	X-Y DIRECTION 1N	0.45	1.35	.3
37, 38)	Y-Z DIRECTION 2N	0.45	0.180	.4

- Note: 1) P.S.D. units are in G^2
2) Pump Speed units are in Radians/SCE
3) Sinusoidal amplitude units are in GRMS

TABLE 3. BASIC RANDOM VARIABLES AND THEIR STATISTICS (INPUT)

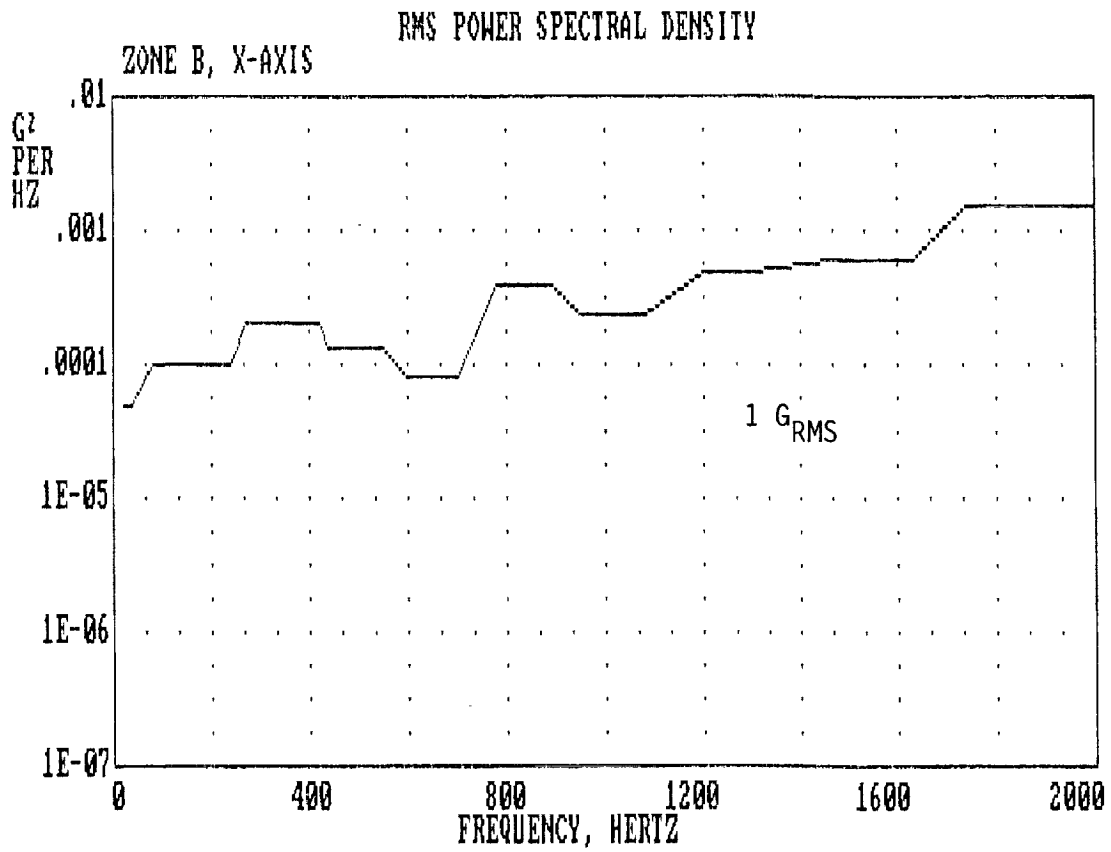


FIGURE 11. TYPICAL NORMALIZED PSD

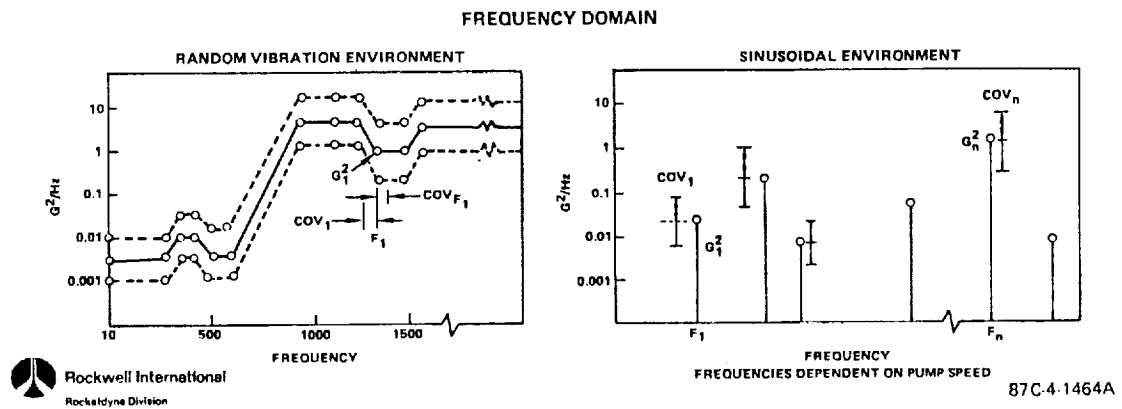


FIGURE 12. RANDOM AND SINUSOIDAL VIBRATION

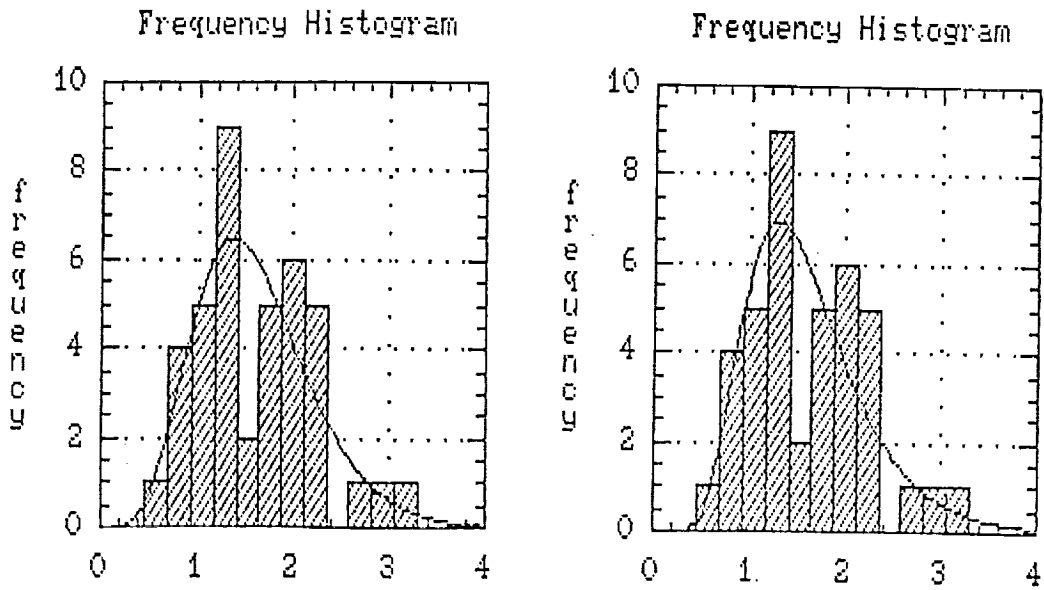


FIGURE 13. HPOTP SYNCHRONOUS MAGNITUDE DISTRIBUTION AT CONSTANT POWER

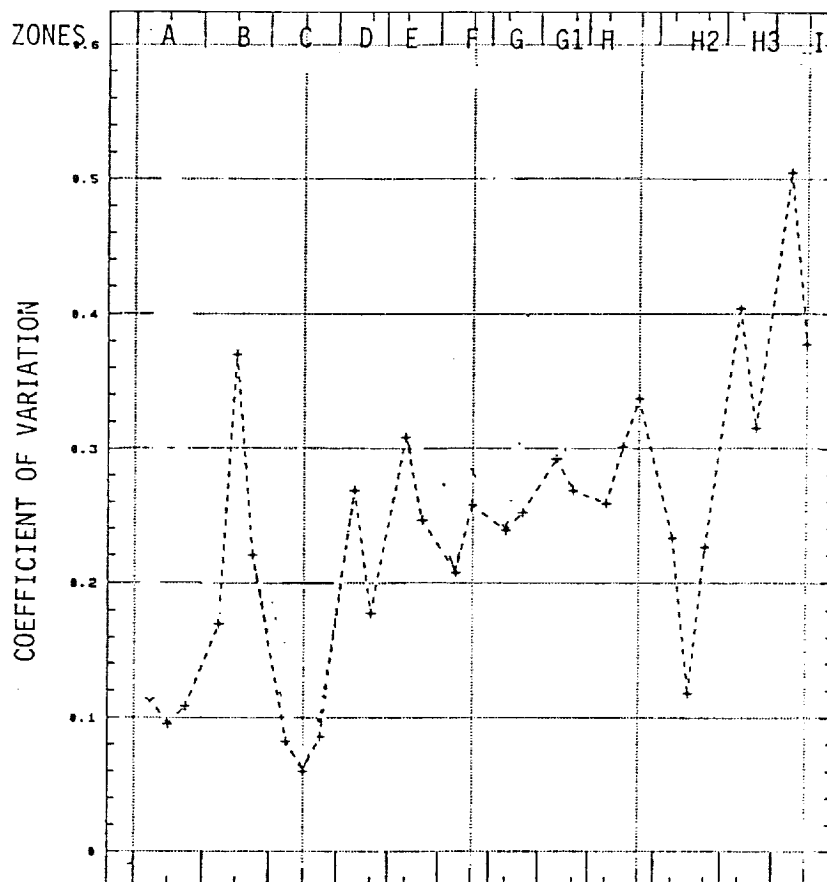


FIGURE 14. SSME ZONAL VIBRATION COMPOSITE GRMS COEFFICIENTS OF VARIATION

PROBABILISTIC FINITE ELEMENTS FOR FRACTURE AND FATIGUE ANALYSIS

W.K. Liu, T. Belytschko, M. Lawrence, and G.H. Besterfield
Department of Mechanical Engineering
Northwestern University
Evanston, Illinois

The fusion of the probabilistic finite element method (PFEM) and reliability analysis for probabilistic fracture mechanics (PFM) is presented. The authors have developed a comprehensive method for determining the probability of fatigue failure for curved crack growth. The criterion for failure or performance function is stated as: the fatigue life of a component must exceed the service life of the component; otherwise failure will occur. An enriched element that has the near crack-tip singular strain field embedded in the element is used to formulate the equilibrium equation and solve for the stress intensity factors at the crack-tip. The crack growth law (e.g., Paris law) and crack direction law (e.g., direction which gives rise to the maximum tangential stress at the crack-tip) are also incorporated into the formulation. The loading is mixed-mode (i.e., opening mode and in-plane shear mode which are designated mode I and mode II, respectively) with randomness in the applied loads, material properties, component geometry, crack geometry, crack growth law, and the crack direction law. Examples of random crack geometry are the initial and final crack lengths, initial crack angle, and initial crack position. The methodology consists of calculating the reliability index, which is used to calculate the first-order probability of failure, by solving a constrained optimization problem. Included in the optimization for reliability is the equilibrium equation for stress intensity factors, the crack growth law, and the crack direction law.

Performance and accuracy of the method is demonstrated on a classical mode I fatigue problem. The initial and final crack lengths, material parameters in the Paris law,

and the applied stress are modeled with random variables. The results imply that the service life of a component must be well below the deterministic fatigue life of the component when many parameters are considered random. The fusion of PFEM and reliability for fatigue crack growth is computationally quite efficient and provides a powerful tool for the design engineer.

SCOPE OF WORK

Probabilistic Finite Element Method (PFEM)

- Uncertainties
 - Random Load
 - Random Material Properties
 - Random Geometry
- Statics and Dynamics
- Elasticity and Nonlinear Elasticity

Brittle Fracture by PFEM

- Probability of the Stress Intensity Factor exceeding the Fracture Toughness of the Material

$$P (\kappa_I > \kappa_{Ic})$$
$$P (G > G_c)$$

Fatigue Crack Growth by PFEM

- Probability of the Desired Service Life exceeding the Fatigue Life

$$P (T_s > T)$$

INTRODUCTION

Probabilistic Fracture Mechanics (PFM)

- Model the crack-tip singularity in stress.
- Determine statistics of stress intensity factors.
- Probability of fracture and fatigue failure.

Uncertainties which need to be considered in PFM are:

- Random load, material properties, and geometry;
- Random crack geometry;
 - length,
 - location,
 - orientation,
- Random crack growth laws;
- Random crack direction laws;
- Random correlation among detectable cracks and micro-cracks.

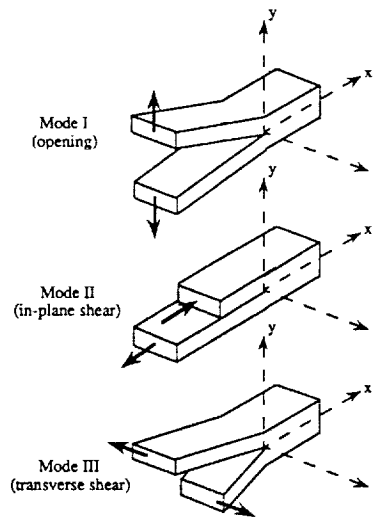
RELIABILITY OF COMPONENTS SUBJECT TO FATIGUE CRACK GROWTH BY PROBABILISTIC FINITE ELEMENTS

METHODOLOGY AND OBJECTIVE

- Given :
 - Component with Crack Subject to Cyclic Stress
 - Method for Determining Stress Intensity Factors
 - Crack Growth Law
 - Crack Direction Law
- With Randomness in :
 - Applied Loads
 - Component Geometry
 - Crack Geometry
 - Crack Direction Parameters
 - Crack Growth Parameters
 - Material Properties
- Determine Probability of Fatigue Failure
 - Probability that the desired service life is greater than the fatigue life.

$$P (T_s > T)$$

STRESS INTENSITY FACTOR



κ_I = mode I stress intensity factor
 κ_{II} = mode II stress intensity factor
 κ_{III} = mode III stress intensity factor

Consider only Modes I and II: $\kappa = \begin{bmatrix} \kappa_I \\ \kappa_{II} \end{bmatrix}$

RANDOM VARIABLES

System Uncertainties

- Applied Loads
- Component Geometry
length, height, width, etc.
- Crack Geometry
length, orientation, position
- Crack Direction Parameters
- Crack Growth Parameters
- Material Properties
elastic modulus, poisson's ratio,
fracture toughness, etc.,

Modeled by a correlated random variable vector

$$\mathbf{b} \ (q \times 1)$$

Transform \mathbf{b} to a Independent Standard Normal Random Variable Vector

$$\mathbf{r} \ (q \times 1)$$

- Eigenvalue Orthogonalization (Normal R.V.'s)
Covariance Matrix for \mathbf{b}
- Rosenblatt Transformation (Non-normal R.V.'s)
Joint Probability Distribution for \mathbf{b}

RELIABILITY ANALYSIS

Performance Function or Margin of Safety

$$\begin{array}{ccc} g > 0 & g = 0 & g < 0 \\ \text{safe state} & \text{limit-state} & \text{failure state} \end{array}$$

Probability of Failure

$$p_f = P(g \leq 0)$$

First-Order Estimate of the Probability of Failure

$$p_{f1} \approx \Phi(-\beta)$$

Φ is the standard normal cumulative distribution,
 β is the reliability index.

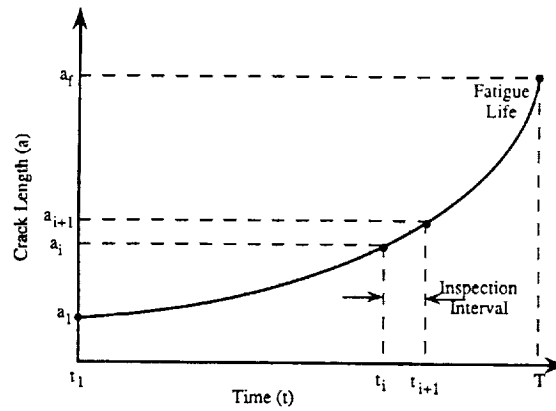
Reliability Index

Minimum Distance from Limit-State Surface to
Origin in Independent Standard Normal Space

$$\beta^2 = \sqrt{\mathbf{r}^T \mathbf{r}}$$

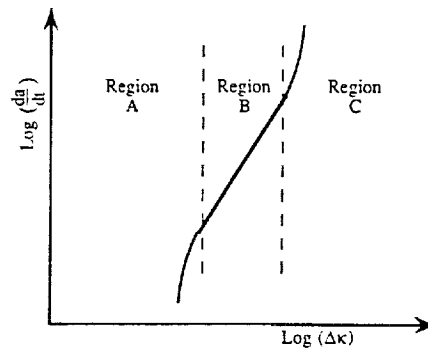
CRACK GROWTH LAW

Experimental fatigue crack growth data for different materials.



$$\frac{da}{dt} = f(\Delta\kappa_{eq})$$

$\Delta\kappa_{eq}$ is equivalent stress intensity factor range



Region A: A sufficient level of activity at the crack-tip has not been attained resulting in very slow crack growth.

Region C: Corresponds to rapid unstable crack growth.

Region B: Represents the zone where most fatigue crack growth is analyzed.

Paris Law: $\frac{da}{dt} = D (\Delta\kappa_{eq})^n$

D is a material parameter
n is a material parameter

Integrating from the initial crack length to the final crack length gives in the fatigue life

$$T = \int_{a_1}^{a_f} \frac{da}{D (\Delta\kappa_{eq})^n}$$

Equivalent Stress Intensity Factor

- Maximum Stress Theory

$$\kappa_{eq} = \Theta^T \kappa$$

$$\Theta = \cos^2\left(\frac{\theta}{2}\right) \begin{bmatrix} \cos \frac{\theta}{2} \\ -3 \sin \frac{\theta}{2} \end{bmatrix}$$

CRACK DIRECTION LAW

- Maximum Tangential Stress Criterion
- Minimum Strain Energy Density Criterion
- Maximum Energy Release Rate Criterion

Maximum Tangential Stress Criterion

- Crack grows in a radial direction from the crack
 - Crack grows in the plane perpendicular to the direction of maximum tension
- ∴ Crack grows in the direction where the tangential stress is a maximum and the shear stress is zero.

$$Z(\kappa, \theta) \equiv \Phi^T \kappa = 0$$

$$\Phi = \begin{bmatrix} \sin \theta \\ 3 \cos \theta - 1 \end{bmatrix}$$

For mode I fracture, $\theta = 0^\circ$ and is constant

For mode II is fracture, $\theta = 70.54^\circ$ and changes

PERFORMANCE FUNCTION FOR FATIGUE

Basis for determining the reliability and/or probability of failure depends on the choice of a performance function.

$$p_f = P(g \leq 0)$$

Performance function for fatigue crack growth

$$g = T - T_s$$

T_s is the desired service life

T is the fatigue life

The component fails when the fatigue life is less than the desired service life.

DISCRETIZATION

Discretize the Crack Path into "nint" Integration Points

- Crack Length

$$a_i = \frac{1}{2} [(a_f - a_i) \xi_i + (a_f + a_i)] \quad i = 1, \dots, \text{nint}$$

- Crack Growth Law

$$T = \int_{-1}^{+1} \frac{J}{D (\kappa_{eq})^n} d\xi \quad J = \frac{da}{d\xi}$$

- Crack Direction Law

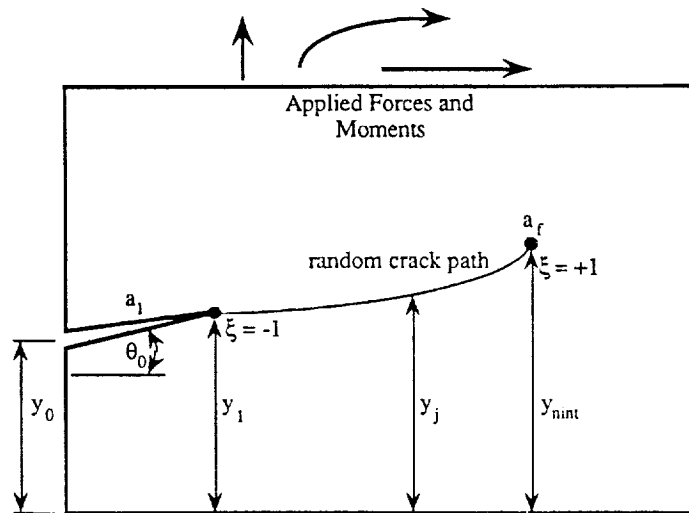
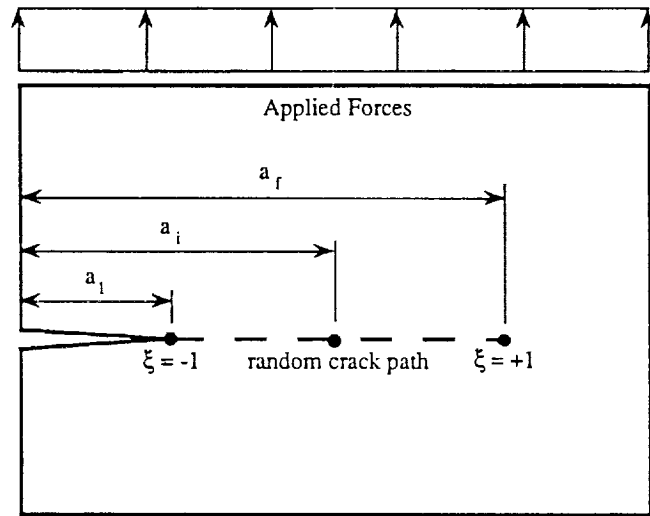
$$Z_k = \Phi_k^T \kappa_k = 0 \quad k = 1, \dots, \text{nint}$$

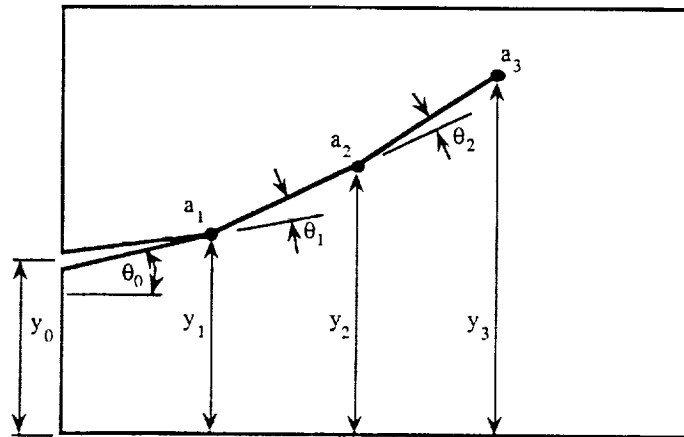
Crack direction is calculated at each integration point
Crack grows to the next integration point

- Equilibrium

$$K_i \delta_i = f_i \quad i = 1, \dots, \text{nint}$$

$$\delta_i = \begin{bmatrix} d \\ \kappa \end{bmatrix}_i$$





RELIABILITY AS AN OPTIMIZATION PROBLEM
FOR FATIGUE CRACK GROWTH

First-Order Probability of Failure

→ Reliability Index

→ Constrained Optimization Problem

Minimize the Reliability Index

$$\beta^2 = \sqrt{r^T r}$$

Subject to Equality Constraints

Crack growth direction law

$$Z_k = 0 \quad k = 1, \dots, nint$$

Equilibrium

$$K_i \delta_i = F_i \quad i = 1, \dots, nint$$

Subject to Inequality Constraint

Limit-State Surface and Failure State

$$T - T_s \leq 0$$

Define a Lagrange Functional

$$\begin{aligned} \mathcal{L} & (\mathbf{b}, \mu_1, \dots, \mu_{nint}, \delta_1, \dots, \delta_{nint}, \alpha, \lambda, \\ & \quad \varphi_1, \dots, \varphi_{nint}, \theta_1, \dots, \theta_{nint}) \\ & = \beta^2 + \sum_{i=1}^{nint} \mu_i^T [F_i - K_i \delta_i] \\ & \quad + \sum_{k=1}^{nint} \varphi_k [Z_k = 0] \\ & \quad + \lambda \{T - T_s + \alpha^2\} \end{aligned}$$

Necessary Conditions
(derivatives w.r.t. independent variables)

Probabilistic Finite Element Method
(PFEM)

Eliminate Lagrange Multipliers

Final Form of Optimization for Reliability

$$L^\beta + \lambda L^g = 0$$

$$L^\beta = \frac{\partial \beta^2}{\partial \mathbf{b}}$$

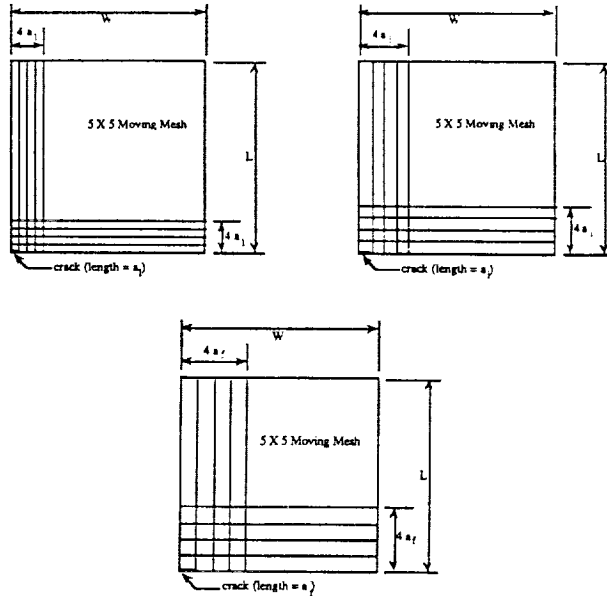
$$\begin{aligned} L^g & = \sum_{i=1}^{nint} \left[\sum_{k=1}^i \left(\frac{T, \theta_k}{(Z_k), \theta_k} (Z_k), \kappa_i \right) + T, \kappa_i \right] \frac{\partial \kappa_i}{\partial \mathbf{b}} \\ & \quad + \sum_{k=1}^{nint} \left(\frac{T, \theta_k}{(Z_k), \theta_k} (Z_k), \mathbf{b} \right) + T, \mathbf{b} \end{aligned}$$

Solve for \mathbf{b} via an Optimization Algorithm

- Lagrange Multipliers
- Gradient Projection Algorithm
- HL-RF Algorithm (Tangent Matching)
- Modified HL-RF Algorithm

CRACK GROWTH MOVING MESH

- Variation of ALE formulation
Pseudo-Static (neglect transport term)
- Moving Element Mesh with Constraints
Aspect ratio of elements must remain one



EXAMPLE

Single-Edged Cracked Plate with an Applied Load

$$\mathbf{b} = [a_i, a_f, D, n, \sigma]^T$$

a_i is the initial crack length

a_f is the final crack length

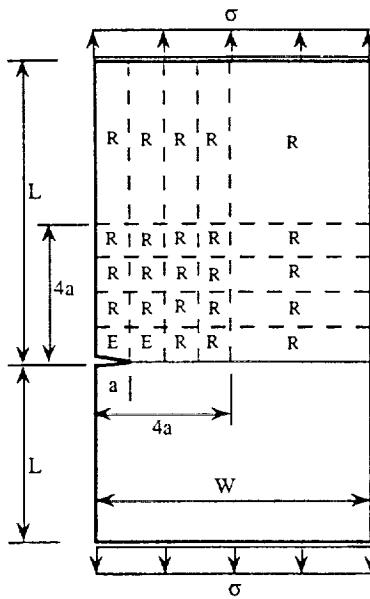
D is a material parameter

n is a material parameter

σ is the applied stress

Parameter	Mean	Standard Deviation	Percent
Length (L)	10.0 in	0.0	0.0
Width (W)	4.0 in	0.0	0.0
Thickness (t)	1.0 in	0.0	0.0
Young's Modulus (E)	30,000.0 ksi	0.0	0.0
Poisson's Ratio (ν)	0.3	0.0	0.0
Applied Stress (σ)	12.0 ksi	3.0 ksi	25.0
Initial Crack Length (a_i)	0.01 in	0.01 in	100.0
Final crack Length (a_f)	0.1 in	0.01 in	10.0
Fatigue Parameter (D)	1.0×10^{-10}	3.0×10^{-11}	30.0
Fatigue Parameter (n)	3.25	0.08	2.5

- Variations in the parameters are reasonable.
- $n_{int} = 50$
- Deterministic fatigue life, $T = 7,500,000$ cycles

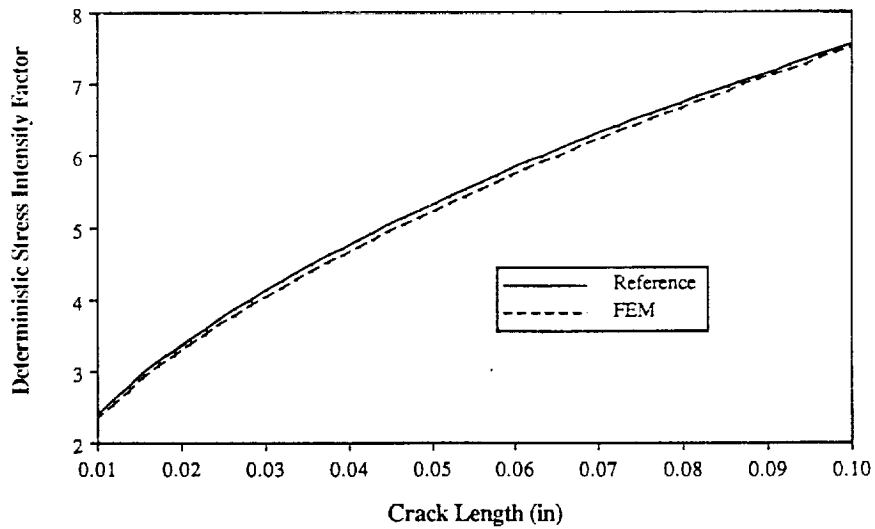


Reference Solution

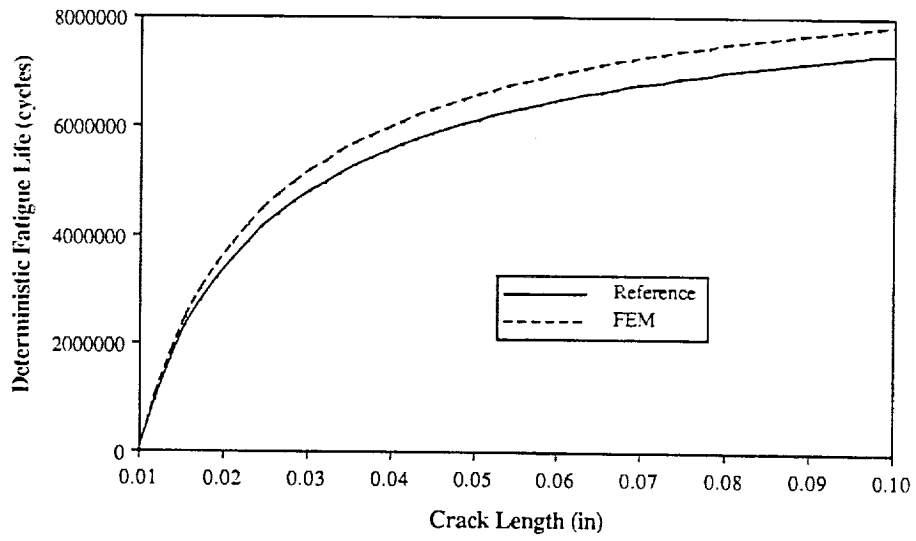
$$\kappa_I = \gamma \sigma \sqrt{a}$$

$$\gamma = 1.99 - 0.41 \frac{a}{W} + 18.7 \left(\frac{a}{W}\right)^2 - 38.48 \left(\frac{a}{W}\right)^3 + 53.85 \left(\frac{a}{W}\right)^4$$

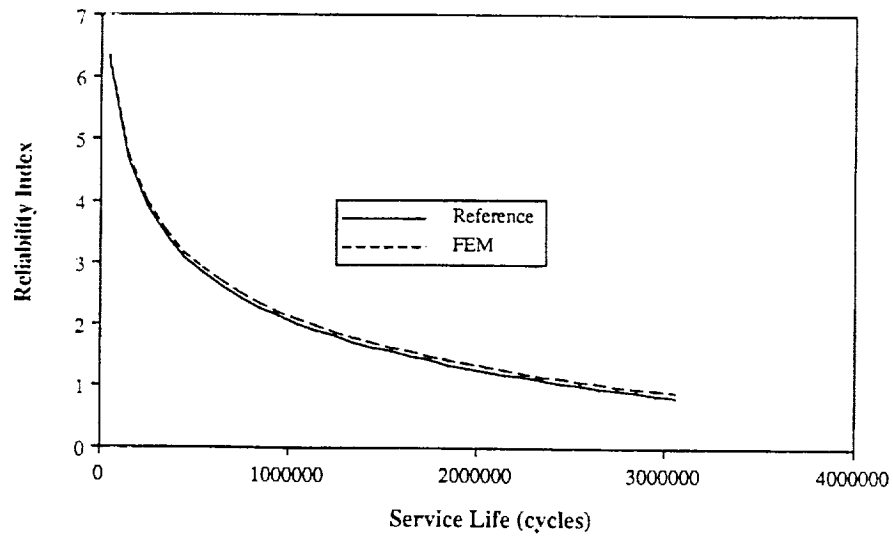
Deterministic Stress Intensity Factor for Reference and FEM Solutions



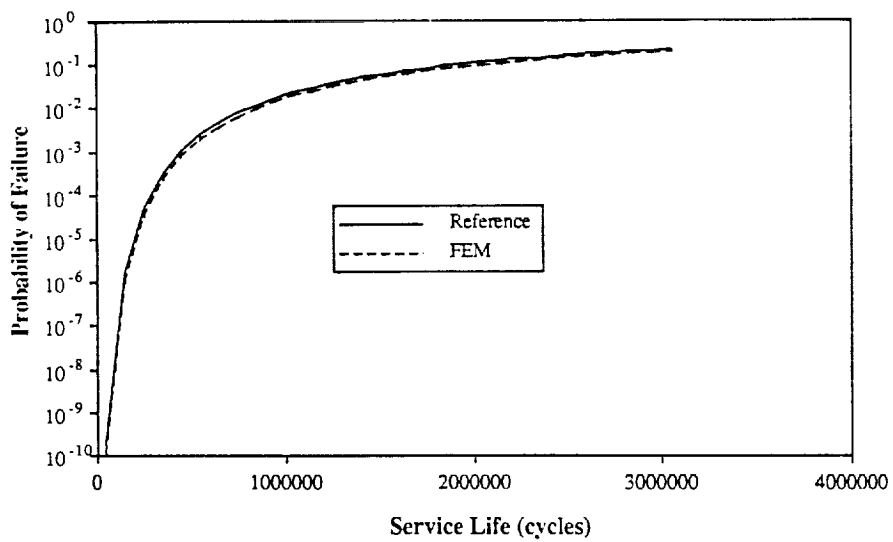
Deterministic Fatigue Life for Reference and FEM Solutions



Reliability Index for Combined Randomness



Probability of Failure for Combined Randomness





PROBABILITY OF FAILURE AND RISK ASSESSMENT
OF PROPULSION STRUCTURAL COMPONENTS526-39
19883

Michael C. Shiao
NASA Lewis Research Center Group
Sverdrup Technology, Inc.
Cleveland, Ohio

ABSTRACT

The probabilistic structural analysis method (PSAM) has been developed to analyze the effects of fluctuating loads, variable material properties, and uncertain analytical models especially for high performance structures such as SSME turbopump blades. In the deterministic approach, uncertainties in the responses were not quantified and the actual safety margin remains unknown. Risk is calculated after expensive service experience. However, probabilistic structural analysis provides a rational alternative method to quantify uncertainties in the structural performance and the durability. NESSUS (Numerical Evaluation of Stochastic Structures Under Stress) has been developed by SwRI under the PSAM research project sponsored by NASA Lewis. It is a probabilistic structural analysis computer code which integrates finite element methods and reliability algorithms, capable of predicting the probability distributions of structural response variables such as stress, displacement, natural frequencies, and buckling loads etc. In the design and analysis practice, it is also important to assess the risk associated with a new or existing structure for safety or serviceability consideration. Probable failure criteria should be identified for different structures due to various structural functions. For example, failure events such as stress greater than strength or the displacement exceeds maximum allowable are often used for the reliability assessment. Probability of occurrence of those failure events can be determined once the probability distributions of the stress or displacement are calculated by NESSUS.

In undertaking a reliability/risk analysis, all suspected sources in uncertainties should be taken into account in order to control the probability of failure in service environments within an acceptable range. Reliability and risk obtained by a probabilistic structural analysis can be useful in evaluating the traditional design, setting quality control requirements and inspection intervals. It can also be used to identify candidate material and design concepts in the absence of technology base. In this presentation, a risk/cost assessment and a reliability analysis using NESSUS with a generic probabilistic material model is described.

The risk assessment includes the initial cost and the cost due to failure. The initial cost is defined as the cost for component service readiness which can be a function of several key design variables. The consequential cost is the cost incurred due to failure. Total cost is the sum of initial cost and a fraction of consequential cost. The fraction is weighted by the probability of failure. Since the lower initial cost is often associated with higher risk for the structural failure, higher initial cost

will normally reduce the risk. How to minimize the total cost for an acceptable structural reliability/risk is also described in this presentation.

In previous studies, probability distributions of material properties such as Young's modulus, thermal expansion coefficient, and material strength were assumed. In the present study, a generic probabilistic material model is incorporated in NESSUS. The assumption for this model is that the probability distributions of material properties are simulated by using primitive random variables. These variables can be temperature, stress, fatigue cycles, etc. The model is especially attractive for the structures under high temperature environments. A risk analysis of an SSME blade is performed under this concept. Since the material properties are functions of stress, yet stress is a function of material properties in an implicit way, an iterative procedure is necessary to obtain a convergent solution for stress and material properties. During the iteration process, the joint cumulative distribution functions of nodal stresses are required in order to apply the generic probabilistic material model. It is found that only a few iterations are needed for a converged result. From this analysis, a Risk-Fatigue cycle curve is developed for critical locations. This curve is useful for assessing the risk of existing structures. For instance, at a given acceptable risk level, the number of fatigue cycles to initial local failure can be determined. With this information available, criteria can be set for quality control, inspection intervals and retirement for cause.

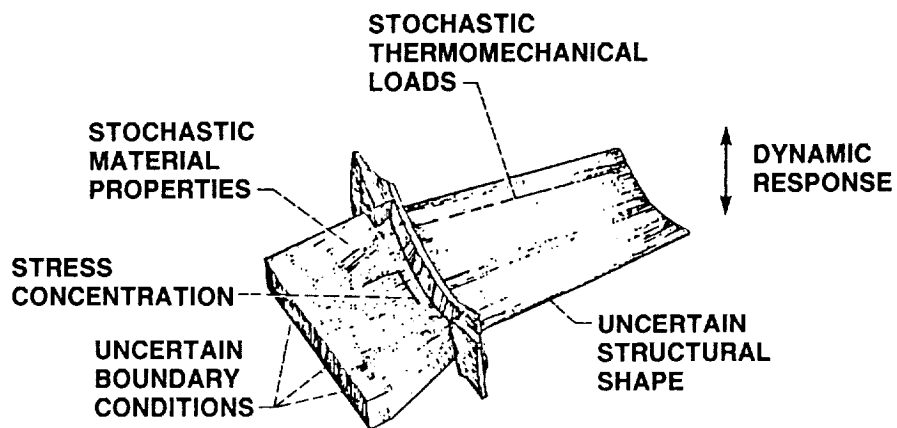
In summary, a reliability/risk cost methodology has been developed. It consists of a probabilistic structural analysis by NESSUS and a generic probabilistic material model. The methodology is versatile and particularly applicable to high temperature structures where data is difficult to obtain. It is demonstrated by using it to assess the risk associated with fatigue cycles to initiate local failure.

OBJECTIVE

DEVELOP A METHODOLOGY TO EVALUATE PROBABILITY OF FAILURE
AND PERFORM A RISK ASSESSMENT USING NESSUS AND A GENERIC
PROBABILISTIC MATERIAL MODEL OF COMPLEX STRUCTURES
OPERATING IN HIGH TEMPERATURE SERVICE ENVIRONMENTS

CD-89-39416

UNCERTAINTIES IN THE PROBABILISTIC STRUCTURAL ANALYSIS



CD-89-39417

PROBABILISTIC STRUCTURAL ANALYSIS

BY NESSUS & A GENERIC PROBABILISTIC MATERIAL MODEL

ITERATION 0

STEP 1: CALCULATE THE PROBABILITY DISTRIBUTIONS OF MATERIAL PROPERTIES USING THE GENERIC MATERIAL MODEL WITHOUT STRESS AND FATIGUE CYCLES

STEP 2: CALCULATE THE NODAL STRESS BY NESSUS

ITERATION 1

STEP 1: CALCULATE THE PROBABILITY DISTRIBUTIONS OF MATERIAL PROPERTIES USING COMPLETE GENERIC MATERIAL MODEL

STEP 2: CALCULATE THE NODAL STRESS BY NESSUS WITH UPDATED MATERIAL PROPERTIES

ITERATION 2

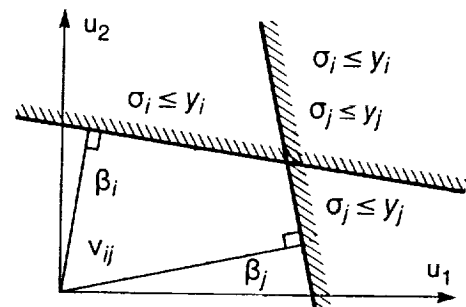
(REPEAT THE ITERATIONS UNTIL THE PROBABILITY DISTRIBUTIONS OF MATERIAL PROPERTIES AND STRESS HAVE CONVERGED)

CD-89-39422

JOINT CUMULATIVE DISTRIBUTION FUNCTION OF NODAL STRESSES

σ_i & σ_j CALCULATED BY FIRST-ORDER SECOND-MOMENT METHOD

σ_i = NODAL STRESS
 y_i = REAL VALUE
 β_i = RELIABILITY INDEX
 Φ = NORMAL CDF
 ϕ = NORMAL PDF
 $\rho_{ij} = \cos v_{ij}$



NORMALIZED COORDINATE SYSTEM

$$P(\sigma_i \leq y_i \text{ and } \sigma_j \leq y_j) = \Phi(-\beta_i)\Phi(-\beta_j) + \int_0^{\rho_{ij}} \phi(-\beta_i - \beta_j; z) dz$$

CD-89-39423

GENERIC PROBABILISTIC MATERIAL PROPERTY MODEL IN TERMS OF PRIMITIVE VARIABLES

$$M_P = M_{P0} \left[\frac{T_F - T}{T_F - T_0} \right]^n \left[\frac{S_F - \sigma}{S_F - \sigma_0} \right]^p \left[\frac{\log N_{MF} - \log N_M}{\log N_{MF} - \log N_{M0}} \right]^q$$

PRIMITIVE VARIABLES

M_P = MATERIAL PROPERTY

T = TEMPERATURE

S = STRENGTH

σ = STRESS

N_M = MECHANICAL CYCLES

SUBSCRIPTS

F = FINAL CHARACTERISTIC VALUE

0 = REFERENCE PROPERTY

CD-89-39420

PRIMITIVE VARIABLE PROBABILITY DISTRIBUTIONS FOR PROBABILISTIC MATERIAL PROPERTY MODEL

VARIABLE	DISTRIBUTION TYPE	MEAN	STANDARD DEVIATION	
			(VALUE)	(% OF MEAN)
T_F	NORMAL	2750 °F	51.4 °F	2.0
T_0	NORMAL	68 °F	2.04 °F	3.0
S_F	NORMAL	212.0 ksi	10.6 ksi	5.0
σ_0	CONSTANT	0	0	0
N_{MF}	LOGNORMAL	10^8	5×10^6	5.0
N_{M0}	LOGNORMAL	10^3	50	5.0
n	NORMAL	0.25		3.0
p	NORMAL	0.25		3.0
q	NORMAL	0.25		3.0

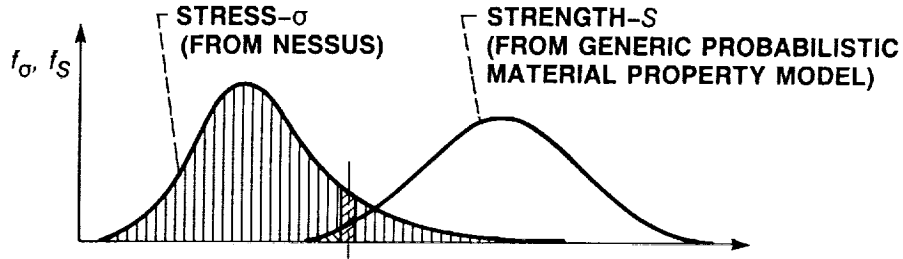
CD-89-39421

RISK ASSESSMENT

$$P_f = P (\sigma \geq S)$$

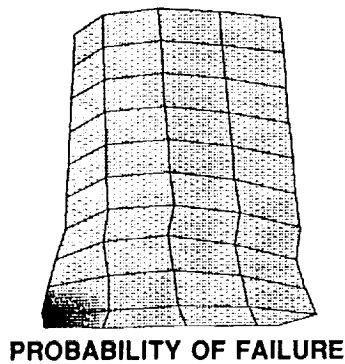
P_f — PROBABILITY OF FAILURE σ — STRESS S — STRENGTH

$$P_f = \int_{-\infty}^{\infty} \left(\int_{-\infty}^x f_S(s) ds \right) f_{\sigma}(x) dx$$

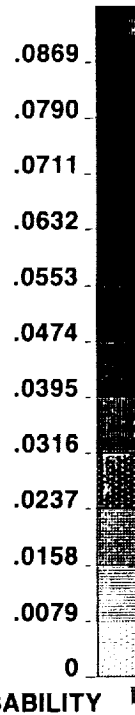


CD-89-39418

PROBABILITY OF LOCAL FAILURE CAN BE QUANTIFIED (STRESS EXCEEDS STRENGTH)



PROBABILITY OF FAILURE



CD-89-39419

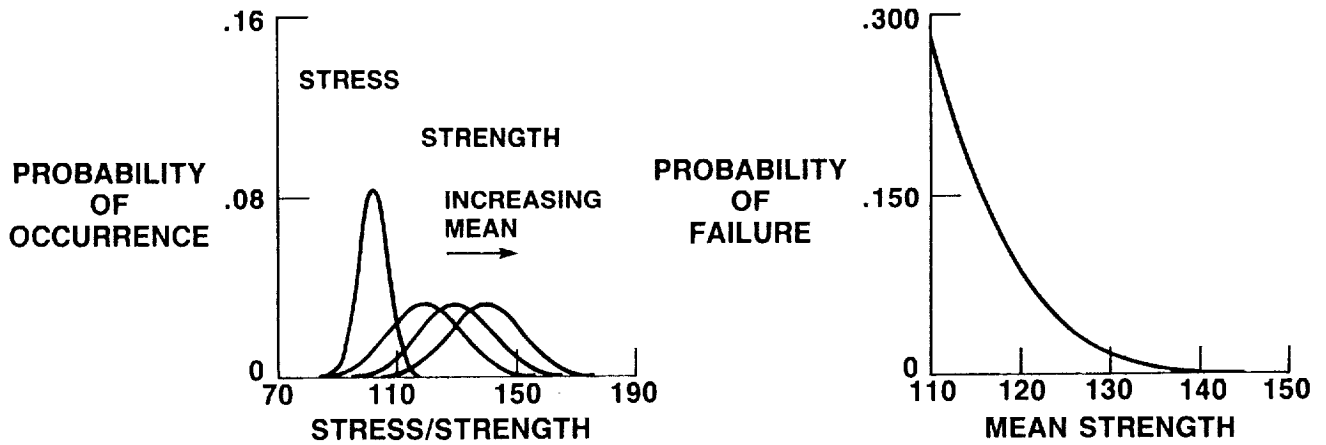
HYPOTHESIS FOR QUANTIFYING ACCEPTANCE OF RISK

C_i INITIAL COST	=	COST OF COMPONENT SERVICE READINESS
C_f CONSEQUENTIAL COST	=	COST DUE TO FAILURE OCCURRENCE
P_f	=	PROBABILITY OF FAILURE
C_t	=	TOTAL COST

$$C_t = C_i + P_f C_f$$

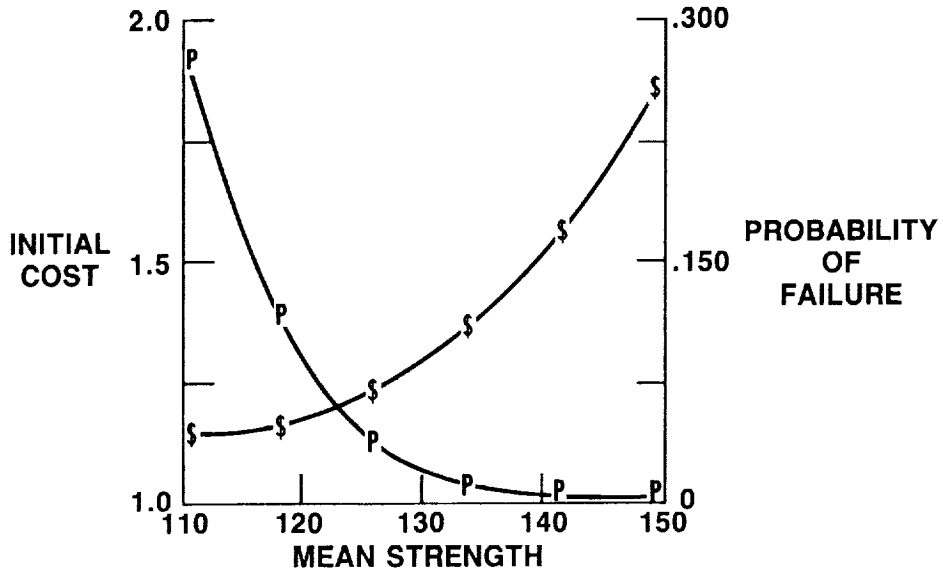
CD-89-39424

PROBABILITY OF FAILURE CAN BE QUANTIFIED IN TERMS OF IMPROVED MEAN STRENGTH



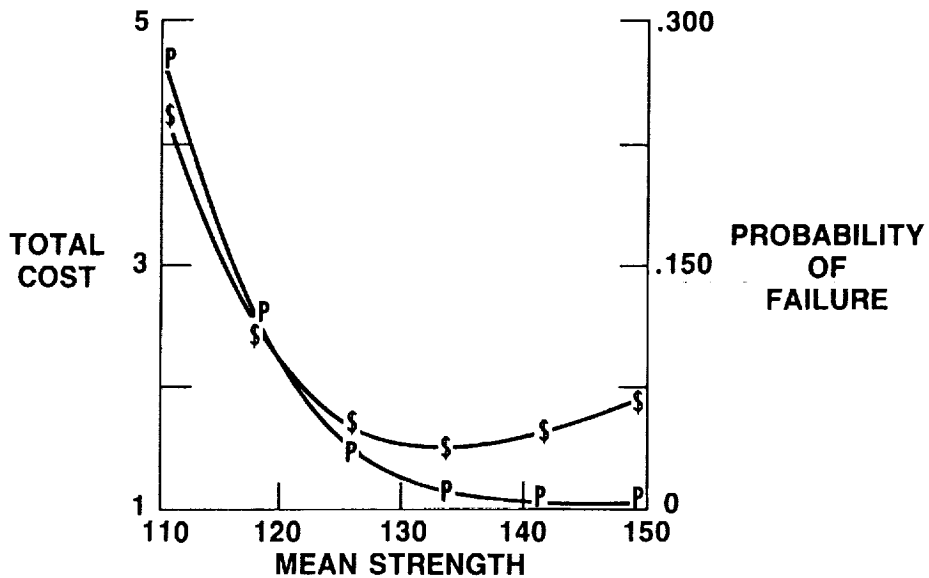
CD-89-39425

THE INITIAL COST TO IMPROVE THE STRUCTURAL RELIABILITY CAN BE QUANTIFIED IN TERMS OF MEAN STRENGTH (GIVEN QUALITY)



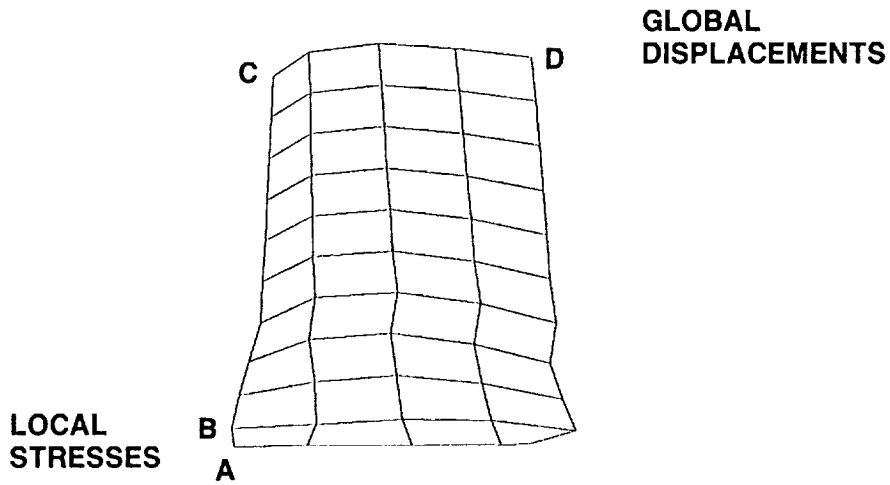
CD-89-39426

THE TOTAL COST TO IMPROVE THE STRUCTURAL RELIABILITY CAN BE QUANTIFIED IN TERMS OF MEAN STRENGTH (GIVEN QUALITY)



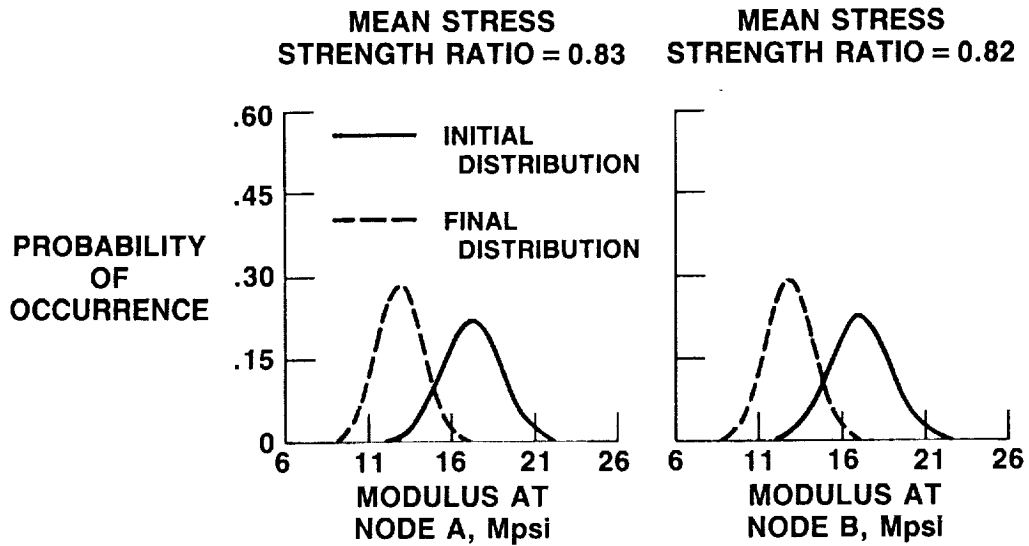
CD-89-39427

SSME BLADE SHOWING LOCATIONS WHERE PROBABILISTIC STRUCTURAL RESPONSE WAS EVALUATED



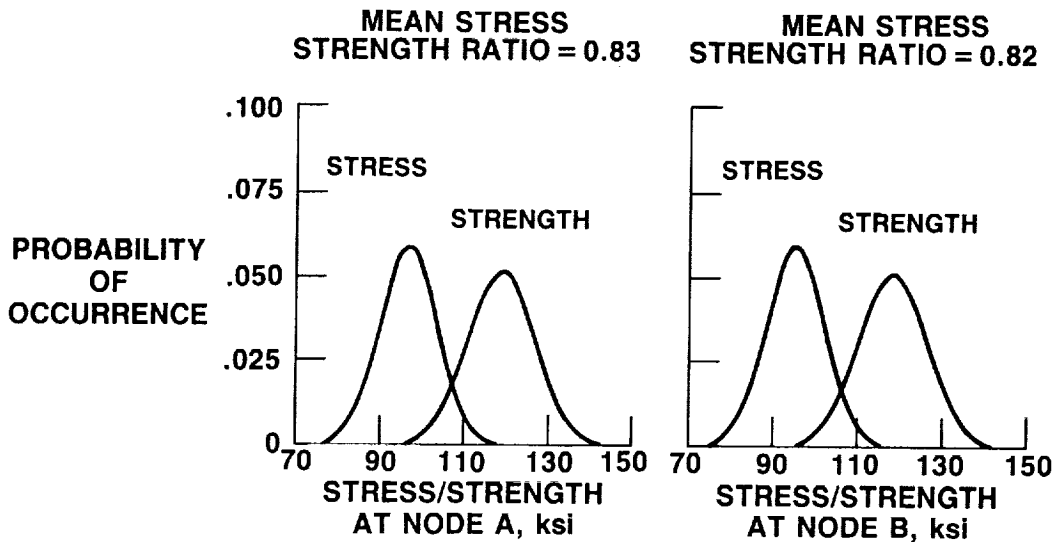
CD-89-39428

PROBABILISTIC MODULUS SIMULATED BY USING THE GENERIC PROBABILISTIC MATERIAL PROPERTY MODEL



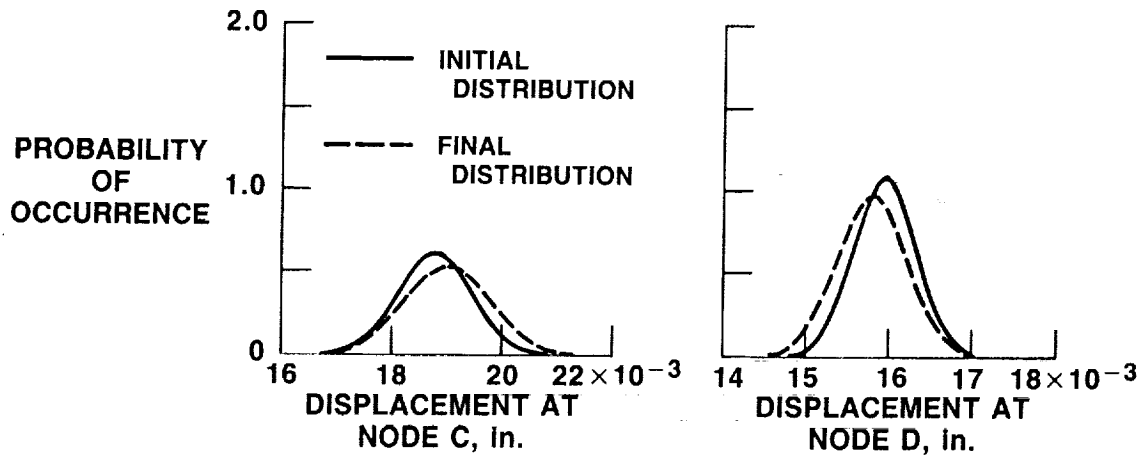
CD-89-39429

PROBABILISTIC FATIGUE STRESS/STRENGTH SIMULATED BY USING THE GENERIC PROBABILISTIC MATERIAL PROPERTY MODEL



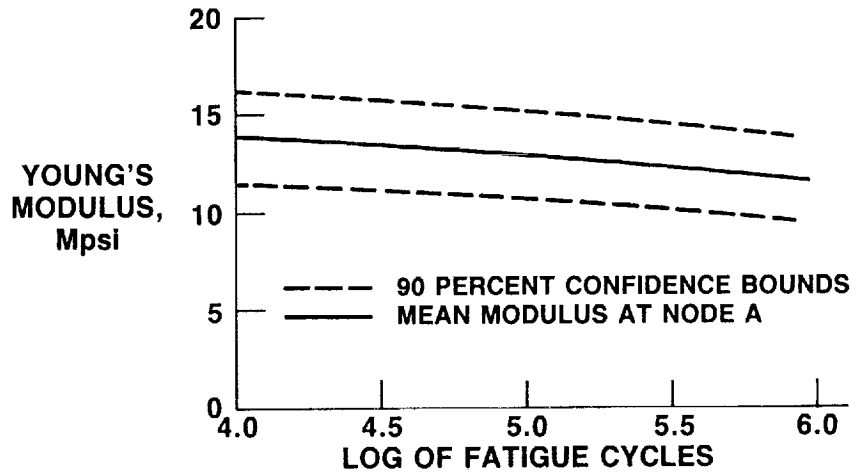
CD-89-39431

PROBABILISTIC DISPLACEMENTS CALCULATED BY NESSUS



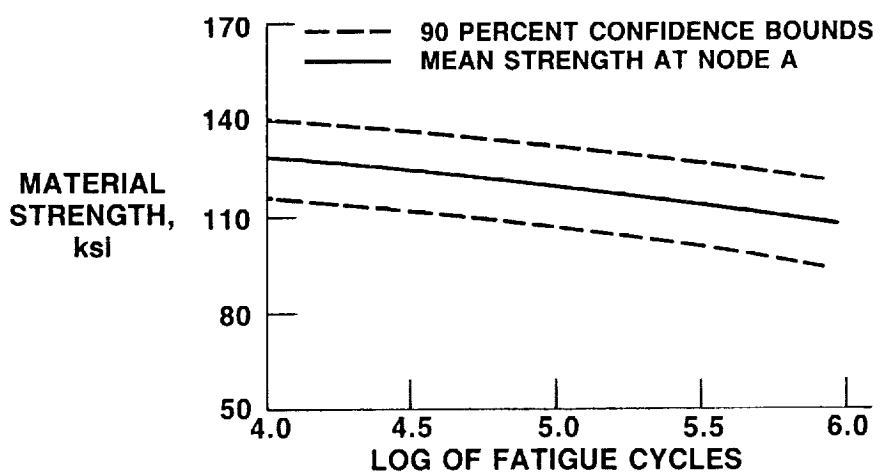
CD-89-39430

PROBABILISTIC CYCLIC LOAD EFFECTS ON MODULUS



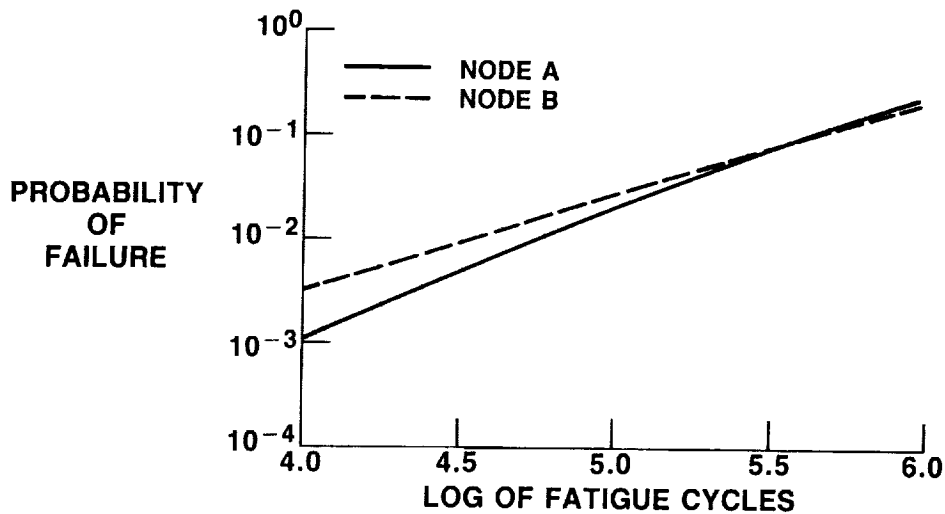
CD-89-39432

PROBABILISTIC CYCLIC LOAD EFFECTS ON STRENGTH



CD-89-39433

PROBABILITY OF LOCAL FAILURE DUE TO FATIGUE CYCLES



CD-89-39434

CONCLUDING REMARKS

- A METHODOLOGY HAS BEEN DEVELOPED FOR PERFORMING RELIABILITY/RISK COST BASED ASSESSMENTS OF AEROSPACE PROPULSION STRUCTURES
- THE METHODOLOGY CONSISTS OF PROBABILISTIC STRUCTURAL ANALYSIS (NESSUS) AND A PROBABILISTIC GENERIC MATERIAL PROPERTY MODEL
- THE METHODOLOGY IS ILLUSTRATED BY USING IT TO ASSESS THE RISK FOR QUALITY CONTROL, STRENGTH IMPROVEMENT, AND FATIGUE CYCLES TO INITIATE LOCAL FAILURE

CD-89-39435

OVERVIEW OF AEROTHERMODYNAMIC LOADS DEFINITION STUDY

Raymond E. Gaugler
NASA Lewis Research Center

507-39
19884

For a number of years now, NASA has been conducting the Advanced Earth-to-Orbit (AETO) Propulsion Technology Program, now part of the Civil Space Technology Initiative (CSTI) Program. The program objective is to provide the knowledge, understanding, and design methodology that will allow the development of advanced Earth-to-orbit propulsion systems with high performance, extended service life, automated operations, and diagnostics for in-flight health monitoring. This program supports both current and future engine and vehicle developments. The technology needs of the current Space Shuttle Main Engine (SSME) have thus far provided the main focus for the AETO efforts. Organizationally, the program has been divided into technology working groups made up of people from both the Marshall Space Flight Center and the Lewis Research Center. The focus of this report is the Lewis effort under the Fluid and Gas Dynamics working group, the Aerothermodynamic Loads Definition Study.

The objective of the Aerothermodynamic Loads Definition Study is to develop methods to more accurately predict the operating environment in AETO propulsion systems, such as the Space Shuttle Main Engine (SSME) powerhead. Development of time-averaged and time-dependent, three-dimensional viscous computer codes as well as experimental verification and engine diagnostic testing are considered to be essential in achieving that objective. Time-averaged, nonsteady, and transient operating loads must all be well defined in order to accurately predict powerhead life. Improvements in the structural durability of the SSME turbine drive systems will depend on our knowledge of the aerothermodynamic behavior of the flow through the preburner, turbine, turnaround duct, gas manifold, and injector post regions.

The approach taken under this study consists of two parts: (1) to modify, apply, and disseminate existing computational fluid dynamics (CFD) tools in response to current needs and (2) to develop new technology that will enable more accurate computation of the time-averaged and unsteady aerothermodynamic loads in the SSME powerhead. The new technology development effort is further divided into three parts: (1) new computer code development, (2) experiments to provide data for physical models required by the codes, and (3) experiments to provide data for validating the codes. With the more accurate aerothermodynamic load predictions providing boundary conditions to improved structural and fatigue life analyses, the goal of improved durability will be met.

The Aerothermodynamic Loads Definition Study was begun in October 1983. The initial effort involved the use of existing CFD tools to analyze problems in the fuel and oxidizer turbopump turbines, the fuel turbine turnaround duct, the fuel-side preburner, and the main injector liquid oxygen posts. Results

of those efforts have been presented previously and will not be discussed here. What follows is a description of the currently active tasks and their status.

H4(a). UNSTEADY VISCOUS MULTIBLADE-ROW TURBINE ANALYSIS

In this task, the objective is to develop a numerical simulation capability for unsteady viscous flow and heat transfer in multiblade-row turbines.

The numerical simulation of unsteady viscous flows in multiblade-row turbines requires a means of reducing the three-dimensional, nonperiodic, multi-row problem to one of more manageable proportions. This work will develop a two-dimensional test bed to be used in exploration for ways of solving the full problem. The approach is to use an existing quasi-3D viscous cascade code as the basis of a 2D multipassage rotor-stator interaction code.

A detailed description of the latest efforts under this task will be presented later in this session.

H4(b). COMPUTATION OF THREE-DIMENSIONAL FLOW WITH HEAT TRANSFER

In this task the objective is to develop an accurate, efficient numerical analysis of steady 3D viscous flow and heat transfer in turbine blade rows.

The approach being taken is to modify a 3D viscous turbomachinery code (RVC3D) to include an advanced turbulence model and increased resolution of near-wall gradients and to validate and upgrade the code by application to suitable 3D data sets.

H4(e). THREE-DIMENSIONAL STATOR-ROTOR BLADE FLOW EXPERIMENT

The objective of this task is to investigate the steady and unsteady 3D viscous flow field in an axial turbine stage, including stator-rotor interaction, mixing effects, blade and end wall boundary layers, and temperature gradient effects on secondary flow development. This work is being done in the Pennsylvania State University Axial Flow Turbine Research Facility. A progress report will be presented later in this session.

H4(m). TURBULENCE MODELING FOR PROTEUS TURBOMACHINERY CODE

The objective of this task is to develop the capability to predict turbulent flow losses and heat transfer in the SSME turbines using the Proteus 3D Navier-Stokes code. Existing turbulence models are inadequate or require empirical tuning to generate reasonable results. Efforts have begun, working first with a 2D version of the code.

H5(a). IMPROVED MODELING, PREBURNER FLOW

In this task the objective is to obtain steady-state reacting hydrogen data of mean and fluctuating velocities and concentrations and to compare

benchmark data with predictions from computer models and evaluate turbulence-chemistry interactions.

Computations of the 3D flow in the SSME turbopump turbines requires knowledge of the condition of the gases exiting the preburner. Current models for predicting those conditions are inadequate. Fluctuating concentration and velocity data can now be obtained with laser diagnostics. These measurements are necessary to determine the unmixedness of the reacting flow and the reaction rates. The measurements are also necessary for differentiating the various computer models.

For this task a team of computer modelers and experimentalists have defined the measurements required to verify turbulent-reacting flow models. Existing optical techniques will be used to make measurements within the shear layer: two-component laser Doppler velocimetry (LDV), fluorescence for OH and temperature, and $TiCl_4$ for seeding and H_2O concentration.

Hardware fabrication is nearly complete. Figure 1 is a schematic view of the test rig, and figure 2 is a photograph of the test section, mounted in an inspection facility.

H5(f). HIGH REYNOLDS NUMBER AND UNSTEADY HEAT TRANSFER EXPERIMENT

In this task the objective is to develop a fundamental understanding of the effects of high Reynolds numbers and Reynolds number variations, and also upstream unsteadiness, on heat transfer in turbulent boundary layers typical of turbine airfoils in the SSME turbopump turbines.

In order to predict the surface pressure and temperature distributions within engine flow passages, an accurate turbulence and unsteadiness model is needed. Data in the proper range of Reynolds number and disturbance frequency are necessary for accurate modeling. A new in-house experimental rig, shown schematically in figure 3, is being built in which the major features of an SSME turbine airfoil will be simulated, particularly the Reynolds number. A particular feature of the rig will be the ability to span the Reynolds number range from conventional gas-turbine levels up to SSME levels. Figure 4 is a photograph of the test section, instrumented and awaiting installation in the facility. Testing will be underway in the near future.

H5(g). UNSTEADY HEAT TRANSFER ANALYSIS

In this task the objective is to formulate analytic models to aid in the prediction of the unsteady aerothermal loads expected in the SSME turbopump turbines.

The ability to predict the aerothermal loads in the turbine unsteady flow environment is an essential input to the ability to predict life and durability. There are two aspects to the unsteadiness which occurs on turbine blades. The first is due to free-stream turbulence and wakes shed from upstream vanes and blades. The second is due to laminar to turbulent boundary layer transition which occurs some distance downstream from the blade leading edge. Both of these issues are being addressed in this research program.

For the unsteady wake interaction problem, a viscous-inviscid boundary layer theory has been used to model the effects of passing wakes and free-stream turbulence on the heat transfer to the SSME turbine airfoils, particularly near the stagnation region. For the boundary layer transition experiments, an experimental approach is being used to study the effects of concave curvature, which occurs on the pressure side of the SSME turbine airfoil, during the transition process.

H5(h). IMPROVED AERO AND HEAT TRANSFER PREDICTION

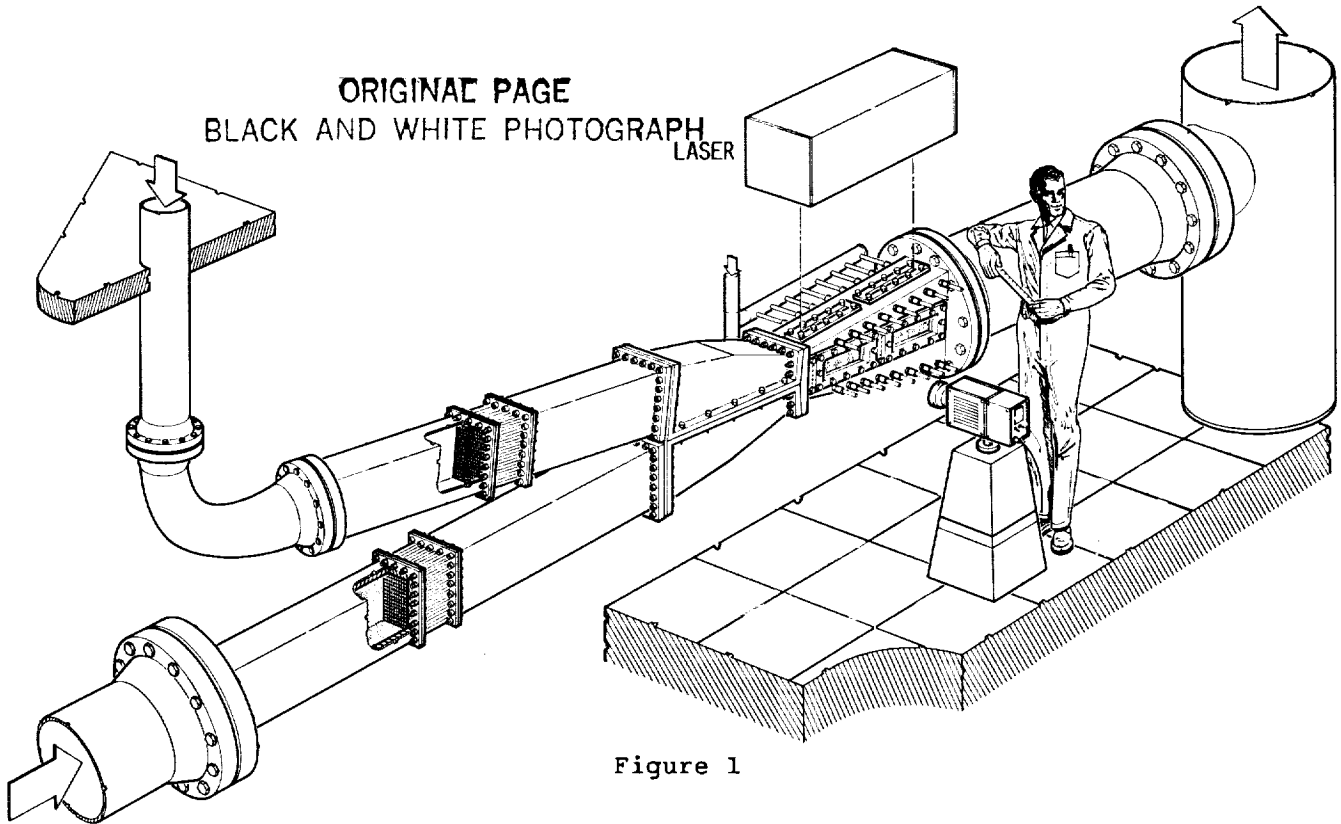
In this task the objective is to improve the calculation of the aerodynamic environment in low-aspect-ratio turbines and to experimentally obtain the unsteady surface heat transfer response to a temperature disturbance.

Knowledge of the local flow environment of turbine vanes and blades is essential for the accurate prediction of turbine temperatures and heat-transfer rates. In addition, the response of the turbine blade surfaces to rapid changes in stagnation temperature is unknown. Improved steady and unsteady heat transfer prediction is required for improved life and for turbine efficiency. An existing quasi-3D computer code will be activated at Calspan and used to compute pressure distributions over stator and rotor surfaces, substantially reducing the uncertainty in the aerodynamic environment and providing a reliable base for heat transfer predictions. The experimental phase will use a low-aspect-ratio turbine instrumented with thin-film heat flux sensors located on the vanes and rotor blades. The temperature level, disturbance, blade passing frequency, and Reynolds number will be varied. A detailed description of the latest results under this task will be presented in another paper at this meeting.

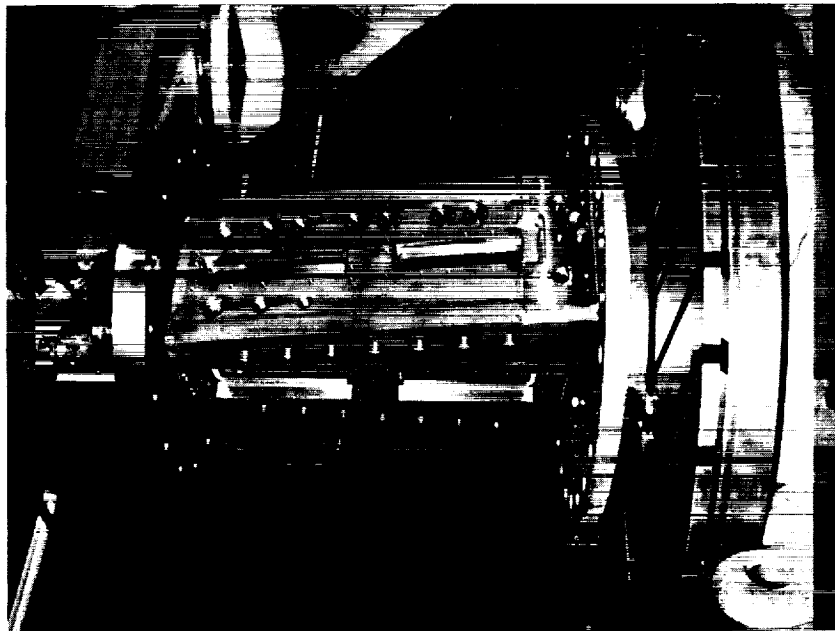
SUMMARY

Significant progress is being made in the Aerothermodynamic Loads Definition Study, particularly in the turbomachinery area, where there is a distinct overlap between the AETO efforts and research in the aeronautical gas turbine field. The continuing work under this program will provide the knowledge, understanding, and design methodology that will allow the development of advanced Earth-to-orbit propulsion systems with high performance, extended service life, automated operations, and diagnostics for in-flight health monitoring.

PLANAR REACTING SHEAR LAYER



SSME AERO-THERMODYNAMIC LOADS FLUID AND GAS DYNAMICS WORKING GROUP



CD-89-39277

Figure 2

ORIGINAL PAGE IS
OF POOR QUALITY

ORIGINAL PAGE
BLACK AND WHITE PHOTOGRAPH

HIGH REYNOLDS NUMBER HEAT TRANSFER RIG

(REYNOLDS NUMBER UP TO 7,500,000)

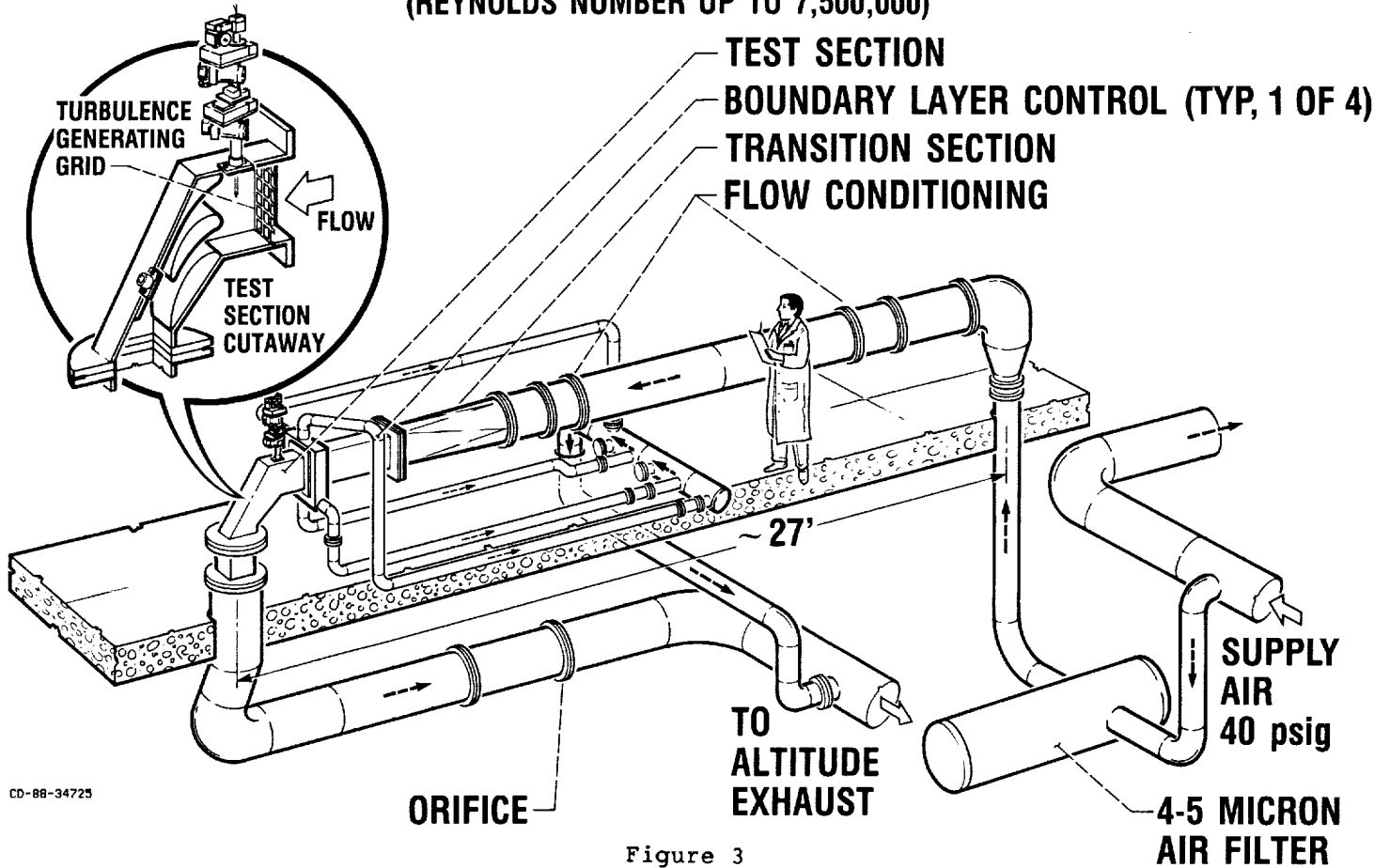


Figure 3

HIGH REYNOLDS NUMBER & UNSTEADY HEAT-TRANSFER RIG TEST SECTION

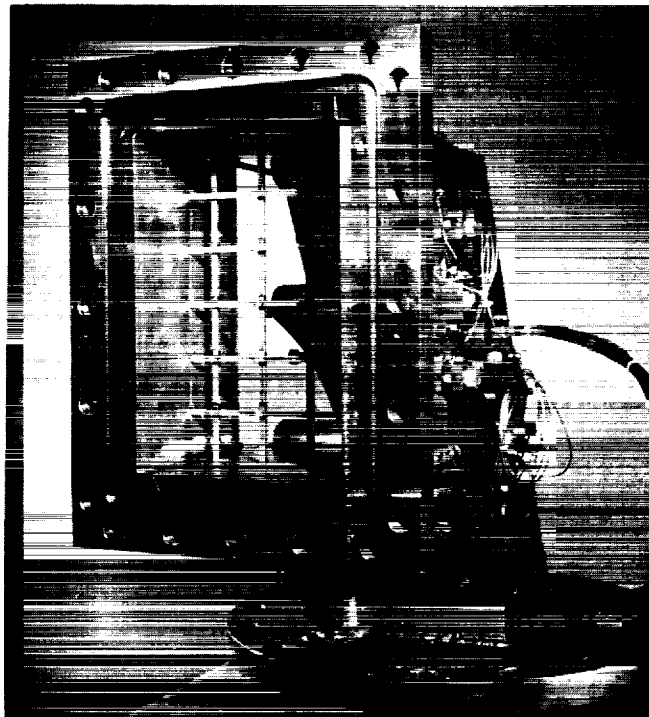


Figure 4

CD-89-39276

**HEAT-TRANSFER AND SURFACE-PRESSURE MEASUREMENTS
FOR THE SSME FUEL-SIDE TURBOPUMP TURBINE***

by

Michael G. Dunn

Calspan-UB Research Center
Buffalo, New York 14225528-37
19885

INTRODUCTION

An experimental research program is currently underway at the Calspan-UB Research Center (CUBRC) that is designed to obtain detailed heat-flux and surface-pressure distribution on the first-stage vane and first-stage blade of the SSME fuel-side turbopump turbine. This particular turbine is a two-stage machine and both stages will be in use. However, at the present time, the first-stage vane, the first-stage blade, and the second stage vane will be instrumented. The specific turbine being utilized is a combination of actual engine hardware and reproduced hardware consistent with that being used at NASA Marshall Space Flight Center for the initial measurements in their newly constructed blow-down turbine test facility.

The facility being used at CUBRC is also a blow-down type facility, but it is of the short-duration shock-tunnel variety. The short-duration nature of the shock-tunnel facility permits use of thin-film thermometers which are used to measure the surface temperature histories at prescribed locations on the turbine component parts. Heat-flux values are then inferred from the temperature histories using standard data reduction procedures. Miniature surface mounted pressure transducers are also used on both the vane and the rotating blade to obtain the desired pressure distributions.

*The research described in this paper was supported by NASA Lewis Research Center under Grant No. NAG 3-581.

EXPERIMENTAL APPARATUS

The experimental apparatus sketched in Figure 1 consists of a 0.47-m (18.5-in) i.d. helium-driven shock tube with a 12.2-m (40-ft.) long driver tube and an 18.2-m (60-ft.) long driven tube as a short-duration source of heated air, supplying the test section device located near the exit of the primary shock-tunnel nozzle. The 2.7-m (9-ft.) i.d. receiver tank is initially evacuated to a pressure on the order of 1 torr in order to minimize the flow establishment characteristics of the model. The useful test time in this facility for the test conditions to be used for the SSME measurements is on the order of 35 ms, which is nearly two times greater than the test time available for the facility used in the previous CUBRC full-stage turbine studies (References 1-6). A more detailed photograph of the test section device housing the two-stage turbine is shown in Figure 2. This device consists of a forward transition section with a circular opening facing the supersonic primary nozzle flow. This transition section is followed by the 360 deg. annular passage containing the turbine stages. Downstream of the second rotor exit is an annular passage with a contoured nozzle at the exit. This nozzle is used to establish the desired pressure ratio across the turbine. The internal model configuration duplicates the SSME turbopump configuration including the twelve upstream struts and the protruding bolt head on the dome. In our configuration, this forward dome houses an air motor that is used to accelerate the turbine from test to the desired speed just prior to initiation of the experiment and prior to arrival of the test gas. The aft internal cavity houses a 200-channel slip ring that is used to transfer the pressure and heat-transfer data from the rotor blade to the laboratory data recorders.

Figures 3 and 4 are front and rear photographs of the first stage nozzle guide vane ring. A contoured leading-edge insert containing ten thin-film heat-flux gages will be installed at midspan on vane No. 32. Button-type thin-film gages will be installed on vane No. 16 (pressure surface) and vane No. 17 (suction surface) at 10%, 50%, and 90% span. Miniature surface mounted pressure transducers will be installed at 10% span on vane No. 13 (pressure surface) and vane No. 14 (suction surface), at 50% on vane No. 23 (pressure surface) and vane No. 24 (suction surface), and at 90% span on vane No. 29 (pressure surface) and vane No. 30 (suction surface). The specific vanes and instrumentation locations on those vanes at which pressure measurements will be performed are consistent with the Marshall instrumentation plan. The heat-flux measurements will be performed at locations such that direct comparisons can be made between the heat-flux and surface-pressure results.

ORIGINAL PAGE IS
OF POOR QUALITY

Figure 4 illustrates removal of a portion of the vane near the hub wall. This cut in vane profile is consistent with flight engine hardware. Several heat-flux gages have been placed near this cut on both the pressure and suction surfaces and on the hub endwall in order to investigate the influence of the cut on the flow field.

Figure 5 is a photograph of one of the first-stage rotor blades that will be instrumented with flush-mounted miniature pressure transducers and thin-film heat-flux gages. Both heat-flux and pressure instrumentation will be placed at selected chordwise locations at 10%, 50% and 90% spans. The heat-flux instrumentation will be composed of button-type gages and a leading-edge insert.

The measurements in and along the flowpath are important for determining the gas dynamics into and out of the turbine stage. The turbine model shown in Figure 2 has approximately twenty static pressure measurements distributed between the inner and outer portions of the model flow path. Static pressure measurements of particular importance are those at the inlet to the guide vane row, the intra stage measurements, and the static pressure measurements downstream of the second rotor. A spanwise total pressure rake is placed downstream of the second rotor and an attempt is being made to fit such a rake into the flow just downstream of the first rotor. Further, an attempt is being made to install a spanwise rake of total temperature probes downstream of the first rotor. The rakes just described may result in excessive flow blockage at the location of interest, and if so would be moved to a station downstream of the second rotor.

EXPERIMENTAL CONDITIONS

The SSME turbopump operates with a test gas composed of hydrogen plus steam. The facility to be used at CUBRC will operate with air as the test gas, but the appropriate scaling has been done to achieve the corrected conditions at the turbine inlet. It is important that the experiment duplicate the design flow function ($\dot{w}\sqrt{\theta}/\delta$), the corrected speed ($N_{phy}/\sqrt{\theta}$), the wall to total temperature ratio (T_w/T_o), and the stage total to static pressure ratio ($(P_o)_{in}/(P_s)_{out}$). It is also important to produce a turbine inlet Reynolds number sufficiently close to the operating value that the inlet boundary-layer characteristics are representative.

The SSME turbopump turbine measurements will be performed in a large turbine test facility at the Calspan Corporation. Because of the large dimensions of this facility it is possible to place the inlet to the model housing the two-stage turbine at a couple of different locations in the nozzle expansion (see Figure 1), and in this manner, change the turbine inlet total pressure and Reynolds number while holding the turbine inlet total temperature constant.

The nominal flow conditions for the SSME fuel side turbopump are; $T_0 = 1890^\circ\text{R}$, $P_0 = 5526$ psia, inlet Mach No. = 0.14, inlet density = 4.29 lbm/ft³ (H_2 + steam), Flow Function = 2.28, and overall total to static pressure ratio = 1.52.

For the proposed measurements, air would be used as the test gas instead of hydrogen plus steam. Two experimental test conditions will be run, both at a total temperature of the turbine inlet gas equal to 1000°R and both at the appropriate flow function, overall total to static pressure ratio, and corrected speed. The two test conditions would provide two different turbine inlet total pressure values and Reynolds number values as noted in Table 1.

Table 1
TEST CONDITIONS WITH AIR AS TEST GAS

Test Condition	Shock-Tube Conditions			Model Conditions Ahead of Vane			Turbine Conditions		
	P_0 psia	T_0 $^\circ\text{R}$	$W_{*})_{\text{throat}}$ lbm/sec	P_0 psia	T_0 $^\circ\text{R}$	Re /ft	\dot{W} lbm/sec	Rotor Speed rpm	T_w/T_0
#1	1100	1000	523	270	1000	1×10^7	31.6	9731	0.53
#2	2500	1000	1188	615	1000	2×10^7	71.7	9731	0.53

CONCLUSIONS

The current status of the measurement program described herein is as follows: (a) The model to house the two stage turbine has been designed and detailed engineering drawings have been prepared. Construction of the model has been initiated and is planned for completion in July 1989, (b) the pressure and heat-flux gages have been constructed and calibrated. Installation of this instrumentation in the components shown

in Figures 3 and 5 is scheduled for completion in June 1989, and (c) upon delivery of the model components, the instrumented vanes and blades will be installed and the measurement program will begin in the Summer of 1989.

REFERENCES

1. Dunn, M.G., "Experimental Measurements of Heat-Flux Distributions in a Turbine Stage with Upstream Disturbances," paper presented at the 1986 Advanced Earth to Orbit Propulsion Technology Conf., Huntsville, Alabama, 13-15 May 1986.
2. Dunn, M.G., "Heat-Flux Measurements for the Rotor of a Full-Stage Turbine: Part I - Time-Averaged Results," ASME Journal of Turbomachinery, vol. 108, pp. 90-97, July 1986 (also presented at the 31st International Gas Turbine Conf. June 8-12, 1986, paper no. 86-GT-77).
3. Dunn, M.G., George, W.K., Rae, W.J., Woodward, S.H., Moller, J.C., and Seymour, P.J., "Heat-Flux Measurements for the Rotor of a Full-Stage Turbine: Part II - Description of Analysis Technique and Typical Time-Resolved Measurements," ASME Journal of Turbomachinery, Vol. 108, pp. 98-107, July 1986. (Also Presented at the 31st International Gas Turbine Conf., June 8-12, 1986, Paper No. 86-GT-78.)
4. Dunn, M.G., "Phase and Time-Resolved Measurements of Unsteady Heat Transfer and Pressure in a Full-Stage Rotating Turbine," Paper Presented at the 1988 Conference on Advanced Earth-to-Orbit Propulsion Technology, 10-12 May 1988.
5. Dunn, M.G., Seymour, P.J., Woodward, S.H., George, W.K., and Chupp, R.E., "Phase-Resolved Heat-Flux Measurements on the Blade of a Full-Scale Rotating Turbine," ASME Journal of Turbomachinery, Vol. III, pp. 8-13, January 1989. (Also Presented at the 33rd International Gas Turbine Conference Paper No. ASME 88-GT-173, 5-9 June 1988.)
6. Dunn, M.G., "Phase and Time-Resolved Measurements of Unsteady Heat Transfer and Pressure in a Full-Stage Rotating Turbine," Paper to be Presented at the 34th ASME International Gas Turbine Conference, 4-9 June 1989. (Also accepted for publication in the ASME Journal of Turbomachinery.)

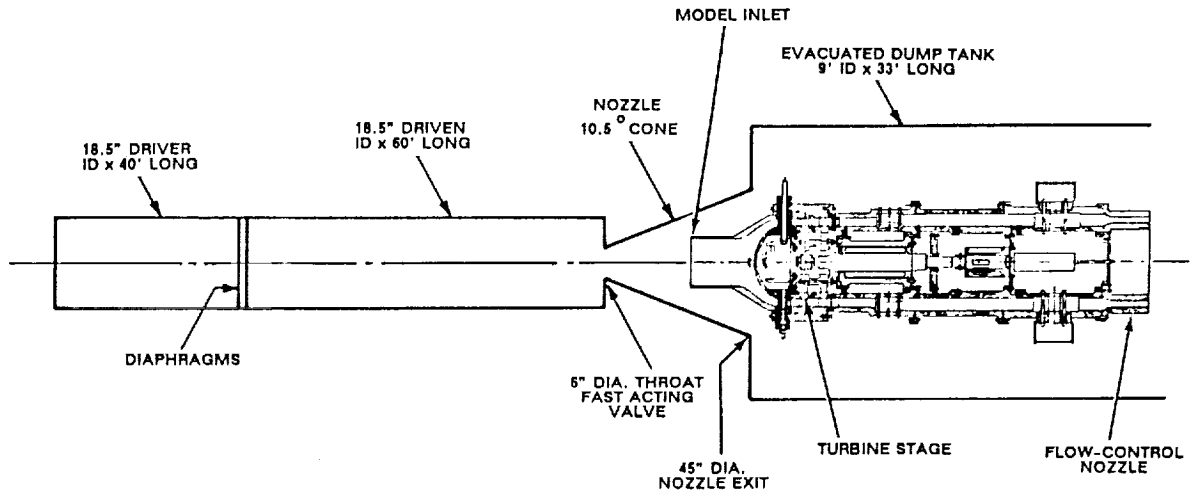


Figure 1 SKETCH OF MODEL HOUSING TURBINE STAGE LOCATED IN FACILITY

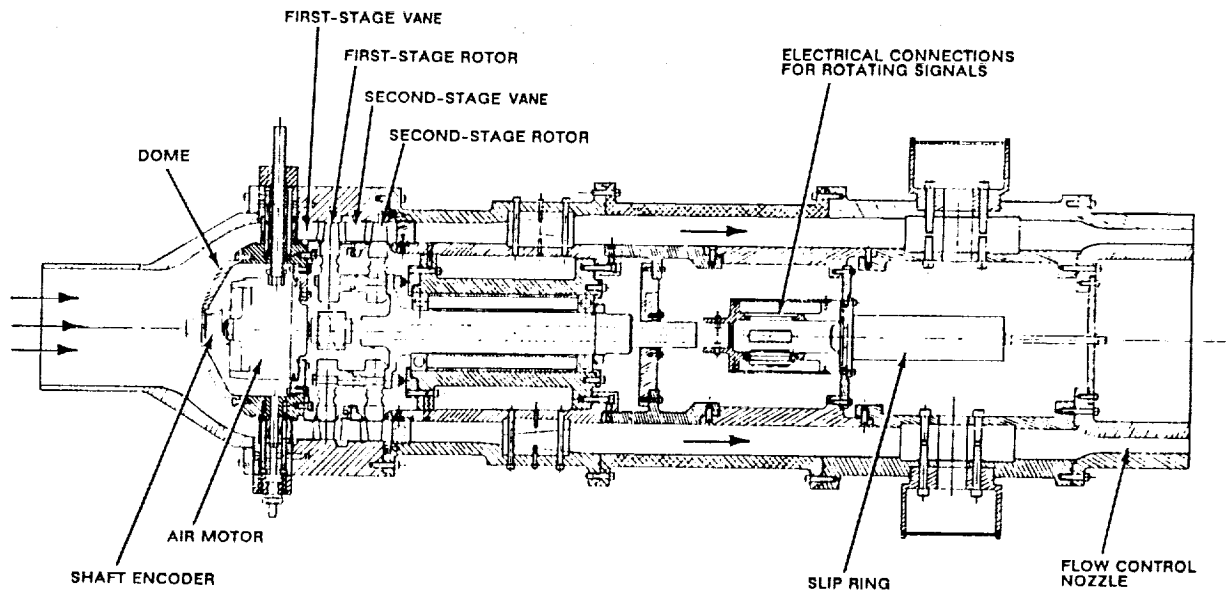


Figure 2 SKETCH OF MODEL TO HOUSE TURBINE STAGE

ORIGINAL PAGE IS
OF POOR QUALITY

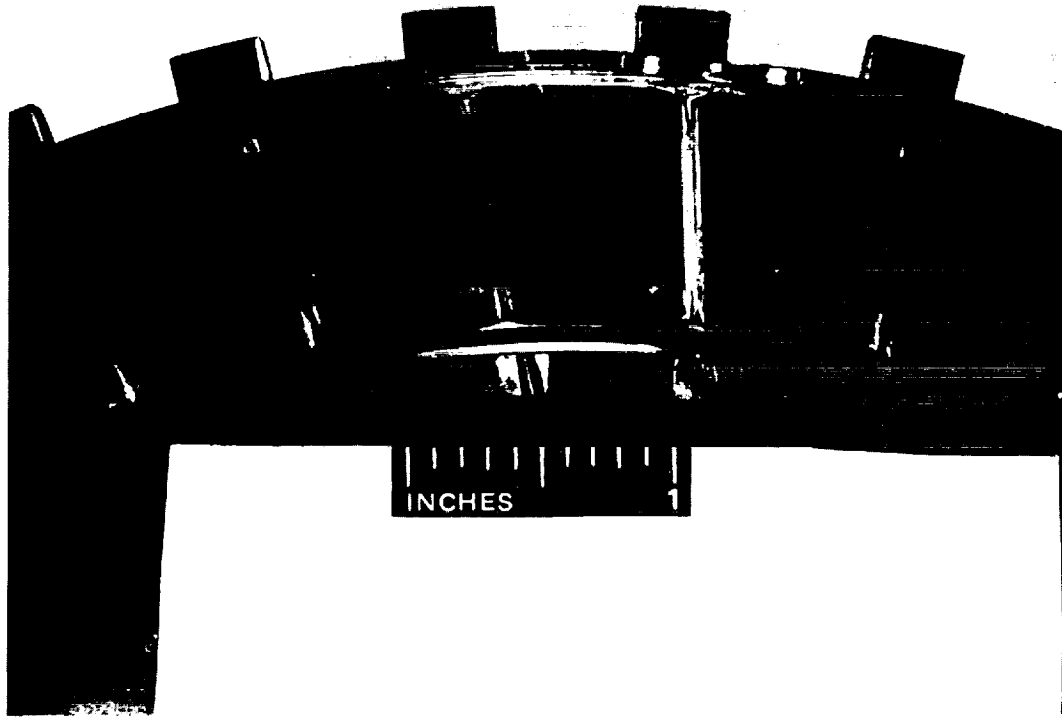


Figure 3 FRONT-VIEW PHOTOGRAPH OF FIRST-STAGE VANE



Figure 4 REAR-VIEW PHOTOGRAPH OF FIRST-STAGE VANE

ORIGINAL PAGE IS
OF POOR QUALITY

ORIGINAL PAGE
BLACK AND WHITE PHOTOGRAPH

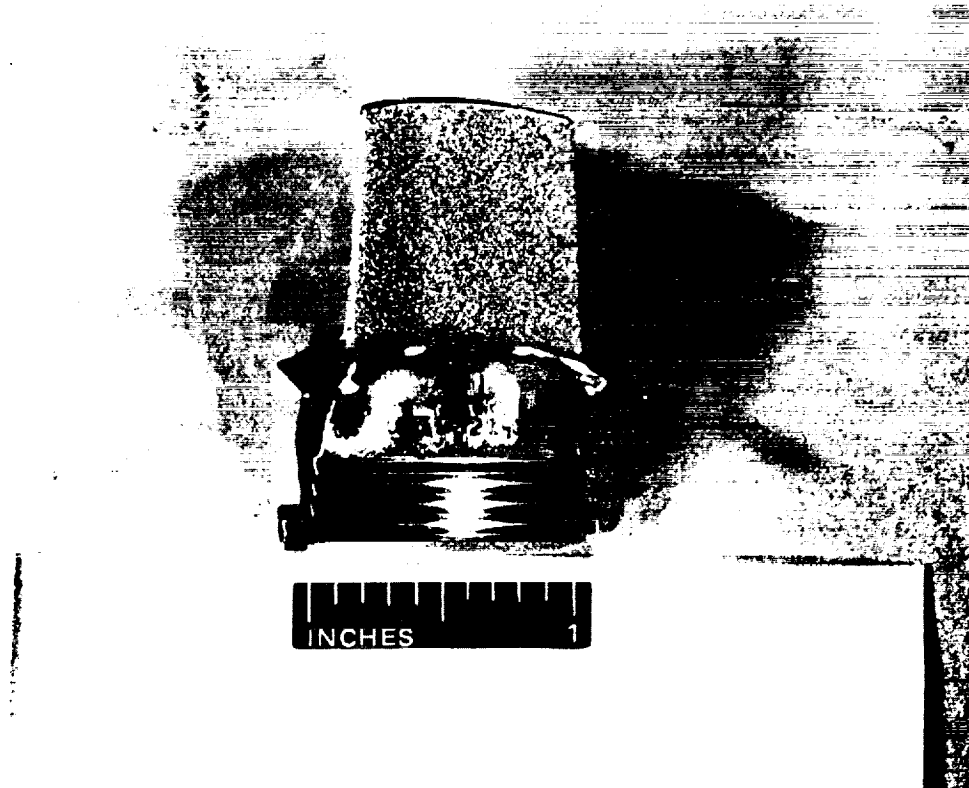


Figure 5 PHOTOGRAPH OF FIRST-STAGE BLADE

ORIGINAL PAGE IS
OF POOR QUALITY

ORIGINAL PAGE
BLACK AND WHITE PHOTOGRAPH

A New Facility to Study Three Dimensional
Viscous Flow and Rotor-Stator
Interaction in Turbines - A Progress Report

B. Lakshminarayana and C. Camci
Dept. of Aerospace Engineering
The Pennsylvania State University
University Park, PA 16802

529-34
19886

I. Halliwell
Aircraft Engine Group
General Electric Company
Cincinnati, OH 45215

A description of the Axial Flow Turbine Research Facility (AFTRF) being built at the Turbomachinery Laboratory of the Pennsylvania State University is presented in this report. The purpose of the research to be performed in this facility is to obtain a better understanding of the rotor/stator interaction, three dimensional viscous flow field in nozzle and rotor blade passages, spanwise mixing and losses in these blade rows, transport of wake through the rotor passage, and unsteady aerodynamics and heat transfer of rotor blade row. The experimental results will directly feed and support the analytical and the computational tool development. This large scale low speed facility is heavily instrumented with pressure and temperature probes and has provision for flow visualization and laser doppler anemometer measurement. The facility design permits extensive use of the high frequency response instrumentation on the stationary vanes and more importantly on the rotating blades. Furthermore, it facilitates detailed nozzle wake, rotor wake and boundary layer surveys. The large size of the rig also has the advantage of operating at Reynolds numbers representative of the engine environment.

1. BRIEF OUTLINE OF RESEARCH PROGRAM

The objective of the proposed research is to gain a thorough understanding of the flow field in a turbine stage, including three dimensional inviscid and viscid effects, unsteady flow field and heat transfer in the rotor passage, three dimensional mixing in inter and intra-blade passages, tip clearance effects, effects of film and convective cooling on flow and thermal field. A brief outline of the research programs proposed for the near future is given below:

Recent investigations have shown that three dimensional effects have considerable influence on the performance, and heat transfer in turbine stages. A knowledge of the characteristics of the three dimensional flow field inside the turbine rotors, including the blade boundary layers, endwall flows and the inviscid velocities, is essential for the analysis and the design of turbines used in military and civilian aircraft. Viscous

and turbulence effects play a very significant role in the study of improved design, better efficiency, cooling air requirements, mechanical reliability, flow induced vibration, and flutter of the turbine blades. Because of the complicated nature of the problem, the three dimensional viscous, turbulent, unsteady flow field inside the rotors is one of the least understood phenomena in turbines.

The Pennsylvania State University research group has recently completed a detailed experimental and computational study of the three dimensional flow field in the axial flow compressors and this has provided valuable information on the endwall flow characteristics, blade boundary layers, tip leakage flow and the inviscid flow field (including blade pressure distribution) (example Refs. 1-3). The boundary layers developing on turbines are also very complex; these are three dimensional with laminar, transitional, turbulent and separated zones. The flow field is a function of several parameters such as the solidity, incidence, camber, radial and chordwise pressure gradients, speed of rotation, blade geometry and the Mach number. Because of these complications, very few have attempted measurement of the rotor flow field. The objective of this investigation is to measure the entire flow field inside a turbine rotor and nozzle at the design condition. An additional objective is to develop analysis and computational techniques for the prediction of this flow field. The laser doppler velocimeter system (non-intrusive) is most desirable for flow measurements inside the rotor of the proposed facility. The wall and blade shear layers will be measured using hotwire sensors. The measurement will be taken at sufficient chordwise, radial, and tangential locations so as to derive a continuous variation of the flow field (including the blade and the annulus wall boundary layers) across the entire passage (hub to tip, leading to trailing edge, and pressure to suction surfaces). These measurements will provide information on the transition, turbulence properties, three dimensional flow velocities, and blade pressure distribution.

In addition, the unsteadiness into rotor inlet will be resolved through detailed measurement of nozzle wake characteristics. This will be carried out 50 and 20 percent (of nozzle chord) spacing between the nozzle and the rotor. The nozzle wake survey at several radial and axial locations, including stations close to the nozzle trailing and rotor leading edge will be carried out.

All the investigations carried out hitherto concern an independent study of steady and unsteady aerodynamics, or steady and unsteady heat transfer. These are usually from different set of facilities and operating conditions. Since heat transfer and aerodynamic phenomena are closely coupled, this approach has not led to a basic understanding of the flow and thermal field. One of the major objectives of the Penn State program is to carry out both the aerodynamic and heat transfer measurements in the same facility with identical operating conditions. The program for the measurement of steady aerodynamics was described earlier. The unsteady aerodynamics, including unsteady boundary layer properties will be measured using the hot wire techniques developed at the Pennsylvania State University. It is also planned to carry out unsteady convective heat transfer research in the Axial Flow Turbine Research Facility at a later date. The objective is to model the turbulent heat fluxes near the solid walls in complicated viscous flow zones such as the areas affected by wake passing. During the investigations, unsteady features of wall heat flux, stagnation temperature and wall temperatures will be investigated

experimentally and interpreted. The vane-blade interaction phenomenon will be captured by using thin film platinum wall heat flux sensors located in the areas where the wakes from the upstream rows impinge. These sensors are excellent indicators of phenomena such as laminar to turbulent transition, separation, reattachment etc. Their time response is sufficiently high to capture the unsteady features of the vane-blade interaction process. A new method of obtaining unsteady heat transfer information from the large scale cold turbine rig is discussed in detail in ref. 4. The measurement techniques are described in refs. 5 and 6.

2. FACILITY DESCRIPTION

A complete description of the facility and instrumentation is given in ref. 4. Only a brief summary is provided below. The Axial Flow Turbine Research Facility of the Pennsylvania State University is an open circuit facility 91.4 cm in diameter and a hub to tip radius ratio of 0.73, with advanced axial turbine blading configurations. The facility consists of a large bellmouth inlet, a turbulence generating grid section, followed by a test section with a nozzle vane row and a rotor as shown in figure 1. There are 23 nozzle guide vanes and 29 rotor blades followed by outlet guide vanes. Provisions exist for changing the vane-blade axial spacing from 20 to 50 percent of chord. The bellmouth inlet is housed in an enclosure (not shown) covered with wire mesh and a thin layer of rubber foam to filter the air prior to entry to the inlet.

A variable through flow is provided by two auxiliary, adjustable pitch, axial flow fans and an aerodynamically designed throttle. This system allows accurate control of the mass flow through the experimental stage up to a maximum of 22,000 cfm. The two fans in series produce a pressure rise of 74.7 mm Hg (40" of water) with a mass flow of 10.4 m³ per second under nominal operating conditions. The power generated by the experimental turbine rotor assembly is absorbed by an eddy-current brake which is capable of absorbing up to 90 Hp. The speed of the rotor can be varied between 175 and 1695 RPM with the "dynamic-adjusto speed" control system and can be held constant to ± 1 RPM, with normal fluctuations in line voltage. The eddy current brake is cooled by a closed loop chilled water cooling system.

The rotor and nozzle vane passages are instrumented with high frequency response instrumentation to measure steady (time averaged) and unsteady pressures and shear stresses. The details of the instrumentation used on the nozzle vane, rotor blade, nozzle casing, rotor hub, nozzle hub will be described in the next section. Provision has been made for a laser window (item B in Fig. 1) for LDV measurement of flow field upstream of the nozzle, nozzle passage, spacing between the rotor and the nozzle, rotor passage and downstream of the rotor passage.

The facility is equipped with two traversing mechanisms. One of the probe traverse unit is mounted directly behind the rotor disk and has provisions for the radial and circumferential traverses in the rotating frame. It is driven by a stepping motor driven by a computer controlled indexer at tangential increments of 0.019 degrees/step to allow accurate measurement of the rotor wakes. The intra blade radial and tangential surveys are accomplished with the use of the L.C. Smith stationary probe traverse unit. This mechanism is also driven by a computer controlled indexer and stepping motor in 0.05 mm steps and 0.0234 degree steps in the radial and circumferential directions respectively.

The rotating to stationary interface data transmission system, attached to the rotor shaft ahead of the nose cone, is an integral part of the facility. It consists of a 150 ring mechanical (brush/coin type) slip ring unit, and a specialized ten-channel low noise/signal ratio mercury slip ring unit. A 32 channel electronic pressure scanner unit is located in the rotating drum downstream of the turbine rotor. The electrical signals carrying the pressure information is carried to the stationary frame through the slip ring assembly. The rotor frequency will be accurately determined by using an infrared emitter/receiver circuit located on the casing of the turbine rotor. This device generates the reflected infrared emissions from the tip of a selected rotor blade and directly provides the rotor frequency (once per revolution pulse-OPR).

A data processing system is built around a microcomputer with a clock rate of 10MHz. The system consists of a 16 bit computer with 1MB random access memory, a disk operating system, 40 Mb hard disk storage space, printer and plotter. All of the data from both stationary and rotating instrumentation can be processed on-line. One of the long range goals of the turbine research is to acquire unsteady heat transfer and aerodynamics data simultaneously.

A unique feature of Axial Flow Turbine Research Facility is its ability to generate the aerodynamic and unsteady heat transfer data simultaneously. This feature allows the generation of benchmark quality data to validate three dimensional viscous codes, which includes heat transfer. It is expected that this integrated approach will improve the heat transfer prediction capabilities, especially in the rotor stator interaction region.

The vane and blade design was carried out by General Electric Company's Aircraft Engine group. The aerodynamic design, while not representing any specific current or future GE product, does embody modern design philosophy. Stage loading, flow coefficient, reaction, aspect ratio, blade turning angles are all within the range of current design practice. State-of-the-art quasi three dimensional design methods are used to design airfoil shapes. The details of the design are incorporated in reference [7]. The blade geometry is shown in figure 2. Absolute Mach number at the inlet of the rotor changes from 0.30 to 0.23 from hub to tip. Exit absolute Mach number is in a range from 0.11 to 0.10 from hub to tip. Figure 3 shows a rotor blade and a nozzle guide vane after final machining.

The design features of the blading and facility are given in Table 1.

**ORIGINAL PAGE IS
OF POOR QUALITY**

TABLE 1

OVERALL PERFORMANCE PARAMETERS		
Total temperature at inlet	TTO	520°R
Total pressure at inlet	PTO	14.7psia
Mass flow rate	W	24.32 lbm/s
Specific work output	ΔH	2.36 $\frac{\text{Btu.s}}{\text{lbm}}$
Rotational speed	N	1300 rpm
Total-to-total isentropic efficiency	η_{TT}	0.8930
Total pressure ratio	PTO/PT2	1.0778
Pressure drop	PT02-PT01	30" of water (56.04 mm Hg)
Pitchline reaction	RXP	0.3820
Power	HP	81.2hp
Torque	T	328.1 lbf.ft
Stator efficiency	η_s	0.9421
Rotor efficiency	η_r	0.8815
Mean swirl angle at exit of rotor (meas. from tangential dir.)	$\bar{\alpha}_2$	29.97°
No. of stators	n_v	23
No. of rotors	n_R	29

$$\text{where } \eta_s = \frac{\text{actual exit k.e.}}{\text{ideal exit k.e.}}$$

$$\eta_r = \frac{\text{actual relative exit k.e.}}{\text{ideal relative exit k.e.}}$$

$$\text{reaction} = \frac{\text{ideal static enthalpy drop across rotor}}{\text{ideal static enthalpy drop across stage}}$$

3. FACILITY INSTRUMENTATION

The Axial Flow Turbine Research facility is equipped with large number of static pressure holes (nearly 500) at carefully selected locations on the blade, vane, casing and hub walls. Static pressure measurements in the rotating frame will be taken by a 32 channel electronic pressure scanner located in the rotor frame. The signal output, after multiplexing in the rotor frame, will be passed through a slip ring unit for processing in a computer controlled data acquisition system.

To measure the shear stress on the walls and the blades, shear stress sensors are used in the turbine rig. These are deposited thin film, (V array) "glue on dual probes" manufactured by Dantec company. The construction is similar to those used by McCroskey (Ref. 8) and is shown in Fig. 4. A total of 23 dual element sensors are mounted around the rotor blade at mid span, with close spacing near the leading edge of the blade. In addition, five sensors will be located on the hub (endwall) of the rotor blade passage. The data from these shear stress sensors will be acquired using a PSI 156 channel data acquisition system (20 KHz). Unsteady shear stresses, which are extremely important quantities in the study of vane-blade interaction, will be recorded by a Kinetic Systems (CAMAC) high speed data acquisition system (1 MHz).

The implementation of the dynamic pressure transducers in the turbine rig was driven by space limitations. The pressure transducers are inserted into chambers, which in turn are connected to the turbine airfoil surfaces through 0.5 - 0.8 mm diameter holes. The design objective is to achieve a frequency response of 40 KHz. The sensors used are Kulite model XCS-093 with a pressure range of maximum 5 psia. They are capable of measuring pressure fluctuations to an accuracy of 0.01 psia. Details of a dynamic pressure transducer used in the Turbine Facility are given in Figure 5. Sixteen Kulite transducers are located along the chord at the mid span of the rotor blade. Seven transducers will be on the pressure side and the remaining nine will be located on the suction surface of the next blade in the same passage. A schematic showing the location of dynamic pressure transducers on the blade at midspan (sixteen) and on the hub (endwall) surface (five) is shown in Fig. 6. The low level signals from the dynamic pressure transducers are amplified in the rotating frame by using miniature instrumentation amplifiers. The amplifiers will rotate in the rotor frame and provide a high level signal output before the signal reaches the slip ring unit. These amplifiers are located inside the instrumentation drum shown in Fig. 7. It is expected that this amplification may help to improve the quality of output signal from the dynamic pressure transducers. A preliminary static calibration study of an XCS-093 transducer was performed for implementation in the turbine rig.

The LDV system available in the Turbomachinery Laboratory is a two channel fringe type laser anemometer (LDA) with on-axis back scatter light collection (TSI model 9100-6). The system operates with a 4 W Lexel argon-ion laser tuned for the green line (514.5 nm). The entire system comprising the laser, the transmitting and receiving optics is mounted on a table. The table can be moved along and perpendicular to the optical axis and can also be tilted in the vertical plane. The assembly is fitted on a hydraulic bench capable of moving in the vertical direction. The three degrees of freedom with the possibility to tilt the table helps to position the bisector of the beam in the radial direction. The LDV system will be used to measure most of the flow field, except the nearwall regions.

Provision has been made for hot wire measurement in both rotating and stationary system. Both two sensor and three sensor hot wire probes will be used in a stationary frame of reference to measure the boundary layers on stationary walls (on both the casing and hub walls) and the nozzle vane surface.

The mechanism used for traversing the rotating hot wire probe consists of both the circumferential and the radial traversing units. The hot wire probe location can be incrementally changed by using 0.019 degree steps, in circumferential direction. This motion is also checked and corrected for possible errors by an angular encoder device. The planetary gearbox providing this precision motion is driven by a stepping motor having a 25000 steps per revolution. Both the radial and circumferential traversing units will be simultaneously controlled by a computer based system.

4. DATA ACQUISITION AND PROCESSING

The Kulite, skin friction, heat transfer, hotwire and static pressure data from the rotor will be transmitted through the rotating drum to a slip ring unit (figure 1). The rotating drum consists of two probe traversing mechanisms for both the radial and the circumferential traverse, 4 constant temperature anemometers, a 32 channel electronic pressure scanner/transducer unit and a 30 channel data acquisition system for voltage inputs. The data acquisition system is shown in Fig. 8.

The slip ring unit is of brush type and has 150 channels. The slip ring unit is housed in a cowling in front of the facility (Fig. 1). The unit has a rigid one piece housing eliminating bearing alignment problems. Each ring carries four brushes made of silver graphite. The rings are made up of coin silver which withstands up to current levels of 5 Amps. The brushes are individually removable and replaceable. The contact resistance is about 5 milli.ohms maximum.

A medium speed data acquisition system with 96 channels of pressure transducers having a 20,000 samples per second capacity is available in the laboratory. The PSI model 780-B pressure measurement system is a fully integrated test instrument which offers a transducer per port for multipressure measurement applications. The present system is also capable of using an additional 60 channels which may be described as "electrical input" channels for signal types such as thermocouples, strain gauges, RTD's etc. This is a complete data acquisition system with a special emphasis on pressure measurement. Total system inaccuracy for pressure measurements including sensors is in the order of ± 0.10 percent full scale for the worst case. However, a typical value is in the order of ± 0.07 percent. The system is interfaced to an IBM compatible personal computer through an IEEE-488 (GPIB) with input output rates up to 30,000 bytes per second.

For high speed data acquisition, a 16 channel, 12 bit transient recorder with a 1 Megabyte solid state memory is planned (Kinetic Systems Int., 4022-DIA-4050-23A). This system will be built in a CAMAC crate. The acquisition system will be controlled by a parallel bus crate controller interfaced to an IBM PC-AT computer. With the current configuration the system will be able to store 500,000 measurements for a maximum duration of one second either in its own memory or in the computer storage medium. The main use of this system will be in the area of hotwire measurements, wall shear stress measurements, Kulite dynamic pressure measurements.

List of References

1. Lakshminarayana, B., Pouagare, M., Davino, R., "Three dimensional flow field in the tip region of a compressor rotor passage," Parts 1 and 2, J. Engineering for Power, Vol. 104, No. 4, P. 760-771, Oct. 82.
2. Pandya and Lakshminarayana, "Investigation of the tip clearance flow inside and at the exit of a compressor rotor passage," Parts 1 and 2, J. Engineering for Power, Vol. 105, p. 1-17, Jan. 83.
3. Lakshminarayana, B., et al., "Annulus wall boundary layer growth in a compressor stage including the effects of tip clearance," AGARD CP 351, p. 21-1 to 21-17, 1983.
4. Lakshminarayana, B., Camci, C., "Description of Axial Flow Turbine Facility and a Broad Outline of Proposed Research," unpublished Penn State Report, 1989.
5. Camci, C. and Arts, T., "Experimental Heat Transfer Investigation Around the Film Cooled Leading Edge of a High Pressure Gas Turbine Rotor Blade," Trans. of the ASME, J. of Engr. for Gas Turbines and Power, Vol. 106, No. 4, pp. 1016-1020, October 1985.
6. Camci, C. and Arts, T., "Short Duration Measurements and Numerical Simulation of Heat Transfer Along the Suction Side of a Film Cooled Gas Turbine Blade," J. of Engr. for Gas Turbines and Power, Vol. 106, No. 4, pp. 991-997, October 1985.
7. Halliwell, I., Blade Design for Penn State Axial Flow Turbine Facility, unpublished, 1988.
8. McCroskey, W. J. and E. J. Durbin, "Flow Angle and Shear Stress Measurements using Heated Films and Wires," Transactions of the ASME, March 1972, pp. 46-52.

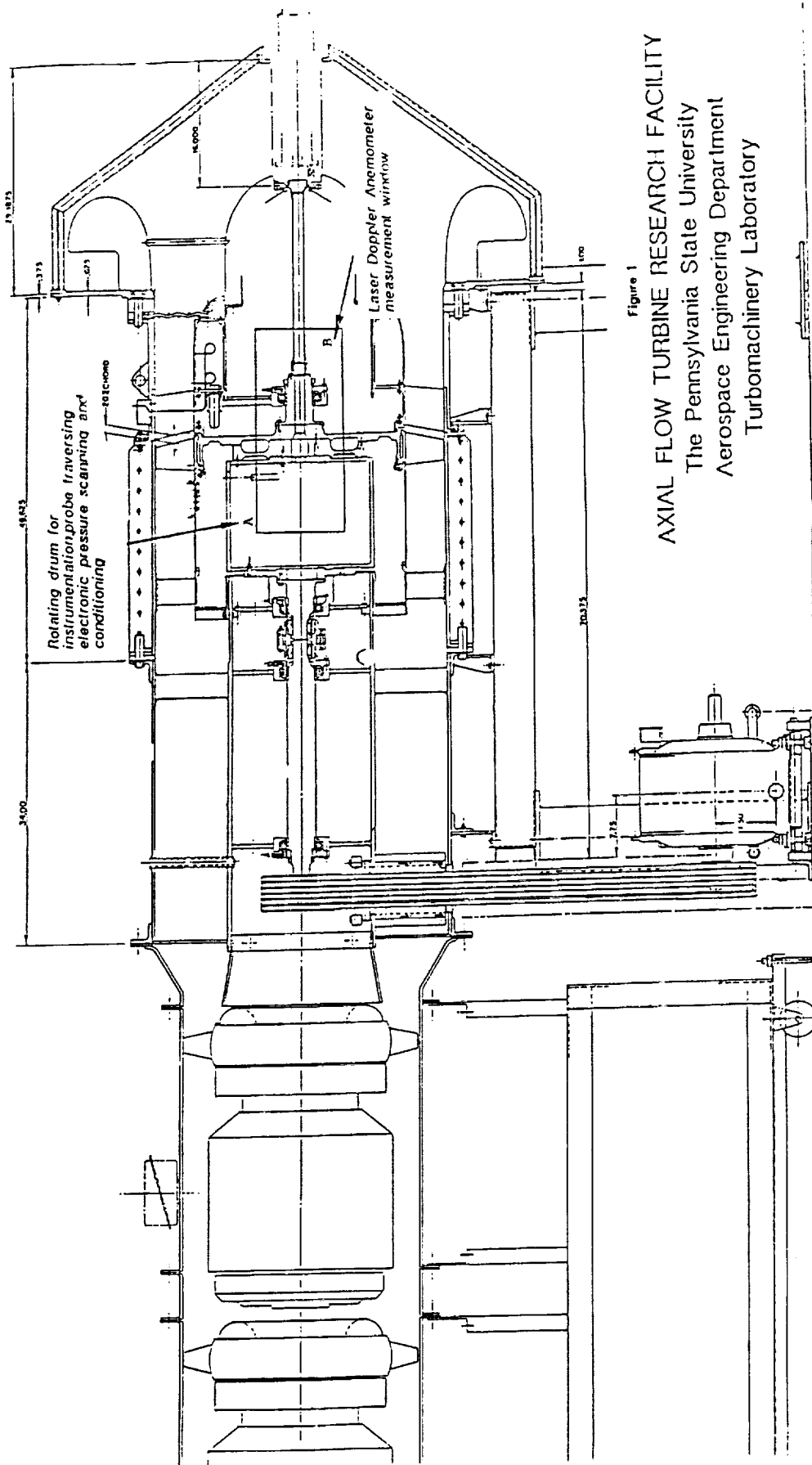


Figure 1
AXIAL FLOW TURBINE RESEARCH FACILITY
The Pennsylvania State University
Aerospace Engineering Department
Turbomachinery Laboratory

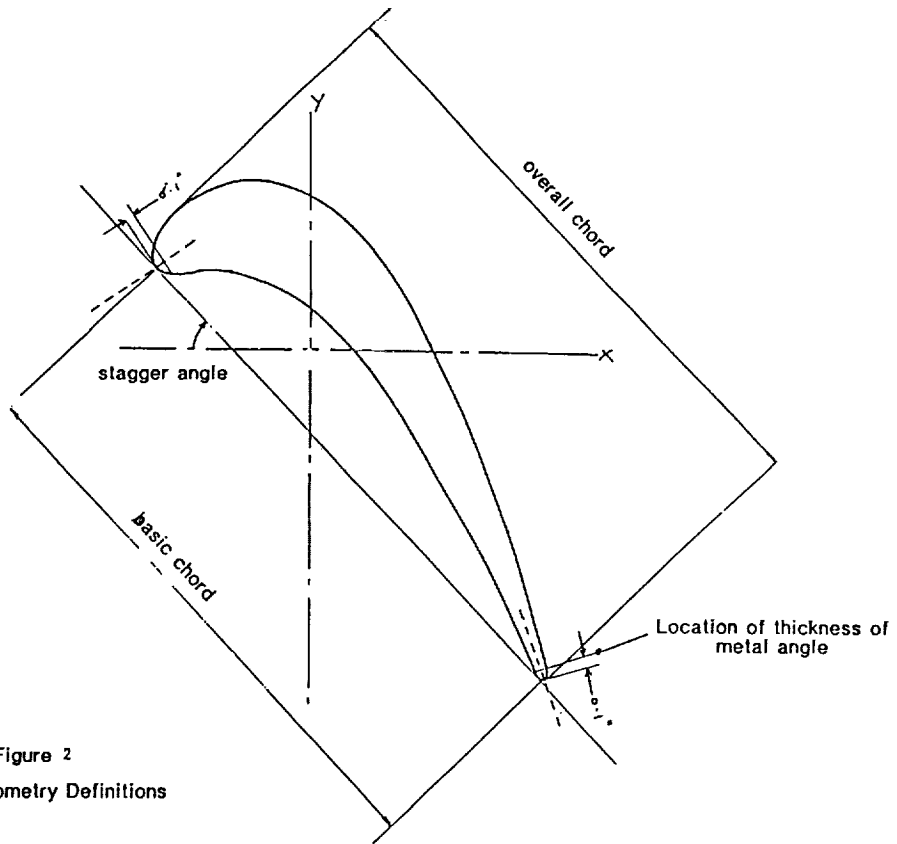


Figure 2
Blade Geometry Definitions

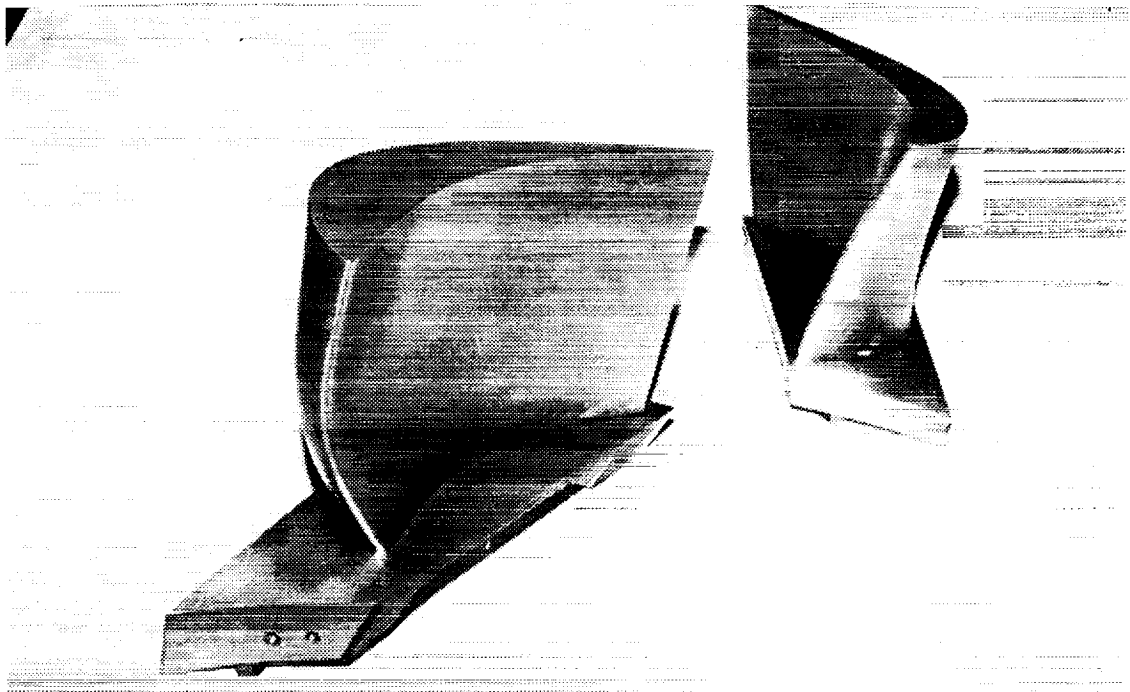


Figure 3
A Nozzle Guide Vane and a Rotor Blade
After Final Machining

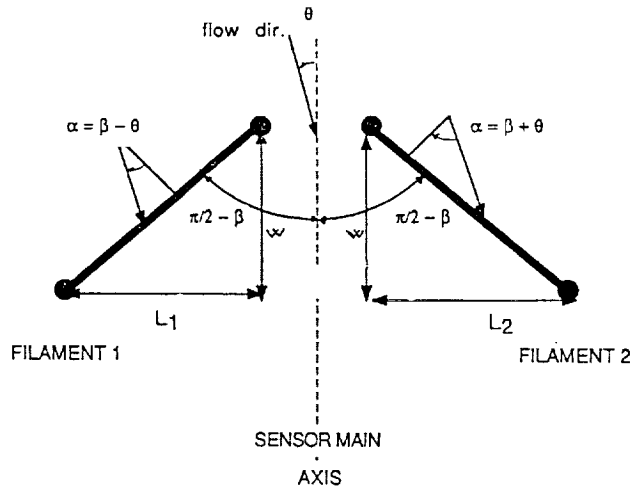


Figure 4

Geometry of a Twin Element, V configuration
Shear Stress Gauge

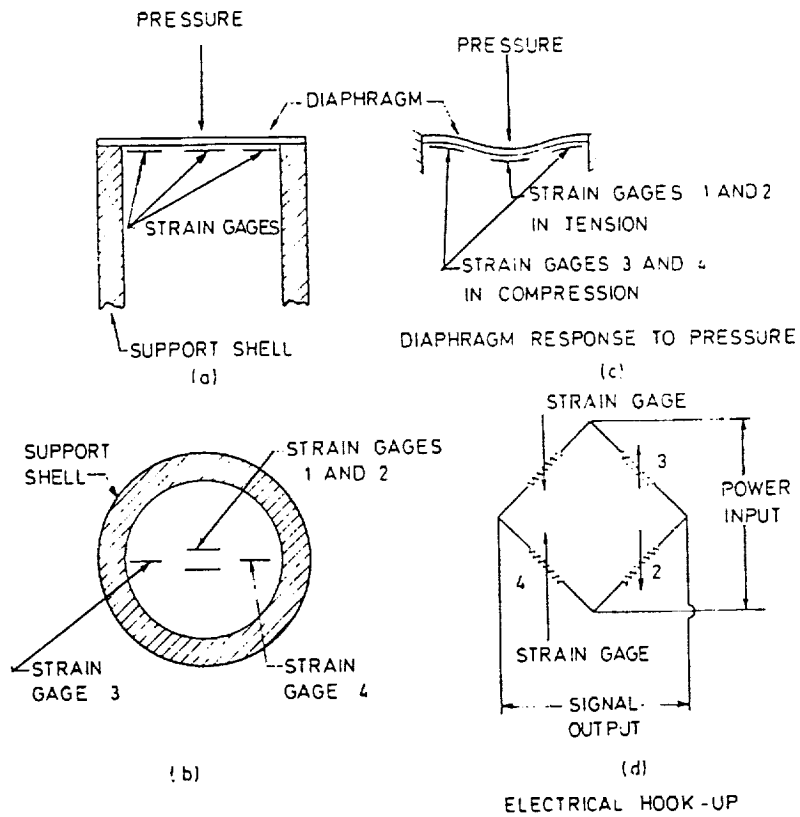
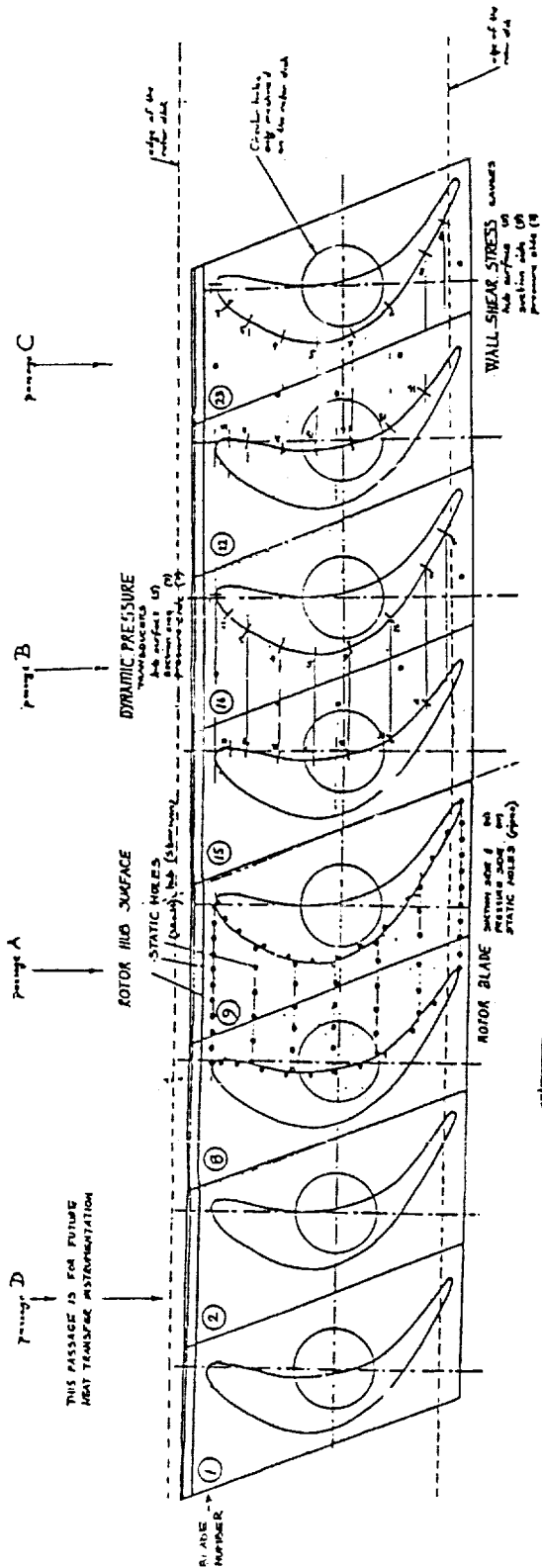


Figure 5

Silicon Based Semiconductor Strain Gauge
Pressure Transducer



FIGIT CIRCULAR OPENINGS ARE TO BE MACHINED ON THE DIAR SURFACE

PASSAGE A		MAX 8 / MIN 2
STATIC PRESSURE HOLES		
Hub surface	(10, 11)	
Pressure surface	(10)	
Suction surface	(11)	
PASSAGE B		MAX 8 / MIN 2
DYNAMIC PRESSURE TRANSDUCERS		
Hub surface	(5)	
Pressure surface	(6)	
Suction surface	(7)	
PASSAGE C		MAX 22 / MIN 23
WALL SHEAR STRESS GAUGES		
Hub surface	(8)	
Pressure surface	(9)	
Suction surface	(10)	
PASSAGE D		MAX 1 / MIN 2
FOR FUTURE HEAT TRANSFER INSTRUMENTATION		

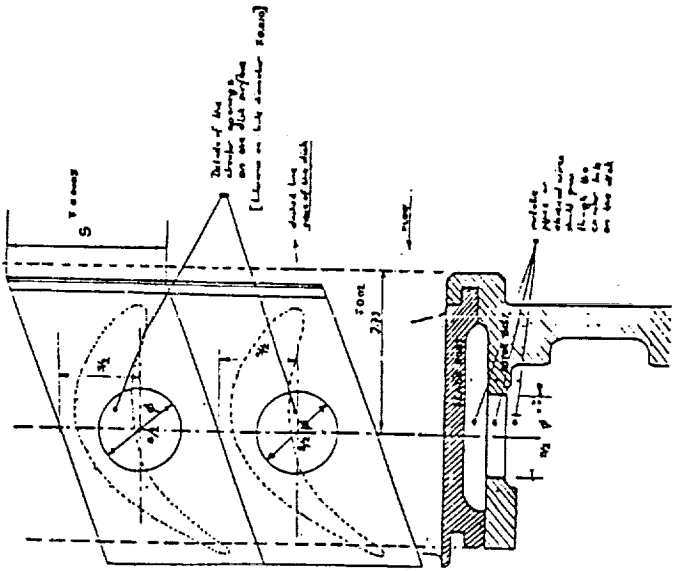


Figure 6
Rotor Instrumentation Details

ORIGINAL PAGE IS
OF POOR QUALITY

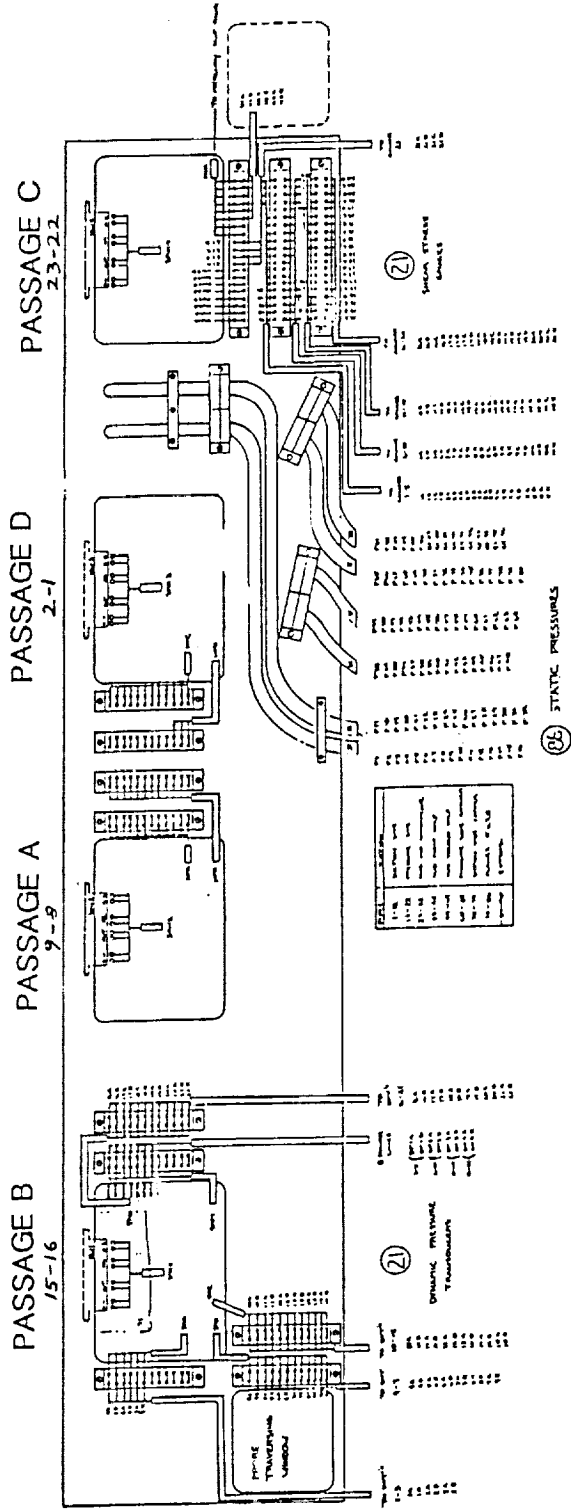
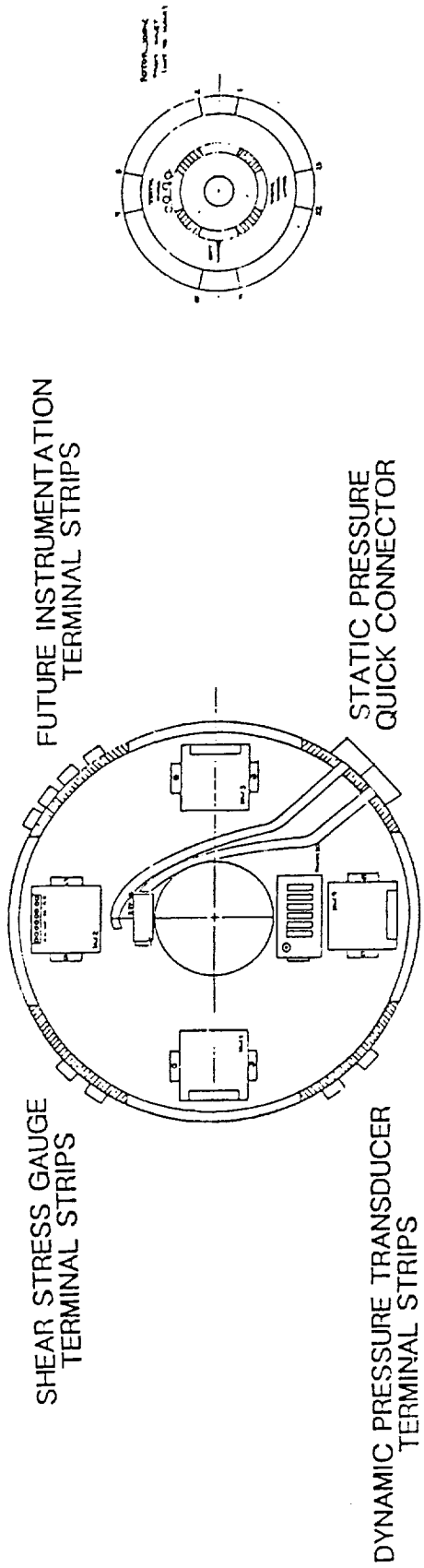


Figure 7
Details of the Rotating Instrumentation Drum

ORIGINAL PAGE IS OF POOR QUALITY

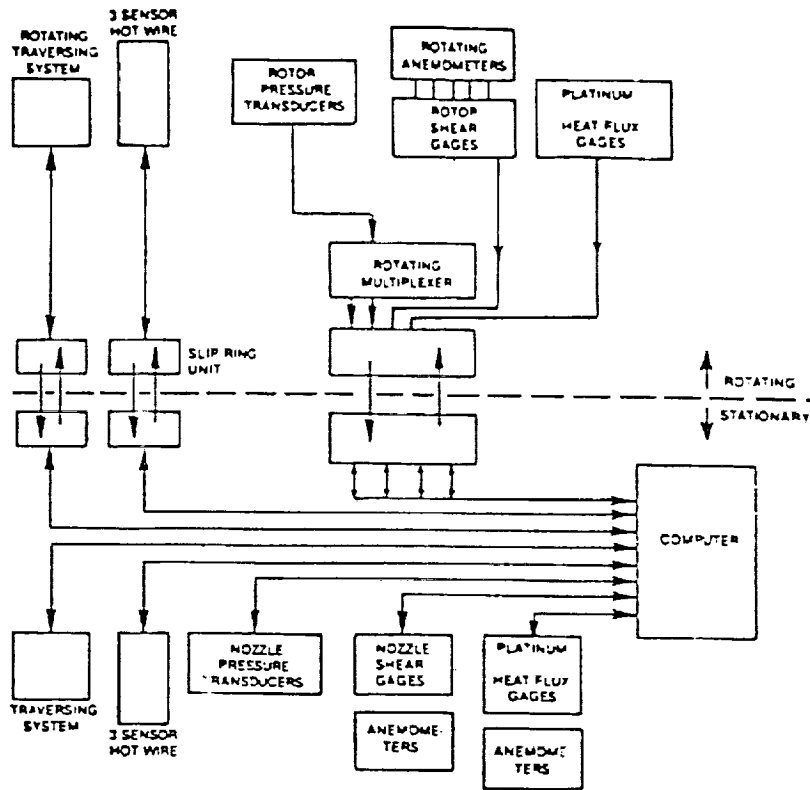


Figure 8

Measurement Chain and Data Acquisition System
 in the Stationary and Rotor Frame of the
 Pennsylvania State University AFTRF

ORIGINAL PAGE IS
 OF POOR QUALITY

AN UNCONDITIONALLY STABLE RUNGE-KUTTA METHOD FOR UNSTEADY
ROTOR-STATOR INTERACTION

Rodrick V. Chima and Philip C.E. Jorgenson
NASA Lewis Research Center

530-34
19887

A quasi-three-dimensional analysis has been developed for unsteady rotor-stator interaction in turbomachinery. The analysis solves the unsteady Euler or thin-layer Navier-Stokes equations in a body-fitted coordinate system. It accounts for the effects of rotation, radius change, and stream-surface thickness. The Baldwin-Lomax eddy-viscosity model is used for turbulent flows. The equations are integrated in time using an explicit four-stage Runge-Kutta scheme with a constant time step. Implicit residual smoothing is used to increase the stability limit of the time-accurate computations. The scheme is described, and stability and accuracy analyses are given.

Results are shown for the stage of the space shuttle main engine high pressure fuel turbopump. Two stators and three rotors were used to model the 41:63 blade ratio of the actual machine. Implicit residual smoothing was used to increase the time step limit of the explicit scheme by a factor of six with negligible differences in the unsteady results. We feel that the implicitly smoothed Runge-Kutta scheme is easily competitive with implicit schemes for unsteady flows while retaining the simplicity of an explicit scheme.

REFERENCE

Jorgenson, P.C.E.; and Chima, R.V.: An Unconditionally Stable Runge-Kutta Method for Unsteady Flows. AIAA paper 89-0205, Jan. 1989.

UNSTEADY ROTOR-STATOR INTERACTION CODE

DEVELOPED BY P. C. E. JORGENSEN & R. V. CHIMA

DESCRIPTION

- UNSTEADY THIN-LAYER NAVIER-STOKES SOLVER FOR ROTOR-STATOR INTERACTION

FEATURES

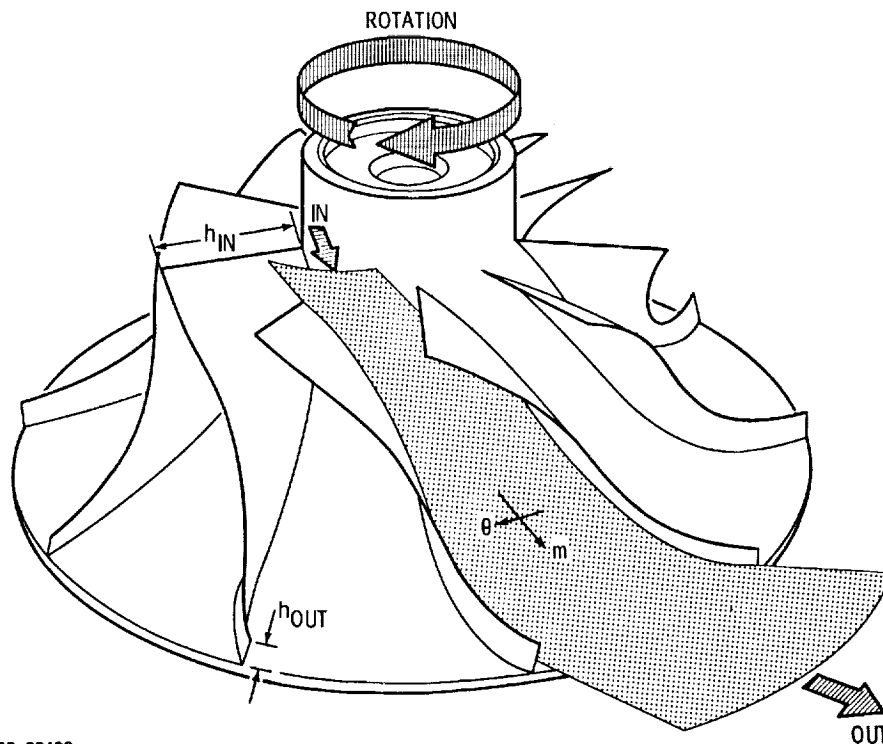
- QUASI-3-D FORMULATION
INCLUDES ROTATION, RADIUS CHANGE, & STREAM SURFACE THICKNESS
- C-TYPE GRIDS OVERLAP AT INTERFACE
- MULTI PASSAGE CAPABILITY
- EXPLICIT RUNGE-KUTTA SCHEME + IMPLICIT RESIDUAL SMOOTHING
UNCONDITIONALLY STABLE (PRACTICAL LIMIT $CFL = O(20)$)
2nd ORDER TIME ACCURATE
FIRST USE OF IMPLICIT SMOOTHING FOR UNSTEADY PROBLEMS

RESULTS

- SPACE SHUTTLE MAIN ENGINE TURBINE

CD-89-39438

QUASI-THREE-DIMENSIONAL STREAM SURFACE



CD-89-39439

QUASI-3-D THIN LAYER NAVIER-STOKES EQUATIONS

$$\partial_t \hat{q} + \partial_\epsilon \hat{E} + \partial_\eta (\hat{F} - Re^{-1} \hat{S}) = \hat{K}$$

$$\hat{q} = 1/\bar{J} \begin{bmatrix} \rho \\ \rho v_m \\ \rho v_\theta r \\ e \end{bmatrix}, \hat{E} = 1/\bar{J} \begin{bmatrix} \rho W^\epsilon \\ \rho v_m W^\epsilon + \epsilon_m p \\ (\rho v_\theta W^\epsilon + \bar{\epsilon}_\theta p) r \\ (e + p) W^\epsilon + r \Omega \bar{\epsilon}_\theta p \end{bmatrix}, \hat{F} = 1/\bar{J} \begin{bmatrix} \rho W^\eta \\ \rho v_m W^\eta + \eta_m p \\ (\rho v_\theta W^\eta + \bar{\eta}_\theta p) r \\ (e + p) W^\eta + r \Omega \bar{\eta}_\theta p \end{bmatrix}, \hat{K} = 1/\bar{J} \begin{bmatrix} 0 \\ K_2 \\ 0 \\ 0 \end{bmatrix}, \hat{S} = 1/\bar{J} \begin{bmatrix} 0 \\ S_2 \\ S_3 r \\ S_4 \end{bmatrix}$$

WHERE

$$\left. \begin{aligned} W^\epsilon &= \epsilon_m v_m + \bar{\epsilon}_\theta w_\theta \\ W^\eta &= \eta_m v_m + \bar{\eta}_\theta w_\theta \end{aligned} \right\} \text{CONTRAVARIANT VELOCITY COMPONENTS IN RELATIVE SYSTEM}$$

$$w_\theta = v_\theta - r\Omega \quad \text{RELATIVE TANGENTIAL VELOCITY}$$

$$\Omega = \text{BLADE ROTATION SPEED}$$

$$K_2 = (\rho v_\theta^2 + p - Re^{-1} \sigma_{22}) \partial_m r/r + (p - Re^{-1} \sigma_{33}) \partial_m h/h$$

= CENTRIFUGAL FORCE TERM + $\rho \partial_m$ (AREA)

$$\bar{\epsilon}_\theta = \epsilon_\theta / r$$

: θ -METRICS SCALED BY $1/r$

$$\bar{\eta}_\theta = \eta_\theta / r$$

$$1/\bar{J} = rh/J : \text{JACOBIAN SCALED BY AREA}$$

CD-89-39440

ROTOR-STATOR INTERACTION CODE DETAILS

INITIAL CONDITIONS

ANALYTIC 1-D SOLUTION OF FLOW EQUATIONS WITH AREA CHANGE

BOUNDARY CONDITIONS

INLET

P_0 , T_0 , AND v_θ SPECIFIED

$$R^- = v_m - \frac{2a}{\gamma-1} \quad \text{EXTRAPOLATED}$$

EXIT

P SPECIFIED

3 CONSERVATION VARIABLES EXTRAPOLATED

WALLS

INVISCID FLOW = TANGENCY, ρ EXTRAPOLATED

VISCOUS FLOW = NO-SLIP, T_w SPECIFIED

NORMAL MOMENTUM EQUATION FOR PRESSURE

PERIODIC BOUNDARIES

SOLVED LIKE INTERIOR POINTS

CD-89-39441

MULTISTAGE RUNGE-KUTTA ALGORITHM

GOVERNING EQUATIONS

$$\partial_t q = -J [R_I - (R_V + D)]$$

R_I = INVISCID RESIDUAL

R_V = VISCOUS RESIDUAL

D = ARTIFICIAL DISSIPATION TERM

MULTISTAGE SCHEME

$$q_0 = q_n$$

$$q_1 = q_0 - \alpha_1 J \Delta t [R_I q_0 - (R_V + D) q_0]$$

⋮

$$q_k = q_0 - \alpha_k J \Delta t [R_I q_{k-1} - (R_V + D) q_0]$$

$$q_{n+1} = q_k$$

R_V & D EVALUATED AT FIRST STAGE ONLY

CD-89-39442

ARTIFICIAL DISSIPATION

NONCONSERVATIVE VERSION OF JAMESON FORMULATION

$$Dq = (D_\xi + D_\eta) q$$

ξ -DIRECTION OPERATOR

$$D_\xi q = C (V_2 q_{\xi\xi\xi} - V_4 q_{\xi\xi\xi\xi})$$

WHERE:

$$C = \frac{1}{J \Delta t_{i,j}}$$

(LOCAL $\Delta t_{i,j}$ MINIMIZES DISSIPATION)

$$V_2 = \mu_2 \max(\nu_{i+1}, \nu_i, \nu_{i-1})$$

$$V_4 = \max(0, \mu_4 - V_2)$$

AND

$$\nu_{i,j} = \frac{|P_{i+1,j} - 2P_{i,j} + P_{i-1,j}|}{|P_{i+1,j} + 2P_{i,j} + P_{i-1,j}|}$$

$$\mu_2 = O(1)$$

$$\mu_4 = O\left(\frac{1}{16}\right)$$

CD-89-39443

IMPLICIT RESIDUAL SMOOTHING

USE A TIME STEP GREATER THAN THE STABILITY LIMIT
MAINTAIN STABILITY BY SMOOTHING THE RESIDUAL IMPLICITLY
REWRITE STAGE (K) OF MULTISTAGE SCHEME AS

$$\Delta q^{(k)} \equiv q^{(k)} - q^{(0)} = -\alpha_k \bar{J} \Delta t \left[Rq^{(k-1)} - Dq^{(0)} \right]$$

IMPLICIT SMOOTHING STEP

$$(1 - \varepsilon \delta_{\xi\xi})(1 - \varepsilon \delta_{\eta\eta}) \overline{\Delta q^{(k)}} = \Delta q^{(k)}$$

$$q^{(k)} = q^{(0)} + \overline{\Delta q^{(k)}}$$

UNCONDITIONALLY STABLE IF

$$\varepsilon \geq \frac{1}{4} \left[\left(\frac{CFL}{CFL^*} \right)^2 - 1 \right]$$

WHERE

CFL^* IS COURANT LIMIT OF THE UNSMOOTHED SCHEME
 CFL IS THE LARGER OPERATING COURANT NUMBER

CD-89-39444

IMPLICIT RESIDUAL SMOOTHING

TWO-DIMENSIONAL LOCAL SMOOTHING PARAMETER

$$\varepsilon_{ij} = \max \left\{ 0, \frac{1}{4} \left[\left(\frac{CFL_{ij}}{CFL^*} \right)^2 - 1 \right] \right\}$$

WHERE

CFL^* IS COURANT LIMIT OF THE UNSMOOTHED SCHEME
 CFL_{ij} IS THE LOCAL COURANT NUMBER

CD-89-39445

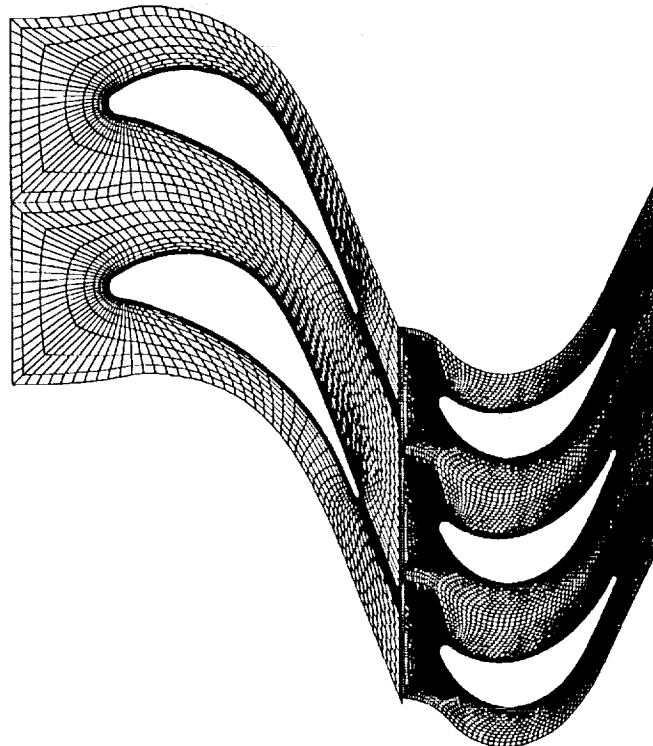
IMPLICIT RESIDUAL SMOOTHING

FEATURES

- IRS DOES NOT EFFECT FORMAL TIME ACCURACY OF R-K SCHEME
- SMOOTHING ONLY OCCURS WHERE LOCAL COURANT NUMBER CFL_{ij} IS GREATER THAN THE COURANT LIMIT OF THE R-K SCHEME CFL^* (EG - VISCOUS REGION)
- CAN USE $CFL = O(10 - 20)$ IN VISCOUS REGIONS WHILE $CFL = O(.1)$ IN INVISCID CORE
- ϵ_{ij} EASY TO COMPUTE, OR CAN BE STORED
- IRS REQUIRES SCALAR TRIDIAGONAL INVERSION ALONG EACH GRID LINE
ADDS APPROXIMATELY 26% TO CPU TIME BUT BOOSTS TIME STEP BY 652% FOR A NET DECREASE OF 460% IN CPU TIME
- EXPLICIT R-K SCHEME WITH IRS COMPETITIVE WITH IMPLICIT SCHEMES FOR UNSTEADY PROBLEMS

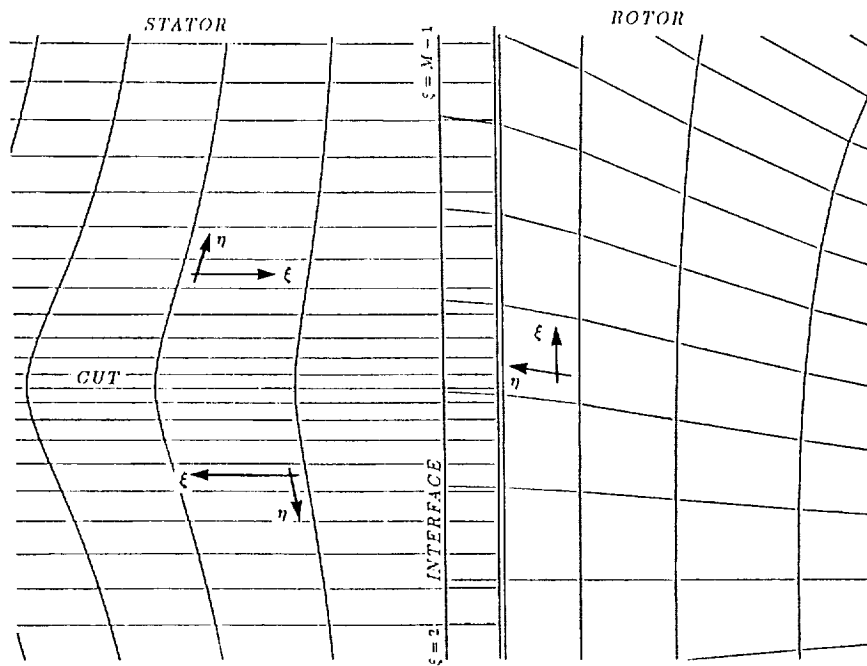
CD-89-39446

SSME STATOR AND ROTOR GRIDS



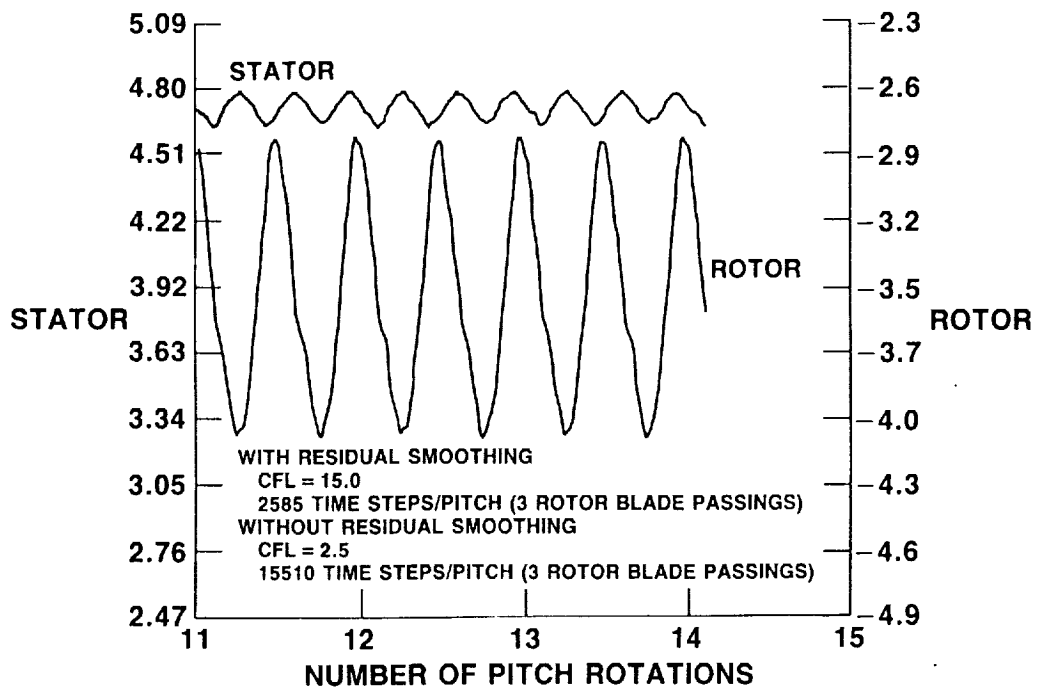
CD-89-39447

DETAIL OF STATOR/ROTOR GRID OVERLAP



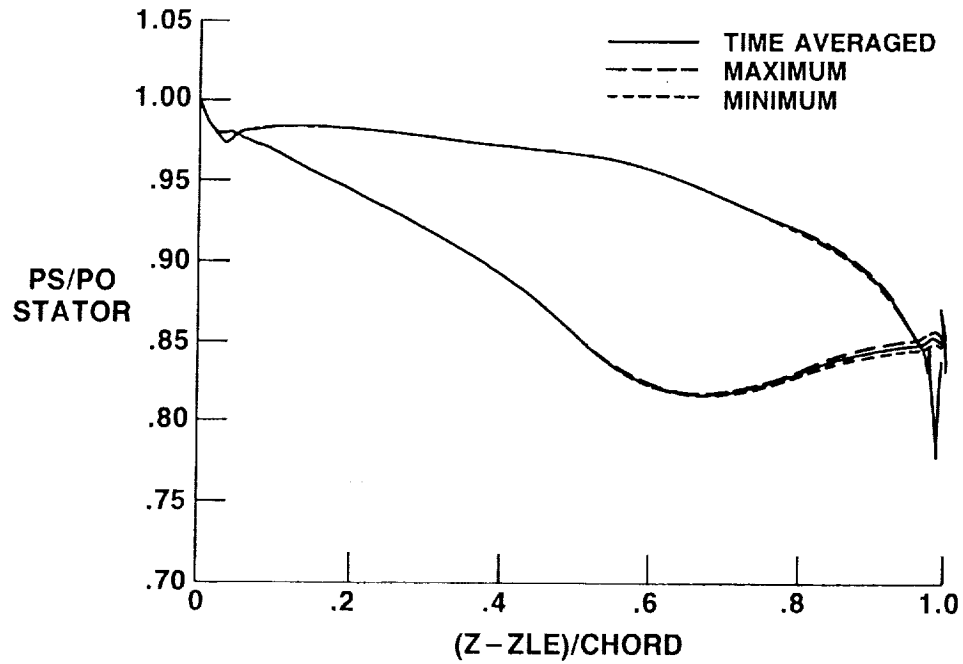
CD-89-3944B

UNSTEADY LIFT COEFFICIENTS ON STATOR AND ROTOR



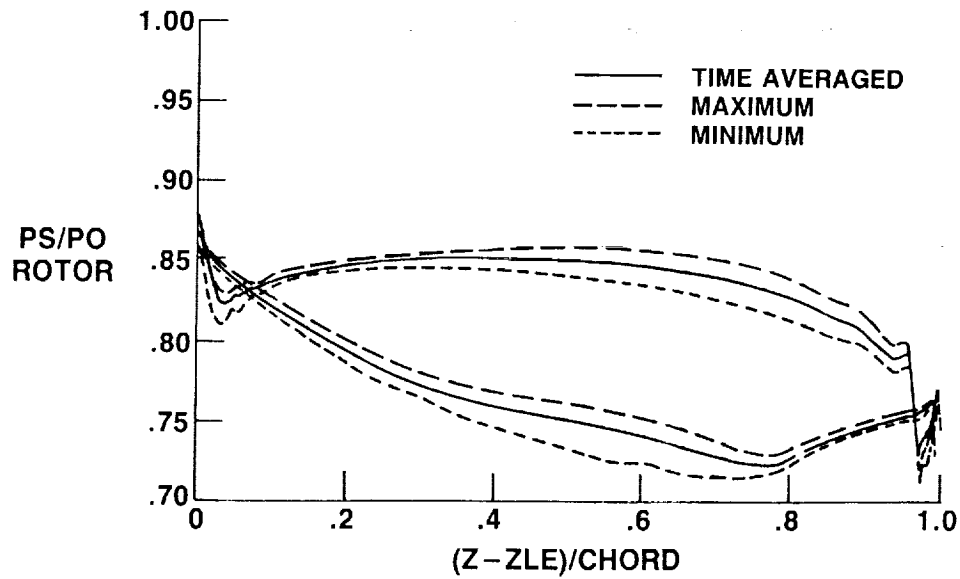
CD-89-39449

PRESSURE DISTRIBUTION ENVELOPE ON STATOR



CD-89-39450

PRESSURE DISTRIBUTION ENVELOPE ON ROTOR



CD-89-39451

ABSOLUTE MACH NUMBER CONTOURS



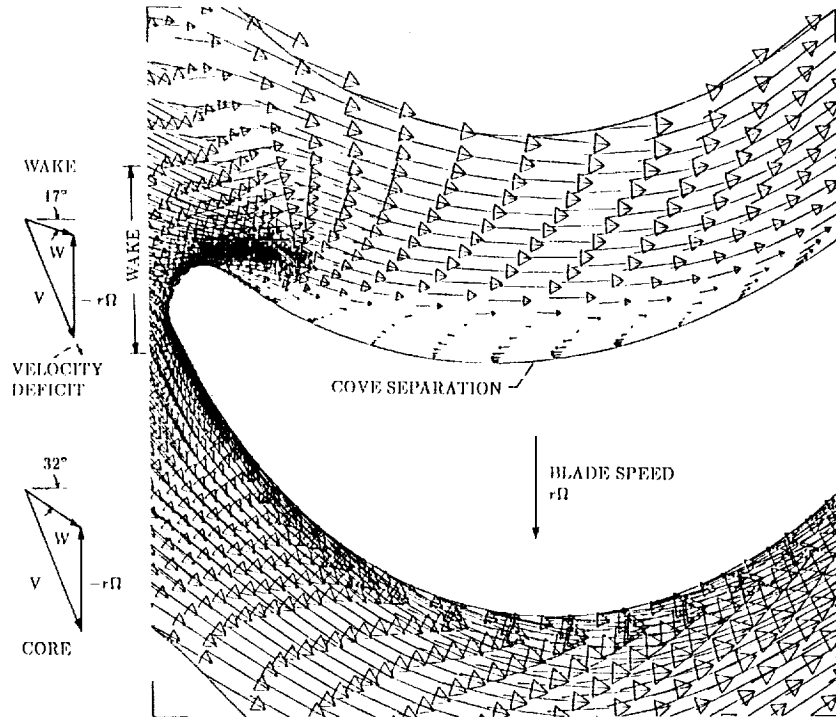
CD-89-39452

ENTROPY CONTOURS



CD-89-39453

VELOCITY VECTORS AROUND ROTOR



CD-89-39454

UNSTEADY ROTOR/STATOR INTERACTION CODE

CONCLUDING REMARKS

- TIME-ACCURATE ROTOR/STATOR INTERACTION CODE HAS BEEN DEVELOPED
- CODE IS APPLICABLE TO AXIAL OR RADIAL MACHINES
- VISCOUS RESULTS FOR SSME TURBINE SHOW UNSTEADY LOADING & SEPARATION, & MIGRATION OF STATOR WAKES
- IMPLICIT RESIDUAL SMOOTHING DOES NOT EFFECT FORMAL TIME ACCURACY OF R-K SCHEME
 ADDS 26% TO CPU TIME
 INCREASED TIME STEP BY A FACTOR OF 6.0
 RESULTS IN A NET DECREASE OF ABOUT 450% IN CPU TIME
 MAKES EXPLICIT R-K SCHEME COMPETITIVE WITH IMPLICIT SCHEMES FOR UNSTEADY PROBLEMS

CD-89-39455

531-34
19888

AVERAGE-PASSAGE FLOW MODEL DEVELOPMENT

John J. Adamczyk
NASA Lewis Research Center

Mark L. Celestina, Tim A. Beach, Kevin Kirtley,
Sverdrup Technology, Inc.
Lewis Research Center Group

and

Mark Barnett
United Technologies Research Center

A research effort has been underway to develop a three-dimensional model for simulating multistage turbomachinery flows using today's supercomputers. This model, referred to as the "average passage" flow model, describes the time-averaged flow field within a typical passage of a bladed wheel within a multistage configuration. To date, a number of inviscid simulations have been executed to assess the resolution capabilities of the model. Recently, the viscous terms associated with the "average passage" model have been incorporated into the inviscid computer code along with an algebraic turbulence model. A simulation of a stage-and-one-half, low-speed turbine has been executed. The results of this simulation, including a comparison with experimental data, is the subject of this report.

A goal of computational fluid dynamics for turbomachinery is the prediction of performance parameters and the flow processes which set their values. Achieving this goal for multistage machinery is made difficult by the wide range of length and time scales in the associated flow fields. Currently, the procedure used in the design and off-design analysis is based on a quasi-three-dimensional flow model whose origins can be traced to the late forties and early fifties.

Although proven useful, this flow model has its limitations. Among these are the inability to analyze off-design performance and unconventional machinery where extrapolation of the underlying empirical data base is required. Other problems arise whenever there are large local variations in the radial velocity component within a blade passage. It is generally agreed that a way of overcoming these shortcomings is the development of true three-dimensional flow models. The "average passage" flow model under development at Lewis Research Center is such a model. The objective of this paper is to present the status of the development of this model for multistage turbines. This will include several comparisons with measurements obtained from a recently completed experimental program at the United Technologies Research Center.

SIMULATION RESULTS

The simulation executed was the low-speed rotating rig at United Technologies Research Center. The low-speed rotating rig (LSRR) is a stage-and-one-half turbine consisting of an inlet guide vane, a rotor, and a stator. The inlet guide vane contains 22 blades, and the rotor and stator both contain 28 blades. The flow coefficient, ϕ , is 0.78, and the spacing between blades, B_x , is 0.5. The LSRR grid contains 228 axial, 25 radial, and 41 circumferential points. Each blade row contains 40 axial points distributed along the chord with 26 axial points between each blade row, the inlet and exit.

The results presented required 11 hours of Cray 2 CPU time. They represent but a small fraction of the information obtained from the simulation. They are intended to illustrate the degree to which one can quantitatively predict performance parameters that are of interest to designers and to reveal qualitative information identifying flow phenomena that may have an effect on performance. These results also reflect the current state of model development. The first series of results shows the predicted pressure distribution on the surface of each blade row of the turbine as a function of axial chord length and percent of span height. The span locations measured from the hub are 1.3, 12.5, 50, 87.5, and 98.7 percent, respectively. The experimental measurements taken at these locations are also shown. Experimental data were also available for 25 and 75 percent of span, but were not used, since they provided little additional information relative to the current discussion. The results for the first vane are shown in figure 1. The predicted loading level is in good agreement with the measurements of Dring (1988). The predicted pressure-surface pressure distribution is in excellent agreement with the experimental results. For the suction surface the agreement between measurement and simulation is good for the region forward of the minimum pressure peak. Aft of the peak the agreement between experiment and simulation deteriorates. This deterioration is believed to be related to viscous effects (i.e., turbulence and transition modeling) whose modeling could be improved. Some exploratory calculations suggest that the boundary layer aft of the suction-surface minimum pressure is growing too rapidly and, as a result of the radial pressure gradient, is being transported toward the hub to an extent greater than that suggested by flow visualization studies. Improvements in the agreement between simulation and experiment have been obtained by incorporating a simple transition model in which the flow remains laminar forward of the minimum pressure peak and Baldwin-Lomax turbulence model as implemented by Dawes (1986).

Figure 2 shows the results for the first blade row, which incorporated these changes in the turbulence model. The improvement is obvious. The remaining results for the rotor and second stator incorporated the modified turbulence model. Figure 3 shows the predicted and measured pressure distribution for the rotor. The predicted loading levels appear to be in good agreement with measurements, with the exception of the hub and tip region. The present simulation does not include a clearance region, which should account for some of the discrepancy in the tip region. The pressure distribution along the pressure surface is once more in excellent agreement with the measurements. At the midspan and at 25 and 75 percent (not shown) of span, the predicted pressure distribution along the suction surface is in good agreement with the data. At 1.3 and 12.5 percent of span, the suction-surface pressure coefficient is lower than that measured. As a result, the loading is lower over the forward portion of the rotor than what has been measured. Although

the cause of this discrepancy is, at present, unknown, one could speculate that it may be due to an improper estimate of the magnitude and extent of the low momentum fluid exiting the first vane.

The pressure distribution for the last vane is shown in figure 4. Once again, the loading level is well predicted, with the exception of the 1.3 percent of span location. The underpredicted suction-surface pressure coefficient at 1.3 and 12.5 percent of span suggests that the flow incidence to these sections is underestimated. There also appears to be a shift of the predicted pressure distribution relative to the measured distribution. This shift is believed to be caused by an overestimate of the loss generated by the first two blade rows. With the exception of this discrepancy, the pressure distribution on the pressure surface is in good agreement with measurements. Similarly, the predicted suction-surface distribution at midspan agrees well with the experimental distribution.

Currently, the results of this simulation are being reduced to a format which will allow for the comparison with measurements of total pressure level and flow angle. This comparison should provide additional information for judging the accuracy of the simulation.

SUMMARY AND CONCLUSION

Given the early state of the average passage model development, the results presented in this report are very encouraging. The amount of empirical information used in the stage-and-one-half turbine simulation is considerably less than that required to achieve comparable results using today's quasi-three-dimensional flow models.

FIRST BLADE PRESSURE DISTRIBUTIONS FIRST VANE

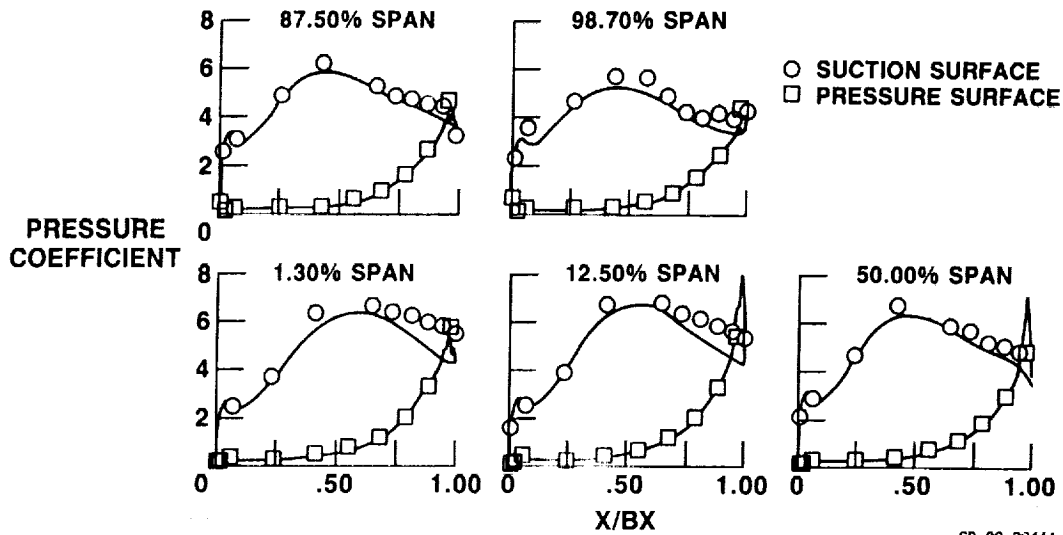


Figure 1

CD-89-39411

BLADE PRESSURE DISTRIBUTIONS FIRST BLADE ROW

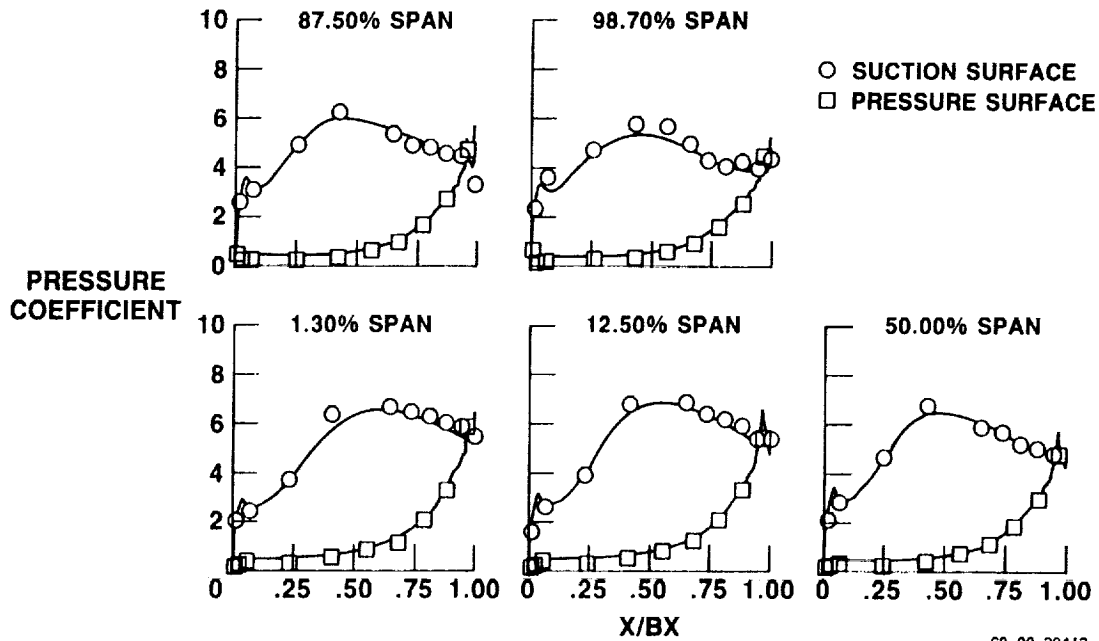


Figure 2

CD-89-39412

BLADE PRESSURE DISTRIBUTIONS ROTOR

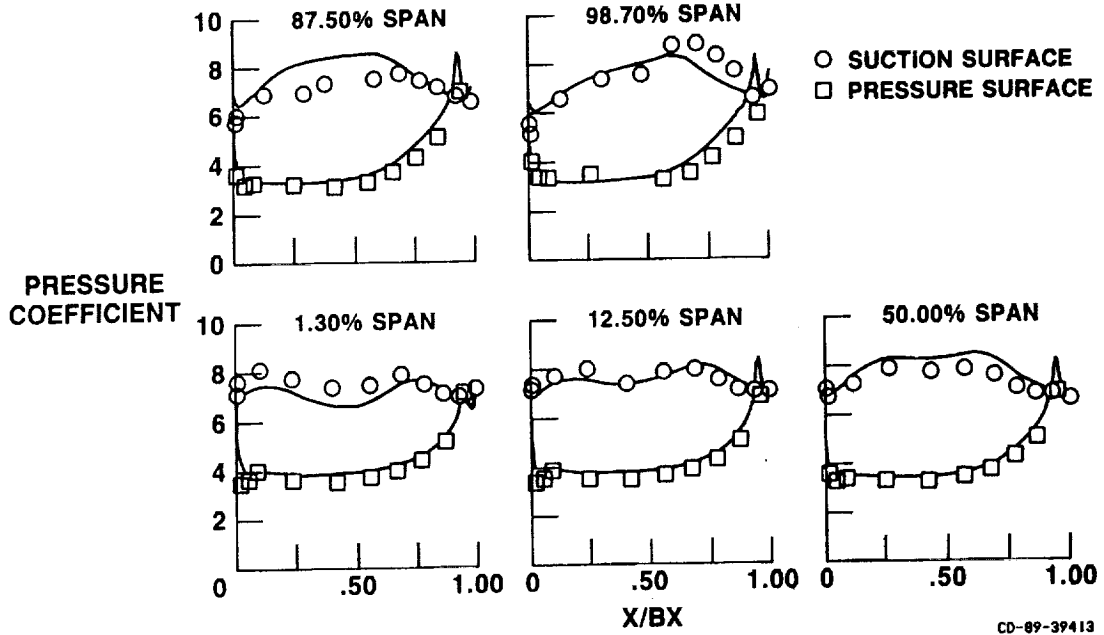


Figure 3

BLADE PRESSURE DISTRIBUTIONS LAST VANE

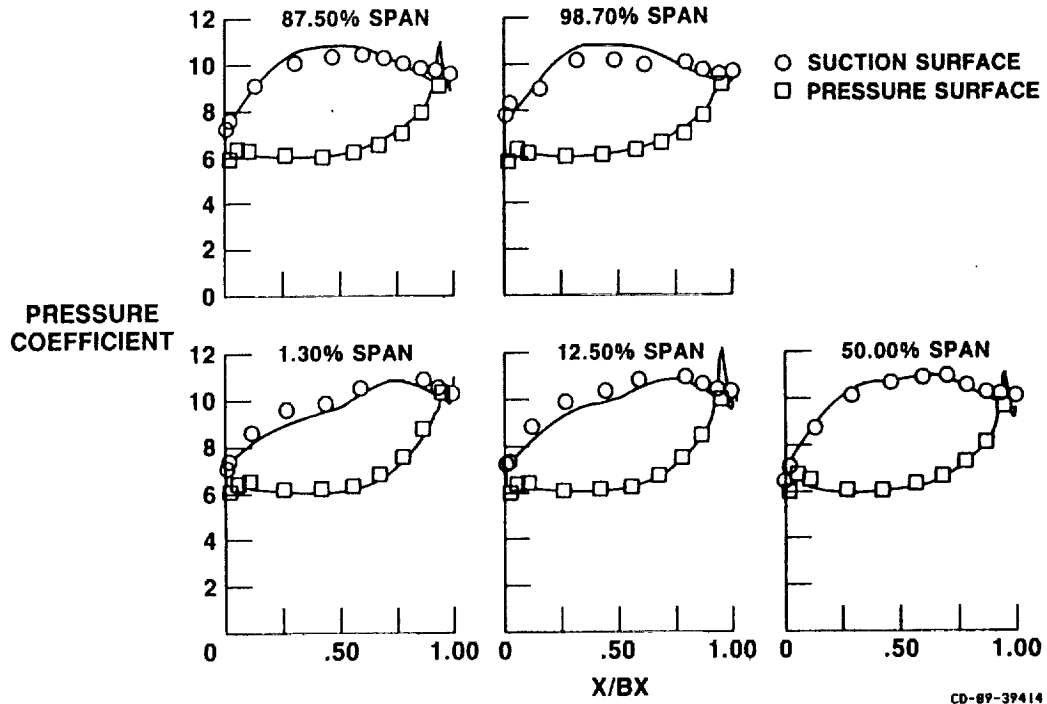


Figure 4



Report Documentation Page

1. Report No. NASA CP-10030	2. Government Accession No.	3. Recipient's Catalog No.	
4. Title and Subtitle Structural Integrity and Durability of Reusable Space Propulsion Systems		5. Report Date April 1989	6. Performing Organization Code
		7. Author(s)	
9. Performing Organization Name and Address National Aeronautics and Space Administration Lewis Research Center Cleveland, Ohio 44135-3191		8. Performing Organization Report No. E-4628	10. Work Unit No. 553-13-00
		11. Contract or Grant No.	
12. Sponsoring Agency Name and Address National Aeronautics and Space Administration Washington, D.C. 20546-0001		13. Type of Report and Period Covered Conference Publication	
		14. Sponsoring Agency Code	
15. Supplementary Notes			
16. Abstract A two-day conference on the structural integrity and durability of reusable space propulsion systems was held on April 18 and 19, 1989, at the NASA Lewis Research Center. Presentations were made by industry, university, and government researchers organized into four sessions: aerothermodynamic loads; instrumentation; fatigue, fracture, and constitutive modeling; and structural dynamics. The principal objectives of the conference were to disseminate research results to date and future plans in each of the four areas. This publication contains the extended abstracts and visual material presented during the conference.			
17. Key Words (Suggested by Author(s)) Earth-to-orbit proportion; Reusable rocket systems; Aerothermodynamic loads; Fatigue; Constitutive modeling; Instrumentation			
		Date for general release _____ April 1991 _____	
		Subject Category 20	
19. Security Classif. (of this report) Unclassified	20. Security Classif. (of this page) Unclassified	21. No of pages 232	22. Price* A11